PREPARATION, CHARACTERIZATION AND MATERIAL STUDIES ON SPINEL FERRITES AND MIXED RARE EARTH OXIDES

THESIS

Submitted to

GOA UNIVERSITY

For the award of the degree of

DOCTOR OF PHILOSOPHY

In

CHEMISTRY

By

Mr. CHANDAN CHANDRAKANT NAIK

Under the guidance of

PROF. A. V. SALKER

Professor in Chemistry,School of Chemical Sciences,

Goa University

Taleigao Plateau, Goa

AUGUST 2019

DECLARATION

I hereby declare that the work embodied in the thesis entitled "**Preparation, characterization and material studies on spinel ferrites and mixed rare earth oxides.**" is the result of investigations carried out by me under the guidance of **Prof. A. V. Salker**at School of Chemical Sciences, Goa University and that it has not previously formed the basis for the award of any degree or diploma or other similar titles.

In keeping with the general practice of reporting scientific observations, due acknowledgment has been made wherever the work described is based on the findings of other investigators.

Mr. ChandanChandrakantNaik
Research Student
School of Chemical Sciences
Goa University
Goa-403206, India.

August2019

CERTIFICATE

This is to certify that the thesis entitled, "**Preparation, Characterization and Material Studies on Spinel Ferrites and Mixed Rare Earth Oxides**" submitted by **Mr.CHANDAN CHANDRAKANT NAIK**, is a record of research work carried out by the candidate during the period of study under my supervision and that it has not previously formed the basis for the award of any degree or diploma or other similar titles.

Prof. A. V. Salker
Research Guide
School of Chemical Sciences
Goa University
Goa -403206, India

August 2019

CONTENTS

CHAPTER 6

ABBREVIATIONS

AC	Alternating current
BE	Binding energy
DC	Direct current
DRS	Diffused reflectance spectroscopy
DTA	Differential thermal analysis
EDX	Electron diffraction X-ray Spectroscopy
HR	High resolution
ICP-AES	Inductively coupled plasma – atomic emission spectrometry
IR	Infrared
JCPDS	Joint committee on powder diffraction standards
RE	Rare earth
RT	Room temperature
SAED	Selected area electron diffraction
SEM	Scanning electron microscopy
TEM	Transmission electron microscopy
TG	Thermo gravimetry
UC	Up-conversion
UV	Ultra violet
VSM	Vibrating sample magnetometer
XPS	X-ray photoelectron Spectroscopy
XRD	X-ray diffraction

ACKNOWLEDGMENT

I would like to express my sincere gratitude to my guide **Prof. A.V. Salker,** Professor, School of chemical sciences, Goa University, for his valuable guidance, continuous support, motivation, and timely suggestions.

I extend my thanks to **Prof. V. S. Nadkarni,** Dean, School of chemical sciences, Goa University, **Prof. B. R. Srinivasan and Prof. S. G. Tilve** former Head of the department, **Prof. Gourish Naik**, Dean, Faculty of natural sciences, Goa University, former Dean **Prof. J. B. Fernandes** and my subject expert **Dr.V. M. S. Verenker**, for their continuous evaluation and valuable comments.

I thank **Prof. V.Sahni**, Vice-chancellor Goa University, Registrar **Prof. Y. V. Reddy, Prof. S. Shetye**, former Vice-Chancellor, and **Prof. V. P. Kamat,** former registrar, for allowing me to work in the university and for providing me with the necessary facilities. I also thank **Dr. R. N.Shirsat, Dr. S. N. Dhuri, and Dr. Mahesh Majik** for their kind help when needed.

I am indebted to **Prof. I. Furtado** and **Mr. Sanket Gaonkar,** Department of Microbiology, Goa University for their collaboration in carrying out biological studies. I would like to thank **Mr. Ganesh Bera**, Bilaspur University, Chattisgarh, **Dr. Rupesh Kunkalkar**, IIT Bombay, and **Mr. Hemant Dassari** University of Hyderabad for the help rendered in measurements.

I would like to acknowledge **Mr. Girish Prabhu and Mr. Arif Sirdar**, Dona Paula NIO-Goa, **Dr. V. R. Reddy, Dr. A. Banerjee, and Dr. V. Sathe,** UGC-DAE Consortium for scientific research, Indore, Madhya Pradesh, **Dr. K. Kumar**, IIT-ISM Dhanbad, **Dr. Rahul Mohan,** NCAOR – Goa, **Mr. Madhusudan Lanjewar**, USIC,

Goa university, SAIF-IIT Bombay, SAIF-IIT Madras, ACMS IIT Kanpur, MNIT Jaipur, for providing instrumental facilities for characterization of my compounds.

My sincere thanks to **Dr. Shambhu S. Parab, Dr. Madhavi Z. Naik and Dr. Sudarshana Mardolkar** for their continuous help and motivation throughout my research. I am grateful to **Dr. Mithil Faldessai, Dr. Mira Parmekar, Dr. Celia Braganza, Dr. Satu Gawas, Dr. Shrikant Naik, Dr. Rohan Kunkalekar, Mr. Daniel Coutinho, Dr. Dattaprasad Narulkar, Dr. Pranav Naik and Mr. Jeyakantham** for rendering their help in my analysis and in discussions.

I also thank my seniors **Dr. Sagar, Dr. Prajesh, Dr. Kiran, Dr. Sandesh, Dr. Diptesh, Dr. Savita, Dr. Rita, Dr. Durga** and **Dr. Hari**, my friends**, Mr. Aniket Gaonkar, Mr. Pratik Asogekar, Mr. Sudesh Morajkar, Mr. Vishnu Chari, Ms. Apurva Narvekar, Mr. Johnross Albuquerque, Mr. Abhijeet, Mr. Ketan, Mr. Shashank, Mr. Vishal, Ms. Siddhi, Ms. Seneca, Ms. Supriya, Mr. Pavan, Mr. Pushkraj, Ms. Pratiksha, Mr. Rakesh, Dr. Dipesh, Mr. Salman, Ms. Madhavi, Ms. Divya, Ms. Alisha, Ms. Sajiya, Ms. Pooja, Dr. Bhakti, Dr. Neha, Dr. Milind** and my juniors **Ms. Luann, Mr. Vipul, Mr. Ratan, Ms. Neha, Mr. Dinesh, and Ms. Amaraja,** for their support.Thanks for all your encouragement.

I take this opportunity to thank the teaching and non-teaching staff of the School of Chemical Sciences - Goa University, the librarian and other staff in the library of Goa University for being kind and helpful. Very special gratitude goes out to UGC-BSR fellowship for helping and providing the funding for the work

Finally, I must express my profound gratitude to my parents and my brother and sister for providing me with unfailing support and continuous encouragement throughout my studies.

INTRODUCTION

The field of material chemistry is progressing at a tremendous pace in the various field of science and technology. The growth of material chemistry has not merely the extension of the field but newer areas like an optical, laser, optoelectronics, sensors, fuel cells, catalysts, magnetic, biomedical applications, etc have emerged as major thrust areas in recent years. Among the materials, transition and rare earth metal compounds exhibit a wide range of properties due to the presence of ‘d’ and ‘f’ unpaired electrons and variable valence states of the metals.

The advancement in thestudies of nano or micro materials with controlled chemical and physical parameters has provided opportunities in exploring various new phenomenons. By controlling the structure, shape,and size of the particles, a significant improvement in magnetic, optical, luminescence and catalytic propertiesof the materials can be achieved[1–4]. Here, the designing andfunctionalizing of inorganic materials with controlled preparations targeting specific sizes and shapes have been attracting the eyeballs of researchers overthe years.

In recent times metal oxides have been at the heart of numerous dramatic advances in the field of chemistry, physics andmaterials science. Owing to their extensive structural, physical, chemical properties and functionalities, they stand out as one of the most common, most diverse and most probably the richest class of materials. Theycan adopt a wide range ofgeometries with different crystal and electronic structure, which can exhibit metallic,semiconductor, or insulator behavior.

In the nano size, the properties of metal oxides vary considerably than in its bulk counterparts. The substitution of various metals in the host lattice is also responsible for tuning the properties of the metal oxides towards specific applications. The properties such as optical, optoelectronic, magnetic, electrical, mechanical, thermal, catalytic, photochemical, etc can be tuned which makes themexcellent potential candidates for various high-level technological applications[5–14].

Among the several metal oxides studied, spinel structures with the general formula AB_2O_4 are present at the core of current nanoscience owing to of its huge application potential. Here specifically, spinel ferrites are mixed-valence oxides where oxygen anions form a close-packed cubic array, whereas metallic cations inhabit randomly, occupying one-eighth of the tetrahedral sub-lattice and one-half of the octahedral sub-lattice [15]. Very fascinating characteristics of the spinel ferrites are their exceptional magnetic features frequently escorted by other useful properties, such as catalytic activity [15,16].

Spinel ferrites can be divided into three types(a) normal spinel (b) inverse spineland (c) mixed spinel. In inverse spinel structure of ferrite, Fe(III) ions are uniformlyshared at both sites whereas, M(II) ions occupythe octahedral sites. Fe_3O_4 and $NiFe_2O_4$ are common examples of inverse spinel ferrite.In a normal spinel structure, M(II) ions are positioned at tetrahedral sites while Fe(III) ions are placed at octahedral sites. Normal spinel ferrites include $ZnFe_2O_4$.Mixed spinels lie between the normal and inverse spinel structure.They have a random distribution of M(II) and Fe(III) ions in the tetrahedral and octahedral sites.By selectingappropriate combinations of substituent ions in the spinel ferrite, a wide range of properties such as magnetizations,

magnetocrystalline anisotropy, magnetostriction constants,and hysteresis could be achieved and also can be manipulated. Hence, there is hugeattention given tospinel ferrite nanoparticles by the researchers over the globe, starting from their preparation, characterizations and followed by their severalpotential applications. Spinel ferrites are economical and easy to prepare and haveexcellent stabilityover a wide range of conditions. Depending on the type of the cations and their occupancy in the two sub-lattices they can be magnetic or non-magnetic materials.One of the most prominent features of spinel ferrite nanoparticles is their ability to formsuperparamagnetic material[17]. This phenomenon plays akeyroleinnumerousbiomedical applications, catalysis,and environmental remediation strategies.Based on the magnetic properties, ferrites can be classified as “soft ferrites” and “hard ferrites” depending on their low or high coercivity, respectively. Soft ferrites consist ofthe small value of coercivity, so they give rise to low hysteresis loss at higher frequencies.

Ferrites are extensivelyemployed in the electromagnetic core of transformers[18], switching circuits in computers and radio-frequency (RF) inductors, e.g. lithium ferrite, Nickel ferrite,andMn–Zn ferrite.Hard ferrites consist of the large value of coercivity after magnetization, so they can be applied in permanent magnets [19],in radios, e.g. barium and strontium ferrite. In a series of nanoparticles ferrites of the type MFe_2O_4 (where M = Mn^{2+}, Co^{2+}, Ni^{2+}, and Zn^{2+}), the type and quantity of substituent ionplaya key role in generating the changes in the physical properties since the substitution of impurity ions can give rise to new ferrite materials with improved properties.

Although many investigations have been initiated by different researchers around the globe on cobalt and copper ferrites individually, however, a limited extent of work

has been found in the literature on monophasic Cu^{2+} substituted $CoFe_2O_4$. The substitution of Cu^{2+} is expected to alter the magnetic, electronic, catalytic, sensing and biomedical properties. There are hardly any reports available on the effect of non-magnetic Sb^{3+} ion, In^{3+} ion substitution on $CoFe_2O_4$ and Co-Cu ferrite [20,21]. The substitution of Sb^{3+} ions and In^{3+} ion is expected to alter the magnetic, electric and dielectric properties of the host material. Also to the best of our knowledge, the detailed structural, magnetic and dielectric behavior of magnetic ions like RE^{3+} (Where RE= Gd, Dy, Sm, Yb, Eu), Cr^{3+} and Mnion substituted Cobalt-Copper ferrite has not been reported yet. The substitution of these ions is expected to improve the magnetic and dielectric properties.

So it isaimed to prepare a magnetic material having improved electric, catalytic, gas sensing and biomedical properties by sol-gel auto combustion process at a relatively lower temperature.It will be very interesting to analyze the effect of the simultaneous introduction of divalent and trivalent ions on the properties of $CoFe_2O_4$. Also, the procured literature supports intensive research on the substitution of these metal ions in $CoFe_2O_4$ with higher mole percentages but the effect of fractional substitution has seldom been reported. Hence in this report, the basic composition $CoFe_2O_4$ and $Co_{0.9}Cu_{0.1}Fe_2O_4$ has been substituted with small fractions of these ions. The prepared compositions have been thoroughly characterized employing various characterization techniques. The prepared compounds have been further evaluated for their magnetic, electrical, dielectric properties and inhibitory activity against different emerging pathogens.

Owing to the energy crisis and environmental pollution, energy efficiency has become an essentialaspect for all of the energy-consuming products, which is not limited

toan industrial circle but also in everyday life. Light and illumination sources are crucial in numerous fields. It has been reported that electric lighting covers up to 25% of the average energy budget, and lighting and displays occupy 20% of the electricity budget in the world[22].

For several decades down-conversion and Up-conversion luminescent materials havedrawnthe attention of the researchers dueto their numerous applications[23–32].For luminescent properties,the host material is a vitalaspect and plays akey role to achieve highly efficient luminescence. It should possess low phonon frequency, which reduces the non-radiative transitions significantly and henceprovides strong photoluminescence. The Ln_2O_3 types of rare earth sesquioxide especiallycubic Gd_2O_3 and Y_2O_3 are considered as suitablelaser host materials for the progress of down-conversion and Up-conversion luminescent material by substituting with RE^{3+} ions. The essentialconditions required for ideal host material likeexcellent chemical durability, photothermal and photochemical stabilities, low phonon energy, low toxicity, high refractive index, high melting point, and broad transparency range are readily accessible in these materials. These phosphor materials offer intense photoluminescence owing to frequency downshifting as well as Up-conversion processes.

In the down-conversion process, the materials absorb high energy photons and emita large number of photons having low energy. In Up-conversion process materials absorb two or more photons of lower energy (NIR or IR photons) and convert them into high energy photons.The RE ions when substituted in a host material and excited by anappropriate wavelength, offer high luminescence yield with desirable chromaticity. The RE ions consist of abundant energy levels, a lot of them are metastable. They are rich

enoughto generate a large number of narrowband emissions ranging from ultraviolet (UV) to near-infrared (NIR) regions. The luminescence observed in these materials is credited to the f-f or f-d transitions of RE ions and the intensity rely on the site symmetry and the nature of the host matrix. The lanthanide ion consists oflong-lived ladder-like energy levels, which can maintain the large population and emit large photoluminescence intensity for the activator substituted phosphor. The lanthanide ions provide very rich emissions ranging from ultraviolet (UV) to near-infrared (NIR) regions. Thus, the desired emission could be attained after substituting the lanthanide ion in anappropriate host material.

When the RE ions such as Eu^{3+},Tb^{3+}, Er^{3+}, $Ho^{3+,}$and Yb^{3+} are incorporated into the Ln_2O_3 structures; the emission efficiency was reported to enhance drastically[33–38]. The major emission colors of Ln_2O_3substituted with Tb^{3+},Dy^{3+},$Eu^{3+,}$ andTm^{3+} ions are green, yellow, red, and blue respectively. By making use of multiple substituents in the same host matrix and by adjusting the quantityof the substituents various colors can be achieved.The white light-emitting diodes aresteadily becoming a new form of lighting, and they have already surpassed the traditional incandescent and fluorescent sources owing to their eco-friendly and energy-saving lighting applications in the general lighting.Theyhave advantages over traditional incandescent or fluorescent lightings, like higher luminous efficiency, long persistence, energy-saving, and environmentally friendly properties. White light emission can be achieved by a combination of red, green and blue, in suitable proportions. The RE ions are rich producers of red, green, blue and complementary colors. Therefore, white light emission from different combinations of

RE ions has been reported in the literature by several researchers in different host materials[32].

The Eu^{3+}substituted red phosphors have been investigated extensively over the years due to itsgood stability and higher brightness than almost all other red-emitting phosphors[39–44]. The Eu^{3+} activated Y_2O_3 is one of the most frequently used commercial lighting and cathode-ray phosphor[45,46]. The $Tb^{3+}$is one of the activator ionswhich has received enormous attention for its intense green photoluminescence and consists ofa large number of energy levels in which many of them are long-lived[47–53]. However, it may also emit weak blue and red photoluminescence.The Dy^{3+} ion as an activator has two intense fluorescence transitions from the $^4F_{9/2}$ level to the $^6H_{15/2}$ and $^6H_{13/2}$ levels emitting blue and yellow light [44,54–57]. Many researchers attempted to improve this emission intensity by employing different preparationroutes and by the inclusion of sensitizers. It is observed that after the co-doping of Yb^{3+} (sensitizer) with an activator ion, the emission intensity was enhanced[58–61]. Also,Bi^{3+}ion acts as anexcellent sensitizer and has large absorption in VUV/UV regions and emission in the visible region[62–64].

The concept of frequency Up-conversion (UC) was reported in 1960 by Auzel. The emission characteristics of UC materials are majorly dependent on the crystal structure of the host matrix.The energy transfer between the sensitizer and activator ion activelyrely on their separation distance and is determined by their composition ratio in the host matrix. Thus, the UC materials are capable candidates as a spectral converter and generally contains an inorganic host and the incorporated RE ions.In order to attain desired and efficient UC color output, strategies like adjusting the activators like Ho^{3+},

Er^{3+}, and Tm^{3+} with ladder-like arranged energy levels are frequentlyselected,while the Yb^{3+} which comprised of large absorbance in the NIR region around 980 nm acts as a sensitizerto obtain red, green and blue UC outputs[58,59,65]. Under NIR excitation of 980 nm, the Yb^{3+} ions continuously absorb 980 nm photons and transfer the energy to the activator ion, which results in the emission of photons.The Er^{3+}substitutedRE oxides are anexcellent luminescent material for the down-conversion and Up-conversion luminescence [44,59,66–68]. It has a rich and ladder-like electronic energy level structure and is anexceptional candidate mostly for UC luminescence.

Although an enormousquantity of research has been carried out on such systems it still remains a formidable challenge to produce high chromatic purity red UC emissions in Er^{3+} self-sensitized UC systems through suppressing or quenching the probability of green emitted transitions.The UC emission color of Er^{3+} ion can be efficiently tuned from green to red through selectively populating red-emitted level and/or quenching green-emitted levels.The Er^{3+}, Yb^{3+} substituted Gd_2O_3 has been found to be extremely efficient and has been successfully employed in several applications[61,68–70]. For Gd_2O_3:Yb^{3+}/Tm^{3+} UC materialan intense blue and weak red emissions were achieved[71]. For Gd_2O_3:Yb^{3+}/Ho^{3+}, an intense green,andfeeble red emission was attained[44]. The intense red emission with weak emissions in the green region was reported for Gd_2O_3:Yb^{3+} /Er^{3+}phosphors[44].Gd_2O_3as a host material has received a lot of attention because of its excellent UC luminescence and paramagnetic features which are not accessible in the other RE oxides. These excellent optical and magnetic features make it potential magnetic-luminescence dual-mode probe material[72].

Wet chemical methods are most frequentlyemployed to prepare nano-sized particles, however, they take a long time and generate much waste. Many methods such as microemulsion[73], solid-state reaction[74], sol-gel[75], coprecipitation[76,77], hydro-/solvothermal[40,78], spray pyrolysis[79,80], solution combustion [39,81]and microwave method [78,82]etc have been used to synthesize different metal oxides. Thepreparation technique must produce well-dispersed particles having better crystallinity and uniform size; further, it should allow themodification of the structure and material properties by changing the conditions.

Highlights of the thesis

- A series of pristine and substituted Magnetic spinel ferrites have been prepared by using the sol-gelauto combustion method.
- The prepared compounds are thoroughly characterized using various characterization techniques.
- The solid-state studies like DC-electrical resistivity, dielectric properties, magnetic properties, and Mossbauer studies were carried out on the prepared compositions.
- The prepared materials have been also evaluated for their antimicrobial activity.
- A series of pristine and substituted yttrium oxide and gadolinium oxide have been prepared using a chemical combustion method.
- The materials were characterized using several techniques and were studied for down-conversion and Up-conversion photoluminescence processes.

Organization of the thesis

Chapter 1. Introduction: The significance of spinel ferrites and mixed rare earth oxides have been discussed.

Chapter 2. Literature review: This chapter presents a detailed literature review on the spinel ferrites, substituted spinel ferrites, and substituted Y_2O_3 and Gd_2O_3.

Chapter 3. Preparation and instrumental techniques: This chapter describes the sample preparation procedures used in the present work.It also gives brief procedures and principles regardingthe instrumental techniques employed in the characterization process.

Chapter 4.Characterization and spectroscopic studies: The detailedcharacterization and spectroscopic studies of the prepared spinel ferrites and mixed rare earth oxides have been discussed in this chapter.

Chapter 5.Solid-state and optical studies: This chaptercontains the solid-state studies and optical studies carried out on the prepared compositions.

Chapter 6.Summary and conclusion: The overall summary and conclusion based on the results obtained havebeen discussed in this chapter.

LITERATURE REVIEW

2.1 Introduction

Spinel ferrites substituted with magnetic and non-magnetic metal ions have gathered the attention of several researchers over the years. The effects of substitution on the various properties of host material have been documented in the literature. The luminescence study of RE^{3+} substituted RE_2O_3 phosphors has also been reported by several research groups indicating their application in various fields. These metal oxides were reported to be prepared by several methods. In this chapter, the previous literature reports related to thecurrent studies have been discussed.

2.2 Preparation methods

There are several preparative techniques reported in the literature for the preparation of metal oxides. Among all these methods, the most efficient ones such as co-precipitation, sol-gel, sol-gel auto combustion, hydrothermal, and combustion method are discussed in this section. The solid-state reaction method is a conventional preparation route widely employed for preparing ceramics. It requires prolonged heating at high temperatures (1000 – 1500 °C) and thus has several drawbacks as far as the fabrication of nanosized ceramics is concerned. This method produces agglomeratedparticles having micrometer-size and exhibit irregular morphology. It is an environment-friendly technique and does not produce toxic or unwanted wastebut require high energy and more time.

The co-precipitation process is a well-established method and is considered asasimple, efficient, scalable, rapid, and economical, which is frequently employed for

the preparation of several compositions. It is a wet chemical method and involves dissolving two or more water-soluble metallic salts in water and their simultaneous precipitation with the help of base such as NaOH or NH_4OH under controlled pH.In the co-precipitationmethod, the calcination temperature required for the formation of the desired material is low, hence results in lower particle size.

The sol-gel process is the most versatile technique used for the preparation of metal oxide nanoparticles. In this method, metal ions in an aqueous medium are complexed with the suitable complexing agent. The metal complexes formed in water as sols can be converted to gel with the evaporation of water. After complete evaporation of water, it forms a carbonaceous char which after calcination at higher temperature gives metal oxide.

The sol-gel auto combustion technique follows the same procedure as above if the ensuing gel contains sufficient oxidizing moieties like nitrates it can undergo a redox reaction with reducing organic moieties, proceeding to redox combustion with a little initiation of heat. Since the sol-gel process ends up with innate combustion, the process is called auto-combustion and the method is sol-gel auto-combustion. This method reduces the char content of the metal oxide precursors where most of the carbon is oxidized to CO_2. Organic acids like citric acid, succinic acid, oxalic acid, tartaric acid, acrylic acid, etc. can be employed with metal ion sources to form the sol.

In the hydrothermal method, the pH of the aqueous solutions of the desired metal ions is adjusted by the addition of a base, and the mixture is pressurized in an autoclave at the desired temperature. Parameters like pressure, temperature, and reaction time, are

adjusted to manage the nucleation rate which controls the crystal growth. In this process the metal hydroxides are formed initially, which are oxidized and converted into the crystalline material because of heat treatment and pressure [15]. The hydrothermal process allows altering the particle size and shapes by varying the starting material, reaction temperature and reaction time and pressure. In the solvothermalprocess, an organic solvent is used replacing water.

Combustion processuses the energy generated by the exothermic decomposition of a redox mixture of metal nitrates with an organic compound, which plays the role of fuel to form oxides. Combustion method involves an exothermic decomposition of fuel-oxidant precursor-like urea - nitrate, glycine - nitrate, DHF - nitrate, etc, relatively at lower temperatures [15,83,84].

2.3 Spinel ferrites

The spinel ferrites can be chemically represented MFe_2O_4 where M is a divalent metal ion, for example, Mg^{2+}, Ni^{2+}, Co^{2+}, Zn^{2+}, Mn^{2+}, Cu^{2+}, Cd^{2+} or a combination of these ions, for instance, Mn-Zn, Ni-Zn, Ni-Co, Co-Cu, and Cu-Zn, etc. Spinel ferrites can be classified as normal spinel, inverse spinel and mixed spinels [85].

2.4 Magnetic properties

To understand the magnetic features of the spinel ferrites one has to consider the Neel model of ferrimagnetism. In the ferrite of the type AB_2O_4,there are three A-A, B-B and A-B super-exchange interactions, among them A-B interaction is the strongest. The overall magnetization (M) in spinel ferrites is the difference between the magnetization of the two sub-lattices i.e. ($M = M_B – M_A$) [86]. Therefore the decline in magnetization at B

sub-lattice decreases the net magnetization. The magnetic features of the spinel ferrite can be tuned through site-specific occupation of the substituents in spinel lattice. However, the site occupation should be carefully assessed and controlled. In the inverse spinels the distribution of the ions is $(Fe^{3+})_{tet}[M^{2+}Fe^{3+}]_{oh}O_4$ while in normal spinels, the distribution is $(M^{2+})_{tet}[Fe^{3+}\ Fe^{3+}]_{oh}O_4$. Substitutions of cations alter the magnetic properties of the spinel ferrite, which is the replacement of Fe^{3+} ions or M^{2+} ions by magnetic, diamagnetic or weakly magnetic ions of almostthe same size. The size and quantity of metal ions incorporated, site preference, the valency of the substituent, and cation distribution are the several aspects that affect the magnetic properties.

2.5 Applications

2.5.1 Magnetic application

Spinel ferrites are well known for their magnetic properties. Several researchers explored the magnetic properties of spinel ferrites and claimed their potential application in permanent magnet [87–89]. Hu et al. reported the application of spinel ferrites in nonvolatile memory devices [90]. The application of spinel ferrites in magnetic hyperthermia has been studied by several research groups [91–94]. The potential application of spinel ferrites in micromagnetic actuation technology has been proposed by Dubraja et al. [95]. The magnetic property of spinel ferrite makes it a suitable candidate for magnetic drug delivery application [96–98]. Spinel ferrites have been extensively investigated for magnetic resonance imaging (MRI) [99–101].

2.5.2 Removal of contaminants by adsorption

Adsorption is the mostpreferred technique for the separation and to get rid of harmful materials from the contaminated waters, mostly owing to its ease and high efficiency. The separation of the sorbent after the adsorption process is the major difficulty faced, which can be energy and time consuming. Nevertheless, the utilization of magnetic compounds for adsorption makes the process of separation more convenient by allowing magnetic separation with an external magnet. The high surface area and great adaptability for binding particular functional groups on their surfaces for specific contaminants makes spinel ferrites the perfect material for the design and development of novel adsorption strategies[15].

Extensive utilization of organic dyes has turned out to be a severe environmental concern since these classes of organic compounds are not easy to decompose. The waste discharged from textile industry consists of dyes that can pollute the water bodies and develop certain health hazards and environmental pollution. The stable and complex aromatic molecular structure of dyes makes them difficult to degrade. They have carcinogenic and mutagenic effects on humans and aquatic lives [15]. In recent times, the application of pure and modified MFe_2O_4 is found to be the finest option owing to their excellent adsorption capacity, ease of recovery and reuse. The $CoFe_2O_4$ have claimed to get rid of direct red 80, direct green 6, and acid blue 92 dyes from aqueous solution. The $CoFe_2O_4$ coated by PEG chains were found to be great adsorbents for numerous dyes, for instance, methyl orange, methylene blue, congo red, trypan blue, and brilliant blue malachite green [102,103]. Similarly, $NiFe_2O_4$ was applied for the removal of reactive

blue 5 dye [104]. The $ZnFe_2O_4$ have shown improved degradation capacity in the removal of acid red 88 dye from an aqueous solution [105].

Industrial wastes and agriculture activities release hazardous and toxic substances in the water sources which leads to the contamination of drinking water. Continuous consumption of this water may cause chronic diseases such as renal failure, liver cirrhosis, hair loss, and chronic anemia. These diseases are related to the presence of heavy metals like arsenic, mercury, lead, cadmium, and chromium in water. Hence, cost-effective technology for the purification of water is necessary. The application of magnetic nano-materials has immense potential to improve water purification [84]. Recently, $CuFe_2O_4$ NPs have been used for removal of As and Cd from the wastewater [106,107]. Viltuznik et al. investigated the removal of Pb(II) from wastewater by adsorption using $CoFe_2O_4$@SiO_2-RSH nanosystem [105]. The γ-Fe_2O_3 NPs incorporated into graphene, and cellulose was employed as an adsorbent for the removal and recovery of Cr(VI) from the wastewater [108,109]. The $CoFe_2O_4$ NPs were claimed as promising materials to be used for the removal of toxic Cr(VI) from printing press wastewater [110].

2.5.3 Catalysis

Magnetic spinel ferrite nanoparticles and their composites have been emerging as a capable material in the near future for the catalytic applications. The benefit of magnetic ferrites in catalysis is that they can be easily separated and recovered from the system after completion of the reactions with an external magnet. Recently Dutta and Phukan reported Cu-doped $CoFe_2O_4$ as a magnetically recoverable catalyst for C-N cross-

coupling reaction[16]. Lakshminarayana et al. reported $CuFe_2O_4$ nanowires as a highly active catalyst for C–C couplings and synthesis of benzofuran derivatives[111].Kiyokawa and Ikenagareported oxidative dehydrogenation of but-1-ene at low temperature with copper ferrite catalysts[112]. One-pot synthesis of benzimidazole using DMF using $CuFe_2O_4$catalystwas proposed by Rasal and Yadav[113].Goyalet al. studied $CoMn_{0.2}Fe_{1.8}O_4$ ferrite as a versatile catalyst for the reduction of nitroaromatic compounds[114]. Bhatet al. proposed nickel hydroxide/cobalt−ferrite for alcohol oxidation[115].Deng et al.reported$CoFe_2O_4$ magnetic nanoparticles as a highly active heterogeneous catalyst of oxone for the degradation of diclofenac in water[116].$NiFe_2O_4$ was reported to be an efficient catalyst in a typical industrial process like the water–gas shift reaction[117].The photocatalytic performance of spinel ferrites has been evaluated by several researchers over the years [118–121].

2.6 Copper substituted cobalt ferrite

Among spinel ferrites, $CoFe_2O_4$ is an interesting material and has been studied extensively considering its unique and exciting features, such as large cubic magneto-crystalline anisotropy, moderate *Ms*, higher *Hc*, and high *Tc*. $CuFe_2O_4$ is known to exist in two phases, namely cubic and tetragonal due to Jahn–Teller distortion.The incorporation of divalent Cu^{2+} ions in $CoFe_2O_4$ enables some tunable modifications in its properties hence found to have potential application in various fields. It was observed that the copper could enhance the catalytic activity of $CoFe_2O_4$. It has been also investigated for its potential in antimicrobial activity and as a sensor. The Cu^{2+} substitution generates a structural phase transition accompanied by the decrease in the crystal symmetry due to co-operative Jahn–Teller effect [8]. The introduction of copper renders $CoFe_2O_4$ as an

appropriate material for application in catalysis, sensing, and wastewater treatment. Since Cu^{2+} is a weakly magnetic ion ($3d^9$) the incorporation of Cu^{2+} ions in place of Co^{2+} ions ($3d^7$), the magnetic moment is expected to decrease. Literature studies show that Cu^{2+} ions prefer to occupy the B sites [122]. The B site occupancy of the Cu^{2+} ions will force some of the magnetically crucial Co^{2+} ions to migrate from B to A site. The overall magnetization in ferrites is $M = M_B - M_A$ i.e. difference in magnetization at B and A sites. Hence the M_s values with Cu^{2+} substitution decreases in most of the cases as reported by several authors[123–126]. The *Hc* values decreased with Cu^{2+} substitution due to decreased magnetic anisotropy as Cu^{2+} ions have lower anisotropy than Co^{2+} ions. Batoo et al. [127] also observed a decreasing trend in *Ms* values with Cu^{2+} substitution but an increasing trend in *Hc* was also seen [127]. Reports show that AC magnetic susceptibility studies carried out showed a decreasing trend in *Tc* with Cu^{2+} substitution in $CoFe_2O_4$ due to the weakening of A – B super-exchange interactions [128]. Although Ahmed et al. [129] reported an increase in *Tc*up to (x = 0.3) and decreased thereafter. The dielectric properties of Cu^{2+} substituted $CoFe_2O_4$ have been investigated by many researchers. Ahmed et al. [130] and Faraz et al. [131] observed an enhancement in dielectric constant with Cu^{2+} substitution while Jnaneshwara et al. [132] and Hashim et al. [125] observed a decreasing trend. The above observations were credited to the cation rearrangement owing to substitution. Also, the Cu^{2+} ion substitution is observed to show an enhancement in the catalytic activity of $CoFe_2O_4$. Alamdari et al. [4] claimed that the Co-Cu ferrite is highly active and magnetically separable nanocatalyst for the synthesis of chromene derivatives. Recently Ghadari et al.[133] studied graphene oxide supported copper-cobalt ferrite material as an efficient catalyst for the one-pot tandem oxidative

synthesis of 2-phenyl benzimidazole derivatives in good yields. Dutta and Phukan [16] also examined Cu doped $CoFe_2O_4$nanoparticles as a magnetically recoverable catalyst for C-N cross-coupling reaction. Kirankumar and Sumathi [134] carried out the photocatalytic studies against congo red dye using cobalt copper ferrite. Velinov et al. [135,136] evaluated the superparamagnetic behavior of copper substituted $CoFe_2O_4$ and also investigated its catalytic activity for CO conversion and for methanol decomposition. The copper substituted $CoFe_2O_4$ have been prepared by several methods like co-precipitation [16,123,131], sol-gel [122,125,128,137–139], hydrothermal [4,126,140,141], combustion [127,132,134], microemulsion [142], solid-state reaction [143] and polymeric precursor [144] method.

Antimicrobial properties of transition metal substituted ferrite nanoparticles have been widely studied over the years. The enhanced effect of Cu^{2+} substituted $CoFe_2O_4$ against multidrug-resistant*E. Coli* and *Staphylococcus aureus* has beendemonstrated recently. Substitution of these metals using various synthetic methods allows variation in properties with greater toxicity control and successful application. The separation of these used biocompatible antimicrobial agents from the heterogeneous system is necessary. The recovered agents can be reused to enhance efficiency, reduce the cost and avoid secondary pollution. Although separation strategies like centrifugation, free settling, and filtration have been widely adopted, they require sophisticated operating equipment, high operational costs with loss of antibacterial agents. Therefore, an efficient and inexpensive method like magnetic separation with the assistance of an external magnetic field is exceptionally desirable to achieve the goal of fast and efficient separation. Kirankumar and Sumathi [134] studied the antibacterial activity of Cobalt-Copper Ferrite. Sanpo et al.

[135,136,145–147] and Samavati et al. [148] showed that the Cu^{2+} ion strongly influences the antibacterial properties of $CoFe_2O_4$.

2.7 Antimony substituted spinel ferrites

There are very few reports available on the effect of non-magnetic Sb^{3+} ion substitution in $CoFe_2O_4$. The substitution of Sb^{3+} ions is expected to alter the magnetic, electric and dielectric properties of the host material. Literature studies showed that antimony substituted spinel ferrite have been prepared by several methods such as solid-state reaction [20,149,150], sol-gel [151,152], and hydrothermal method [153–155]. Sb^{3+} substitution preferably occupies B sublattice in spinel ferrite [20,156,157]. Magnetic studies carried out showed that with the substitution of Sb^{3+} ions, the magnetic parameters such as M_s and H_c decreased [20,152–154,156]. The decreased M_s values could be possibly due to B site occupancy and diamagnetic nature Sb^{3+} ions whereas decreased H_c values could be due to decreased magnetic anisotropy [20,156]. Although Sridhar et al. [153] and Lakshmi et al. [154] obtained an increasing trend in *Hc* values with Sb substitution. The dielectric studies carried out by Sridhar et al. [153] and Lakshmi et al. [154] showed a lower value of dielectric constant when doped with Sb^{3+} ions.

2.8 Rare earth substituted Cobalt ferrites

The lower coercivity of spinel ferrites is a major obstacle that considerably limits their usage in high-density magnetic recording application and elevating its value is a challenge. Hence substantial efforts have been made for hunting down the novel materials with higher coercivity. Substitution of rare earth metal ions having larger ionic

radii significantly enhances the coercivity due to the presence of stronger magneto-crystalline anisotropy. Hence the storage capacity of the magnetic recording systems like $CoFe_2O_4$ can be enhanced by substituting rare earth metal ions. In this regard, many researchers investigated the effect of Rare earth ion substitution on magnetic structural,and dielectric features of cobalt ferrite. In rare-earth metals, the carriers of magnetism are the 4f electrons, the introduction of these metal ions in spinel ferrite gives rise to fascinating materials. The magnetic moments of lanthanide elements vary from 0 (La) to 10.6 μ_B (Dy). Despite their fascinating magnetic properties, pure rare earth metals cannot be applied in practical applications because of their low T_c. The rare-earth substituted $CoFe_2O_4$ is a promising material for magneto-optical recording applications, displaying lower T_c compared to pristine $CoFe_2O_4$. Various methods have been applied for the preparation of RE substituted $CoFe_2O_4$ namely co-precipitation [158–162], sol-gel [163–167], hydrothermal/ solvothermal [168–171], solid-state reaction method [172–176], reverse micelle process [177,178], combustion method [179], and polyol method [180]. Most of the literature reports show that with RE ion substitution in $CoFe_2O_4$ magnetization gets lowered [159,173,181–187] while coercivity enhanced [181–183,185,188,189]. The reduction in $M_s$is because of the migration of relatively crucial Co^{2+} ions ($3d^7$) from the B to the A sites in the ferrite lattice [190]. In spinel ferrites, the overall magnetic moment depends upon the interactions of magnetic ions residing at A and B sites. The lowering of M_s with substitution could be because of the decreased strength of A-B super-exchange interactions. According to literature, in the RE substituted ferrites, RE^{3+}-O-$Fe^{3+,}$and RE^{3+}-O-RE^{3+} interactions also exist but are relatively weak as compared to Fe^{3+}-O-Fe^{3+} interaction. Hence, the overall magnetic

moment should show a decrease when substituted with RE ions. For RE ions, also the proper ordering of magnetic moment originating from the localized 4f electrons can be observed only at less than 40 K [191]. Therefore, the addition of Cu^{2+} and RE ions in the ferrite lattice resembles the inclusion of non-magnetic atoms in the B site. The improved H_c with RE substitution compared to pristine Co-Cu ferrite is ascribed to the large single-ion anisotropy of RE ions. A larger magnetic anisotropy gives rise to larger H_c when RE ions partially replace Fe^{3+} ions. Hence, enhancement in H_c is accountable for magnetic anisotropy. TheincreasedM_s values with RE substitution have been reported by Lohar et al. [192] and Prathapani et al. [193]. While a decreased $H_c$has been reported by Guo et al [186]. Mössbauer study of Y^{3+} substituted $CoFe_2O_4$ showed a superparamagnetic behavior [194]. An increase in dielectric constant with RE^{3+} ion substitution has been reported and was attributed to the cation rearrangement and size effect [183,195,196]. While a decrease in dielectric constant with RE substitution has been reported by several authors [159,173,183,184]. Demicri et al. [158] investigated $CoFe_2O_4$ nanoparticles by substituting La^{3+} ions in place of Fe^{3+} ions for efficient hyperthermia heating. Kevadiya et al. [197] proposed application of Eu^{3+} doped core-shell silica $CoFe_2O_4$ functionalized nanoparticles in MRI, Kharat et al. [198] proposed Dy^{3+} substituted Fe rich $CoFe_2O_4$ for magnetoelectric sensor applications. Gd^{3+} substituted ferrites have also been investigated extensively for their multifunctional behavior as active hyperthermia and MRI contrast agents.

2.9 Chromium substituted $CoFe_2O_4$

Several methods were employed for the preparation of Cr substituted $CoFe_2O_4$ namely coprecipitation [199–201], sol-gel [202–206], solid-state reaction [207–210], and hydrothermal method [211–213]. According to literature studies, the magnetic studies revealed a decrease in M_s and H_c values with Cr substitution in $CoFe_2O_4$ [199,200,202,203] indicating a lesser magnetic character, B site occupancy [209,214] and weaker A-B super-exchange interactions. But the magnetic investigations carried out by Toksha et al. [205] showed a decreasing trend of M_s but the H_c values increased which was attributed to the size effect. The Mossbauer studies carried out by Raghasudha et al. [215] indicated a super-paramagnetic behavior with Cr substitution in $CoFe_2O_4$. The dielectric studies revealed that higher dielectric constant was observed with Cr substitution in $CoFe_2O_4$[199,202]. With the increase in Cr content in $CoFe_2O_4$ increase in DC electrical resistivity was also reported [200,215]. Singh et al. [216] showed that the partial substitution of Fe by Cr in $CoFe_2O_4$ greatly enhances the electrocatalytic activity.

2.10 Manganese substituted cobalt ferrite

Manganese substituted $CoFe_2O_4$ have been studied by many researchers in recent years. The methods like coprecipitation [217,218], combustion [219–222], sol-gel [223–225], solid-state reaction [226–229] and hydrothermal method [230] have been employed for the preparation of manganese substituted $CoFe_2O_4$. Magnetic studies carried out by several researchers on Mn substituted $CoFe_2O_4$ revealed that magnetization initially increases with Mn substitution followed by decrease [227,229,231,232]. A decrease in H_c values was also observed with Mn substitution attributed to decreased magnetic

anisotropy [224,227,229,231,232]. The increased $M_s$values could be attributed to the initial A site occupancy of Mn ions at lower concentration and further occupies B site at higher concentration. Ramana et al. [232] proposed that initially Mn could have been substituted as Mn^{2+} and then as Mn^{3+}. A continuous decrease in M_s values with Mn substitution in $CoFe_2O_4$ have been reported by Jauhar et al. [224] and Goyal et al.[225]. The decrease was attributed to the substitution of Fe^{3+} ions (5 μ_B) with lesser magnetic Mn^{3+} ions (4 μ_B) in the B site. Cojocariu et al. [218] reported an increase in M_s and H_c values with Mn substitution in $CoFe_2O_4$ which was accounted for the size effect. A significant decrease in T_c values with Mn substitution in $CoFe_2O_4$ was also claimed by Tsay et al. [227] and Paulsen et al. [233], due to the weakening of A-B exchange interactions. Application of Mn-substituted $CoFe_2O_4$ in magnetic stress sensors has been proposed by many researchers [229,231,233]. The catalytic degradation studies of methylene blue and Remazol turquoise blue indicated that the presence of Mn in $CoFe_2O_4$ enhances the degradation of dyes [224]. Goyal et al. [225] proposed Mn substituted $CoFe_2O_4$ as magnetically separable heterogeneous catalysts for the conversion of nitroarenes to aromatic amines.

2.11 Indium substituted spinel ferrite

The introduction ofnon-magnetic ions like In^{3+} in spinel ferrites can disturb the balance of the tetrahedral and octahedral sites and therefore can affect the properties of the entire material. The preparation of In^{3+} ion substituted spinel ferrite have been reported by sol-gel [234–236], coprecipitation [237–239], hydrothermal [240], and solid-statereaction method [241–243]. Literature reports show that with In^{3+} ion substitution magnetization increases at lower concentrations whereas decreases at higher

concentrations [235,238,242,244–248]. At lower concentrations, In^{3+} ions prefer to occupy the A sub-lattice by the replacement of Fe^{3+} ions and thereby enhance the net magnetization while at higher concentrations they will prefer to occupy the B sub-lattice. A continuous and steady increase in M_s with In^{3+} substitution in spinel ferrite is observed by many researchers and was assigned to the A site occupancy of In^{3+} ions [234,236,241,243,249]. Verma et al. [247] observed a steady decrease in magnetization with In^{3+} substitution in Mg-Mn-Ni ferrite and hence proposed B site occupancy by In^{3+} ions. When In^{3+} ions (0 μ_B) replace Fe^{3+} ions (5 μ_B) at the B site, there arise additional, In^{3+}-O-In^{3+}, In^{3+}-O-Fe^{3+} interactions which are much weaker than Fe^{3+}-O-Fe^{3+} interactions, hence the magnetization of B sub-lattice drops maintaining the magnetization of the A sub-lattice constant. Vlazen et al. [240] also obtained decreased values of *Ms* and *Hc* with In^{3+} substitution which was credited to the formation of secondary phase (In_2O_3). Nongjai et al. [250] also reported enhanced*Hc* values attributed to the transition from multidomain to single domain nature. Kumar et al. [238] observed an increase in H_c with In^{3+} ion substitution in Mn-Zn ferrites and factors such as magnetocrystalline anisotropy, microstrain, shape anisotropy, were held responsible. A decrease in *Hc* with In^{3+} substitution was reported by Shirsath et al. [243] and Meng et al. [248] attributed to its porosity. Literature studies showed a considerable decrease in *Tc* with In^{3+} ion substitution which is due to weaker A-B exchange interactions developed [234,241,243–245]. Mathur et al. [239] observed a superparamagnetic behavior with In^{3+} substitution in Mn-Zn ferrite. The above-mentioned reports reveal that there are still contradictions regarding the site preference by In^{3+} ions which can occupy both A and B sites but have a strong tendency to occupy the A sites at lower concentrations.

Pandit et al. [242] observed a decreasing trend in dielectric constant with indium substitution. When In^{3+} ions replace Fe^{3+} ions at A and B site it acts as an electron trap and obstructs electron hopping between $Fe^{3+}$and Fe^{2+} charge carriers and consequently decreasing the polarisation and hence ε′. The enhanced DC - electrical resistivity with indium substitution in spinel ferrites have been observed by several researchers which were assigned to the reduction in Verwey's hopping mechanism due to cation rearrangement [245,249–251].

2.12 Yttrium oxide (Y_2O_3)

The major resource of yttrium at present is monazite. Y_2O_3 has a high dielectric constant, high refractive index, large band gap (5.8 eV) and a melting point of 2410 ℃. It exhibits cubic, monoclinic and hexagonal crystal structure. The cubic phase and the monoclinic phase are commonly found in most preparation processes and have significantly different thermal and optical properties. Hence it is essential to control the phase of Y_2O_3 in a preparation process. Y_2O_3 has numerous applications in various fields, for instance as laser materials, catalysts or catalyst support, advanced ceramics and transparent matrices for phosphor materials when doped with RE metal ions.

2.13 Y_2O_3: Eu^{3+} Phosphors

Yttrium oxide (Y_2O_3) possessing body-centered cubic structure acts as an exceptional host material when trivalent Ln^{3+} ions (Eu^{3+}, Er^{3+}, Tb^{3+}) are used as dopants. It has a wide band gap ~ 5.8 eV and small phonon energy (380 cm^{-1}) which enhances the probability of radiative transitions among electronic energy levels of RE ions in the host material. The Eu^{3+} activated Y_2O_3 is a red-emitting phosphor and has been examined extensively

because of their much higher brightness compared to other red-emitting phosphors. It is one of the most often employed commercial lighting and cathode-ray phosphor.

The preparation techniques like hydrothermal/ solvothermal [78,252,253], combustion [254–257], sol-gel [258–260], co-precipitation [261–263], and solid-state reaction method [264–266] have been utilized for the preparation of Y_2O_3:Eu^{3+} phosphors. It shows high luminescence efficiency with exceptional red color purity, which makes it a suitable material for its application in red – color emitting luminescent material. The luminescence of Eu^{3+} ions generating from transitions among 4f levels of Eu^{3+} is mostly because of the electric dipole ($^5D_0 \rightarrow {}^7F_2$) and/or magnetic dipole ($^5D_0 \rightarrow {}^7F_1$) transitions [254]. The occurrence of a dominant red luminescence ~ 611 nm under UV excitation of ~ 250 nm is observed in most of the cases [33,252,267,268] but in some instances was observed at ~ 394 nm [258,269]. It has been noticed that with increasing Eu^{3+} concentration the emission intensity enhanced which was attributed to the existence of a higher number of PL active centers[269–271] while above certain concentration the emission intensity reduced owing to the phenomenon called concentration quenching [272–275].

Several researchers claimed that co-doping elements like Li, Ca, Bi, Na, K, Gd, Tb with Eu^{3+} in Y_2O_3 could improve the PL properties [42,254,261,268,274,276–278] following an energy transfer process. The shape and size dependence of PL property of Eu activated Y_2O_3 have been also reported [265,276,279–283]. Kabir et al. [263] and Yu et al. [284] claimed that the surfactant employed in the synthesis process played a crucial role in controlling the luminescence property. The temperature-dependent emission intensity has also been examined [272,285,286]. The Y_2O_3: Eu^{3+} phosphors are proposed

to have potential applications as biomarkers [78], temperature sensors [255] and as a photocatalyst [256].

2.14 Y_2O_3: Er^{3+} Phosphor

Several synthesis methods like sol-gel [66,260,287,288], combustion [255,289–291], hydrothermal [7,292,293], co-precipitation [294–297], and pulsed laser deposition [298] have been used for the preparation of Y_2O_3: Er^{3+} phosphors. The Y_2O_3: Er^{3+} phosphors are mostly used in combination with Yb^{3+} ion as an Up-conversion material. The Y_2O_3: Er^{3+} phosphor gives strong green emission in the region 520-565 nm corresponding to $^2H_{11/2}$, $^4S_{3/2} \rightarrow {}^4I_{15/2}$ transition and feeble red emission in the region 650-665 nm attributed to $^4F_{9/2} \rightarrow {}^4I_{15/2}$ transition [66,260,287,289,291]. The dependence of PL property of Y_2O_3: Er^{3+} phosphor on size and morphology of the particles has been reported by Gruzintsev et al. [295]. Scarangeela et al. [299] and Back et al. [287] observed an increase in PL intensity with co-doping with Bi which acts as a sensitizer. Several researchers proposed their possible usage in high dose dosimetry, biomedicine, optical amplifiers, lasers, displays, bioanalysis, and telecommunications [66,255,300]. Kumar et al. [293] reported Y_2O_3 combined with Er^{3+} and Yb^{3+} as a potential security ink for anti-counterfeiting applications. Rai et al. [301] proposed Y_2O_3 co-doped with Er^{3+}, Eu^{3+} and Yb^{3+} phosphor for lighting and sensing applications.

2.15 Gadolinium oxide (Gd_2O_3)

Gd_2O_3 has been considered as an important metal oxide which has been examined comprehensively in the past few years owing to its technological significance. The most common chemical form of gadolinium is Gd_2O_3, which is a thermally stable having

melting point up to 2420 ℃. It has three structural polymorphs cubic, monoclinic, and the hexagonal. Crystalline Gd_2O_3 usually prevail in a cubic phase at ambient temperature and transforms to monoclinic phase beyond 1250 °C. Due to their optical, electronic, and chemical features arising from 4f electrons, Gd_2O_3 has been extensively employed in the fields of luminescence devices, optical transmission, biochemical probes, and medical diagnostics.

2.16 Gd_2O_3:Yb^{3+}/Er^{3+} Phosphors

Cubic Gd_2O_3 has been reported as host material due to its superior Up-conversion luminescence efficiency. There are a number of reports containing activator ions like Er^{3+}, Tm^{3+}, $Ho^{3+,}$ etc. co-doped with Yb^{3+} ionswhich act as a sensitizer, in Gd_2O_3 host lattice and efficient Up-conversion luminescence could be achieved. Synthetic strategies like co-precipitation [67,302–305], solid-state reaction [31,306–308], sol-gel [309–312], a hydrothermal/solvothermal method [313–316], and combustion method [215,317,318] has been employed for the preparation of Gd_2O_3: Yb^{3+}/Er^{3+} phosphors. In Gd_2O_3: Yb^{3+}/Er^{3+} phosphors the Yb^{3+} ion absorbs the laser photon and goes to its excited state. Then the Yb^{3+} ion in excited state relaxes from an excited state to ground state and transfers its energy to an Er^{3+} ion which enhances the population at the $^4I_{11/2}$ energy level. The populated $^4I_{11/2}$ energy level in an Er^{3+} ion further gets excited to $^4F_{7/2}$ energy level by 3 processes [31].

Many researchers showed that the spectral color purity of Gd_2O_3: Yb^{3+}/Er^{3+} phosphors can be tuned by adjusting the dopant concentration. The Up-conversion spectra of Gd_2O_3:Yb^{3+}/Er^{3+} phosphors mostly shows dominant red emission (~660 nm,

$^4F_{9/2} \rightarrow {}^4I_{15/2}$) accompanied by weak green emission (~560 nm, $^2H_{11/2}$ / $^4S_{3/2} \rightarrow {}^4I_{15/2}$) [302,319]. The reports claimed that by increasing Yb^{3+} content in Gd_2O_3: Yb^{3+}/Er^{3+} phosphor the green emission gets suppressed but an enhancement in red emission was achieved [320–322]. Billir et al. [317] obtained an unexpected white light emission from Er^{3+}/Yb^{3+} co-doped Gd_2O_3 nano-phosphors. Li et al. [323] reported an enhancement in luminescence of Gd_2O_3:Yb^{3+}/Er^{3+} phosphors by co-doping with Zn^{2+} and Li^+ ions. The researchers proposed the potential application of spectrally pure Gd_2O_3:Yb^{3+}/Er^{3+} phosphor material in fingerprint recognition, multicolor printing [302], biomedicine [316], optical thermometry [318,324], solar cells [31], photovoltaic's, photocatalysis [256], wearable optoelectronics [303], sensors [305,325], cancer theranostics, bimodal imaging [319], bioimaging [321,326], and high performance contrast agent for multimodal imaging [327].

2.17 Gd_2O_3: Yb^{3+}/Ho^{3+}

Gd_2O_3: Yb^{3+}/Ho^{3+} phosphors are reported to show Up-conversion luminescence under laser excitation of 980 nm. The Gd_2O_3:Yb^{3+}/Ho^{3+} phosphors were prepared by combustion [328], polymer complex solution [329], co-precipitation [44,330], sol-gel[331] methods. In Up-conversion materials Yb^{3+} is chosen as a NIR sensitizer and Ho^{3+} ion as a luminescent ion. Reports show that the Gd_2O_3: Yb^{3+}/Ho^{3+} phosphors give major green emission (~550 nm, $^5S_2/^5F_4 \rightarrow {}^5I_8$) accompanied by relatively weak red emission (~ 667 nm, $^5F_5 \rightarrow {}^5I_8$) [44,65,330,332,333]. An enhanced Up-conversion emission in the Gd_2O_3: Yb^{3+}/Ho^{3+} phosphors by introducing Zn^{2+} and alkali metal ions have been observed [304,329,331]. The potential applications of these phosphors in temperature sensing, a plasma display, bioimaging, [328], fingerprint detection in

forensic science [65] have been proposed. Yin et al. [333] proposed that Gd_2O_3: Yb^{3+}/Ho^{3+} phosphor has the potential to be developed into a safe and highly efficient magnetic resonance and fluorescence nanoprobe in cell molecular imaging of cancer.

PREPARATION AND INSTRUMENTAL TECHNIQUES

3.1 Preparation

Pristine and substituted spinel ferrites were prepared by employing the sol-gelauto combustionroute utilizing malic acid as a complexing agent. The RE substituted Y_2O_3 and Gd_2O_3 were prepared by employing the combustion method. The heat treatment was given to the materials to obtain desired monophasic compounds.

The compositions obtained were characterized by several instrumentaltechniques such as TG-DTA, XRD, ICP-AES, IR, Raman, and XPS. The obtained materials were further studied using SEM-EDX, TEM-SAED, Mossbauer spectroscopy, VSM, AC magnetic susceptibility, DC- electrical resistivity set up, LCRQ meter for dielectric studies, UV-DRS, fluorimeter for photoluminescence studies, and Up-conversion fluorimeter for Up-conversion studies.

3.1.1 Sol-Gel Auto combustion method

3.1.1.1 Preparation of Cu^{2+} and Sb^{3+} substituted cobalt ferrite.

$Co_{1-x}Cu_xFe_2O_4$ (where x = 0.00, 0.05, 0.10, 0.15, 0.20 and 0.25)

$CoFe_{2-x}Sb_xO_4$ (where x = 0.00, 0.03, 0.06, and 0.09)

An intended quantity of cobalt nitrate hexahydrate ($Co(NO_3)_2 \cdot 6H_2O$, Sigma Aldrich 99%), copper nitrate tri-hydrate ($Cu(NO_3)_2 \cdot 3H_2O$, Sigma Aldrich 99%), and iron nitrate nonahydrate ($Fe(NO_3)_3 \cdot 9H_2O$, Sigma Aldrich 99%) were dissolved separately in water. These solutions were then poured into the malic acid solution ($C_4H_6O_5$,

ThomasBaker 99%) which was prepared by dissolving in a minimum amount of double-distilled water. (In case of Sb^{3+} substituted cobalt ferrite antimony oxide (Sb_2O_3, Sigma Aldrich 99%) was dissolved in malic acid). The pH of the resulting solution was adjusted using 30% ammonia (S D fine chemicals Ltd) till neutral. Ethylene glycol ($C_2H_6O_2$, Thomas Baker 99.5%) in a fixed ratio was added to the above solution. The obtained solution was heated at 100 °C with vigorous stirring and was allowed to form an anhydrous gel by placing it in an oven. The gel obtained was subjected to auto-combustion in an oven at 200 °C to get a fluffy powder and was further subjected to calcination at 400 °C for 5 h in a muffle furnace. The calcined powder was further heat-treated at 800 °C for 8 h to get a pure cubic phase.

3.1.1.2 Preparation of RE^{3+}, Cr^{3+}, In^{3+}, and Mn ion substituted cobalt-copper ferrite.

$Co_{0.9}Cu_{0.1}Fe_{2-x}RE_xO_4$ (where RE = Gd, Dy, Sm, Yb, Eu and x = 0.00, 0.03, 0.05)

$Co_{0.9}Cu_{0.1}Fe_{2-x}Cr_xO_4$ (where x = 0.00, 0.03, 0.06, 0.09, 0.12, and 0.15)

$Co_{0.9}Cu_{0.1}Fe_{2-x}Mn_xO_4$ (where x = 0.00, 0.03, 0.06, 0.09, 0.12, and 0.15)

$Co_{0.9}Cu_{0.1}Fe_{2-x}In_xO_4$ (where x = 0.00, 0.03, 0.06, 0.09, 0.12, and 0.15)

A stoichiometric amount of cobalt nitrate hexahydrate ($Co(NO_3)_2 \cdot 6H_2O$, Sigma Aldrich 99%), copper nitrate trihydrate ($Cu(NO_3)_2 \cdot 3H_2O$, Sigma Aldrich 99%), and iron nitrate nonahydrate ($Fe(NO_3)_3 \cdot 9H_2O$, Sigma Aldrich 99%) were dissolved in minimum quantity of distilled water separately to get homogeneous aqueous solutions. In the case of RE, chromium, manganese and indium substitution, a stoichiometric quantity of RE_2O_3 (dissolved in conc. HNO_3), chromium nitrate ($Cr(NO_3)_3 \cdot 9H_2O$, Sigma Aldrich

99.0%), manganese nitrate ($Mn(NO_3)_2.4H_2O$, Sigma Aldrich ~97.0%) and Indium oxide (In_2O_3, Sigma Aldrich 99.9%) (dissolved in conc. HNO_3) were added. The above metal ion solutions were added to the known amount of malic acid ($C_4H_6O_5$, ThomasBaker 99%) previously dissolved in distilled water. The pH of the solution was set to near neutral using 30% ammonia (S D fine chemicals Ltd) followed by the addition of ethylene glycol ($C_2H_6O_2$, Thomas Baker 99.5%). The resulting solution was evaporated in an oven at 95 ℃ to obtain an anhydrous brown thick viscous gel. The gel was burnt through the self-propagating combustion process in a preheated oven at 200 ℃ to get a fluffy brownish-black powder. The powder was further calcined at 400 ℃ for 5 h and pressed into pellets to sinter at 800 ℃ for 10 h to obtain the compound in a single phase.

3.1.2 Combustion method

3.1.2.1 Preparation of mixed rare earth oxides

$Y_{2-x}Ce_yEu_xO_3$ (where y = 0.00, 0.01 and x = 0.00, 0.02, 0.04, and 0.06)

$Y_{2-x}Ce_yEr_xO_3$ (where y = 0.00, 0.01 and x= 0.00, 0.02, 0.04, and 0.06)

$Gd_{2-x}Er_{0.04}Yb_xO_3$ (where x = 0.04, 0.08, 0.12, 0.16 and 0.20)

$Gd_{2-x}Ho_{0.04}Yb_xO_3$ (where x = 0.04, 0.08, 0.12, 0.16 and 0.20)

A series of Ce^{3+}/Eu^{3+}, Ce^{3+}/Er^{3+} co-substituted Y_2O_3 and Er^{3+}/Yb^{3+}, Ho^{3+}/Yb^{3+} co-substituted Gd_2O_3 were prepared employing the solution combustion method. The europium oxide (Eu_2O_3, Sigma Aldrich 99.99%), gadolinium oxide (Gd_2O_3, Sigma Aldrich 99.9%), ytterbium oxide (Yb_2O_3, Sigma Aldrich 99.9%), and holmium oxide (Ho_2O_3, Sigma Aldrich 99.9%) were brought into solution by dissolving in concentrated

nitric acid (HNO_3, Fisher Scientific). The yttrium nitrate ($Y(NO_3)_3.6H_2O$, Sigma Aldrich 99.9%), cerium nitrate ($Ce(NO_3)_3.6H_2O$, Sigma Aldrich 99.99%), and erbium nitrate ($Er(NO_3)_3.5H_2O$, Sigma Aldrich 99.9%) were dissolved in double-distilled water. The desired metal ion solutions were added to the calculated amount of glycine ($C_2H_5NO_2$, SDFCL 99.0%) previously dissolved in double-distilled water. The oxidizer-to-fuel ratio was maintained at 1:0.5. The resulting solution was concentrated on a hot plate to get a thick gel. The gel was combusted in a preheated oven at 200 ℃ for 3 h. Further, the obtained samples were calcined at 500 ℃ for 5 h and were then pelletized and sintered at 1000 ℃ for 8 h to obtain a single-phase compound.

3.2 Instrumental Techniques

3.2.1 Thermogravimetric – Differential thermal analysis (TG-DTA)

Thermal analysis is a physico-chemical method associated with the examination of the change in properties of materialsand processes under programmed variation of the surrounding temperature. The thermal analysis reveals information such as; melting, sublimation, enthalpy, thermal capacity, mass changes, thermal degradation reactions, phase transitions, and decomposition temperature [334,335]. Thermo-gravimetric analysis (TGA) is a technique that determines the mass changes occurring in the material when the sample is subjected to a programmed temperature in a controlled atmosphere. This change in mass can be a loss of mass or a mass gain. The weight loss recorded provides information regarding the sample composition and thermal stability of the material. TGA is the most effective technique for investigating processes like adsorption, desorption, combustion, decomposition, hydration, dehydration, and oxidation/reduction processes [334,335]. The differential thermal analysis (DTA) is a technique which determines the difference in temperature between a sample and a reference as a function of temperature when the sample is subjected to temperature scanning in a controlled atmosphere. In the case of DTA, the sample under investigation and the reference are subjected to similar thermal cycles, and the temperature difference among sample and reference is recorded. The DTA profile indicates the transformations which have been developed, such as sublimation, phase change, melting, combustion, crystallization, hydration, dehydration, glass transitions, etc [334].

Thermal measurements (TG-DTA) of the samples were recorded from 30 to 800 °C in the air with the heating rate of 10 °C/min on a Thermogravimetric – Differential

Thermal Analysis (NETZSCH TG/DTA STA 409PC). Alumina (Al_2O_3) crucible was used as a sample holder.

3.2.2 X-ray Diffraction (XRD)

Powder X-ray diffraction (XRD) is animportant and crucial characterization technique employed in material science to recognize the crystal structure, to identify the crystalline and amorphous nature of the materials, to give information on unit cell dimensions and indexing of the peaks, determine crystal structures using Rietveld refinement, to determine the phase purity, crystallite size, lattice parameters, X-ray density and strain in the structure. XRD is based on constructive interference of monochromatic X-rays and a crystalline sample. These X-rays are produced by a cathode ray tube, filtered to generate monochromatic radiation, collimated to concentrate, and headed towards the sample. The interaction of the incident rays with the specimen creates constructive interference when conditions obey the Bragg's Law.

$$\mathbf{n\lambda = 2dSin\theta}$$

Where λ is the X-raywavelength

n is an integer

d is the interplanar distance

θis the X-ray angle

Braggs law relates the wavelength of electromagnetic radiation to the angle of diffraction and the lattice spacing in a crystalline material. The diffracted X-rays are then detected and processed. Conversion of the diffraction peaks to d-spacings allows identification of the mineral under investigation since each mineral consist of unique d-

spacings values. Comparing the d-spacing values with the standard reference patterns the identification of the material could be achieved [336,337].

The lattice constant 'a' was determined using the following relation:

$$\boldsymbol{a = d\sqrt{h^2 + k^2 + l^2}}$$

Where,d is the inter-planar distance and (h k l) are the Miller indices.

The X-ray density (ρx) was calculated using the following equation:

$$\boldsymbol{\rho x = \frac{nM}{Na^3}}$$

Where n is the number of atoms associated with each unit cell, M is molecular weight of the compound, a^3 is the volume of the cubic unit cell and N is the Avogadro's number.

The crystallite size d was determined from the Scherrer's formula

$$\boldsymbol{d = \frac{0.9\lambda}{ß cos\theta}}$$

Whereßis the full width at half maximum, λ is the X-ray wavelength (1.5418 Å) and θ is the angle of diffraction.

The powder XRD measurements were performed on a RIGAKU ULTIMA IV diffractometerutilizing Cu Kα (1.5418 Å) source.

3.2.3 Inductively coupled plasma atomic emission spectroscopy (ICP-AES)

ICP-AES is a very sensitive emission spectrophotometric method for recognition and quantification of elements present in a sample. It is often used for the quantitative detection of trace elements and provides high selectivity between elements, high sensitivity, and a large dynamic range. In this method, a sample in liquid form is injected

into argon gas plasma having a strong magnetic field. This technique uses the inductively coupled plasma to generate excited atoms and ions that emit electromagnetic radiation at wavelengths distinctive of a particular element. It is a flame technique with the flame temperature ranging from 6000 to 10000 K that leads to more effective excitation of atoms of around 60 elements which also includes a few non-metals. This extreme heat inhibits the formation of polyatomic species, consequently enhancing the detection limits for several elements. By determining the wavelengths and intensities emitted by a sample, the elemental composition of the sample can be quantified relative to a reference standard. The detection limits usually vary from parts per million to parts per billion, depending on the element and instrument [338,339].

The samples were digested using concentrated nitric acid. The metal ion concentration was determined by using spectro analytical instruments GmbH, ARCOS, simultaneous ICP Spectrometer.

3.2.4 Infrared Spectroscopy (IR)

IR spectroscopyis a significant characterization technique based on the vibrations of the atoms when interacts with IR light. For a vibrational mode to be "IR active," it should have change in the permanent dipole moment. It is based on the fact that the functional groups absorb definite frequencies, distinctive of their structure.When a functional group absorbs energy, it can vibrate in a bending or stretching mode and the characteristic energy for this vibrational mode is given in wavenumbers. An IR spectrum is achieved by passing IR radiation through the desired sample and determining the fraction of the incident radiation absorbed at a particular energy. The energy at which the

peak is positioned in an absorption spectrum corresponds to the frequency of vibration[340,341].

A small quantity of the sample was finely ground with potassium bromide. This mixture was then pressed into a sample holder through which the beam of the spectrometer could pass. The room temperature IR spectra were recorded in the range of 350 - 3500 cm^{-1} on SHIMADZU IR-PRESTIGE-21 IR spectrophotometer to depict the various vibration bands.

3.2.5 Raman Spectroscopy

Raman spectroscopy is a non-destructive method and can be used to recognize vibrational, rotational, and other low-frequency modes. It can be utilized for the examination and identification of an extensive range of materials and also possible with samples in solution form. Raman spectra of different polymorphs show several similar features along with some distinct differences. It can also offer information regarding the stress in the material, crystal lattice disorder, and phase separation of the supersaturated solution. A material shows a Raman effect, only if it involves a change in its electric dipole-electric dipole and intensity of the Raman scattering is proportional to this change in polarizability. In this method, a laser light source is used to irradiate the sample which develops a small quantity of scattered light, which can be recorded as a Raman spectrum. The distinct pattern in the spectrum helps to recognize the materials including polymorphs, assess crystallinity, and stress in the material [342].

The room temperature Raman spectra were recorded in the range of 150 - 800 cm^{-1} on HORIBA JOBIN YVON HR-800 Raman spectrometer to identify different type of

vibration modes. A 632.8 nm He – Ne laser source with the power of 10 mW was used as the excitation source and on STR - 500 Confocal micro Raman spectrometer with 532 nm DPSS laser.

3.2.6 Scanning Electron Microscopy-Energy Dispersive X-ray spectroscopy (SEM – EDX)

Scanning electron microscopy (SEM) is a surface analysis microscopic technique. It gives HR images of the specimen under investigation by scanning the sample surface with a focused electron beam (0.1-50 keV) and detecting the backscattered and secondary electron signals which generate a grayscale image of the surface morphology. For SEM imaging, the specimens should be electrically conductive, to avoid the buildup of electrostatic charge. Non-conducting materials are generally coated with an ultrathin coating of electrically conducting material which includes Au, Au/Pd alloy, Pt, Ir, Os, and graphite by low-vacuum sputter coating or by high-vacuum evaporation.Energy dispersive X-Ray (EDX) is a surface analysis technique employed for the elemental identification and quantitative information of a sample**.** Besides secondary electrons and backscattered electrons, X-rays are also generated by primary electron bombardment. The intensity of backscattered electrons could be associated with the atomic number of the element. Therefore, some qualitative elemental information could be achieved. The examination of characteristic X-rays emitted from the sample provides quantitative information about the element [336,343].

The sample was dispersed on a carbon tape and was subjected to Au/Pd coating. The surface morphology of the prepared materials and elemental composition were examined on scanning electron microscope Zeiss Evo18.

3.2.7 Transmission Electron Microscopy – Selected Area Electron Diffraction (TEM – SAED)

TEM is a very powerful technique in material research. It can be used in the determination of structure by directing a high energy beam (10-200 keV) of electrons at the sample and recording the consequent diffraction pattern generated by the electrons transmitted through the sample. TEM uses energetic electrons to give morphological, compositional and crystallographic data on the samples. TEM generates HR, two-dimensional images, allowing for a wide range of scientific and industrial fields. TEM data is able to offer information regarding surface features, shape, size, structure, and crystallinity.The SAED of polycrystalline materials provides ring patterns analogous to those from XRDand could be used to differentiate between crystalline and amorphous phases and to identify if more than one phase is present [336,344].

The particle size was estimated using Transmission electron microscope PHILIPS CM 200, working at a voltage of 200 kV and Field emission gun-transmission electron microscope 300 kV (HR-TEM 300 kV) (FEI Tecnai G2, F30).

3.2.8 X-ray photoelectron spectroscopy (XPS)

XPS is an extensively used and well-knownsurface-sensitive spectroscopic method for the analysis of solids. It can be applied to a wide range of materials and gives quantitative and chemical state information of the surface components being analyzed.

XPS can determine the elemental composition, chemical state and electronic state of the elements within the material under study. It is usually used to examine inorganic compounds, polymers, elements, catalysts, glasses, ceramics, corrosion, adhesion, surface treatments, and thin-film coatings. This technique analyzes the outermost depth of a few nanometers (1-10 nm) of the sample. XPS needs an ultrahigh vacuum environment and the monochromatic X-ray source. The incident X-rays cause the ejection of core-level electrons from the samples. The energy of an emitted core electron is a function of its BE and is characteristic of the element from which it gets emitted [336,345]. The energies and intensities of the photoelectron peaks allow us to identify and quantify all the surface elements. XPS can detect all the elements with an atomic number of 3 and beyond 3. The detection limits for most of the elements are in the parts per thousand range.

XPS studies were performed on powdered samples. Full scan XPS spectra along with high-resolution XPS spectra were obtained using PHI Versa probe II and ESCA+ omicron nanotechnology oxford instruments. The high-resolution XPS spectra were charge corrected using carbon as a reference and deconvoluted using XPS peak processing software to determine the exact values of BE.

3.2.9 UV-Vis diffuse reflectance spectroscopy (UV-DRS)

UV-DRS is a nondestructive method and very useful technique in determining the band gap of the material. It is based on the reflection of light in the ultraviolet (UV), visible (VIS) and near IR (NIR) region by a powdered sample. It uses the interaction of light, absorption, and scattering to generate a characteristic reflectance spectrum, which offers information regarding the band gap of the material [346,347].

Room temperatureUV/Visdiffuse reflectance spectra (UV-DRS) were recorded on a Shimadzu UV-2450 spectrophotometer in the 200-800 nm range against a reference barium sulfate. The band gap energy (Eg) was estimated from the fundamental absorption, which corresponds to the excitation of electrons from the valence band to the conduction band. In order to estimate the band gap, the diffuse reflectance (R) of the samples was transformed employing a Kubelka-Munk function which is directly proportional to the absorption coefficient (α). The optical band gap (Eg) and absorption coefficient (α) of a direct band gap semiconductor is related through the Tauc equation.

$$Ah\upsilon = A(h\upsilon - Eg)^n$$

Where A is the proportionality constant, hυ is the energy of the incident photon, and n is an index that characterizes the optical absorption process. The band-gap energies were obtained from the extrapolation of the Tauc's linear portion intersecting with the photon energy axis.

3.2.10 Mossbauer spectroscopy

Mössbauer spectroscopy is a crucial method which could be employed in several fields of science to give vital information. It can provide very detailed information regarding the structural, chemical, magnetic and time-dependent features of the material. In this technique, a solid sample is subjected to a beam of gamma radiation, and a detector records the intensity of the beam transmitted through the sample. The atoms in the source emitting the gamma rays should be of the same isotope as the atoms in the sample absorbing them.This technique is extensively utilized to inspect the chemical state of Fe, which can be 2+, 3+ or metallic Fe [348].

A thin layer of powder sample was introduced between the source and the detector in such a way that the sample will be perpendicular to source and detector. ^{57}Fe Mossbauer measurement was conducted in transmission mode, using ^{57}Co as a radioactive source in constant acceleration mode utilizing a standard PC based Mossbauer spectrometer. The peak fitting was done on the obtained spectra using NORMOS-SITE software.

3.2.11 Magnetic studies

A vibrating-sample magnetometer (VSM) is a very sensitive instrument that records the magnetic features of a sample with respect to applied magnetic field and temperature with very high precision. It works on the Faraday's law of electromagnetic induction, which states that a varying magnetic field will generate an electric field. This electric field can be measured, which provides us with information regarding the magnetic nature of the material.

In the measurement setup, a magnetic sample is moving in the proximity of two pickup coils. A sample is initially magnetized in a uniform magnetic field and then sinusoidally vibrated, using a piezoelectric material. The changes in the signal are converted to values by the software to give a plot of magnetization *(M)* versus the magnetic field *(H)* strength, often referred to as a hysteresis loop. The hysteresis loop obtained contains vital information regarding the magnetic properties of the sample. Characteristic quantities include the saturation magnetization *(M_s)*, the remanent magnetization *(M_r)*, and the magnetic coercivity *(H_c)*. Hence VSM instrument can be

employed in recognition of ferromagnetic, ferrimagnetic, anti-ferromagnetic, paramagnetic, and diamagnetic materials.

The magnetic moment per formula unit in Bohr magneton (n_B) was calculated by employing the following equation.

$$n_B = \frac{M_w \times M_s}{5585}$$

WhereM_w and M_s are the formula weight and saturation magnetization respectively.

The magnetic studies were carried out at 300 K and 50 K with varying magnetic field up to 3 T on a vibrating sample magnetometer (VSM) (Quantum design PPMS). And on a Quantum Design 14 T PPMS – Vibrating Sample Magnetometer by varying a magnetic field up to 5 T at 300 K and 5 K.

3.2.12 AC – Susceptibility

AC magnetic measurements, in which an AC field is applied to a sample and the resulting AC moment is measured, is a significant technique to characterize the magnetic materials. In order to get the overall idea of the ferrimagnetic material, the determination of temperature-dependent magnetic susceptibility (χ_T/χ_{RT}) is vital. The main objective of this measurement is to estimate the Curie temperature (T_c) by applying a weak external magnetic field. T_c is the temperature where the material is fully demagnetized or the temperature where ferromagnetic and ferrimagnetic material transforms to a paramagnetic material upon heating. The initially increasing (χ_T/χ_{RT}) values with temperature are due to the alignment of magnetic domains. The AC magnetic susceptibility study is also an important method to determine the different domain states exhibited by the materials on the basis of particle size distribution. The nature of the

curve in response to temperature gives information on the magnetic domain states such as superparamagnetic, single domain, and multi-domain.

Approximately 100 mg of the sample was placed in a quartz tube and the sensor was introduced into the tube and the Curie temperature (T_c) was recorded at a field of 5 kOe employing temperature-programmed data logger for science experiments supplied by ADEC.

3.2.13 DC – Electrical Resistivity

Electrical resistivity is a fundamental property of a material that quantifies how strongly a given material resists the flow of an electric current. A low value of resistivity suggests that the material readily allows the flow of electric current. It is an important technique to examine semiconductor metal oxides. Resistivity is generally represented by the Greek letter ρ (rho). The DC electrical resistivity of all the ferrite samples was calculated using a two-probe instrument in the temperature range 373–773 K. The sample was pressed into a pellet by applying a pressure of 5 tonnes. DC electrical resistivity (ρ_{dc}) was measured by two probe electrical conductivity unit in the temperature range 373 to 773 K using a Keithley - 6485 system. The annealed ferrite samples were pelletized by applying hydraulic pressure of 5 tonnes. A constant voltage (2 V) was applied across the series combination of sample holder containing sample and a standard resistance whose value was always less than the sample resistance. The measurements were recorded in the steps of 10 ℃. Knowing the current flowing through the circuit and voltage across the sample, the resistivity of the sample could be calculated by using the following equation:

In this case, the electrical resistivity ρ is defined as:

$$\rho = \frac{RA}{l}$$

Where R is the electrical resistance of a uniform specimen in ohm

*A*is the cross-sectional area of the specimen

l is the thickness of the specimen under investigation

The relationship between the DC electrical resistivity (ρ) and the temperature can be expressed according to Arrhenius equation

$$\rho = \rho_0 e^{-\frac{-\Delta E}{k_B T}}$$

where ΔE is the activation energy, k_B is Boltzmann's constant and T is the absolute temperature.

3.2.14 Dielectric properties

A material which can store energy when a voltage is applied resulting in electric polarization is called its dielectric property.Dielectrics materials define most of the parameters of capacitors, like capacitance, voltage capacities, dielectric loss factor, etc. A material possessing a high dielectric constant is extensively utilized in capacitors. Dielectric materials are mostly electrical insulators which under the influence of the electric field, becomes polarizedby proper alignment of the dipole moments of polar molecules. The positive charges shift in the electric field direction and the negative charges shift in the direction opposing the direction of the electric field. When the dielectric material is placed under the influence of an electric field, practically no currentflows through them, instead, the polarization of molecules takes place. The

transfer of electrical energy occurs through the shifting of current and not via the conduction mechanism. A good dielectric material should possess the least dielectric loss. The examples of dielectric materials include paper, glass, mica, plastics, ceramics, and various metal oxides.Dielectric performance of the metal oxides relies on several factors such as the method of preparation, sintering temperature, type and quantity of the substituent.

The dielectric property was investigated as a function of frequency (20 Hz - 1 MHz) and temperature (300 - 773 K) on a silver-coated pellet using LCR meter (Wayne Kerr 6500P).

The dielectric constant (ε') was determined by employing the following equation.

$$\varepsilon' = \frac{Ct}{\varepsilon_0 A}$$

Where *C* is the capacitance, 't' and 'A' are the thickness and area of the pellet, respectively and ε_0 is the permittivity of the free space (8.85×10^{-14}F/cm).

3.2.15 Photoluminescence (PL)

PL is an optical spectroscopic method for the characterization, examination of electronic structure, and detection of point defects of the materials. In this method, when the light is directed on the specimen, it gets absorbed and passes on the excess energy to the material in a process known as photo-excitation. Photo-excitation results in the movement of electrons within the material into permitted excited states. When such electrons come back to their equilibrium position, the excess energy is released and may contain the emission of light. This excess energy can be dissipated by the sample by the

emission of light, or luminescence and the process is called photoluminescence [349]. The luminescence study generally involves the recording of two types of spectra i.e. excitation spectrum and emission spectrum. Emission spectrum records the emissions at a specific excitation in the range of wavelengths, while; the excitation spectrum measures the luminous intensity in the range of the excitation wavelengths by monitoring a specific emission.

Up-conversion nanoparticles are the type of luminescence materials that transform low energy photons to high energy emissions through sequential absorption of two or more photons and emission of light at a shorter wavelength than the excitation wavelength. There are three basic processes for photon Up-conversion in inorganic materials which includes (a)energy transfer Up-conversion (ETU) (b) excited-state absorption (ESA) and (c) photon avalanche (PA) [350]. Some of the ions of d-block elements and f-block elements are capable of photon Up-conversion.

Photoluminescence studies were carried out on a Jobin YvonFlurolog -3-11 spectrofluorimeter having xenon lamp 450 W. The Up-conversion spectra of the samples were monitored by SP-2300 grating monochromator (Princeton Instruments, USA) equipped with a photomultiplier tube using 980 nm diode laser as an excitation source.

CHARACTERIZATION AND SPECTROSCOPIC STUDIES

Several techniques such as TG-DTA, XRD, ICP-AES, IR, Raman, SEM-EDX, TEM-SAED, and XPS were employed for the characterization of the prepared compounds. The results obtained are discussed in this chapter.

4.1 Thermal analysis (TG-DTA)

The thermal analysis was carried out on the gel obtained in the preparation process and on the combusted sample to determine the combustion temperature and calcination temperature respectively. The occurrence of exothermic and endothermic peaks in the DTA curve indicated the different processes occurring in the specimen under analysis.

4.1.1 $Co_{0.90}Cu_{0.10}Fe_2O_4$

The minimum temperature required for the complete combustion of the gel obtained and the minimum temperature for the calcination process was estimated from the thermal behavior of the dried gel. TG-DTA study was performed on the prepared Malic acid-Metal nitrate gel of $Co_{0.90}Cu_{0.10}Fe_2O_4$ and is presented in Fig. 4.1(a). The weight loss observed in the TG curve at around 200 and 400 °C corresponds to the decomposition of nitrates and organic moieties present in the sample as indicated by two exothermic peaks in the DTA curve.

Thermal studies were executed on auto-combusted powder to further confirm the calcination temperature. The TG-DTA profiles of the auto-combusted sample have been represented in Fig. 4.1(b). A significant weight loss in TG and an exotherm in DTA curve at ~ 400 °C signify the removal of organic moieties. No other transformation can be

evidenced in the TG-DTA profiles at temperatures beyond 400 °C, indicating that at this temperature the precursors are entirely decomposed.

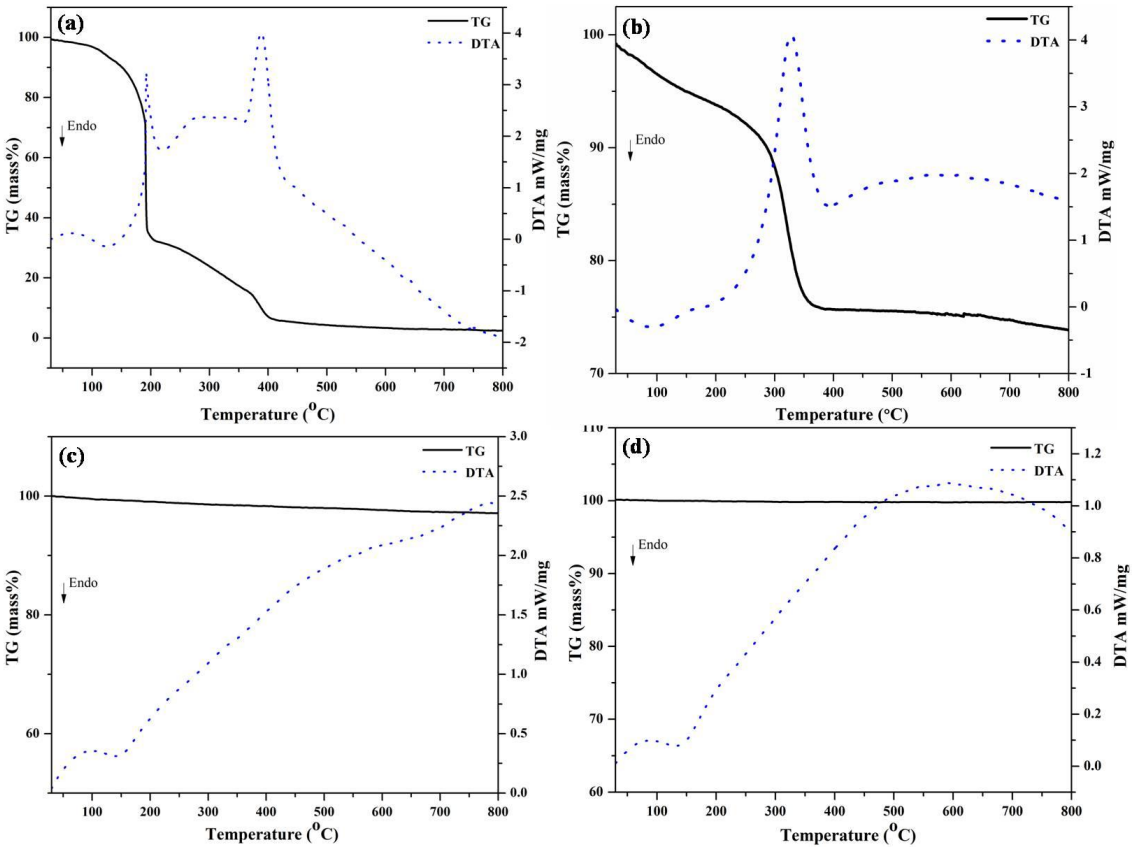

Fig. 4.1 *TG-DTA curves for (a) Malic acid- Metal nitrate gel (b) auto combusted sample (c) sample calcined at 400 ˚C for 5 h (d) sample sintered at 800 ˚C for 8 h.*

Based on the thermal studies, all the samples were combusted and calcined at 200 °C and 400 °C respectively for 5 h. TG-DTA profiles of the sample calcined at 400 °C and sintered at 800 °C is shown in Fig. 4.1(c) and Fig. 4.1(d) respectively. TG pattern shows no weight loss which confirms the complete removal of organic moieties from the sample.

4.1.2 $CoFe_{1.91}Sb_{0.09}O_4$

Thermal analysis of the as a burnt sample of $CoFe_{1.91}Sb_{0.09}O_4$has been carried out and shown in Fig. 4.2. The TG curve shows continuous weight loss till 400 °C. This can

be attributed to the removal of organic moieties present in the sample. The corresponding DTA curve shows an exothermic peak around 400 °C pertaining to the burning of carbon.

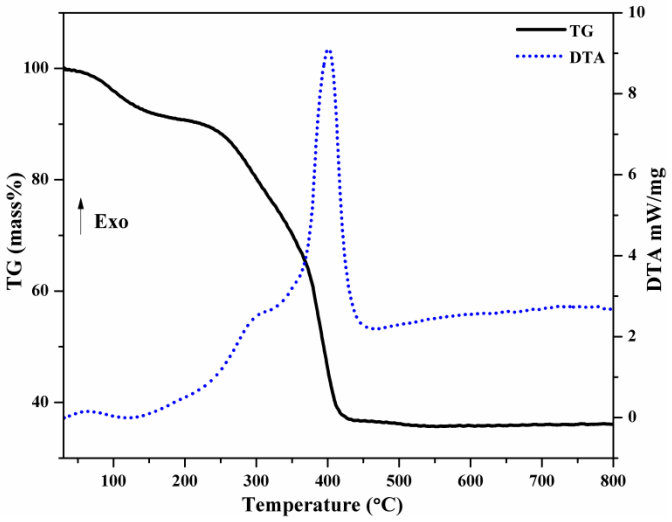

Fig. 4.2 *TG-DTA curves for the auto-combusted sample of* $CoFe_{1.91}Sb_{0.09}O_4$.

4.1.3 $Co_{0.9}Cu_{0.1}Fe_{1.95}Gd_{0.05}O_4$

TG-DTA studies were performed on the combusted powder of $Co_{0.9}Cu_{0.1}Fe_{1.95}Gd_{0.05}O_4$ and are presented in Fig. 4.3.

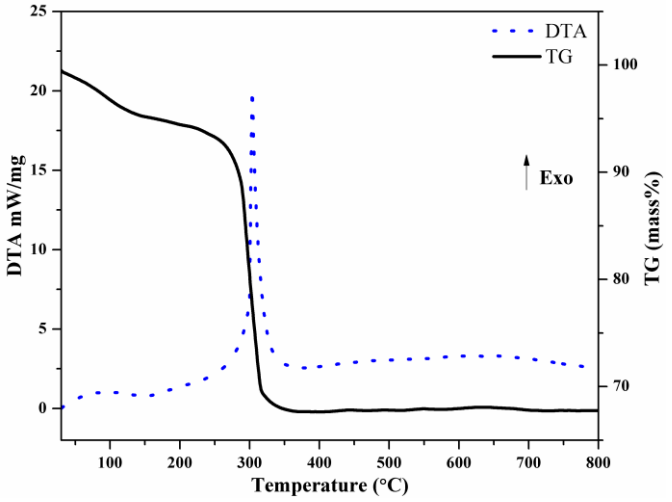

Fig. 4.3 *TG-DTA curves for the auto-combusted sample of* $Co_{0.9}Cu_{0.1}Fe_{1.95}Gd_{0.05}O_4$.

The weight loss observed in the TG curve at around 320 °C corresponds to the decomposition of organic moieties present in the sample as indicated by an

exothermicpeak in the DTA curve. Based on the thermal studies the samples were calcined at 400 °C for 5 h.

4.1.4 $Co_{0.9}Cu_{0.1}Fe_{1.85}Cr_{0.15}O_4$

Figure 4.4 shows the TG-DTA curve of the auto-combusted sample of $Co_{0.9}Cu_{0.1}Fe_{1.85}Cr_{0.15}O_4$obtained during the preparation process. The continuous weight loss till 400 ℃ in the TG curve along with the exothermic peak in the DTA curve can be ascribed to the removal of organic substances from the sample hence the samples were calcined at 400 ℃.When the temperature is increased beyond 400 °C, no further weight loss was observed, indicating the complete removal of organic moieties.

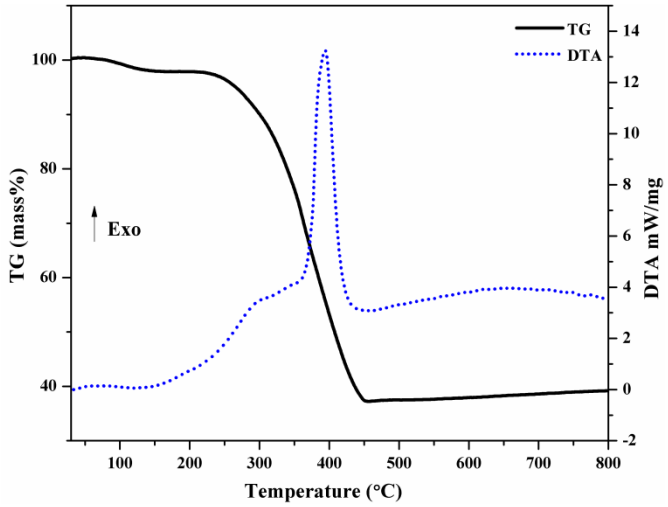

Fig. 4.4 *TG-DTA curves for the auto-combusted sample of* $Co_{0.9}Cu_{0.1}Fe_{1.85}Cr_{0.15}O_4$.

4.1.5 $Co_{0.9}Cu_{0.1}Fe_{1.85}Mn_{0.15}O_4$

The TG-DTA curves for the auto combusted sample of $Co_{0.9}Cu_{0.1}Fe_{1.85}Mn_{0.15}O_4$has been shown in Fig. 4.5. The TG curve shows a gradual mass loss till 100 ℃ which can be due to the loss of residual moisture in the sample. A substantial weight loss was observed in the TG curve around 300 ℃ accompanied by a

sharp exothermic peak in the DTA curve. The observed weight loss (TG) and exothermic peak (DTA) corresponds to the burning of organic moieties in the sample.

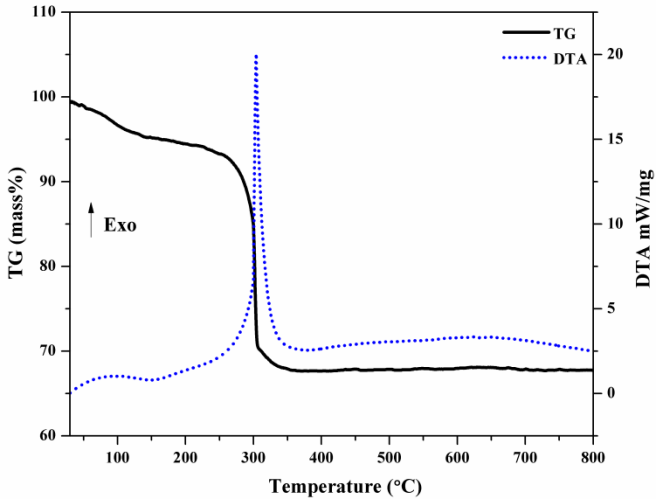

Fig. 4.5 *TG-DTA curves for the auto-combusted sample of* $Co_{0.9}Cu_{0.1}Fe_{1.85}Mn_{0.15}O_4$.

4.1.6 $Co_{0.9}Cu_{0.1}Fe_{1.85}In_{0.15}O_4$

The TG-DTA curves for In^{3+} substituted Co-Cu ferrite has been shown in Fig. 4.6. The TG curve shows a weight loss till 150 ℃ which could be due to the removal of residual water in the sample.

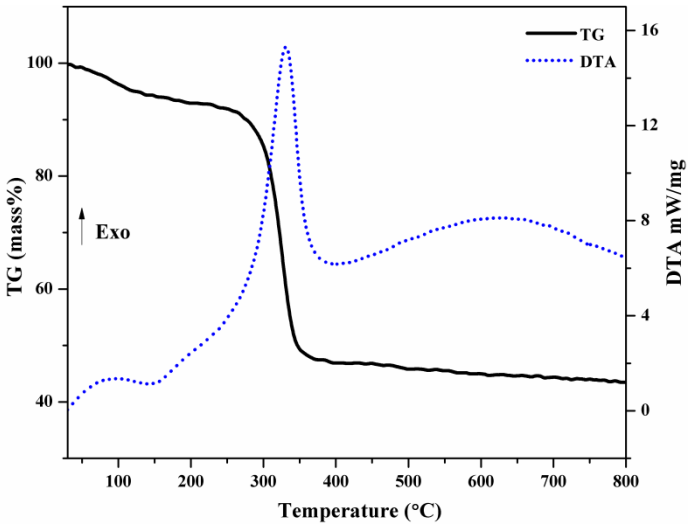

Fig. 4.6 *TG-DTA curves for the auto-combusted sample of* $Co_{0.9}Cu_{0.1}Fe_{1.85}In_{0.15}O_4$.

Further, there is an enormous amount of weight loss till 300 ℃ as observed in the TG curve due to the burning of the organic carbon and other moieties present in the sample. The burning of carbon was confirmed by a sharp exothermic signal in the DTA curve. Above 350 ℃ no weight loss was observed in the sample hence confirming the removal of organic moieties and thermal stability of the compound.

4.2 X-ray diffraction studies

Powder X-ray diffraction studies were performed to determine the phase purity and for phase identification. The XRD pattern also gave an idea about the crystallinity of the samples. The XRD data was utilized to determine the lattice parameters, crystallite size and X-ray density.

4.2.1 $Co_{1-x}Cu_xFe_2O_4$ (where x = 0.00, 0.05, 0.1, 0.15, 0.20 and 0.25)

The XRD profile of $Co_{1-x}Cu_xFe_2O_4$ (where x = 0.00, 0.05, 0.10, 0.15, 0.20 and 0.25) has been depicted in Fig. 4.7.

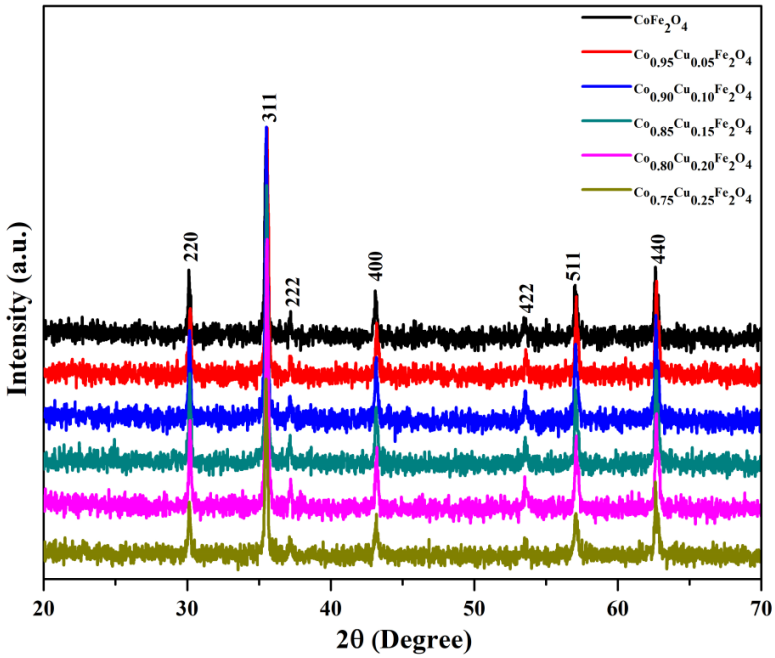

Fig. 4.7 *XRD patterns of $Co_{1-x}Cu_xFe_2O_4$ (where x = 0.00, 0.05, 0.1, 0.15, 0.20 and 0.25).*

The peak position and relative intensities identified from the diffractogram confirm the existence of a monophasic spinel ferrite structure (JCPDS No. 22-1086) (space group $Fd\bar{3}m$). The crystallite size, calculated employing Scherrer's formula was found to decrease with increasing Cu^{2+} ion content. The results show that the insertion of copper ions obstruct the grain growth which consequences in a slight reduction in crystallite size. The enhancement in X-ray density is a result of higher molar mass and density of Cu^{2+} (63.54 g mol^{-1} and 8.96 g cm^{-3}), than those of Co^{2+} (58.93 and 8.91 g cm^{-3}) as X-ray density is directly related to the molecular mass of the samples [132]. The estimated values of crystallite size, lattice constant and X-ray density have been presented in Table 4.1.

Table 4.1 X-ray diffraction data, particulate properties, for Cu^{2+} substituted cobalt Ferrite.

Sample Composition	Lattice constant a (Å)	Crystallite size d (nm)	X – ray density ρ_x (g/cm^3)
$CoFe_2O_4$	8.39	45	5.29
$Co_{0.95}Cu_{0.05}Fe_2O_4$	8.38	45	5.30
$Co_{0.90}Cu_{0.10}Fe_2O_4$	8.38	42	5.31
$Co_{0.85}Cu_{0.15}Fe_2O_4$	8.38	41	5.31
$Co_{0.80}Cu_{0.20}Fe_2O_4$	8.38	40	5.32
$Co_{0.75}Cu_{0.25}Fe_2O_4$	8.38	40	5.32

4.2.2 $CoFe_{2-x}Sb_xO_4$ (where x = 0.00, 0.03, 0.06, and 0.09)

The powder XRD pattern for pristine and Sb^{3+} substituted $CoFe_2O_4$ have been shown in Fig. 4.8. The pattern shows typical reflection peaks for the cubic spinel ferrite phase (JCPDS No. 22-1086) (space group $Fd\bar{3}m$) without traces of any secondary phase. The crystallite size estimated from the Scherrer's equation is found to decline from a

value of 45 nm to 30 nm with the rise in Sb^{3+} ion concentration (Table 4.2). The energy required for crystallization could have been consumed in the incorporation of Sb^{3+} ions into $CoFe_2O_4$, hence a decreasing trend in crystallite size was observed [196].

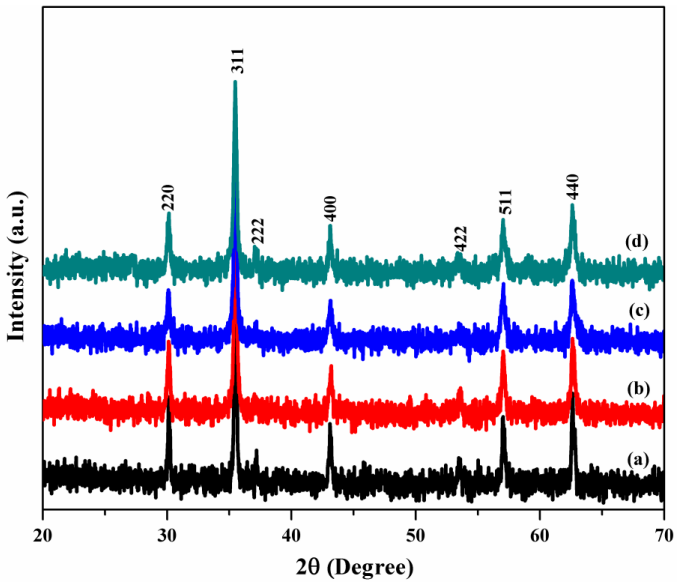

Fig. 4.8 *Powder X-ray diffraction pattern of(a)$CoFe_2O_4$ (b) $CoFe_{1.97}Sb_{0.03}O_4$ (c) $CoFe_{1.94}Sb_{0.06}O_4$ (d) $CoFe_{1.91}Sb_{0.09}O_4$.*

Table 4.2 X-ray diffraction data and particulate properties for $CoFe_{2-x}Sb_xO_4$ where x = 0.00, 0.03, 0.06 and 0.09.

Sample Composition	Lattice constant a (Å)	Crystallite size d (nm)	X – ray density ρ_x (g/cm^3)
$CoFe_2O_4$	8.39	45	5.29
$CoFe_{1.97}Sb_{0.03}O_4$	8.39	35	5.33
$CoFe_{1.94}Sb_{0.06}O_4$	8.39	29	5.36
$CoFe_{1.91}Sb_{0.09}O_4$	8.39	30	5.41

The difference in lattice parameter was not significant for the prepared compositions since the substitution was limited to small fractions. The calculated X-ray density was found to increase with Sb^{3+} ion content in $CoFe_2O_4$, which is attributed to the

increased molecular weight of the compositions, as the atomic mass of Sb (121.76 $gmol^{-1}$) is greater than that of Fe (58.85 $gmol^{-1}$).

4.2.3 $Co_{0.9}Cu_{0.1}Fe_{2-x}RE_xO_4$ (where RE = Gd, Sm, Dy, Yb, Eu and x = 0.00, 0.03, 0.05)

The Fig. 4.9 displays the X-ray powder pattern of $Co_{0.9}Cu_{0.1}Fe_{2-x}RE_xO_4$ (where RE = Gd, Sm, Dy, Yb, Eu, and x = 0.00, 0.03, 0.05). The detailed analysis of the pattern confirms the high purity single phase formation of cubic inverse spinel structure (space group $Fd\bar{3}m$) without any secondary phases (JCPDS No. 22-1086). No foreign peaks were observed which proves the compound to be monophasic. This confirms that the substituted RE^{3+} ions are entirely dissolved into the ferrite lattice. The powder pattern depicted diffraction peaks corresponding to diffraction planes (220), (311), (222), (400), (422), (511) and (440) with the most intense reflection at the (311) plane.

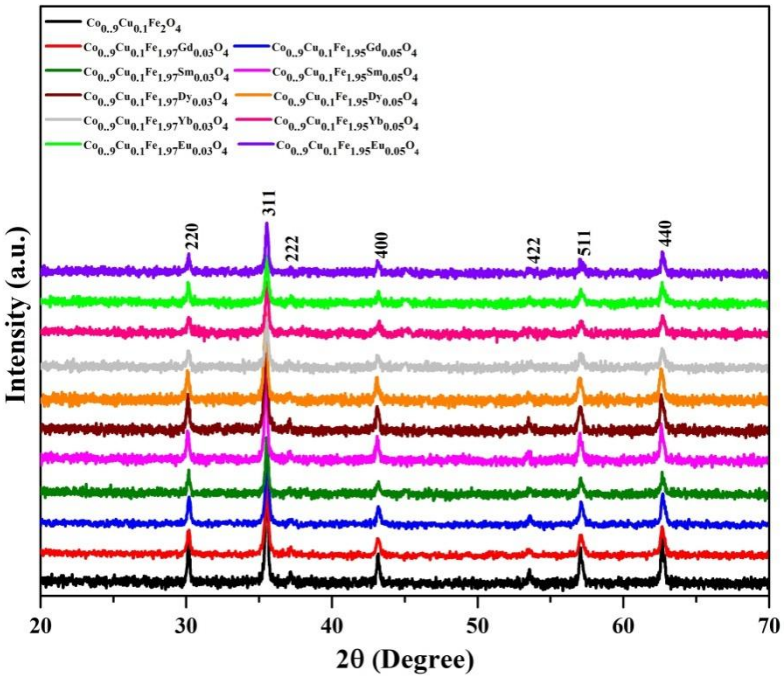

Fig. 4.9 *$Co_{0.9}Cu_{0.1}Fe_{2-x}RE_xO_4$ (where RE = Gd, Sm, Dy, Yb, Eu and x = 0.00, 0.03, 0.05).*

The average crystallite size (d), lattice parameter (a) and X-ray density (ρ_x) was extracted from the XRD analysis and the results obtained are listed in Table 4.3. The crystallite size estimated using Scherrer's formula showed a noticeable decrease with increasing substituent concentration. This might be due to the enormous amount of energy required to introduce RE^{3+} at the octahedral (B) site, this energy might be utilized at the expense of crystallization [196]. This leads to the weakening of diffraction peaks due to lack of crystallization, hence reducing the crystallite size. X-ray density was found to increase linearly with RE^{3+} substitution. The enhanced value of X-ray density was attributed to the improved molecular weight of the samples having RE^{3+} ions.

Table 4.3 X-ray diffraction data and particulate properties for RE^{3+} substituted Co-Cu Ferrite.

Sample Composition	Lattice constant a (Å)	Crystallite size d (nm)	X-ray density ρ_x (g/cm^3)
$Co_{0.9}Cu_{0.1}Fe_2O_4$	8.38	45	5.31
$Co_{0.9}Cu_{0.1}Fe_{1.97}Gd_{0.03}O_4$	8.38	30	5.37
$Co_{0.9}Cu_{0.1}Fe_{1.95}Gd_{0.05}O_4$	8.39	29	5.42
$Co_{0.9}Cu_{0.1}Fe_{1.97}Dy_{0.03}O_4$	8.39	35	5.38
$Co_{0.9}Cu_{0.1}Fe_{1.95}Dy_{0.05}O_4$	8.39	26	5.42
$Co_{0.9}Cu_{0.1}Fe_{1.97}Sm_{0.03}O_4$	8.38	38	5.37
$Co_{0.9}Cu_{0.1}Fe_{1.95}Sm_{0.05}O_4$	8.39	29	5.41
$Co_{0.9}Cu_{0.1}Fe_{1.97}Yb_{0.03}O_4$	8.38	34	5.38
$Co_{0.9}Cu_{0.1}Fe_{1.95}Yb_{0.05}O_4$	8.37	31	5.47
$Co_{0.9}Cu_{0.1}Fe_{1.97}Eu_{0.03}O_4$	8.38	36	5.37
$Co_{0.9}Cu_{0.1}Fe_{1.95}Eu_{0.05}O_4$	8.38	35	5.42

4.2.4 $Co_{0.9}Cu_{0.1}Fe_{2-x}Cr_xO_4$ (where x = 0.00, 0.03, 0.06, 0.09, 0.12, and 0.15)

The powder XRD studies were performed on $Co_{0.9}Cu_{0.1}Fe_{2-x}Cr_xO_4$ (where x = 0.00, 0.03, 0.06, 0.09, 0.12, and 0.15), heat treated at 800 ℃. As can be seen from Fig. 4.10, impurity peaks like CuO, Cr_2O_3, and Fe_2O_3 were not observed and the pattern is consistent with the JCPDS card no 22-1086. Accordingly, the peaks obtained were indexed corresponding to FCC spinel structure possessing space group $Fd\bar{3}m$. Hence it can infered that the substituent ions have been entirely absorbed into the host lattice.

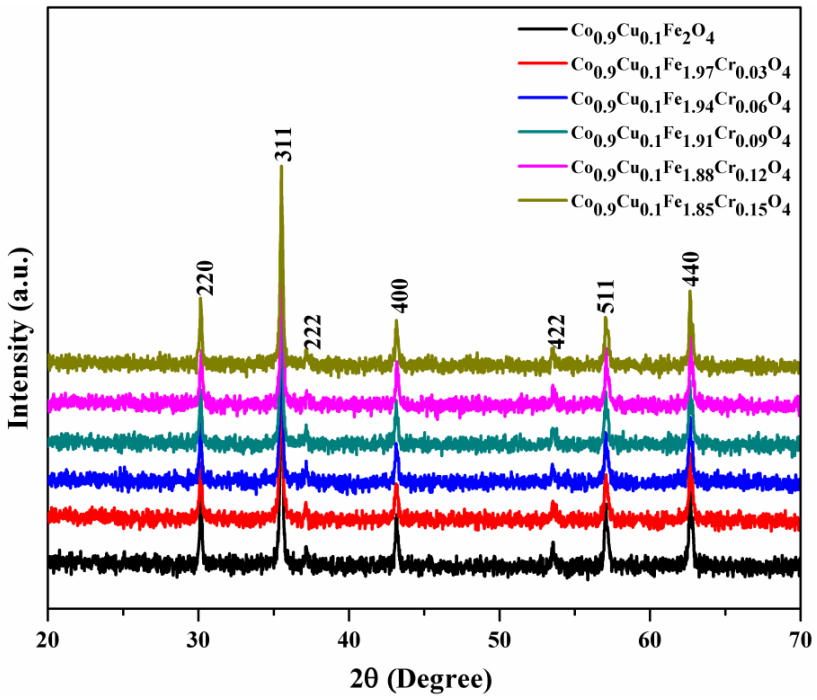

Fig. 4.10 *PowderXRD pattern for $Co_{0.9}Cu_{0.1}Fe_{2-x}Cr_xO_4$ (where x = 0.00, 0.03, 0.06, 0.09, 0.12, and 0.15).*

The average crystallite size was estimated employing the Scherrer's equation and was in the range from 41 – 45 nm.The X-ray density was found to remain almost constant with increasing substituent concentration. The exact values of lattice constant, crystallite size, and X-ray density have been summarized in Table 4.4.

Table 4.4 X-ray diffraction data, and particulate properties, for Cr^{3+} substituted Co-Cu Ferrite.

Sample Composition	Lattice constant a (Å)	Crystallite size d (nm)	X – ray Density ρ_x (g/cm^3)
$Co_{0.9}Cu_{0.1}Fe_2O_4$	8.38	45	5.31
$Co_{0.9}Cu_{0.1}Fe_{1.97}Cr_{0.03}O_4$	8.38	41	5.29
$Co_{0.9}Cu_{0.1}Fe_{1.94}Cr_{0.06}O_4$	8.38	43	5.29
$Co_{0.9}Cu_{0.1}Fe_{1.91}Cr_{0.09}O_4$	8.38	43	5.29
$Co_{0.9}Cu_{0.1}Fe_{1.88}Cr_{0.12}O_4$	8.37	45	5.31
$Co_{0.9}Cu_{0.1}Fe_{1.85}Cr_{0.15}O_4$	8.38	44	5.29

4.2.5 $Co_{0.9}Cu_{0.1}Fe_{2-x}Mn_xO_4$ (where x = 0.00, 0.03, 0.06, 0.09, 0.12, and 0.15)

The powder XRD analysis were performed on $Co_{0.9}Cu_{0.1}Fe_{2-x}Mn_xO_4$ (where x = 0.00, 0.03, 0.06, 0.09, 0.12, and 0.15) sintered at 800 ℃ and the patterns have been presented in Fig. 4.11.

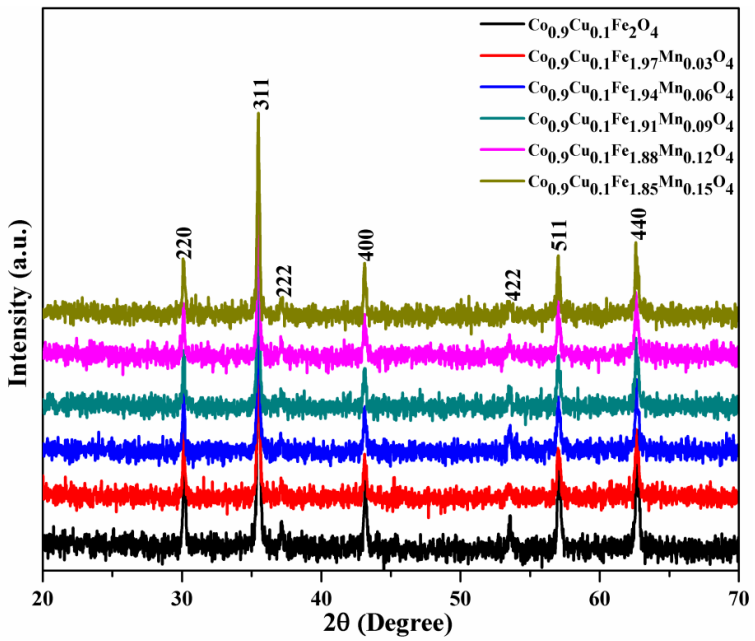

Fig. 4.11 *XRD pattern for $Co_{0.9}Cu_{0.1}Fe_{2-x}Mn_xO_4$ (where x = 0.00, 0.03, 0.06, 0.09, 0.12, and 0.15).*

No impurity peak was detected in the pattern matched well with the JCPDS card No. 22-1086. Hence it can inferred that the substituent ions are completely dissolved in the host lattice. The crystallite size obtained from the Scherrer's equation was found to be in the range 41 – 45 nm. As can be seen from Table 4.5, there is hardly any impact on the particle size with Mn substitution. Lattice parameter was noticed to increase with substituent concentration which might be due to strain-induced in the structure with substitution. No change in X-ray density was observed with Mn ion substitution. The exact values of lattice constantand X-ray density have been summarized in Table 4.5.

Table 4.5 X-ray diffraction data, and particulate properties, for Mn substituted Co-Cu Ferrite.

Sample Composition	Lattice constant a (Å)	Crystallite size d (nm)	X-ray density ρ_x (g/cm^3)
$Co_{0.9}Cu_{0.1}Fe_2O_4$	8.38	45	5.31
$Co_{0.9}Cu_{0.1}Fe_{1.97}Mn_{0.03}O_4$	8.39	46	5.29
$Co_{0.9}Cu_{0.1}Fe_{1.94}Mn_{0.06}O_4$	8.39	45	5.29
$Co_{0.9}Cu_{0.1}Fe_{1.91}Mn_{0.09}O_4$	8.39	42	5.29
$Co_{0.9}Cu_{0.1}Fe_{1.88}Mn_{0.12}O_4$	8.39	48	5.28
$Co_{0.9}Cu_{0.1}Fe_{1.85}Mn_{0.15}O_4$	8.39	46	5.29

4.2.6 $Co_{0.9}Cu_{0.1}Fe_{2-x}In_xO_4$ (where x = 0.00, 0.03, 0.06, 0.09, 0.12, and 0.15)

Room temperature powder X-ray diffraction analysis (Fig. 4.12) showed the single-phase formation of the series of In^{3+} substituted Co-Cu ferrite with no traces of secondary phase. The characteristic reflection peaks observed in the diffraction pattern can be indexed to cubic spinel structure (JCPDS NO.: 22-1086). The inset of Fig.

4.12shows the marginal shifting of 311 peaks towards lower 2θ angle with In^{3+} substitution. The lattice parameter showed a gradual increase on the replacement of Fe^{3+} ions by In^{3+} ions. This increase was credited to the lattice expansion due to the introduction of In^{3+} ions (0.91 Å) having larger ionic radii than Fe^{3+} ions (0.65 Å). This also suggested proper incorporation of In^{3+} ions into the host lattice.

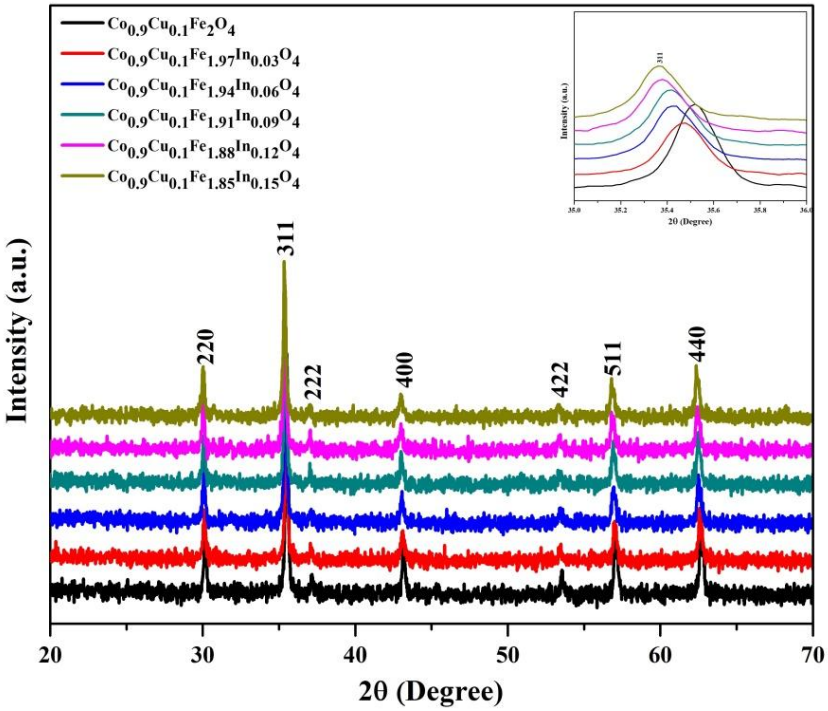

Fig. 4.12 *$Co_{0.9}Cu_{0.1}Fe_{2-x}In_xO_4$ (where x = 0.00, 0.03, 0.06, 0.09, 0.12, and 0.15).*

The X-ray density was seen to increase with In^{3+} ion substitution due to the increased molecular weight of the compound [192]. The average crystallite size, lattice parameter, and X-ray density have been tabulated in Table 4.6.

Table 4.6 X-ray diffraction data and particulate properties for In^{3+} substituted Co-Cu Ferrite.

Sample Composition	Lattice constant a (Å)	Crystallite size d (nm)	X-ray density ρ_x (g/cm^3)
$Co_{0.9}Cu_{0.1}Fe_2O_4$	8.38	45	5.31
$Co_{0.9}Cu_{0.1}Fe_{1.97}In_{0.03}O_4$	8.39	40	5.32
$Co_{0.9}Cu_{0.1}Fe_{1.94}In_{0.06}O_4$	8.40	44	5.34
$Co_{0.9}Cu_{0.1}Fe_{1.91}In_{0.09}O_4$	8.41	41	5.37
$Co_{0.9}Cu_{0.1}Fe_{1.88}In_{0.12}O_4$	8.41	42	5.40
$Co_{0.9}Cu_{0.1}Fe_{1.85}In_{0.15}O_4$	8.42	38	5.44

4.2.7 $Y_{2-x}Ce_yEu_xO_3$ (where y = 0.00, 0.01 and x = 0.00, 0.02, 0.04, and 0.06)

The XRD patterns of the samples sintered at 1000 °Crevealed a pure cubic phase of Y_2O_3 (Fig. 4.13).

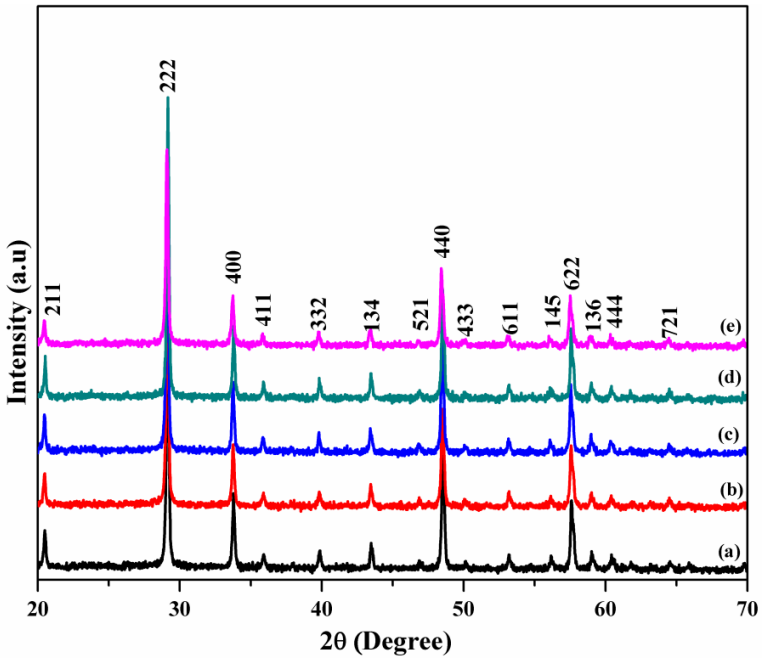

Fig. 4.13 *XRD pattern of (a) Y_2O_3 (b) $Y_{1.99}Ce_{0.01}O_3$ (c) $Y_{1.97}Ce_{0.01}Eu_{0.02}O_3$ (d) $Y_{1.95}Ce_{0.01}Eu_{0.04}O_3$ (e) $Y_{1.93}Ce_{0.01}Eu_{0.06}O_3$.*

The intense XRD peaks are well recognized as planes of (211), (222), (400), (411), (332), (134), (521), (440), (433), (611), (145), (622), (136), (444) and (721) for cubic Y_2O_3 (JCPDS No. 01-71-0099). Co-substitution with Ce^{3+} and Eu^{3+} did not show the formation of any additional phases so it can be deduced that Ce^{3+} and Eu^{3+} ions are well dissolved in the yttrium oxide lattice. It is revealed that the inclusion of Eu^{3+} and Ce^{3+} ions into Y^{3+} sites do not alter the cubic crystal structure which is credited to the matchable ionic radii of substituents and the host ion. The average crystallite size, the lattice constant, and X-ray density are summarized in Table 4.7.

Table 4.7 X-ray diffraction data and particulate properties for $Y_{2-x}Ce_yEu_xO_3$ (where y = 0.00, 0.01 and x = 0.00, 0.02, 0.04, and 0.06).

Sample Composition	Lattice constant a (Å)	Crystallite size d (nm)	X-ray density ρ_x (g/cm^3)
Y_2O_3	10.61	47	5.02
$Y_{1.99}Ce_{0.01}O_3$	10.63	46	5.01
$Y_{1.97}Ce_{0.01}Eu_{0.02}O_3$	10.61	49	5.07
$Y_{1.95}Ce_{0.01}Eu_{0.04}O_3$	10.61	50	5.10
$Y_{1.93}Ce_{0.01}Eu_{0.06}O_3$	10.62	44	5.10

4.2.8 $Y_{2-x}Ce_yEr_xO_3$ (where y = 0.00, 0.01 and x = 0.00, 0.02, 0.04, and 0.06)

The Ce^{3+} and Er^{3+} substituted Y_2O_3 phosphors heat-treated at 1000 ℃ were investigated using XRD analysis (Fig. 4.14). All the diffraction peaks obtained were consistent with pure-phase cubic Y_2O_3 with good crystallinity and there were no traces of impurity peaks (JCPDS card no. 01-71-0099). The estimated lattice parameters are comparable with the reported values. The crystallite size was determined from the width

of the reflection peaks utilizing the Scherrer's equation. The lattice parameters, crystallite size, and X-ray density are listed in Table 4.8.

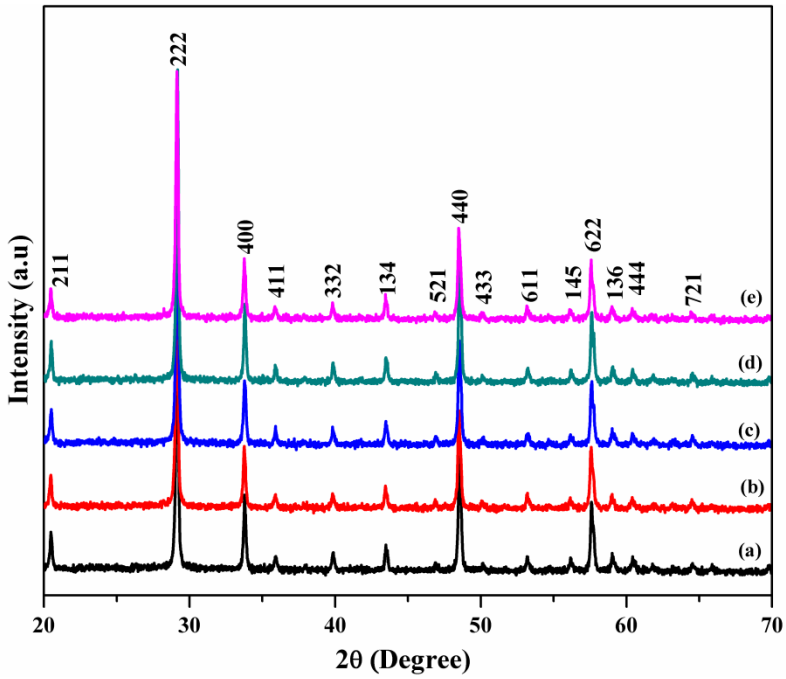

Fig. 4.14 *XRD pattern of (a) Y_2O_3 (b) $Y_{1.99}Ce_{0.01}O_3$ (c) $Y_{1.97}Ce_{0.01}Er_{0.02}O_3$ (d) $Y_{1.95}Ce_{0.01}Er_{0.04}O_3$ (e) $Y_{1.93}Ce_{0.01}Er_{0.06}O_3$.*

.

Table 4.8 X-ray diffraction data and particulate properties for $Y_{2-x}Ce_yEr_xO_3$ (where y = 0.00, 0.01 and x = 0.00, 0.02, 0.04, and 0.06).

Sample Composition	Lattice constant a (Å)	Crystallite size d (nm)	X-ray density ρ_x (g/cm^3)
Y_2O_3	10.61	47	5.02
$Y_{1.99}Ce_{0.01}O_3$	10.63	46	5.01
$Y_{1.97}Ce_{0.01}Er_{0.02}O_3$	10.62	45	5.06
$Y_{1.95}Ce_{0.01}Er_{0.04}O_3$	10.61	49	5.11
$Y_{1.93}Ce_{0.01}Er_{0.06}O_3$	10.61	45	5.13

4.2.9 $Gd_{1.96-x}Er_{0.04}Yb_xO_3$ (where x = 0.04, 0.08, 0.12, 0.16 and 0.20)

Fig. 4.15 presents the powder XRD pattern for $Gd_{2-x}Er_{0.04}Yb_xO_3$ (where x = 0.04, 0.08, 0.12, 0.16 and 0.20) sintered at 1000 ℃ for 10 h. All the peaks match well with the cubic phase Gd_2O_3 (JCPDS No. 01-088-2165) without the presence of any secondary phase. The intense XRD peaks are well identified as reflection planes of 222, 400, 411, 332, 134, 440, 611, 622, 136, and 444 for cubic Gd_2O_3.

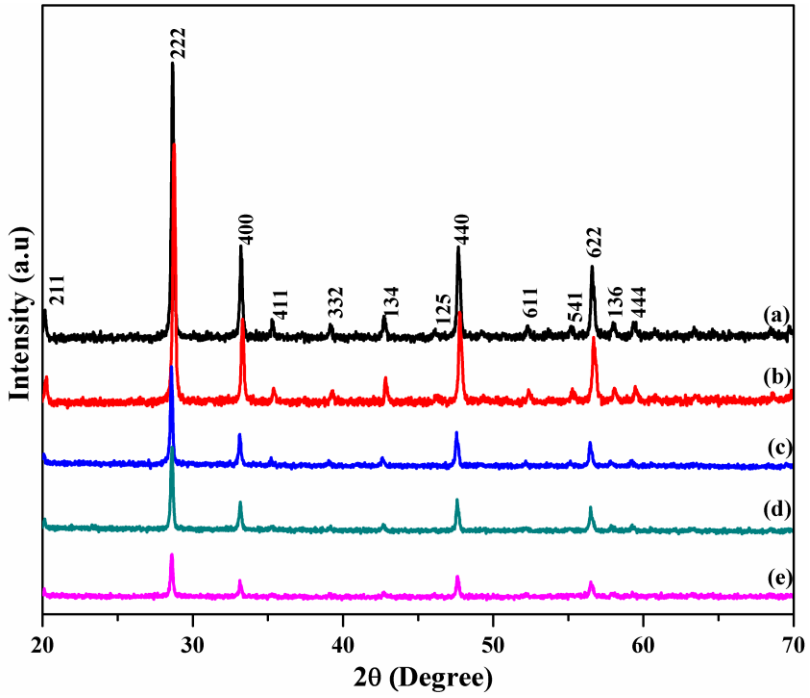

Fig. 4.15*XRD patterns of (a) $Gd_{1.92}Er_{0.04}Yb_{0.04}O_3$ (b) $Gd_{1.88}Er_{0.04}Yb_{0.08}O_3$ (c) $Gd_{1.84}Er_{0.04}Yb_{0.12}O_3$ (d) $Gd_{1.80}Er_{0.04}Yb_{0.16}O_3$ (e) $Gd_{1.76}Er_{0.04}Yb_{0.20}O_3$.*

The calculated lattice parameter values were consistent with the reported literature. From the XRD peaks, the crystallite size was calculated using the Scherrer's formula. The calculated crystallite size, the lattice constant, and X-ray density are presented in Table 4.9.

Table 4.9 X-ray diffraction data and particulate properties for $Gd_{1.96-x}Er_{0.04}Yb_xO_3$ (where x = 0.04, 0.08, 0.12, 0.16 and 0.20).

Sample Composition	Lattice constant a (Å)	Crystallite size d (nm)	X-ray density ρ_x (g/cm^3)
$Gd_{1.92}Er_{0.04}Yb_{0.04}O_3$	10.81	46	7.64
$Gd_{1.88}Er_{0.04}Yb_{0.08}O_3$	10.80	45	7.68
$Gd_{1.84}Er_{0.04}Yb_{0.12}O_3$	10.79	45	7.72
$Gd_{1.80}Er_{0.04}Yb_{0.16}O_3$	10.78	42	7.74
$Gd_{1.76}Er_{0.04}Yb_{0.20}O_3$	10.76	43	7.80

4.2.10 $Gd_{1.96-x}Ho_{0.04}Yb_xO_3$ (where x = 0.04, 0.08, 0.12, 0.16 and 0.20)

The powder XRD pattern of $Gd_{1.96-x}Ho_{0.04}Yb_xO_3$ (where x = 0.04, 0.08, 0.12, 0.16 and 0.20) has been shown in the Fig. 4.16.

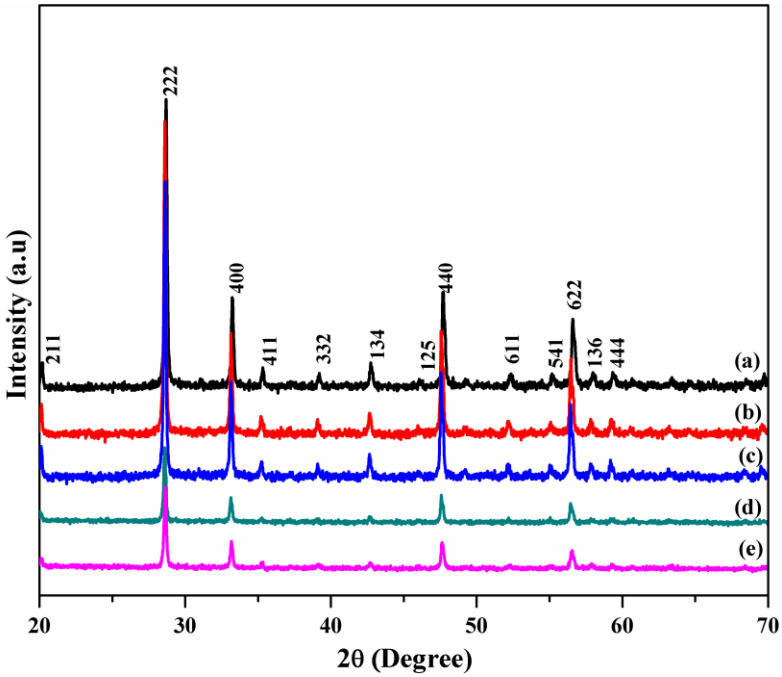

Fig. 4.16 *XRD patterns of (a) $Gd_{1.92}Ho_{0.04}Yb_{0.04}O_3$ (b) $Gd_{1.88}Ho_{0.04}Yb_{0.08}O_3$ (c) $Gd_{1.84}Ho_{0.04}Yb_{0.12}O_3$ (d) $Gd_{1.80}Ho_{0.04}Yb_{0.16}O_3$ (e) $Gd_{1.76}Ho_{0.04}Yb_{0.20}O_3$.*

All the peaks observed in the spectra can be indexed to the cubic phase of Gd_2O_3 according to JCPDS card no. 01-088-2165. The pattern did not show the presence of any impurity phases hence it can be said that Ho^{3+} and Yb^{3+} ions are incorporated in the Gd_2O_3 matrix.Crystallite size was calculated using Scherrer's relation and the average crystallite size was found to be in the range 42-45 nm. Lattice parameter calculated was consistent with the literature reports. The lattice parameter, crystallite size, and X-ray density are listed in Table 4.10.

Table 4.10 X-ray diffraction data and particulate properties for $Gd_{1.96-x}Ho_{0.04}Yb_xO_3$ (where x = 0.04, 0.08, 0.12, 0.16 and 0.20).

Sample Composition	Lattice constant a (Å)	Crystallite size d (nm)	X-ray density ρ_x (g/cm^3)
$Gd_{1.92}Ho_{0.04}Yb_{0.04}O_3$	10.81	45	7.64
$Gd_{1.88}Ho_{0.04}Yb_{0.08}O_3$	10.81	45	7.65
$Gd_{1.84}Ho_{0.04}Yb_{0.12}O_3$	10.81	44	7.66
$Gd_{1.80}Ho_{0.04}Yb_{0.16}O_3$	10.80	44	7.70
$Gd_{1.76}Ho_{0.04}Yb_{0.20}O_3$	10.78	42	7.75

4.3 Inductively Coupled Plasma – Atomic Emission Spectrometry Studies (ICP-AES)

4.3.1 $Co_{1-x}Cu_xFe_2O_4$ (where x = 0.00, 0.05, 0.1, 0.15, 0.20 and 0.25)

The precise metal ion concentration was determined using ICP-AES. The metal ion concentration in weight percent has been summarized in Table 4.11. The actual concentration of Co, Cu, and Fe in the pure and substituted $CoFe_2O_4$ were found to be in agreement with the expected values, indicating that the material composition was achieved as per design.

Table 4.11 Results of the ICP-AES analysis conducted on $Co_{1-x}Cu_xFe_2O_4$ (where x = 0.00, 0.05, 0.10, 0.15, 0.20, and 0.25).

Sample Composition	Metal concentration (wt %)		
	Co	Cu	Fe
$CoFe_2O_4$	25.15	-	50.81
$Co_{0.95}Cu_{0.05}Fe_2O_4$	24.08	1.15	47.26
$Co_{0.90}Cu_{0.10}Fe_2O_4$	23.84	2.56	47.13
$Co_{0.85}Cu_{0.15}Fe_2O_4$	22.41	3.79	48.93
$Co_{0.80}Cu_{0.20}Fe_2O_4$	19.26	5.09	45.63
$Co_{0.75}Cu_{0.25}Fe_2O_4$	19.52	6.92	48.34

4.3.2 $CoFe_{2-x}Sb_xO_4$ (where x = 0.00, 0.03, 0.06, and 0.09)

The ICP-AES analysis carried out on $CoFe_{2-x}Sb_xO_4$ (where x = 0.00, 0.03, 0.06, and 0.09)showed that the percentage of elements obtained was in good agreement with the calculated percentage (Table 4.12).

Table 4.12 Results of the ICP-AES analysis conducted on $CoFe_{2-x}Sb_xO_4$ (where x = 0.00, 0.03, 0.06, and 0.09).

Sample Composition	Metal concentration (wt %)		
	Co	Fe	Sb
$CoFe_2O_4$	25.15	50.81	-
$CoFe_{1.97}Sb_{0.03}O_4$	29.59	49.65	1.20
$CoFe_{1.94}Sb_{0.06}O_4$	29.47	48.49	2.12
$CoFe_{1.91}Sb_{0.09}O_4$	29.24	47.24	3.22

4.3.3 $Co_{0.9}Cu_{0.1}Fe_{2-x}RE_xO4$ (where RE = Gd, Sm, Dy, Yb, Eu and x = 0.00, 0.03, 0.05)

Table 4.13 shows the results of the metal concentration in weight percent for RE^{3+} substituted Co-Cu ferrite. The values obtained for Co, Cu, Fe, Gd, Dy, Sm, Yb and Eu contents are consistent with the theoretical compositions.

Table 4.13 Results of the ICP-AES analysis conducted on $Co_{0.9}Cu_{0.1}Fe_{2-x}RE_xO_4$ (RE = Gd, Dy, Sm, Yb, and Eu, and x = 0.00, 0.03, and 0.05).

Sample Composition	Metal concentration (wt %)							
	Co	Cu	Fe	Gd	Dy	Sm	Yb	Eu
$Co_{0.9}Cu_{0.1}Fe_2O_4$	23.84	2.56	47.13	-	-	-	-	-
$Co_{0.9}Cu_{0.1}Fe_{1.97}Gd_{0.03}O_4$	22.72	2.67	45.48	1.45	-	-	-	-
$Co_{0.9}Cu_{0.1}Fe_{1.95}Gd_{0.05}O_4$	23.96	2.83	47.13	3.17	-	-	-	-
$Co_{0.9}Cu_{0.1}Fe_{1.97}Dy_{0.03}O_4$	23.84	2.58	46.59	-	1.65	-	-	-
$Co_{0.9}Cu_{0.1}Fe_{1.95}Dy_{0.05}O_4$	24.42	2.60	47.34	-	2.94	-	-	-
$Co_{0.9}Cu_{0.1}Fe_{1.97}Sm_{0.03}O_4$	24.55	2.60	48.06	-	-	1.32	-	-
$Co_{0.9}Cu_{0.1}Fe_{1.95}Sm_{0.05}O_4$	23.68	2.69	47.69	-	-	2.31	-	-
$Co_{0.9}Cu_{0.1}Fe_{1.97}Yb_{0.03}O_4$	23.62	2.85	46.75	-	-	-	1.23	-
$Co_{0.9}Cu_{0.1}Fe_{1.95}Yb_{0.05}O_4$	24.87	2.76	45.55	-	-	-	3.17	-
$Co_{0.9}Cu_{0.1}Fe_{1.97}Eu_{0.03}O_4$	23.80	2.85	47.22	-	-	-	-	1.54
$Co_{0.9}Cu_{0.1}Fe_{1.95}Eu_{0.05}O_4$	22.38	2.70	44.07	-	-	-	-	2.50

4.3.4 $Co_{0.9}Cu_{0.1}Fe_{2-x}Cr_xO_4$ (where x = 0.00, 0.03, 0.06, 0.09, 0.12, and 0.15)

ICP-AES analysis results obtsained for Cr^{3+} substituted Co-Cu ferrite were in very close agreement with the expected values (Table 4.14).

Table 4.14 Results of the ICP-AES analysis conducted on $Co_{0.9}Cu_{0.1}Fe_{2-x}Cr_xO_4$ (where x = 0.00, 0.03, 0.06, 0.09, 0.12 and 0.15).

Sample Composition	Metal concentration (wt %)			
	Co	Cu	Fe	Cr
$Co_{0.9}Cu_{0.1}Fe_2O_4$	23.84	2.56	47.13	-
$Co_{0.9}Cu_{0.1}Fe_{1.97}Cr_{0.03}O_4$	22.47	2.63	44.85	0.52
$Co_{0.9}Cu_{0.1}Fe_{1.94}Cr_{0.06}O_4$	22.78	2.57	44.61	1.09
$Co_{0.9}Cu_{0.1}Fe_{1.91}Cr_{0.09}O_4$	22.85	2.49	43.90	1.73
$Co_{0.9}Cu_{0.1}Fe_{1.88}Cr_{0.12}O_4$	22.78	2.63	43.14	2.46
$Co_{0.9}Cu_{0.1}Fe_{1.85}Cr_{0.15}O_4$	24.06	2.69	43.04	3.02

4.3.5 $Co_{0.9}Cu_{0.1}Fe_{2-x}Mn_xO_4$ (where x = 0.00, 0.03, 0.06, 0.09, 0.12, and 0.15)

The elemental composition determined from ICP-AES measurement suggests that the results obtained were in very close agreement with the expected values (Table 4.15).

Table 4.15 Results of the ICP-AES analysis conducted on $Co_{0.9}Cu_{0.1}Fe_{2-x}Mn_xO_4$ (where x = 0.00, 0.03, 0.06, 0.09, 0.12 and 0.15).

Sample Composition	Metal concentration (wt %)			
	Co	Cu	Fe	Mn
$Co_{0.9}Cu_{0.1}Fe_2O_4$	23.84	2.56	47.13	-
$Co_{0.9}Cu_{0.1}Fe_{1.97}Mn_{0.03}O_4$	23.84	2.39	45.84	0.61
$Co_{0.9}Cu_{0.1}Fe_{1.94}Mn_{0.06}O_4$	23.47	2.42	44.55	1.26
$Co_{0.9}Cu_{0.1}Fe_{1.91}Mn_{0.09}O_4$	23.33	2.37	43.29	1.88
$Co_{0.9}Cu_{0.1}Fe_{1.88}Mn_{0.12}O_4$	22.94	2.33	42.23	2.34
$Co_{0.9}Cu_{0.1}Fe_{1.85}Mn_{0.15}O_4$	23.13	2.43	41.70	3.07

4.3.6 $Co_{0.9}Cu_{0.1}Fe_{2-x}In_xO_4$ (where x = 0.03, 0.06, 0.09, 0.12, and 0.15)

The ICP-AES results for In^{3+} substituted Co-Cu ferrite are summarized in Table 4.16. The results acquired were almost consistent with the expected values, confirming the successful formation of the formulated compounds.

Table 4.16 Results of the ICP-AES analysis conducted on the $Co_{0.9}Cu_{0.1}Fe_{2-x}In_xO_4$ (where x = 0.00, 0.03, 0.06, 0.09, 0.12, and 0.15).

Sample Composition	Metal concentration (wt %)			
	Co	Cu	Fe	In
$Co_{0.9}Cu_{0.1}Fe_2O_4$	23.84	2.56	47.13	-
$Co_{0.9}Cu_{0.1}Fe_{1.97}In_{0.03}O_4$	25.48	2.66	48.10	1.45
$Co_{0.9}Cu_{0.1}Fe_{1.94}In_{0.06}O_4$	23.25	2.45	43.34	2.66
$Co_{0.9}Cu_{0.1}Fe_{1.91}In_{0.09}O_4$	23.58	2.44	43.12	4.01
$Co_{0.9}Cu_{0.1}Fe_{1.88}In_{0.12}O_4$	23.24	2.40	41.89	5.19
$Co_{0.9}Cu_{0.1}Fe_{1.85}In_{0.15}O_4$	23.39	2.42	41.53	6.66

4.3.7 $Y_{2-x}Ce_yEu_xO_3$ (where y = 0.00, 0.01 and x = 0.00, 0.02, 0.04, and 0.06)

The obtained results of ICP-AES analysis for Ce^{3+} and Eu^{3+} co-substituted Y_2O_3were in close proximity to the calculated values (Table 4.17). Hence it can be inferred that the compositions were obtained as per the design.

Table 4.17 Results of the ICP-AES analysis conducted on the $Y_{2-x}Ce_yEu_xO_3$ (Where y = 0.00, 0.01 and x = 0.00, 0.02, 0.04, and 0.06).

Sample Composition	Metal concentration (wt %)		
	Y	Ce	Eu
Y_2O_3	77.09	-	-
$Y_{1.99}Ce_{0.01}O_3$	76.58	0.80	-
$Y_{1.97}Ce_{0.01}Eu_{0.02}O_3$	75.75	0.66	1.36
$Y_{1.95}Ce_{0.01}Eu_{0.04}O_3$	74.67	0.62	2.57
$Y_{1.93}Ce_{0.01}Eu_{0.06}O_3$	73.53	0.78	4.24

4.3.8 $Y_{2-x}Ce_yEr_xO_3$ (where y = 0.00, 0.01 and x = 0.00, 0.02, 0.04, and 0.06)

Results of ICP-AES analysis performed on Ce^{3+} and Er^{3+} co-substituted Y_2O_3were close to the expected values and has been presented in Table 4.18.

Table 4.18 Results of the ICP-AES analysis conducted on the $Y_{2-x}Ce_yEr_xO_3$ (Where y = 0.00, 0.01 and x = 0.00, 0.02, 0.04, and 0.06).

Sample Composition	Metal concentration (wt %)		
	Y	Ce	Er
Y_2O_3	77.09	-	-
$Y_{1.99}Ce_{0.01}O_3$	76.58	0.80	-
$Y_{1.97}Ce_{0.01}Er_{0.02}O_3$	74.92	0.82	2.02
$Y_{1.95}Ce_{0.01}Er_{0.04}O_3$	73.30	0.74	3.80
$Y_{1.93}Ce_{0.01}Er_{0.06}O_3$	72.78	0.95	6.77

4.3.9 $Gd_{1.96-x}Er_{0.04}Yb_xO_3$ (where x = 0.04, 0.08, 0.12, 0.16 and 0.20)

The results of ICP-AES analysis for Er^{3+} and Yb^{3+} co-substituted $Gd_2O_3$are listed in Table 4.19. The obtained values are consistent with the calculated values. Hence the compositions were achieved as per the formulations.

Table 4.19 Results of the ICP-AES analysis conducted on the $Gd_{1.96-x}Er_{0.04}Yb_xO_3$ (where x = 0.04, 0.08, 0.12, 0.16 and 0.20).

Sample Composition	Metal concentration (wt %)		
	Gd	Er	Yb
$Gd_{1.92}Er_{0.04}Yb_{0.04}O_3$	82.01	2.32	1.98
$Gd_{1.88}Er_{0.04}Yb_{0.08}O_3$	80.20	2.21	3.91
$Gd_{1.84}Er_{0.04}Yb_{0.12}O_3$	78.74	2.23	5.92
$Gd_{1.80}Er_{0.04}Yb_{0.16}O_3$	76.66	2.10	9.02
$Gd_{1.76}Er_{0.04}Yb_{0.20}O_3$	74.35	2.08	10.25

4.3.10 $Gd_{1.96-x}Ho_{0.04}Yb_xO_3$ (where x = 0.04, 0.08, 0.12, 0.16 and 0.20)

The concentration of Gd, Yb, and Ho in the samples verified by ICP-AES analysis showed that they are in close agreement with the calculated values (Table 4.20).

Table 4.20 Results of the ICP-AES analysis conducted on the $Gd_{1.96-x}Ho_{0.04}Yb_xO_3$ (where x = 0.04, 0.08, 0.12, 0.16 and 0.20).

Sample Composition	Metal concentration (wt %)		
	Gd	Ho	Yb
$Gd_{1.92}Ho_{0.04}Yb_{0.04}O_3$	81.59	2.74	1.12
$Gd_{1.88}Ho_{0.04}Yb_{0.08}O_3$	80.72	1.88	3.92
$Gd_{1.84}Ho_{0.04}Yb_{0.12}O_3$	79.20	1.88	6.01
$Gd_{1.80}Ho_{0.04}Yb_{0.16}O_3$	76.90	2.65	7.98
$Gd_{1.76}Ho_{0.04}Yb_{0.20}O_3$	75.01	2.43	9.18

4.4 Infrared studies

4.4.1 $Co_{1-x}Cu_xFe_2O_4$ (where x = 0.00, 0.05, 0.1, 0.15, 0.20 and 0.25)

IR spectroscopy is a useful method to deduce the stretching and bending vibrations of ferrite materials. It assists in the structural analysis and identifies cation redistribution between octahedral (B) and tetrahedral (A) sites of the spinel structure [351,352]. The IR spectra of $Co_{1-x}Cu_xFe_2O_4$ (where x = 0.00, 0.05, 0.1, 0.15, 0.20 and 0.25)as presented in Fig. 4.17 displays no bands in the region 1000 - 3500 cm^{-1} corresponding to organic moieties thus validating the impurity-free formation of Co-Cu ferrite. All samples show two characteristic and prominent absorption bands υ_1 and υ_2 ~ 600 and 400 cm^{-1} respectively. In ferrite materials, the metal ions are placed in two different sub-lattices designated as tetrahedral (A - site) and octahedral (B - site). The absorption band at ~ 600 cm^{-1} represents the metal-oxygen stretching vibrations at the tetrahedral sites and ~ 400 cm^{-1} to the metal-oxygen stretching vibrations at the octahedral sites [196,353].

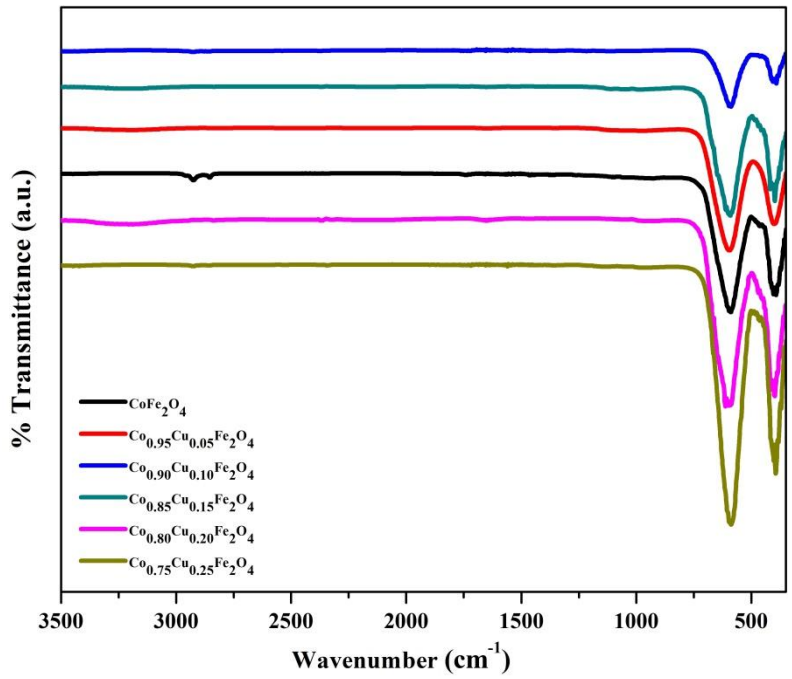

Fig. 4.17 *Infrared spectra of* $Co_{1-x}Cu_xFe_2O_4$ *(where x = 0.00, 0.05, 0.1, 0.15, 0.20 and 0.25).*

4.4.2 $CoFe_{2-x}Sb_xO_4$ (where x = 0.00, 0.03, 0.06, and 0.09)

The room temperature IR spectra of $CoFe_{2-x}Sb_xO_4$ (where x = 0.00, 0.03, 0.06, and 0.09) show typical bands for cubic spinel ferrites ~400 (υ_2) and ~600 (υ_1) cm^{-1} which is due to the frequency of absorption at B and A sites respectively (Fig. 4.18) [354]. Since the Metal-Oxygen bond length in the A site is shorter than in the B site, the band denoting the tetrahedral stretching vibrations emerged at a higher wave number as compared to the octahedral stretching vibrations [355]. A slight shift in band positions with Sb^{3+} substitution was observed in the IR spectra indicative of systematic incorporation of the substituent in the host lattice.

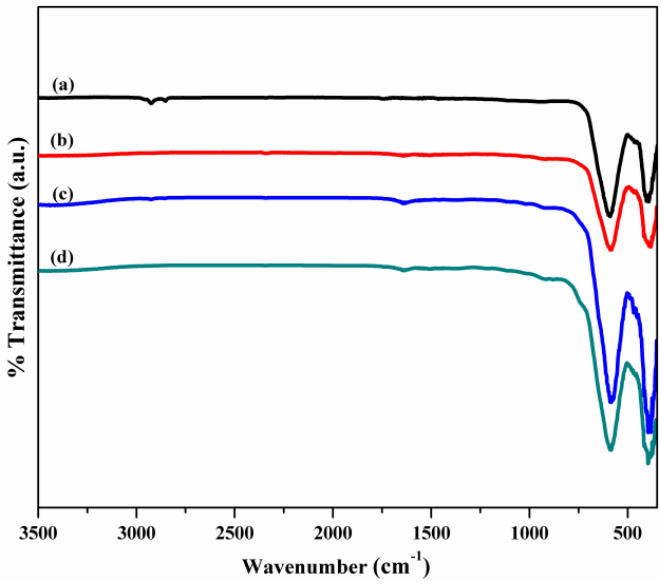

Fig. 4.18 *Infrared spectra of (a) $CoFe_2O_4$ (b) $CoFe_{1.97}Sb_{0.03}O_4$ (c) $CoFe_{1.94}Sb_{0.06}O_4$ (d) $CoFe_{1.91}Sb_{0.09}O_4$.*

4.4.3 $Co_{0.9}Cu_{0.1}Fe_{2-x}RE_xO_4$ (where RE = Gd, Sm, Dy, Yb, Eu, and x = 0.00, 0.03, 0.05)

The room temperature IR spectra of the prepared ferrite materials which are thermally treated at 800 $^{\circ}$C have been shown in Fig. 4.19.

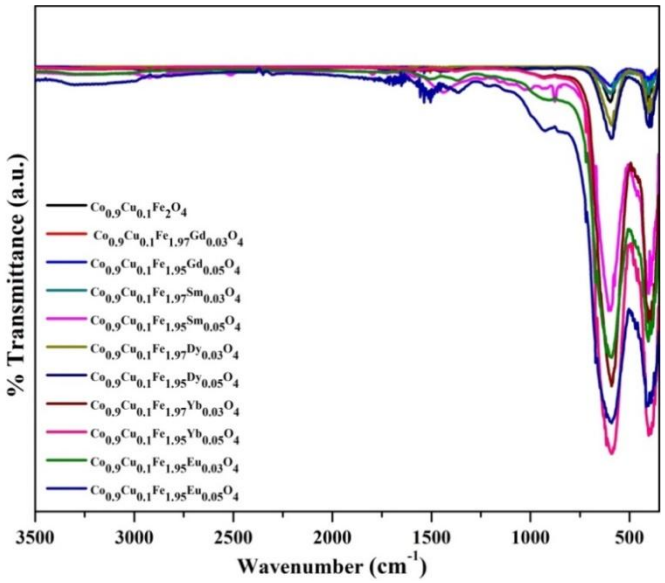

Fig. 4.19 *Infrared spectra of $Co_{0.9}Cu_{0.1}Fe_{2-x}RE_xO_4$ (where RE = Gd, Sm, Dy, Yb, Eu, and x = 0.00, 0.03, 0.05).*

The spectra show two prominent absorption bands around 600 cm^{-1} and 400 cm^{-1}. The IR active signals observed around 600 (υ_1) and 400 (υ_2) cm^{-1} correspond to the frequency of absorption for tetrahedral and octahedral sites of ferrite structure, respectively [354]. A shifting behavior observed in IR signals (ν_1, ν_2) compared to that of corresponding pure Co-Cu ferrite is attributed to the substitution of RE^{3+} ions for Fe^{3+} ions leading to change in the bond length (M−O) and the mass differences in the crystal lattice structure.

4.4.4 $Co_{0.9}Cu_{0.1}Fe_{2-x}Cr_xO_4$ (where x = 0.00, 0.03, 0.06, 0.09, 0.12, and 0.15)

The room temperature IR spectra of $Co_{0.9}Cu_{0.1}Fe_2O_4$ and Cr ion substituted $Co_{0.9}Cu_{0.1}Fe_2O_4$have been shown in Fig. 4.20.

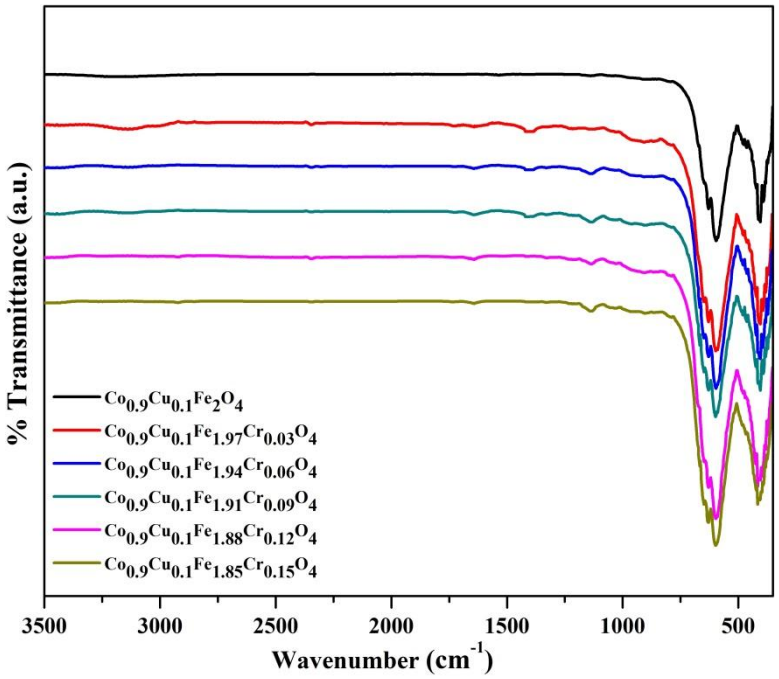

Fig. 4.20 *Infrared spectra of $Co_{0.9}Cu_{0.1}Fe_{2-x}Cr_xO_4$ (where x = 0.00, 0.03, 0.06, 0.09, 0.12, and 0.15).*

The spectra show absorption bands below 1000 cm^{-1}, which is a common feature of all the ferrites. The frequency band (υ_1) obtained at ~600 cm^{-1} is due to M-O stretching

at tetrahedral sub-lattice and frequency band (υ_2) at ~400 cm^{-1} is due to M-O stretching at octahedral sub-lattice [354]. These two absorption bands observed at the expected frequencies reveal the formation of single-phase spinel structure.

4.4.5 $Co_{0.9}Cu_{0.1}Fe_{2-x}Mn_xO_4$ (where x = 0.00, 0.03, 0.06, 0.09, 0.12, and 0.15)

The room temperature IR spectra for $Co_{0.9}Cu_{0.1}Fe_{2-x}Mn_xO_4$ (where x = 0.03, 0.06, 0.09, 0.12 and 0.15) are shown in Fig. 4.21. The IR analysis of the samples show the two expected absorption peaks, confirming the formation of cubic spinel ferrite. The peak at about 400 cm^{-1} is associated with the metal-oxygen vibration at the octahedral site and the second peak at about 600 cm^{-1} is associated with the metal-oxygen vibration at the tetrahedral site [354]. The absorption bands are slightly shifted with the addition of Mn ions.

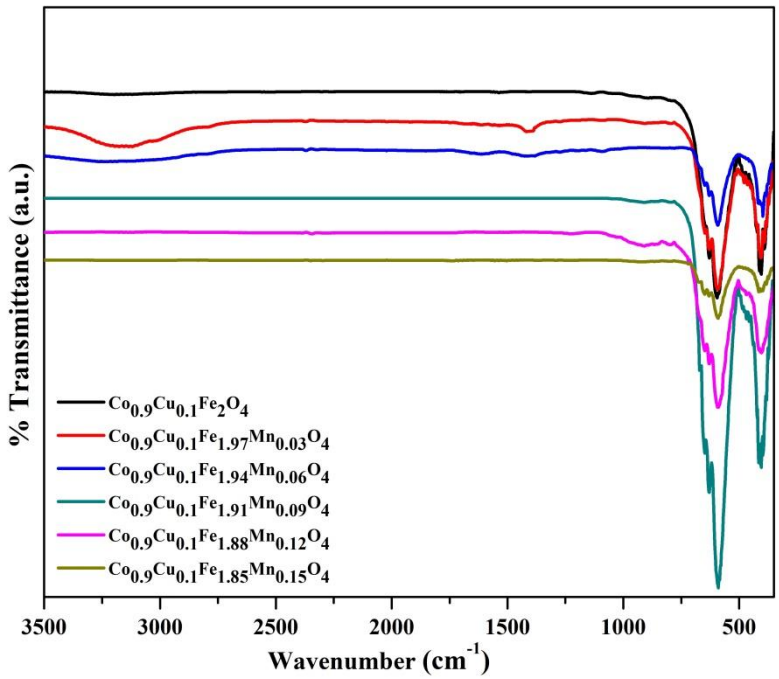

Fig. 4.21 *Infrared spectra of $Co_{0.9}Cu_{0.1}Fe_{2-x}Mn_xO_4$ (where x = 0.00, 0.03, 0.06, 0.09, 0.12, and 0.15).*

4.4.6 $Co_{0.9}Cu_{0.1}Fe_{2-x}In_xO_4$ (where x = 0.00, 0.03, 0.06, 0.09, 0.12, and 0.15)

The IR spectra for the series $Co_{0.9}Cu_{0.1}Fe_{2-x}In_xO_4$ (where x = 0.00, 0.03, 0.06, 0.09, 0.12, and 0.15)are shown in Figure 4.22. The characteristic absorption bands at ~600 and ~400 cm^{-1} corresponds to the metal–oxygen vibration at tetrahedral and octahedral sites respectively, which are indicative of the formation of cubic spinel ferrites [354].

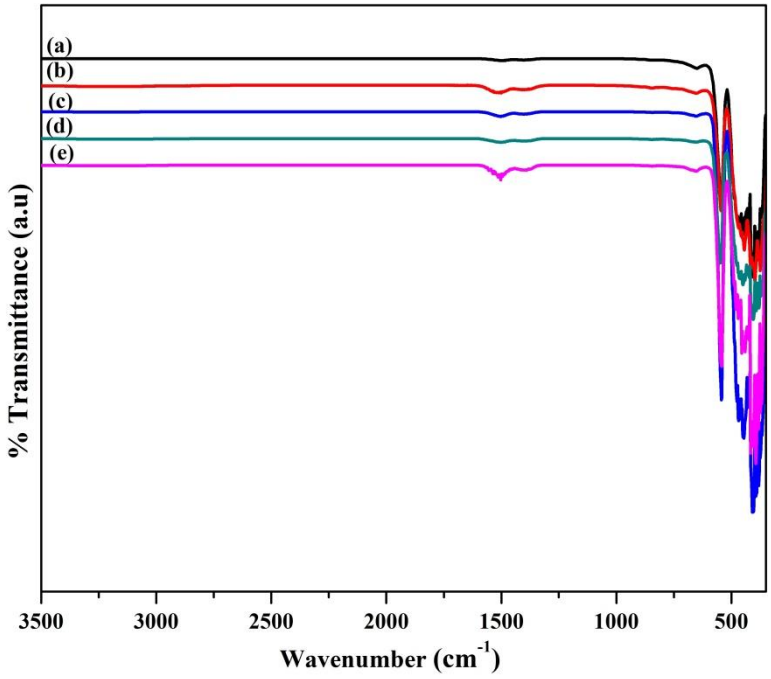

Fig. 4.22 *Infrared spectra of $Co_{0.9}Cu_{0.1}Fe_{2-x}In_xO_4$ (where x = 0.00, 0.03, 0.06, 0.09, 0.12, and 0.15)*

4.4.7 $Y_{2-x}Ce_yEu_xO_3$ (where y = 0.00, 0.01 and x = 0.00, 0.02, 0.04, and 0.06)

The IR spectra of pure Y_2O_3 and substituted Y_2O_3 in the region 400 - 4000 cm^{-1} are shown in Fig. 4.23. The absorption peaks in the region from 400 - 560 cm^{-1} can be clearly observed in the spectra which are attributed to Y–O lattice vibration of cubic Y_2O_3, which is in agreement with literature reports [274].

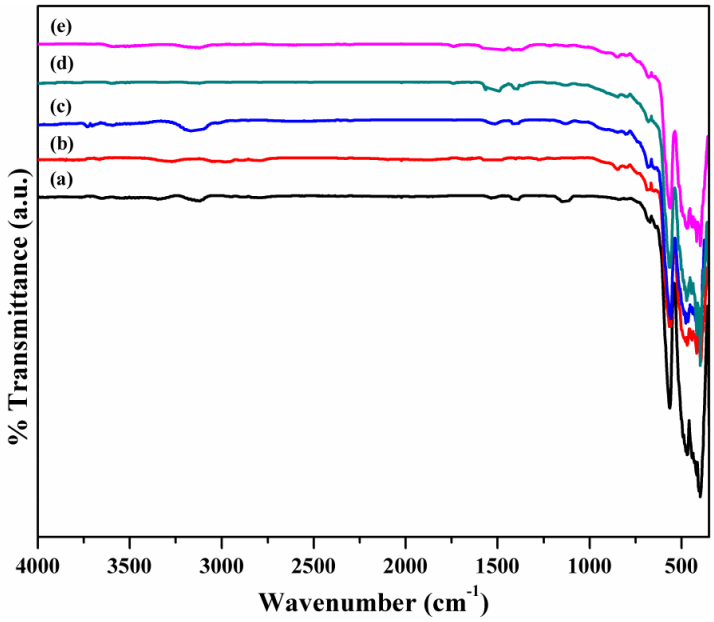

Fig. 4.23 *Infrared spectra for (a) Y_2O_3 (b) $Y_{1.99}Ce_{0.01}O_3$ (c) $Y_{1.97}Ce_{0.01}Eu_{0.02}O_3$ (d) $Y_{1.95}Ce_{0.01}Eu_{0.04}O_3$ (e) $Y_{1.93}Ce_{0.01}Eu_{0.06}O_3$.*

4.4.8 $Y_{2-x}Ce_yEr_xO_3$ (where y = 0.00, 0.01 and x = 0.00, 0.02, 0.04, and 0.06)

The IR spectra of pristine and substituted Y_2O_3heat-treated at 1000 ℃ are shown in Fig. 4.24.

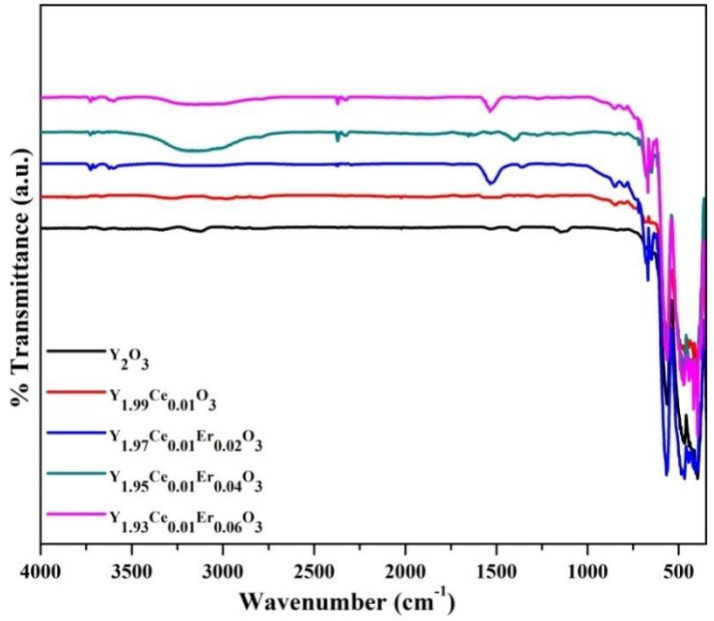

Fig.4.24 *Infrared spectra for $Y_{2-x}Ce_yEr_xO_3$ (where y = 0.00, 0.01 and x = 0.00, 0.02, 0.04, and 0.06).*

All the samples show absorption bands in the range 400 to 560 cm^{-1} due to Y–O lattice vibration in cubic Y_2O_3[274]. No other bands were observed in the spectra which confirm the formation of the desired compound.

4.4.9 $Gd_{1.96-x}Er_{0.04}Yb_xO_3$ (where x = 0.04, 0.08, 0.12, 0.16 and 0.20)

The IR spectra of Yb^{3+} and Er^{3+} co-substituted Gd_2O_3 has been shown in Fig. 4.25. The spectra showed peaks in the region 400 - 560 cm^{-1} which be can be associated with the vibration of Gd-O bond, which also confirmed the formation of impurity-free substituted Gd_2O_3[356].

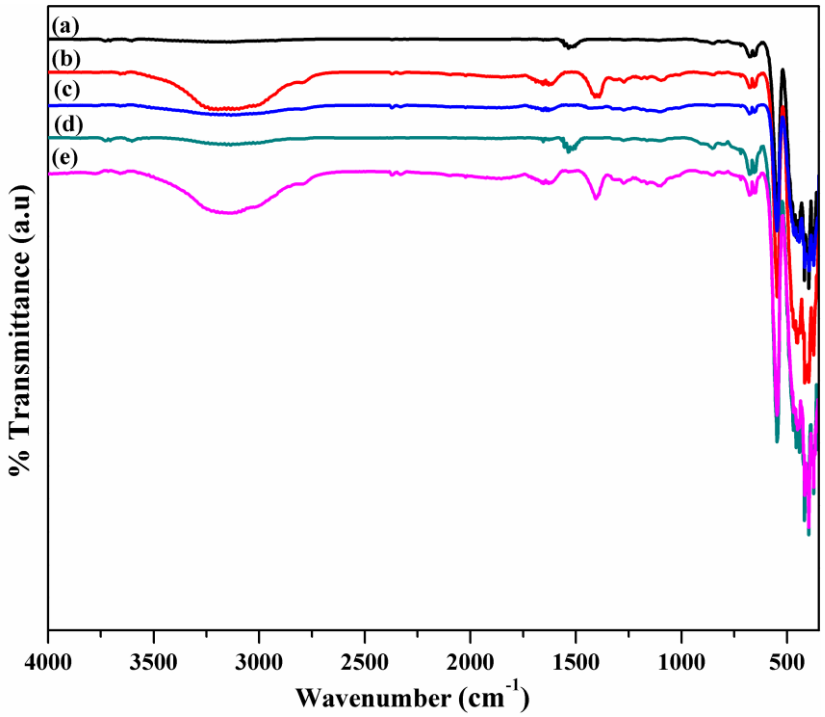

Fig. 4.25 *Infrared spectra for(a) $Gd_{1.92}Er_{0.04}Yb_{0.04}O_3$ (b) $Gd_{1.88}Er_{0.04}Yb_{0.08}O_3$ (c) $Gd_{1.84}Er_{0.04}Yb_{0.12}O_3$ (d) $Gd_{1.80}Er_{0.04}Yb_{0.16}O_3$ (e) $Gd_{1.76}Er_{0.04}Yb_{0.20}O_3$.*

4.4.10 $Gd_{1.96-x}Ho_{0.04}Yb_xO_3$ (where x = 0.04, 0.08, 0.12, 0.16 and 0.20)

Fig. 4.26 shows the IR spectra of the substituted Gd_2O_3 samples heat treated at 1000 °C. The band at about 400 - 560 cm^{-1} can be assigned to the Gd–O stretching frequencies of the cubic Gd_2O_3 [356]. The results obtained with IR analysis further confirm the impurity-free formation of substituted Gd_2O_3.

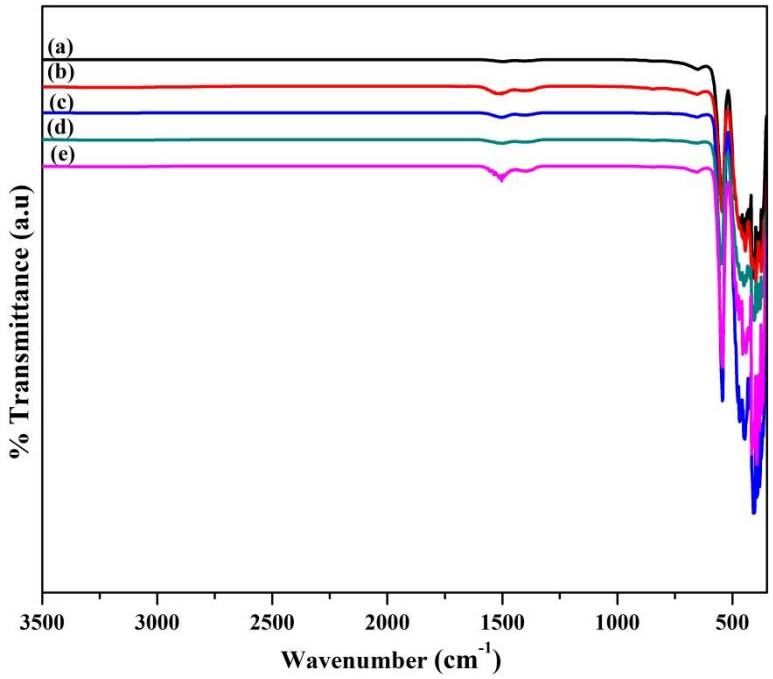

Fig.4.26*Infrared spectra for(a) $Gd_{1.92}Ho_{0.04}Yb_{0.04}O_3$ (b) $Gd_{1.88}Ho_{0.04}Yb_{0.08}O_3$ (c) $Gd_{1.84}Ho_{0.04}Yb_{0.12}O_3$ (d) $Gd_{1.80}Ho_{0.04}Yb_{0.16}O_3$ (e) $Gd_{1.76}Ho_{0.04}Yb_{0.20}O_3$.*

4.5 Raman Spectroscopy

Raman spectroscopy is widely recognized as a powerful and non-destructive method for probing magnetic oxides.

4.5.1 $Co_{1-x}Cu_xFe_2O_4$ (where x = 0.00, 0.05, 0.1, 0.15, 0.20 and 0.25)

The Raman spectra of the pure and Cu^{2+} substituted $CoFe_2O_4$ are displayed in Fig. 4.27. The six Raman modes designated as $2A_{1g}$ (594 - 609 cm^{-1}, 676 - 684 cm^{-1}), E_g (284

- 301 cm^{-1}), $3T_{2g}$ (544 - 547 cm^{-1}, 455 - 464 cm^{-1}, 189 - 200 cm^{-1}) expected for the cubic spinel ferrite system were noticed in the spectra. Substituted Co-Cu ferrite has a cubic mixed inverse spinel ferrite structure with O^7_h ($Fd\bar{3}m$) symmetry space group and has 39 normal vibrational modes predicted from group theory, out of which six are Raman active modes ($2A_{1g}$, E_g, $3T_{2g}$). The vibrational modes above 600 cm^{-1}represent the symmetrical stretching of metal-oxygen bonding at the tetrahedral (A) sites, and the vibrational modes below 600 cm^{-1} can be assigned to the symmetrical and anti-symmetrical bending of metal-oxygen in the octahedral (B) sites [357]. With the Cu^{2+} ion substitution, a shift in Raman mode towards higher frequency is noticed. This shift can be due to the introduction of larger Cu^{2+} ions which may produce strain in the structure. The impurity phases like Fe_2O_3 which show sharp spikes at around 240 and 300 cm^{-1} are absent in the spectra and hence reassures the formation of the monophasic polycrystalline compound.

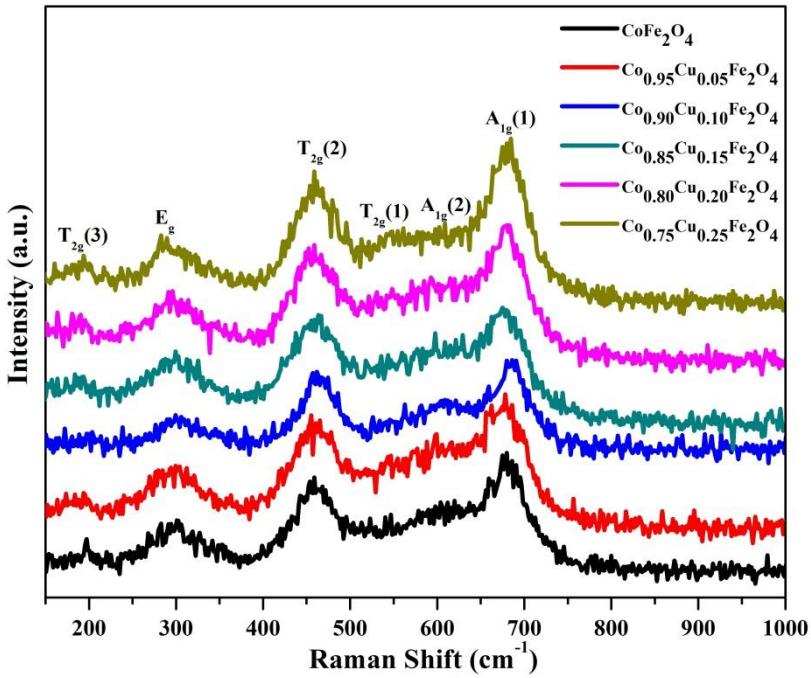

Fig. 4.27 *Room temperature Raman spectra of* $Co_{1-x}Cu_xFe_2O_4$ *(where x = 0.00, 0.05, 0.10, 0.15, 0.20 and 0.25).*

4.5.2 $CoFe_{2-x}Sb_xO_4$ (where x = 0.00, 0.03, 0.06, and 0.09)

The Raman spectra of Sb^{3+} substituted cobalt ferrite exhibited all the characteristic vibration bands for cubic spinel ferrite (Fig. 4.28). The Raman active modes assigned as $2A_{1g}$ (602 – 613, 679 – 684 cm^{-1}), E_g (298 – 304 cm^{-1}), $3T_{2g}$ (539 – 553, 459 – 467, 195 – 198 cm^{-1}) for cubic spinel ferrites can be viewed in the spectra [357]. The modes below and above 600 cm^{-1} can be understood as the vibrational modes due to metal-oxygen bond stretching at octahedral (B) and tetrahedral (A) sites respectively [196].

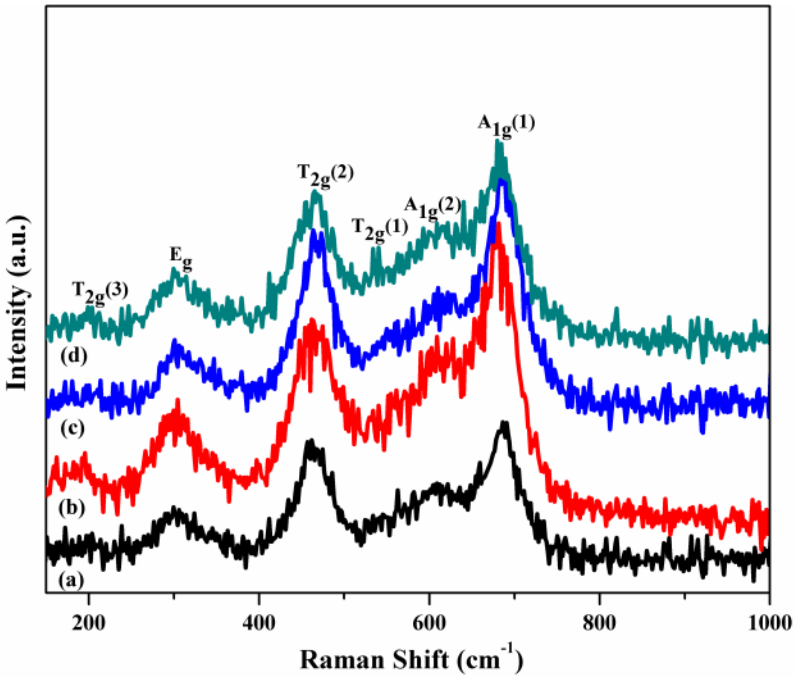

Fig. 4.28 *Room temperature Raman spectra of(a)$CoFe_2O_4$ (b) $CoFe_{1.97}Sb_{0.03}O_4$ (c) $CoFe_{1.94}Sb_{0.06}O_4$ (d) $CoFe_{1.91}Sb_{0.09}O_4$.*

4.5.3 $Co_{0.9}Cu_{0.1}Fe_{2-x}RE_xO_4$ (where RE = Gd, Sm, Dy, Yb, Eu, and x = 0.00, 0.03, 0.05)

The Raman spectra of $Co_{0.9}Cu_{0.1}Fe_{2-x}RE_xO_4$ (where RE = Gd, Sm, Dy, Yb, Eu, and x = 0.00, 0.03, 0.05)are presented in Fig. 4.29. The spectra confirm the impurity-

freecubic phase formation of the polycrystalline compound. All the 6 Raman active modes assigned as $2A_{1g}$ (596 - 613 cm^{-1}, 672 - 688 cm^{-1}), E_g (292 - 305 cm^{-1}), $3T_{2g}$ (538 - 574 cm^{-1}, 454 - 467 cm^{-1}, 182 - 200 cm^{-1}) predicted for the cubic spinel ferrite system can be seen in the spectra. The presence of an A_{1g} active mode usually observed as a shoulder, designated as $A_{1g}(2)$ mode, is a characteristic mode of the inverse as well as mixed spinel ferrites [358]. The vibrational modes beyond 600 cm^{-1} correspond to symmetrical stretching of metal-oxygen bonding at tetrahedral sites and the modes below 600 cm^{-1} correspond to symmetrical and anti-symmetrical bending of metal-oxygen in the octahedral sites [357]. A marginal shifting behavior in Raman modes with RE^{3+} substitution was observed which can be attributed to the strain-induced due to the incorporation of larger ionic size RE^{3+} at the Fe^{3+} site.

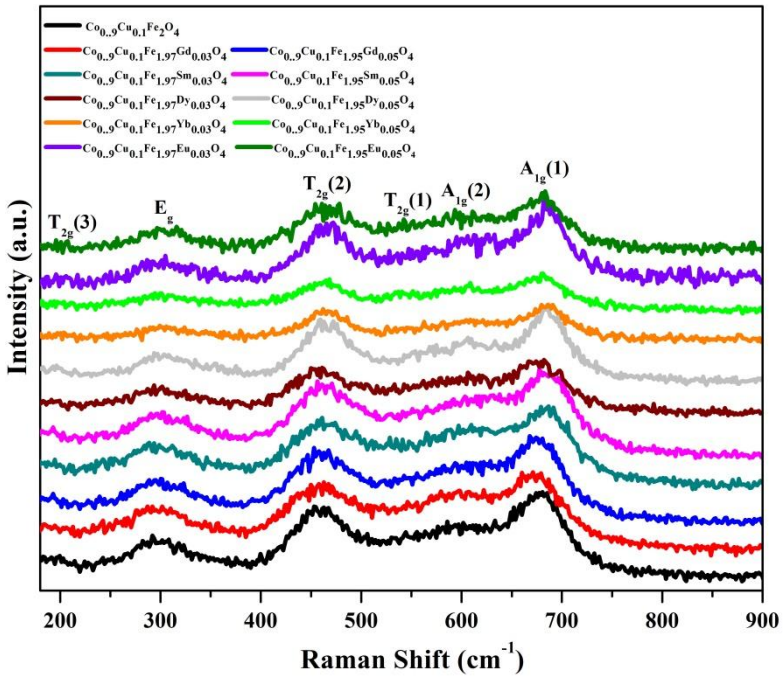

Fig. 4.29 *Room temperature Raman spectra of* $Co_{0.9}Cu_{0.1}Fe_{2-x}RE_xO_4$ *(where RE = Gd, Sm, Dy, Yb, Eu, and x = 0.00, 0.03, 0.05).*

4.5.4 $Co_{0.9}Cu_{0.1}Fe_{2-x}Cr_xO_4$ (where x = 0.00, 0.03, 0.06, 0.09, 0.12, and 0.15)

The Raman spectra of $Co_{0.9}Cu_{0.1}Fe_{2-x}Cr_xO_4$ (where x = 0.00, 0.03, 0.06, 0.09, 0.12, and 0.15) were recorded to acertain the vibrational bands observed in the spinel ferrites. The spectra have been depicted in Fig. 4.30. All the six Raman active modes registered as $2A_{1g}$ (610-617 cm^{-1}, 685-690 cm^{-1}), E_g (297-305 cm^{-1}), $3T_{2g}$ (558-564 cm^{-1}, 468-473 cm^{-1}, and 169-173 cm^{-1}), expected for the cubic spinel ferrite system are evident in the Raman spectra [357]. No other vibrational bands corresponding to the impurities like Fe_2O_3 were noticeable in the spectra. Hence, the Raman studies further reassure the single phase formation of the desired material.

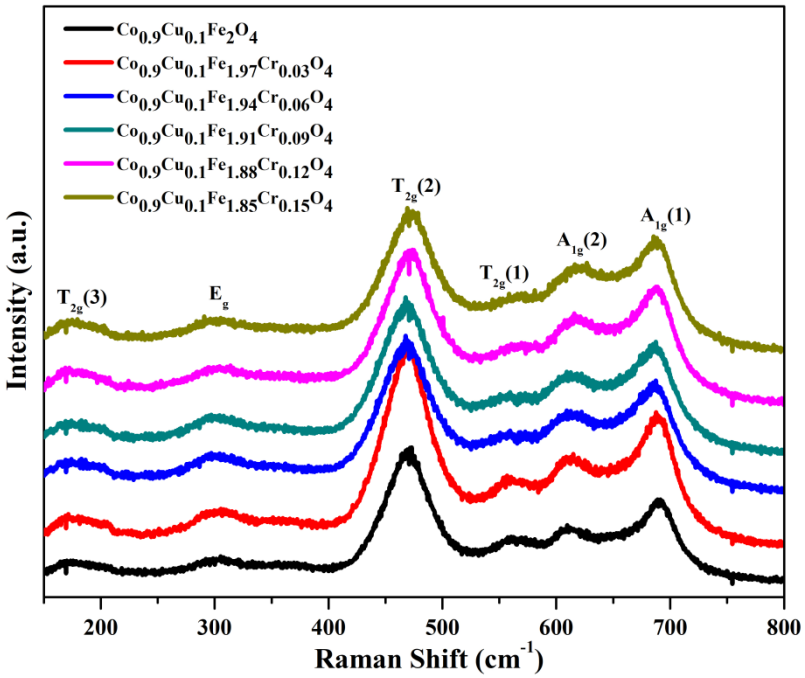

Fig. 4.30 *Room temperature Raman spectra of$Co_{0.9}Cu_{0.1}Fe_{2-x}Cr_xO_4$ (where x = 0.00, 0.03, 0.06, 0.09, 0.12, and 0.15).*

4.5.5 $Co_{0.9}Cu_{0.1}Fe_{2-x}Mn_xO_4$ (where x = 0.00, 0.03, 0.06, 0.09, 0.12, and 0.15)

Fig. 4.31 shows the Raman spectra of Mn ion substituted Co-Cu ferrite in the region 150-800 cm^{-1}. All the 6 Raman active modes designated as $2A_{1g}$ (610-612 cm^{-1},

688-690 cm^{-1}), E_g (301-305 cm^{-1}), $3T_{2g}$ (558-562 cm^{-1}, 468-470 cm^{-1}, 171-174 cm^{-1}) for the cubic spinel ferrite system are detected in the spectra [357]. A marginal shift in peak position with substituent concentration may be regarded as a strain-induced due to the substitution of Mn ions. The spectra do not show any other additional vibration bands hence reaffirm the monophasic formation of prepared compositions.

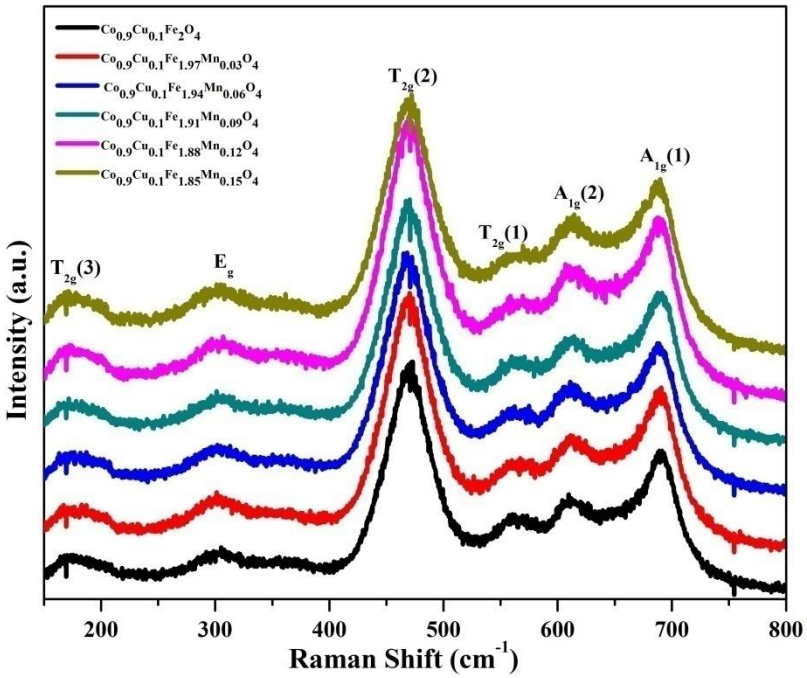

Fig. 4.31 *Room temperature Raman spectra of $Co_{0.9}Cu_{0.1}Fe_{2-x}Mn_xO_4$ (where x = 0.00, 0.03, 0.06, 0.09, 0.12, and 0.15).*

.

4.5.6 $Co_{0.9}Cu_{0.1}Fe_{2-x}In_xO_4$ (where x = 0.00, 0.03, 0.06, 0.09, 0.12, and 0.15)

Fig. 4.32 portrays the Raman spectra of In^{3+} substituted and un-substituted $Co_{0.9}Cu_{0.1}Fe_2O_4$ ferrite in the region 150-800 cm^{-1}. The typical Raman peaks in the lower (150-600 cm^{-1}) and higher (600-750 cm^{-1}) frequency modes represent the octahedral and tetrahedral vibrational modes respectively [357]. Typically, a cubic spinel ferrite displays five Raman active modes, which are E_g, $3T_{2g}$, and A_{1g} but as can be seen from the spectra

6 Raman active modes are visible. The additional mode present in the spectra as a shoulder peak to the A_{1g} mode and labeled as $A_{1g}(2)$ mode, is a distinct feature of inverse and mixed spinel ferrites [358,359]. The absence of impurity peak in the spectra confirms the formation of monophasic cubic spinel ferrite.

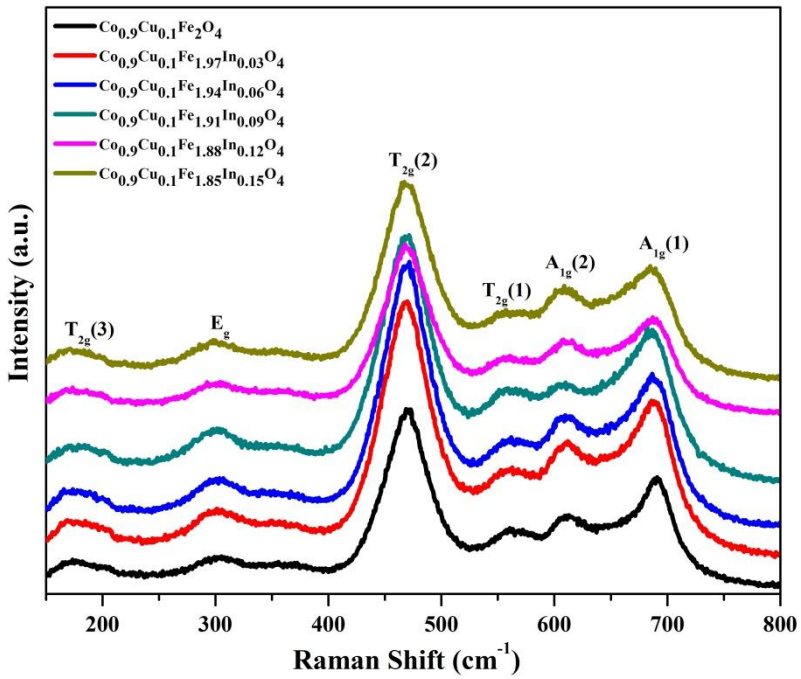

Fig. 4.32 *Raman spectra of $Co_{0.9}Cu_{0.1}Fe_{2-x}In_xO_4$ (where x = 0.00, 0.03, 0.06, 0.09, 0.12, and 0.15).*

4.6 Scanning Electron microscopy – Electron diffraction X-ray Spectroscopy (SEM-EDX)

4.6.1 $Co_{1-x}Cu_xFe_2O_4$ (where x = 0.00, 0.10, and 0.25)

The surface morphology of the materials sintered at 800 $^oC$was assessed by analyzing SEM images as presented in Fig. 4.33(a-c). The micrographs do not show any noticeable difference between the synthesized compositions. Almost homogeneous and uniform distribution of clusters of fine agglomerated spherical particles of uneven size was detected. The sintering process and magnetic behavior of the particles could be

responsible for the agglomeration [360]. The representative EDX pattern for 10 mol% Cu content shows the existence of Co, Cu, Fe and O in the material and no other distinguishable impurities were detected (Fig. 4.33(d)). The peak at around 2.5 keV in the EDX pattern is due to gold overcoating.

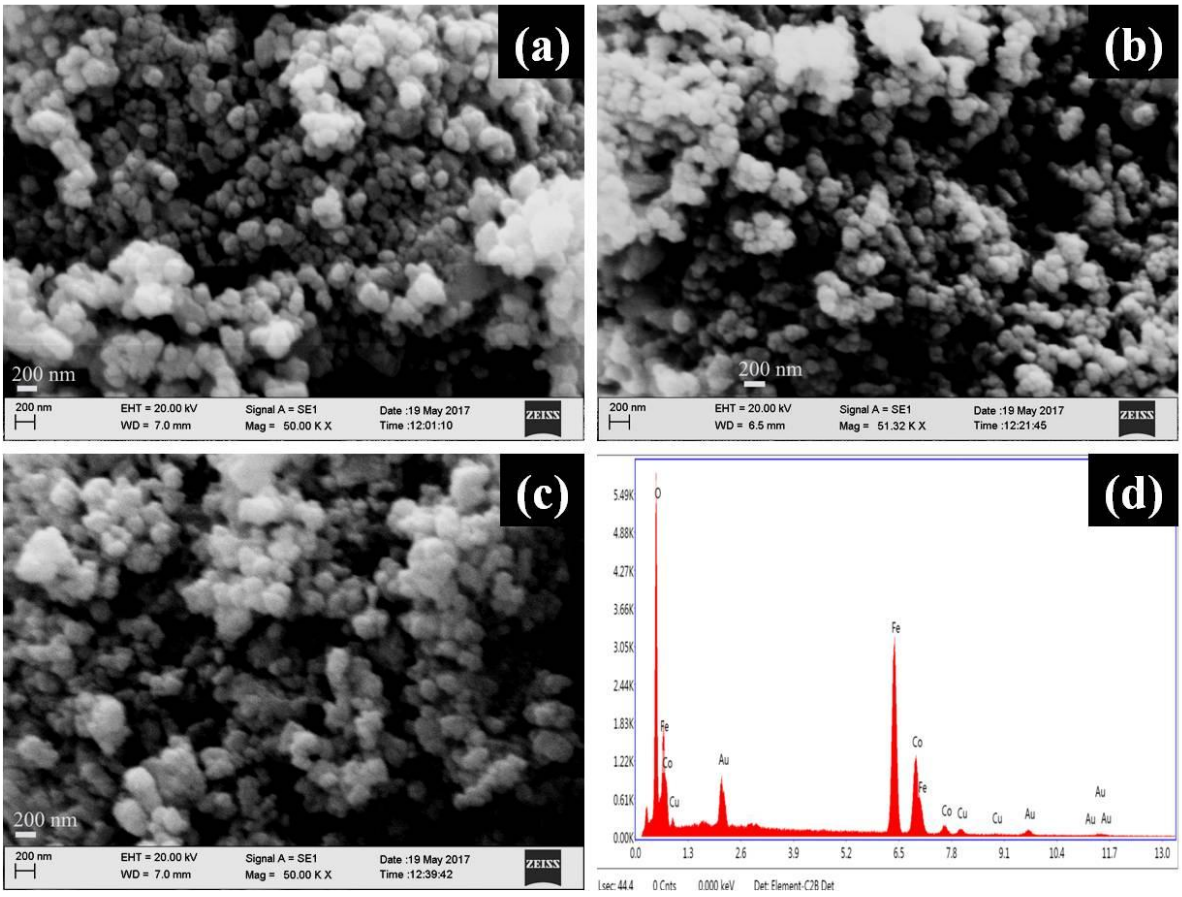

Fig. 4.33*Scanning electron micrographs of (a) $CoFe_2O_4$ (b) $Co_{0.90}Cu_{0.10}Fe_2O_4$ (c) $Co_{0.75}Cu_{0.25}Fe_2O_4$ (d) EDX pattern of $Co_{0.90}Cu_{0.10}Fe_2O_4$.*

4.6.2 $CoFe_{1.94}Sb_{0.06}O_4$

SEM imageof $CoFe_{1.94}Sb_{0.06}O_4$ as displayed in Fig. 4.34(a) showed the presence of spherical agglomerates evenly distributed of almost equal sizes. The agglomeration can be due to the sintering process and magnetic nature of the particles [360]. EDX pattern (Fig. 4.34(b)) confirms the presence of all the expected elements.

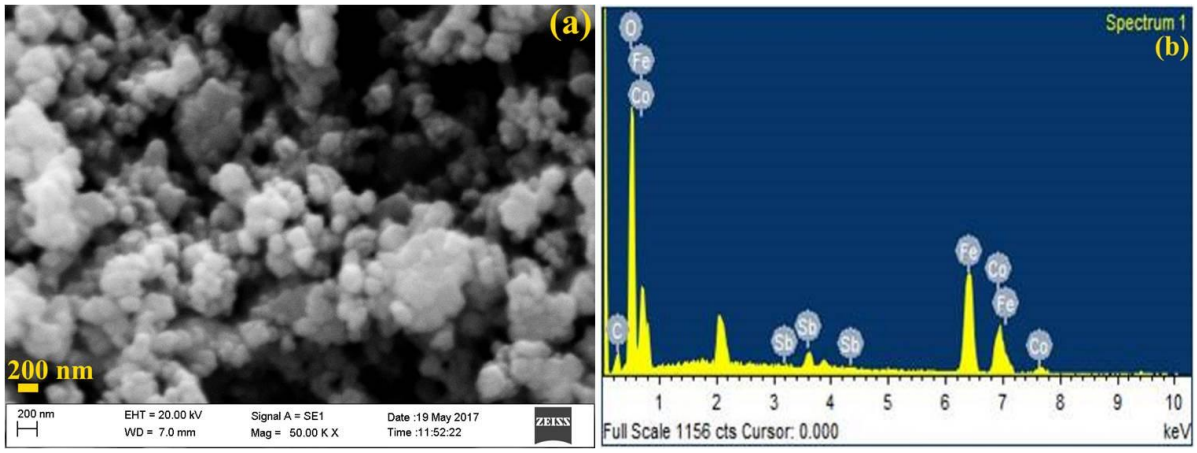

Fig. 4.34 *(a) SEM image of $CoFe_{1.94}Sb_{0.06}O_4$ (b) EDX pattern of $CoFe_{1.94}Sb_{0.06}O_4$.*

4.6.3 $Co_{0.9}Cu_{0.1}Fe_{1.95}RE_{0.05}O_4$ (where RE = Gd, Sm, Dy, Yb, and Eu)

As can be seen from Fig. 4.35(a) - 4.39(a) the RE^{3+} substituted Co-Cu ferrite show uniform distribution of spherical agglomerates with uneven sizes. The presence of agglomerates is due to high-temperature sintering and magnetic nature of the material [360]. The elemental composition has been analyzed using the EDX spectrum and the representative EDX pattern of RE^{3+} substituted Co-Cu ferrite is shown in Fig. 4.35(b) - 4.39(b). The pattern confirms the presence of expected elements in the sample and no other traceable impurities are found within the resolution limit of EDX.

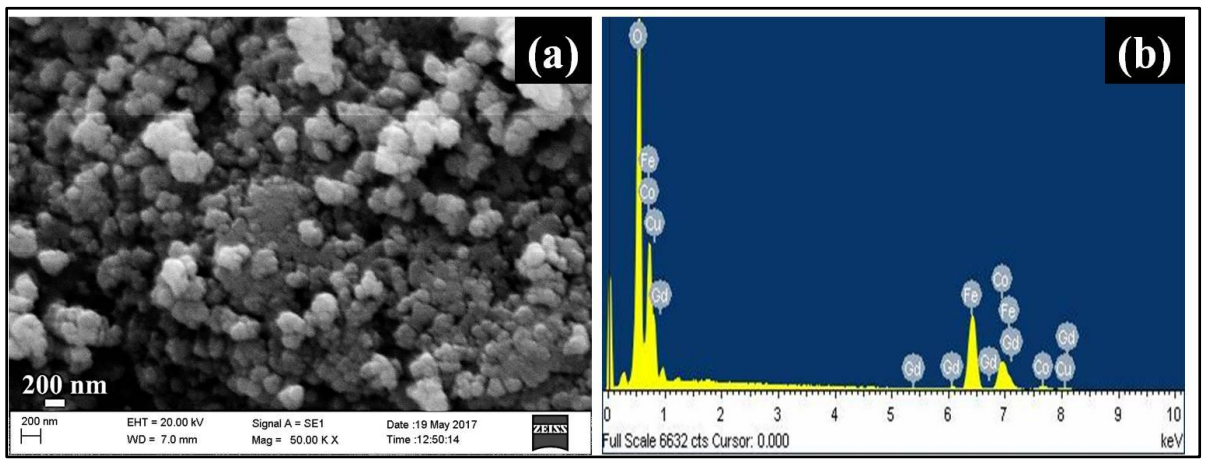

Fig. 4.35 *SEM micrograph of (a) $Co_{0.9}Cu_{0.1}Fe_{1.97}Gd_{0.03}O_4$ (b) EDX pattern of $Co_{0.9}Cu_{0.1}Fe_{1.97}Gd_{0.03}O_4$.*

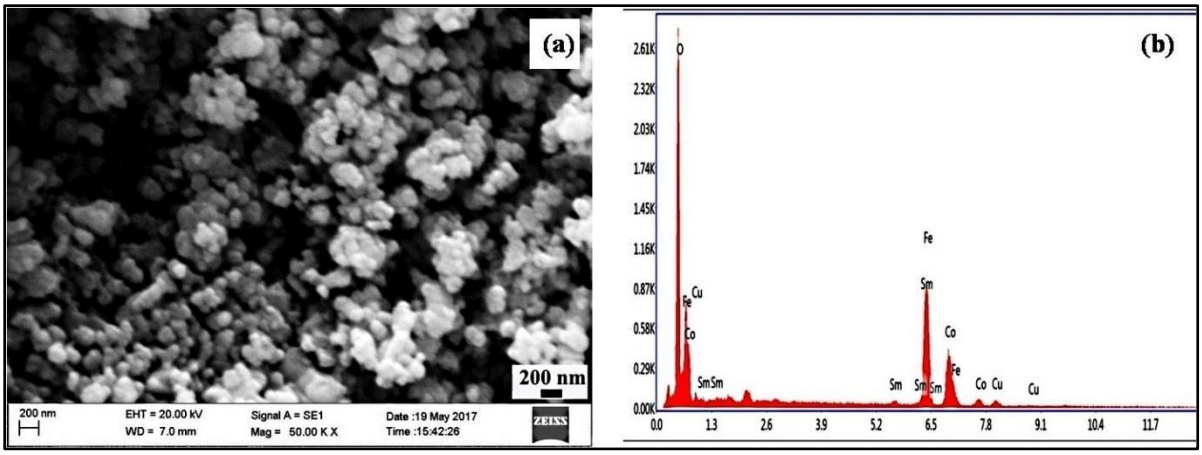

Fig. 4.36 *SEM micrograph of (a) $Co_{0.9}Cu_{0.1}Fe_{1.95}Sm_{0.05}O_4$ (b) EDX pattern of $Co_{0.9}Cu_{0.1}Fe_{1.95}Sm_{0.05}O_4$.*

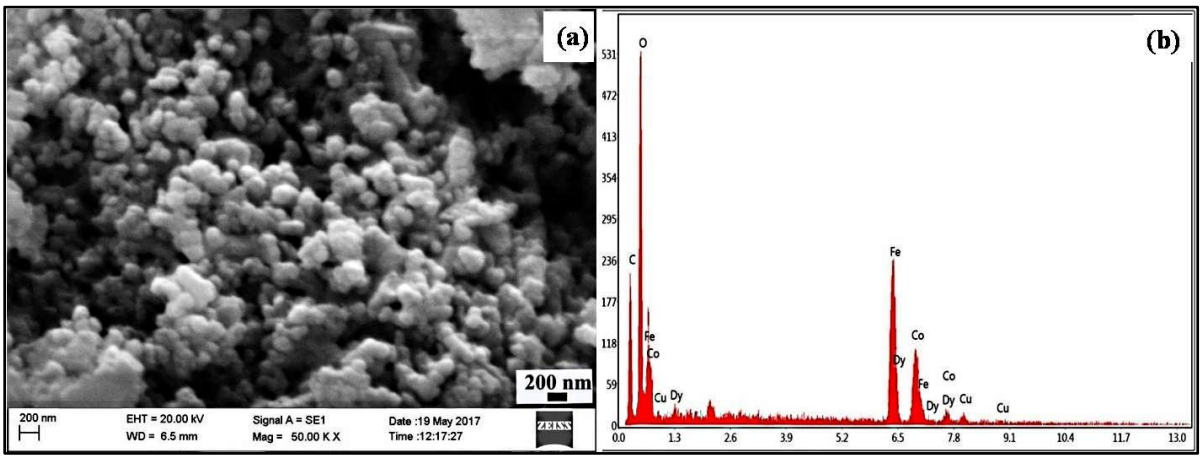

Fig. 4.37 *SEM micrograph of (a) $Co_{0.9}Cu_{0.1}Fe_{1.95}Dy_{0.05}O_4$ (b) EDX pattern of $Co_{0.9}Cu_{0.1}Fe_{1.95}Dy_{0.05}O_4$.*

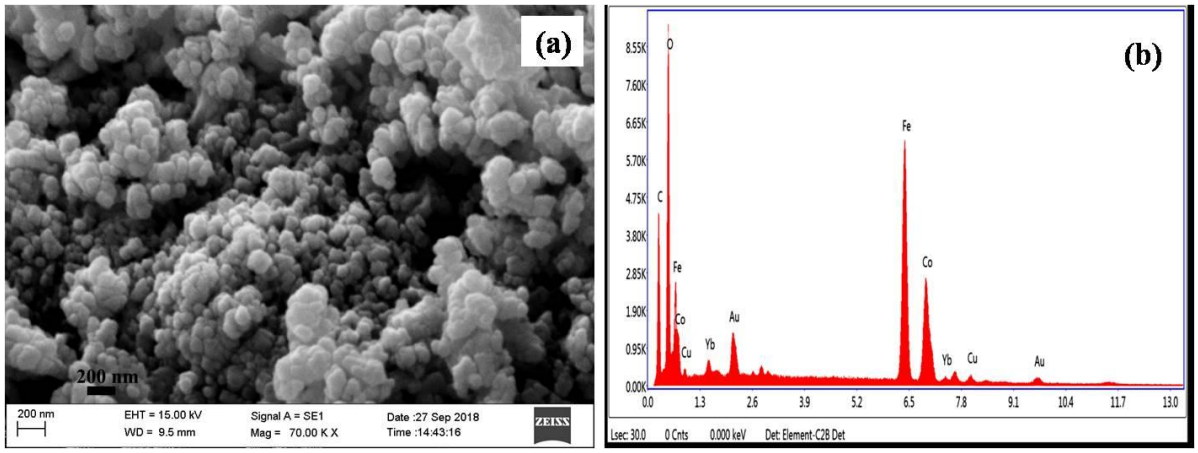

Fig. 4.38 *SEM micrograph of (a) $Co_{0.9}Cu_{0.1}Fe_{1.95}Yb_{0.05}O_4$ (b) EDX pattern of $Co_{0.9}Cu_{0.1}Fe_{1.95}Yb_{0.05}O_4$.*

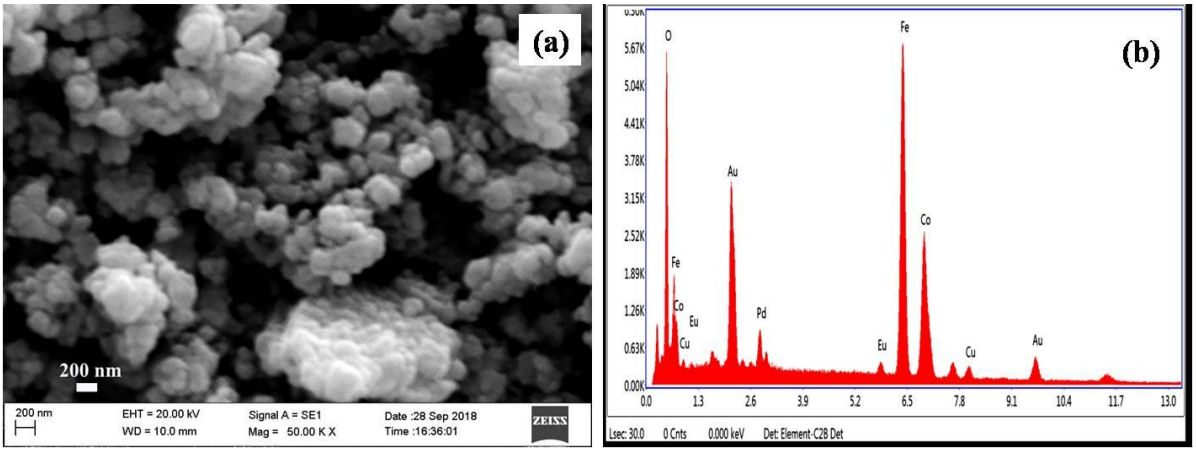

Fig. 4.39 *SEM micrographs of (a) $Co_{0.9}Cu_{0.1}Fe_{1.95}Eu_{0.05}O_4$ (b) EDX pattern of $Co_{0.9}Cu_{0.1}Fe_{1.95}Eu_{0.05}O_4$.*

4.6.4 $Co_{0.9}Cu_{0.1}Fe_{1.85}Cr_{0.15}O_4$

The SEM micrograph of $Co_{0.9}Cu_{0.1}Fe_{1.85}Cr_{0.15}O_4$showed the particles in a uniform shape, homogeneously distributed and agglomerated (Fig. 4.40(a)). The agglomeration of the particles can be credited to magnetic interaction occurring among them and high-temperatureheat-treatment. Fig. 4.40(b) shows the representative EDX pattern that clearly indicates the existence of all the elements expected in the sample.

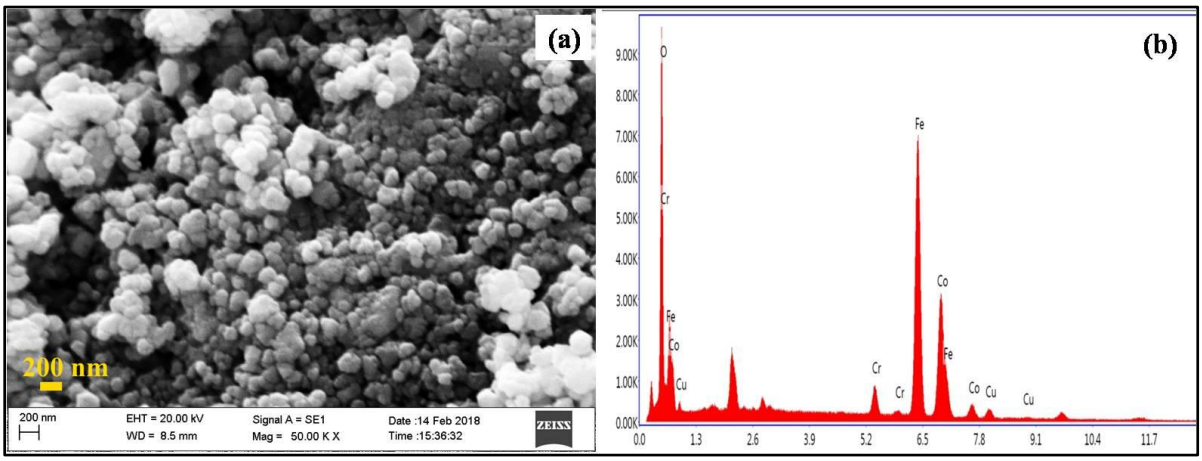

Fig. 4.40 *SEM micrograph of (a) $Co_{0.9}Cu_{0.1}Fe_{1.85}Cr_{0.15}O_4$ (b) EDX pattern of $Co_{0.9}Cu_{0.1}Fe_{1.85}Cr_{0.15}O_4$.*

4.6.5 $Co_{0.9}Cu_{0.1}Fe_{1.85}Mn_{0.15}O_4$

The micrographs show homogeneously distributed and agglomerated particles (Fig. 4.41(a)). The presence of agglomeration can be attributed to magnetic interactions developed among ferrite nanoparticles and high-temperature heating. The corresponding EDX pattern clearly indicates the existence of Co, Cu, Fe, Mn and O in the material (Fig. 4.41(b)).

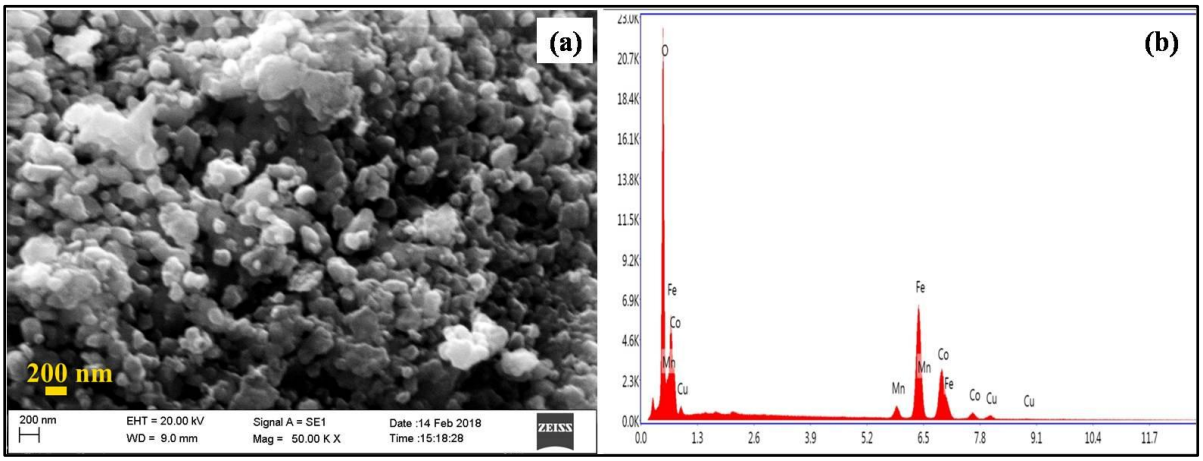

Fig. 4.41 *SEM micrograph of (a) $Co_{0.9}Cu_{0.1}Fe_{1.85}Mn_{0.15}O_4$ (b) EDX pattern of $Co_{0.9}Cu_{0.1}Fe_{1.85}Mn_{0.15}O_4$.*

4.6.6 $Co_{0.9}Cu_{0.1}Fe_{1.85}In_{0.15}O_4$

SEM analysis of In^{3+} substituted Co-Cu ferrite showed a significant amount of agglomeration of spherical particles (Fig 4.42(a)) which is due to the high-temperature sintering process and the magnetic forces present. The representative EDX pattern indicated the presence of all the expected elements in the sample (Fig. 4.42(b)).

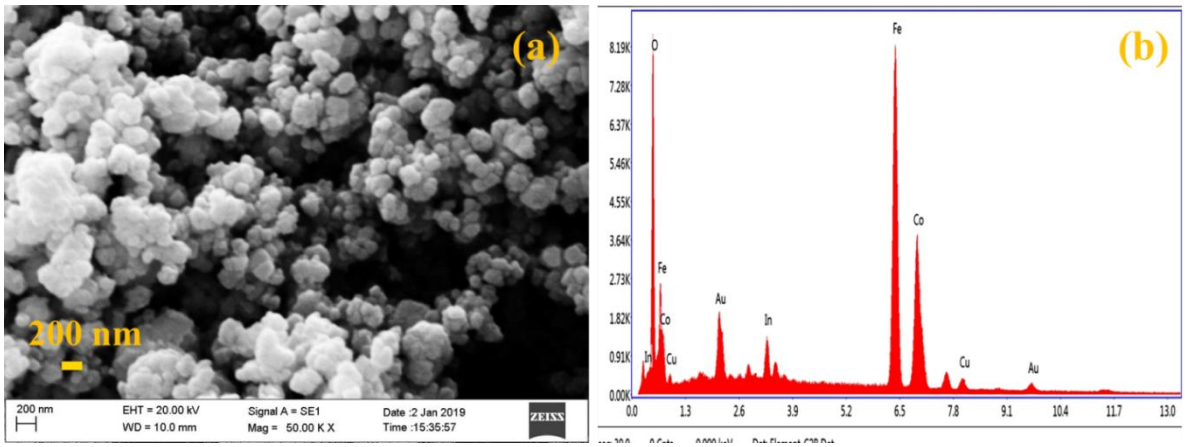

Fig. 4.42 *SEM image of (a) $Co_{0.9}Cu_{0.1}Fe_{1.85}In_{0.15}O_4$ and (b) EDX pattern of $Co_{0.9}Cu_{0.1}Fe_{1.85}In_{0.15}O_4$.*

4.6.7 $Y_{1.99}Ce_{0.01}O_3$

The representative SEM imageof $Y_{1.99}$ $Ce_{0.01}O_3$heat-treated at 1000 ℃ shows spherical particles of almost equal sizes (Fig. 4.43(a)). The particles are uniformly and homogeneously distributed. The corresponding EDX pattern shows the presence of Y, Ce, and O in the sample (Fig. 4.43(b))

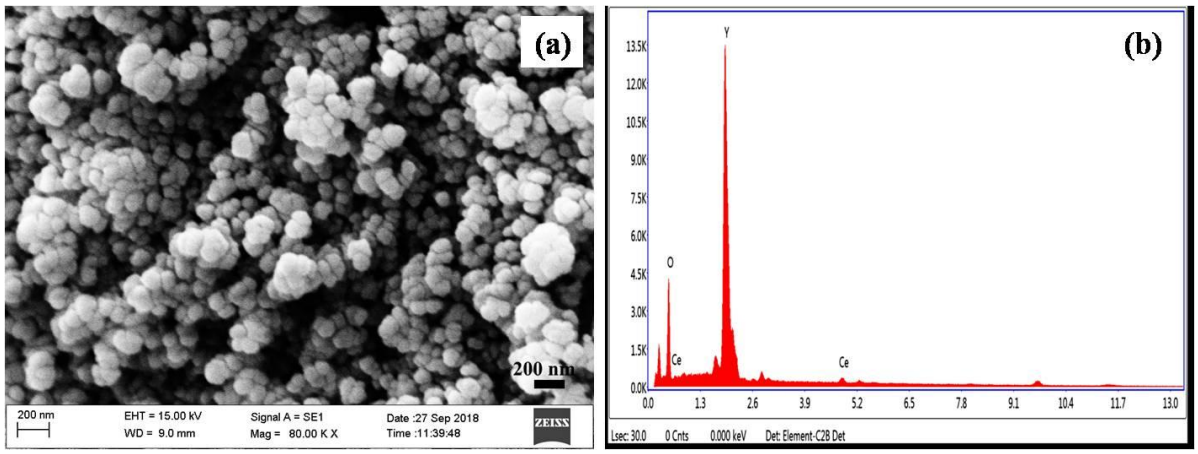

Fig.4.43 *SEM image of (a) $Y_{1.99}$ $Ce_{0.01}O_3$ and (b) EDX pattern of $Y_{1.99}$ $Ce_{0.01}O_3$.*

4.6.8 $Y_{1.93}Ce_{0.01}Eu_{0.06}O_3$

Fig. 4.44(a-c) shows SEM micrographs illustrating the surface morphology for Ce^{3+} and Eu^{3+} co-substituted Y_2O_3.As can be seen, the samples show agglomeration of individual particles having a spherical morphology. The high-temperature heat treatment given to the samples could be a possible explanation for the observed agglomeration.The EDX pattern (Fig. 4.44(d))exhibited the peaks corresponding to Y, Ce, Eu, and O which confirmed their presence in the sample.

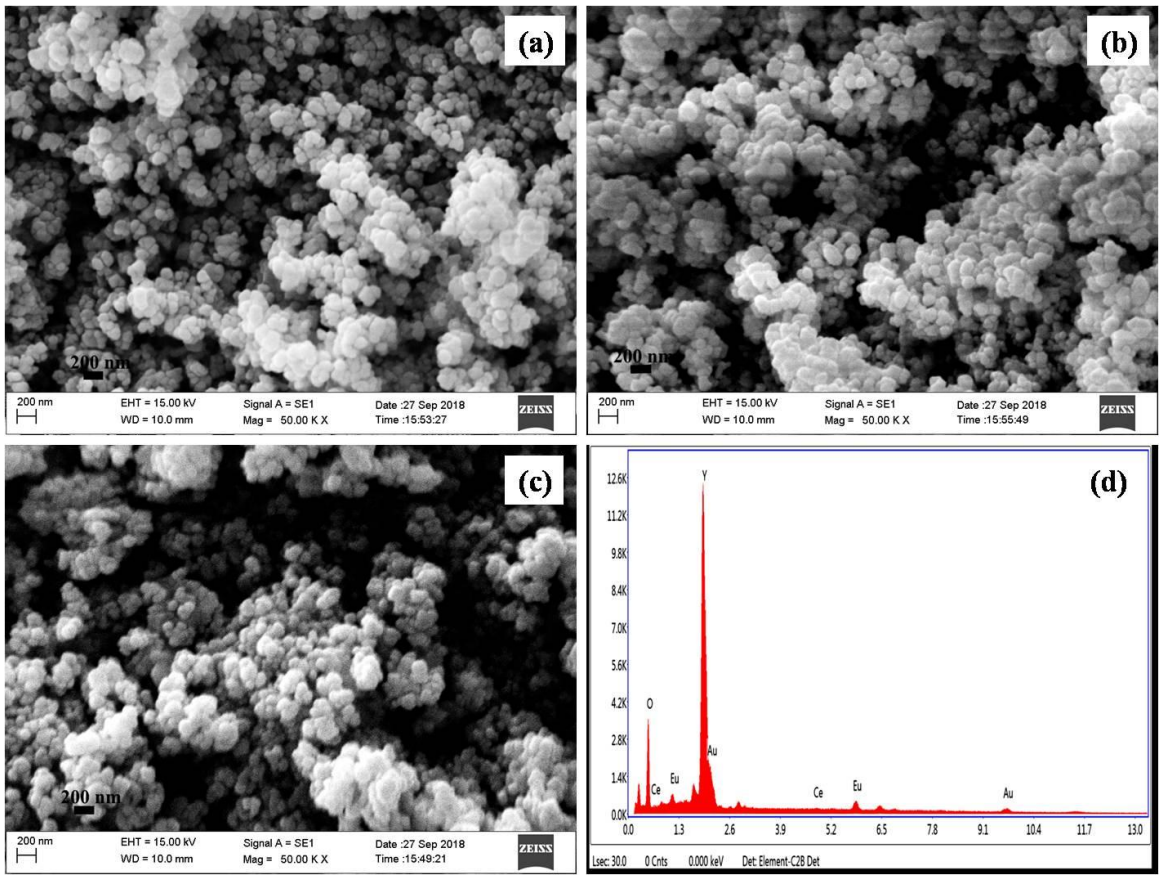

Fig.4.44 *SEM images of (a,b,c)* $Y_{1.93}Ce_{0.01}Eu_{0.06}O_3$ *and (d) EDX pattern of* $Y_{1.93}Ce_{0.01}Eu_{0.06}O_3$.

4.6.9 $Y_{1.93}Ce_{0.01}Er_{0.06}O_3$

The SEM images of $Y_{1.93}Ce_{0.01}Er_{0.06}O_3$ show spherical agglomerates of almost regular size and shape (Fig. 4.45 (a-c)). TheEDX technique verified the existence of Y, Ce, Er and O elements in the prepared sample as shown in Fig. 4.45(d).

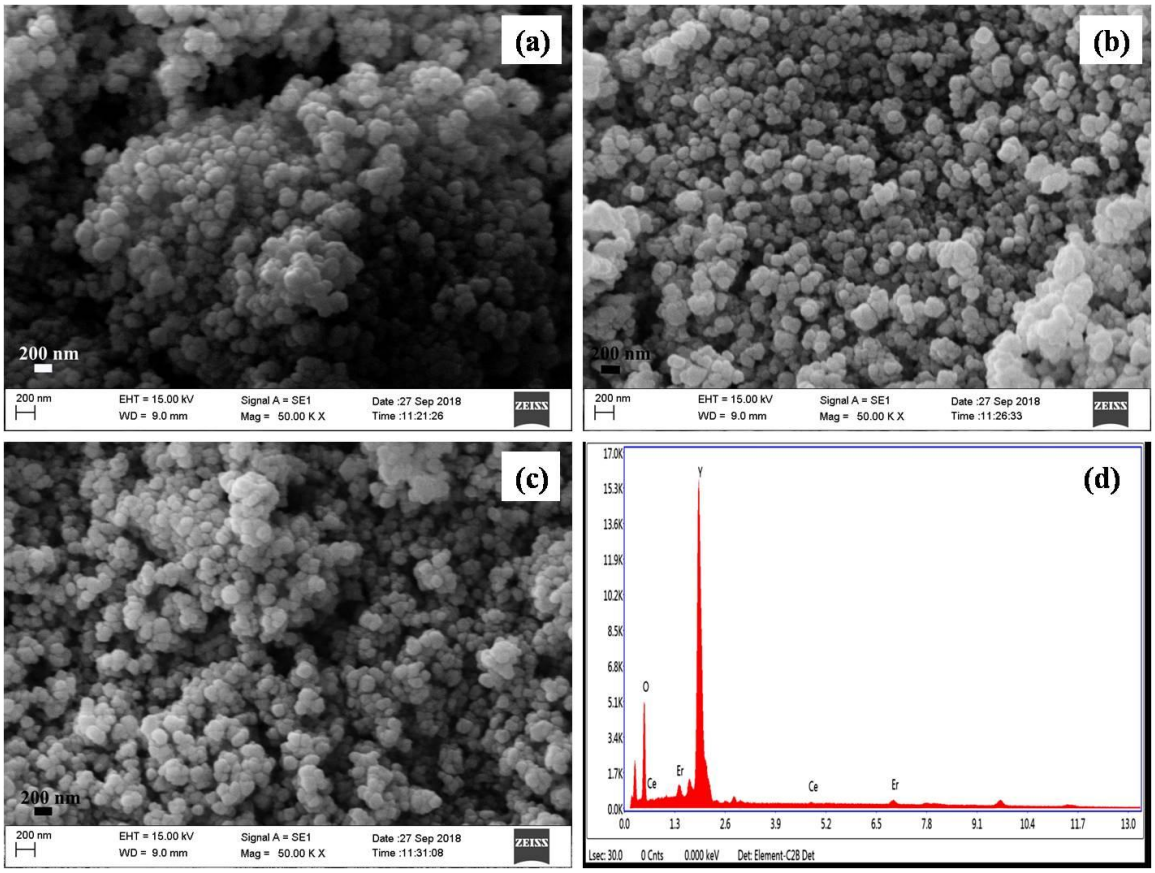

Fig.4.45 *SEM images of (a,b,c)* $Y_{1.93}Ce_{0.01}Er_{0.06}O_3$ *and (d) EDX pattern of* $Y_{1.93}Ce_{0.01}Er_{0.06}O_3$.

4.6.10 $Gd_{1.84}Er_{0.04}Yb_{0.12}O_3$

Fig. 4.46(a-c) shows the SEM images of Yb^{3+} and Er^{3+} co-substituted Gd_2O_3. The samples showed agglomerated spherical particles uniformly distributed. The agglomeration of particles can be explained by the heat treatment given to the material.The EDX analysis shown in Fig. 4.46(d) confirms the presence of Gd, Er, Yb

and O in the sintered sample. The detected peaks of Au and Pd could be due to overcoating.

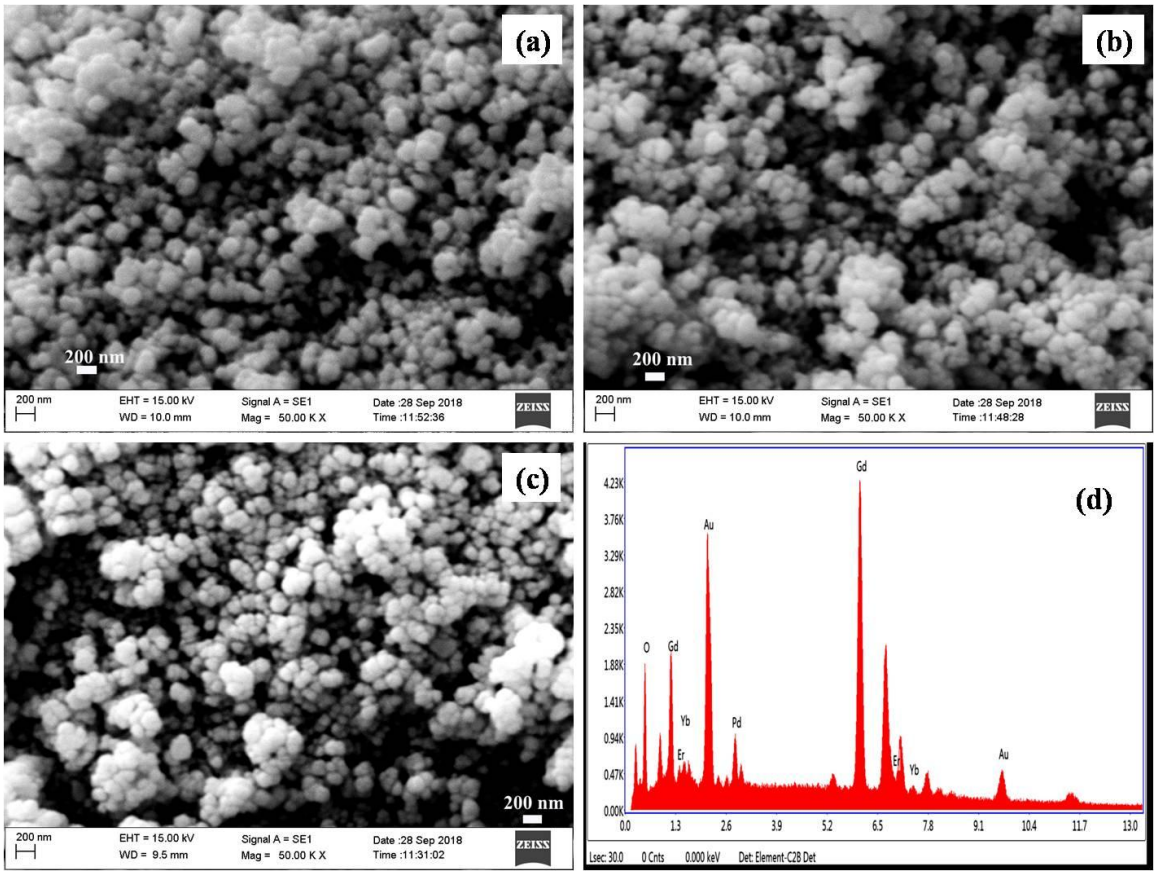

Fig. 4.46 *SEM image of (a,b,c)* $Gd_{1.84}Er_{0.04}Yb_{0.12}O_3$ *and (d) EDX pattern of* $Gd_{1.84}Er_{0.04}Yb_{0.12}O_3$.

4.6.11 $Gd_{1.84}Ho_{0.04}Yb_{0.12}O_3$

Fig. 4.47(a) shows the SEM images of Yb^{3+} and Ho^{3+} co-substituted Gd_2O_3 samples heated at 1000 ℃. In the SEM image, uniformly sized agglomerated spherical-shaped particles are seen.The agglomeration appeared due to the high-temperature treatment applied in the preparation method. EDX pattern (Fig. 4.47(b)) recorded on the corresponding sample verifies the presence of expected elements in the sample.

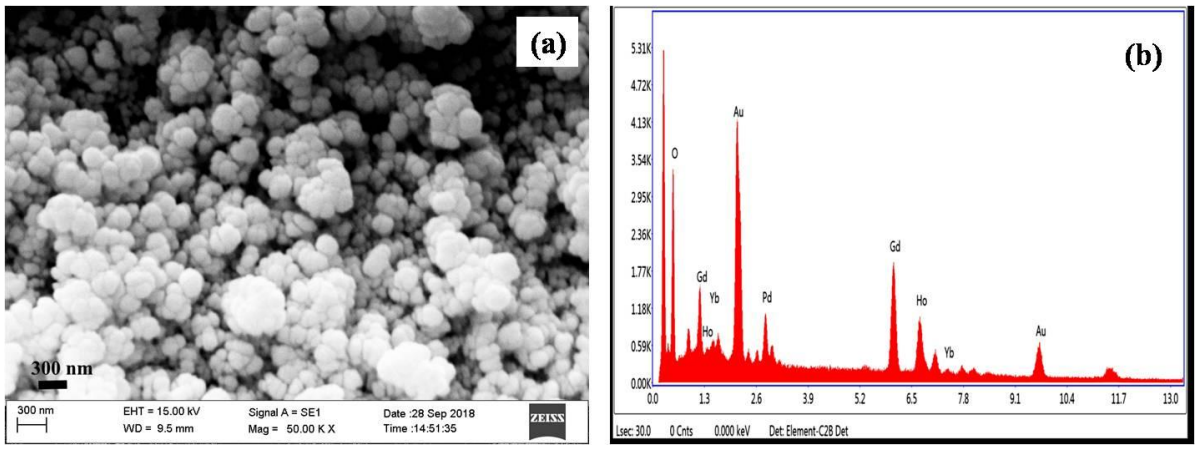

Fig. 4.47 *SEM image of (a) $Gd_{1.84}Ho_{0.04}Yb_{0.12}O_3$ and (b) EDX pattern of $Gd_{1.84}Ho_{0.04}Yb_{0.12}O_3$.*

4.7 Transmission Electron Microscopy - Selected Area Electron Diffraction (TEM-SAED)

4.7.1 $Co_{1-x}Cu_xFe_2O_4$ (where x = 0.00 and 0.25)

The precise particle sizes of $Co_{1-x}Cu_xFe_2O_4$ (where x = 0.00 and 0.25**)** sintered at 800 ℃ were assessed by analyzing TEM images as presented in Fig. 4.48(a,b).

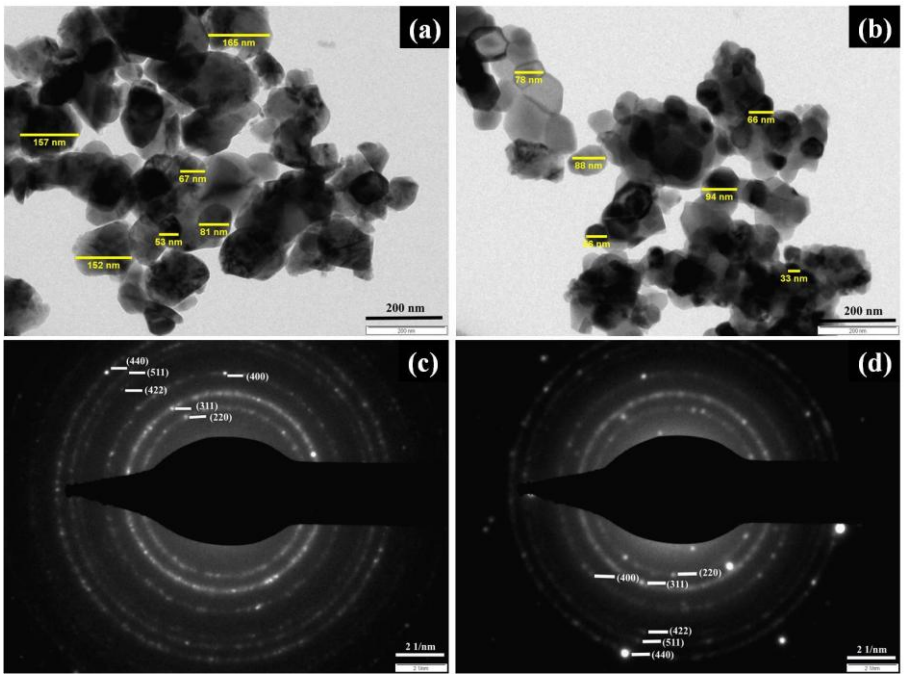

Fig. 4.48 *Transmission electron micrographs of (a) $CoFe_2O_4$ (b) $Co_{0.75}Cu_{0.25}Fe_2O_4$ and SAED patterns of (c) $CoFe_2O_4$ (d) $Co_{0.75}Cu_{0.25}Fe_2O_4$.*

Almost homogeneous and uniform distribution of clusters of fine agglomerated spherical particles of uneven size was detected. Evaluation of TEM images observed a decreasing trend in particle size with increasing Cu^{2+} substitution (Table 4.21). The bright fringes seen from the corresponding SAED patterns (Fig. 4.48(c,d)) implies the polycrystalline nature of the material and all rings have been indexed with reflections belonging to space group $Fd\bar{3}m$.

Table 4.21 Particle size determined from TEM analysis

Sample Composition	Particle size (nm)
$CoFe_2O_4$	50-120
$Co_{0.90}Cu_{0.10}Fe_2O_4$	50-90
$Co_{0.75}Cu_{0.25}Fe_2O_4$	30-80

4.7.2 $CoFe_{1.91}Sb_{0.09}O_4$

Particle size estimated from the TEM analysis showed that the size varies from 60-110 nm for $CoFe_{1.91}Sb_{0.09}O_4$ (Fig. 4.49(a)).

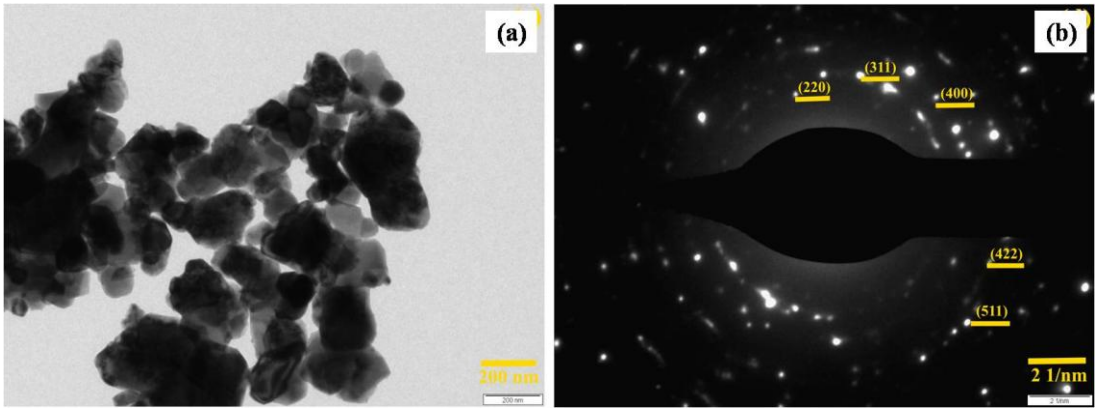

Fig. 4.49 *TEM image of (a) $CoFe_{1.91}Sb_{0.09}O_4$ (b) SAED pattern of $CoFe_{1.91}Sb_{0.09}O_4$.*

The analysis of the corresponding SAED pattern exhibited the characteristic reflections idealfor cubic spinel ferrite (Fig. 4.49(b)). Bright spots and concentric rings observed in theSAED pattern validate the polycrystalline nature of the material.

4.7.3 $Co_{0.9}Cu_{0.1}Fe_{1.95}RE_{0.05}O_4$ (where RE = Gd, Sm, and Dy)

As can be seen from the representative TEM micrographs(Fig. 4.50-4.52) particles with uneven sizes ranging from 25 - 70 nm were detected. The particle size obtained from TEM images were larger than the crystallite size acquired from XRD data. This shows that each particle could have been formed by aggregation of grains or crystallites. The corresponding SAED pattern confirms the polycrystalline nature of the material by the appearance of concentric rings and bright spots in the diffraction pattern. The SAED pattern has been indexed according to diffraction planes of FCC structure.

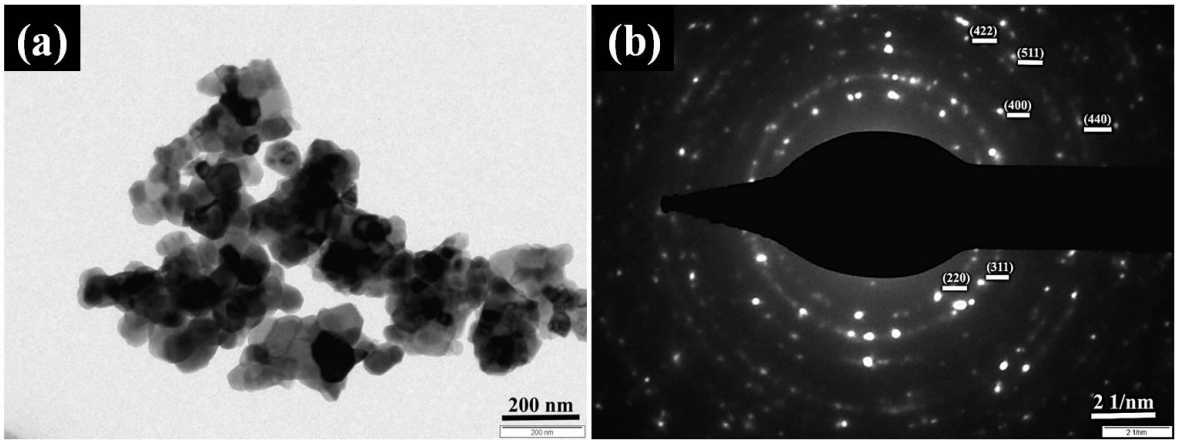

Fig.4.50 *TEM micrograph of (a) $Co_{0.9}Cu_{0.1}Fe_{1.95}Gd_{0.05}O_4$ and SAED pattern of (b) $Co_{0.9}Cu_{0.1}Fe_{1.95}Gd_{0.05}O_4$.*

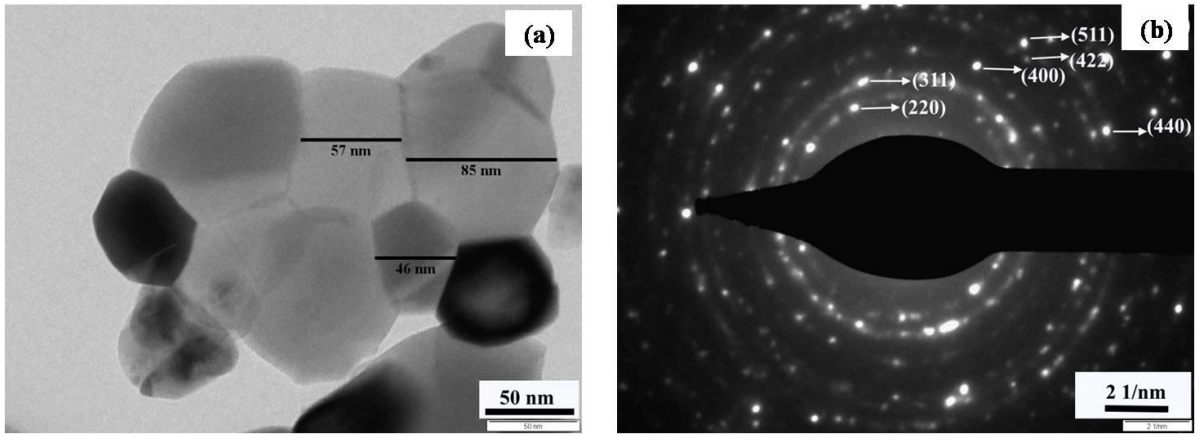

Fig.4.51 *TEM micrograph of (a) $Co_{0.9}Cu_{0.1}Fe_{1.95}Sm_{0.05}O_4$ and SAED pattern of (b) $Co_{0.9}Cu_{0.1}Fe_{1.95}Sm_{0.05}O_4$.*

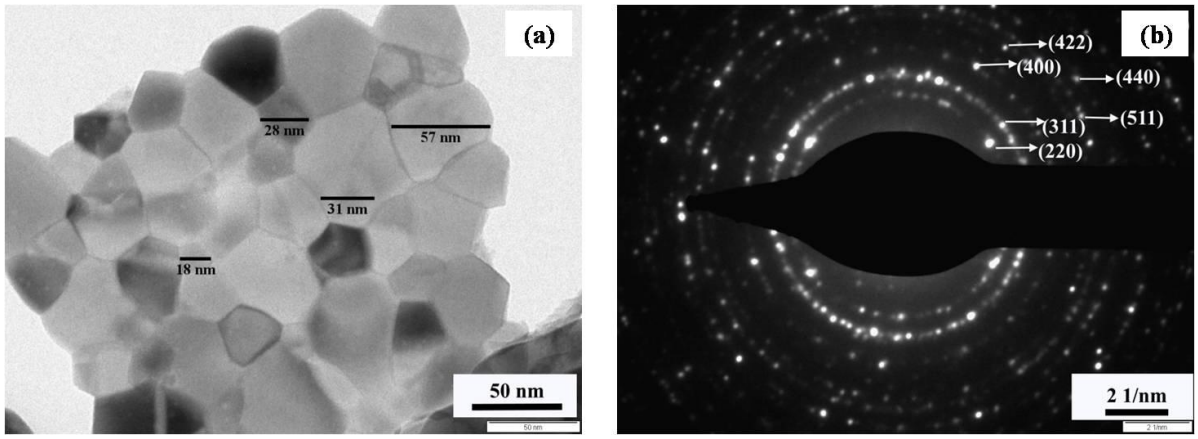

Fig.4.52 *TEM micrograph of (a) $Co_{0.9}Cu_{0.1}Fe_{1.95}Dy_{0.05}O_4$ and SAED pattern of (b) $Co_{0.9}Cu_{0.1}Fe_{1.95}Dy_{0.05}O_4$.*

4.7.4 $Co_{0.9}Cu_{0.1}Fe_{1.85}Cr_{0.15}O_4$

Fig. 4.53 displays the TEM image and SAED pattern of a typical $Co_{0.9}Cu_{0.1}Fe_{1.85}Cr_{0.15}O_4$ ferrite sample. The TEM images gave an authentic proof about the particle size of the materials and also revealed agglomeration in the particles. The average particle size was in the range of 25-60 nm. The SAED pattern further confirms the face-centered cubic spinel structure of the ferrite under investigation.

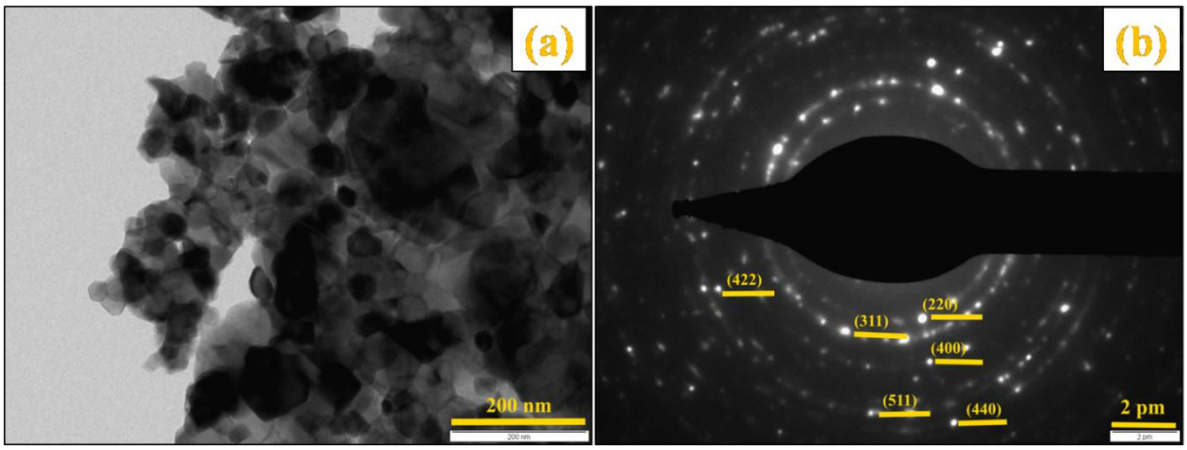

Fig.4.53 *TEM micrographs of (a) $Co_{0.9}Cu_{0.1}Fe_{1.85}Cr_{0.15}O_4$ and SAED pattern of (b) $Co_{0.9}Cu_{0.1}Fe_{1.85}Cr_{0.15}O_4$.*

4.7.5 $Co_{0.9}Cu_{0.1}Fe_{1.85}Mn_{0.15}O_4$

Fig. 4.54 shows the representative TEM image of Mn-substituted Co-Cu ferrite. The estimated particle size was nearly in the range of 55 nm – 105 nm.

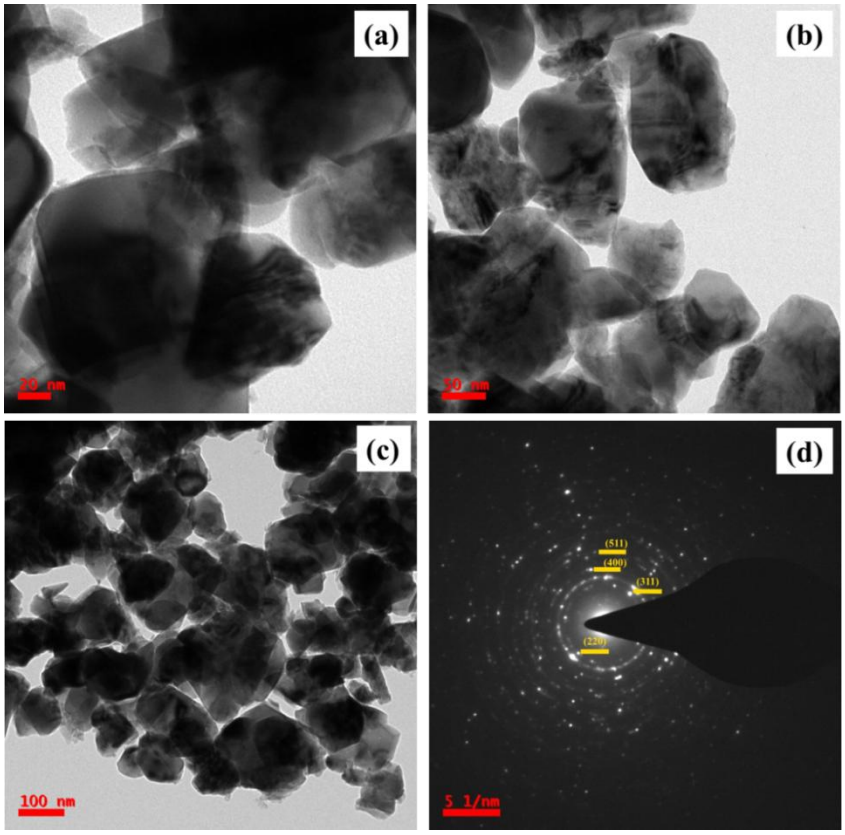

Fig. 4.54*(a,b,c) TEM micrographs and (d) SAED pattern of $Co_{0.9}Cu_{0.1}Fe_{1.85}Mn_{0.15}O_4$.*

The bright spots and concentric rings in the SAED pattern (Fig. 4.54(d)) indicate that the material is well crystallized and can be indexed as the cubic phase, which corresponds to XRD results.

4.7.6 $Co_{0.9}Cu_{0.1}Fe_{1.85}In_{0.15}O_4$

TEM-SAED analyses were carried out on $Co_{0.9}Cu_{0.1}Fe_{1.85}In_{0.15}O_4$ for structural characterization (Fig. 4.55). The particle size determined from TEM analysis was in the range of 35 to 50 nm. The interplanar distances determined from XRD data were in good agreement with the interplanar distances obtained from SAED pattern, while the bright rings and spots in SAED pattern revealed high crystallinity.

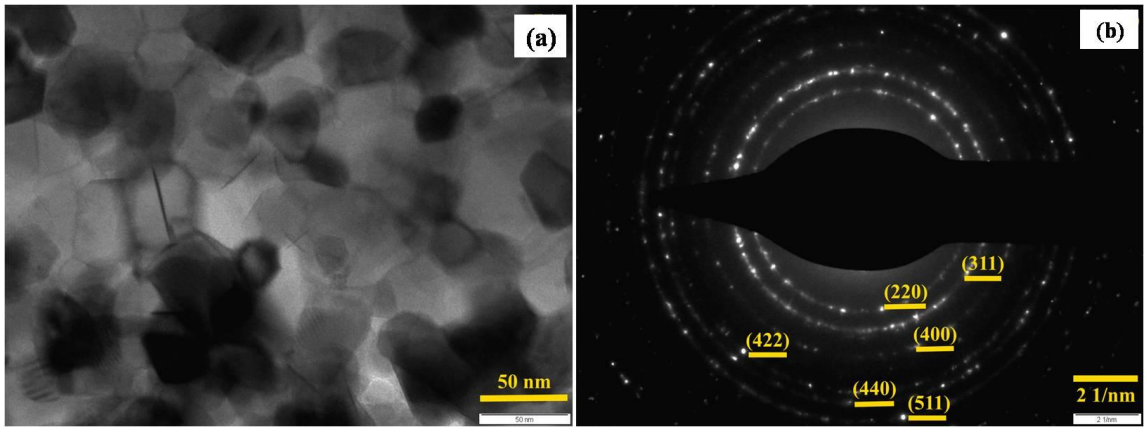

Fig. 4.55 *TEM image of (a) $Co_{0.9}Cu_{0.1}Fe_{1.85}In_{0.15}O_4$,SAED pattern of (b) $Co_{0.9}Cu_{0.1}Fe_{1.85}In_{0.15}O_4$.*

4.7.7 $Y_{1.93}Ce_{0.01}Eu_{0.06}O_3$

The detailed microstructural analyses of the sintered $Y_{1.93}Ce_{0.01}Eu_{0.06}O_3$performed by TEM showed that the sample consists of aggregated particles of uneven shape and sizes (Fig. 4.56). The size of the particles varied from 40 – 85 nm. The observed aggregation and higher particle size could be due to higher heat-treatment given to the sample.

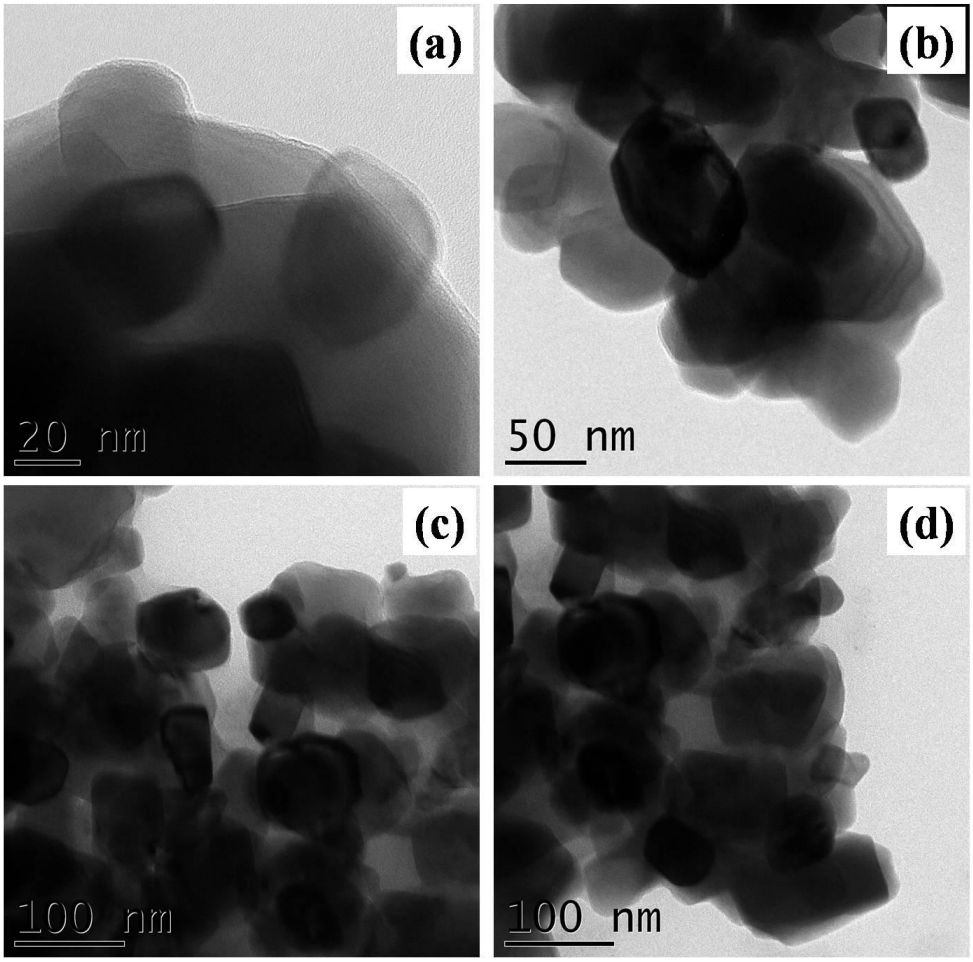

Fig. 4.56 *TEM images of* $Y_{1.93}Ce_{0.01}Eu_{0.06}O_3$.

4.7.8 $Y_{1.93}Ce_{0.01}Er_{0.06}O_3$

The particle size of $Y_{1.93}Ce_{0.01}Er_{0.06}O_3$was evaluated from TEM analysis as shown in Fig. 4.57. The TEM images clearly indicate that the particles are of irregular sizes and shapes. The particle size varied from 45 – 80 nm.

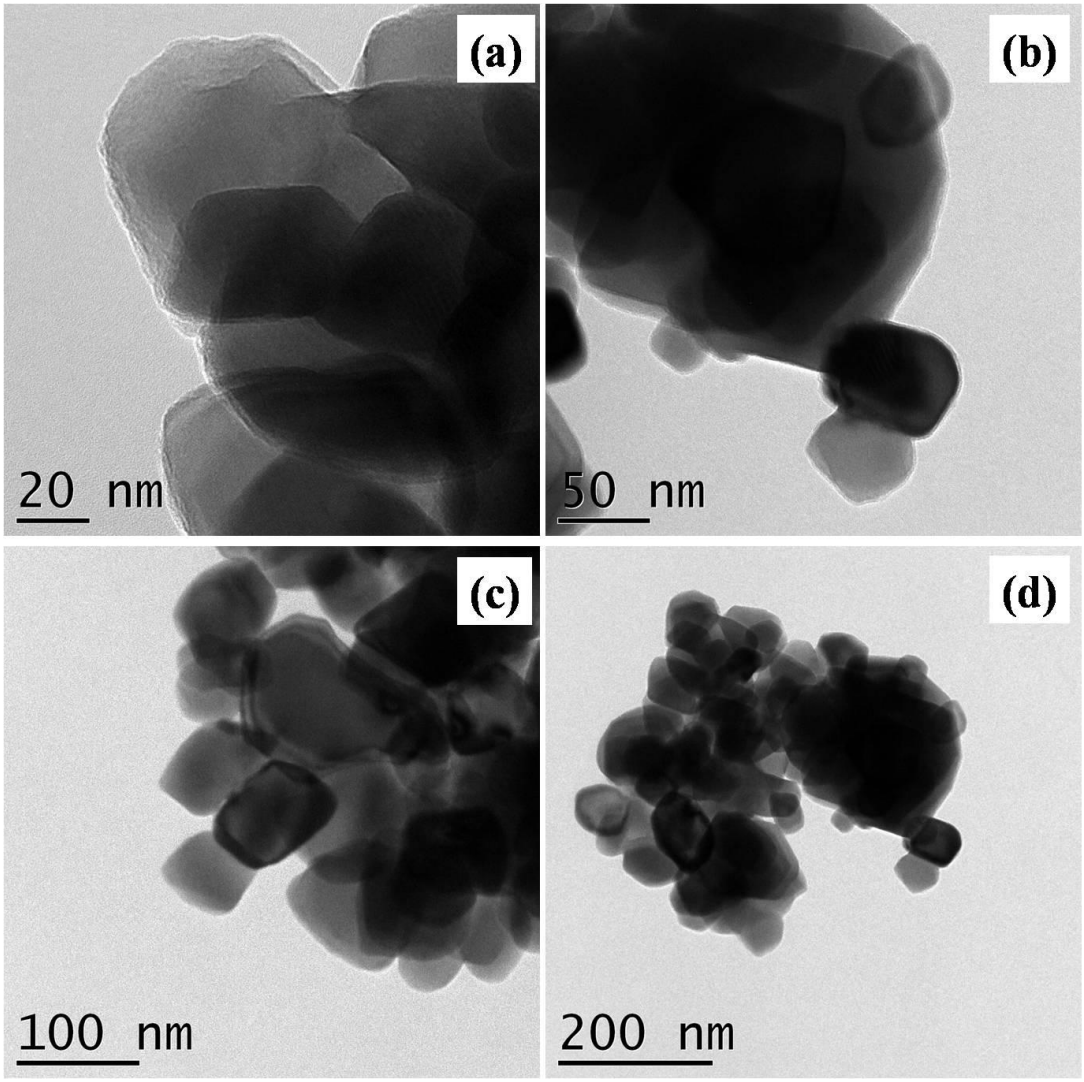

Fig. 4.57 *TEM images of* $Y_{1.93}Ce_{0.01}Er_{0.06}O_3$.

4.7.9 $Gd_{1.84}Er_{0.04}Yb_{0.12}O_3$

The TEM images of $Gd_{1.84}Er_{0.04}Yb_{0.12}O_3$ sintered at 1000 ℃ have been shown in Fig. 4.58. The detailed analysis suggests the presence of agglomeration of unevenly sized particles ranging from 60 – 120 nm.

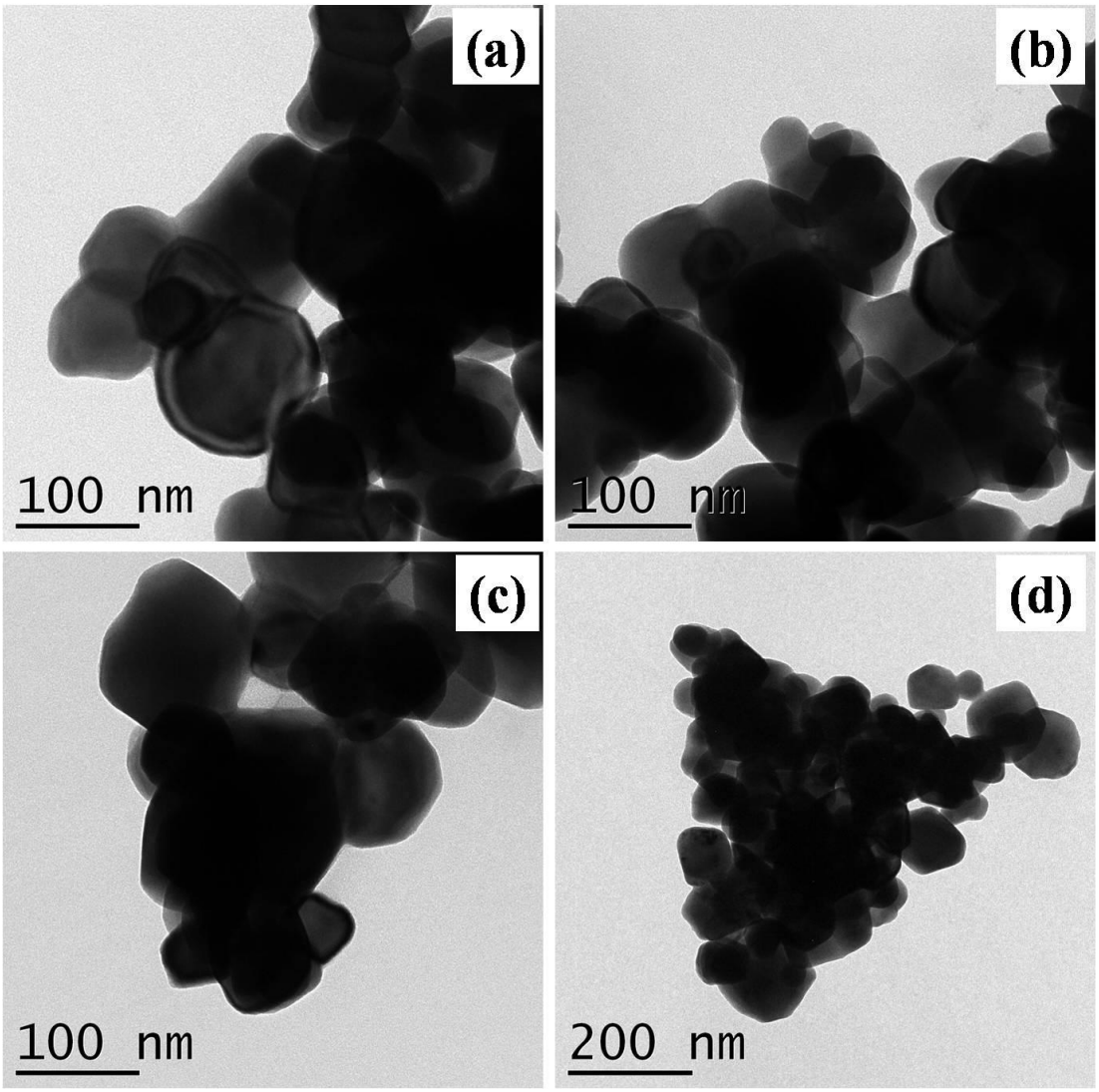

Fig. 4.58 *TEM images of* $Gd_{1.84}Er_{0.04}Yb_{0.12}O_3$.

4.7.10 $Gd_{1.84}Ho_{0.04}Yb_{0.12}O_3$

The TEM images of the representative sample sintered at 1000 ℃ show particles of irregular shapes and sizes. The detailed analysis of the micrographs revealed that the particle size varied from 45 – 105 nm (Fig. 4.59).

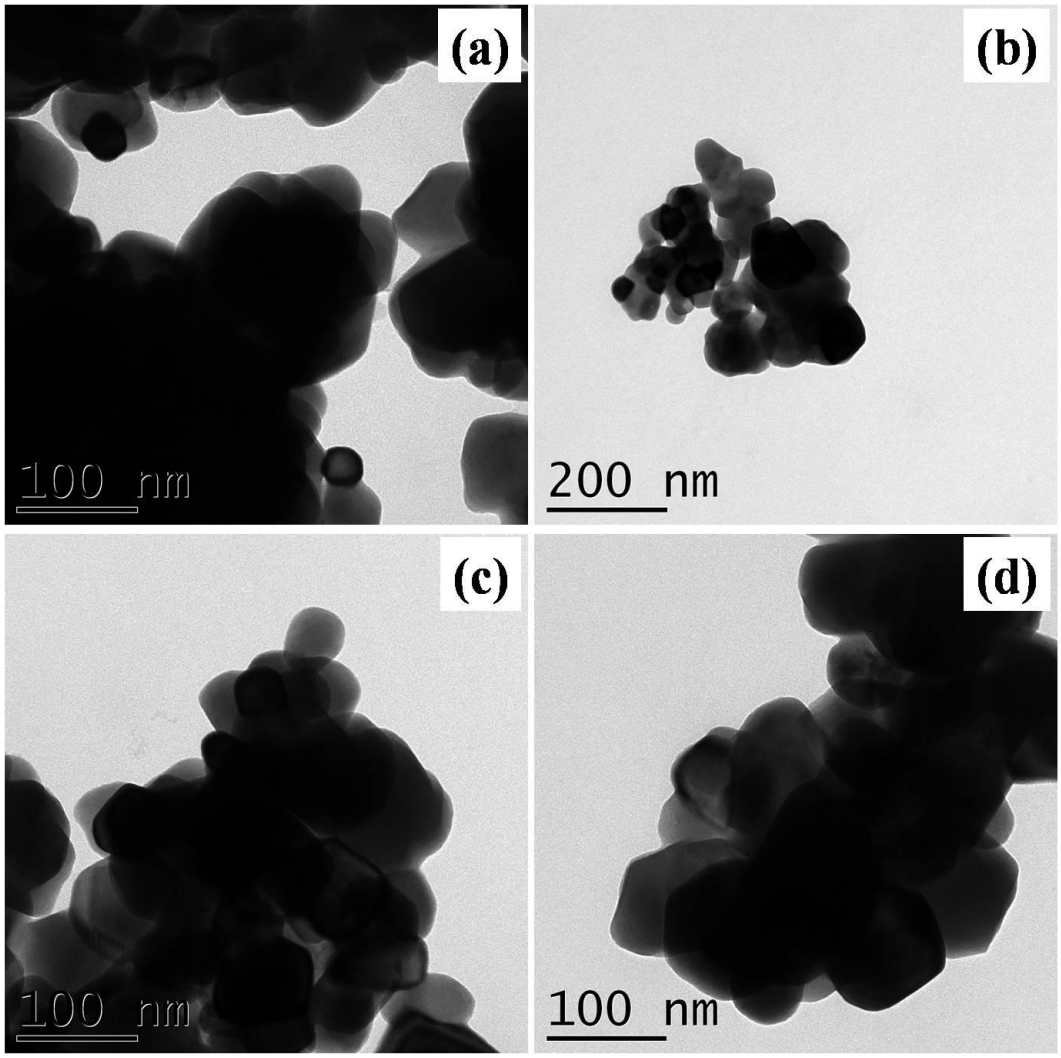

Fig. 4.59 *TEM images of* $Gd_{1.84}Ho_{0.04}Yb_{0.12}O_3$.

4.8 X-ray photoelectron spectroscopy (XPS)

4.8.1 $Co_{0.80}Cu_{0.20}Fe_2O_4$

The chemical states and chemical composition of the surface of Co-Cu ferrite were verified by implementing X-ray photoelectron spectroscopy (XPS). XPS spectra were charge corrected by setting the C 1s binding energy (B.E) at 284.8 eV. The full range survey scan spectrum and also the deconvoluted high-resolution (HR) spectra of Co 2p, Cu 2p, Fe 2p, and O 1s have been presented in Fig. 4.60 and Fig. 4.61 respectively.

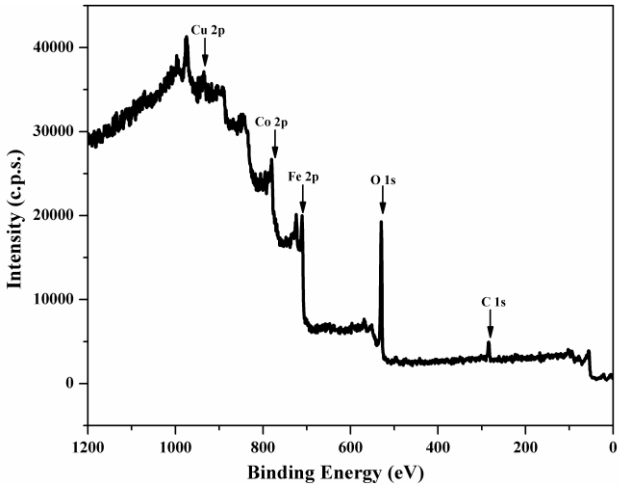

Fig. 4.60 *XPS survey spectrum of $Co_{0.80}Cu_{0.20}Fe_2O_4$.*

In the XPS spectrum of Co 2p, the peaks for Co $2p_{3/2}$ and Co $2p_{1/2}$ are centered at B.E of 779.8 and 795.2 eV respectively; these are typical B.E. signals for the Co^{2+} state [190]. Strong satellite peaks appearing at 785.1 and 802.3 eV imply the existence of Co in 2+ oxidation state. In the XPS spectrum of Cu 2p, two distinct signals for Cu $2p_{3/2}$ and Cu $2p_{1/2}$ are seen at 933.2 and 953.6 eV respectively, with a characteristic satellite feature of Cu^{2+} at 942.2 eV suggesting the existence of Cu^{2+} species[361]. In the spectrum of Fe 2p, the distinct peaks of Fe $2p_{3/2}$ and Fe $2p_{1/2}$ are centered at 710.0 and 724.1 eV respectively having a satellite feature at 718.1 eV. The two peaks positioned at 710.0 and

712.4 eV signify the octahedral and tetrahedral occupancy of Fe^{3+} ions respectively [362]. The occurrence of a satellite peak at a distance of 6.1 eV from Fe $2p_{1/2}$ peak (724.1 eV) has been considered as Fe in 3+ state [363]. The XPS spectrum of O 1s shows signals centered at 529.2 eV ascribed to the lattice oxygen and the B.E. signal at 530.8 eV is due to the existence of oxygen defects [364].

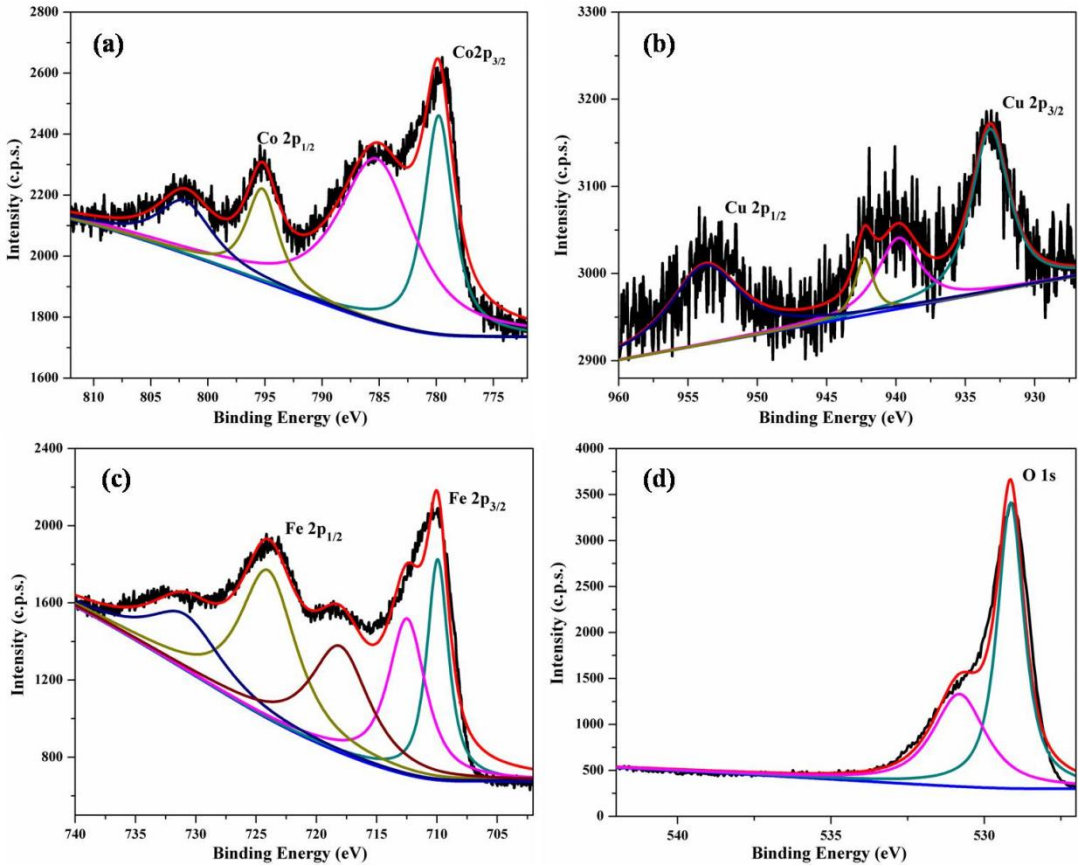

Fig. 4.61 *HRdeconvoluted XPS spectra of (a) Co 2p (b) Cu 2p (c) Fe 2p (d) O 1s.*

4.8.*2* $CoFe_{1.94}Sb_{0.06}O_4$

The full scan XPS spectrum along with HR spectra of Co 2p, Fe 2p, Sb 3d, and O 1s for $CoFe_{1.94}Sb_{0.06}O_4$has been presented in Fig 4.62.The binding energies were determined by fitting the HR spectra with peak fitting software. The Co 2p spectrum exhibited Co $2p_{3/2}$ and Co $2p_{1/2}$ signals positioned at 781.0 and 796.5 eV respectively.

The satellite features identified at 786.5 and 803.2 eV proved the presence of cobalt in 2+ oxidation state [355]. The Fe 2p spectrum exhibited two peaks, Fe $2p_{3/2}$ and Fe $2p_{1/2}$ centered at B.E. of 710.9 and 725.1 eV respectively. The signals at 710.9 and 713.1 eV could be due to the presence of Fe at octahedral and tetrahedral sites respectively [362]. The satellite feature present at 718.1 and 732.9 eV confirms the presence of Fe in 3+ oxidation state. The Sb 3d spectrum showed Sb $3d_{5/2}$ and Sb $3d_{3/2}$ peaks positioned at 530.0 and 539.3 eV corresponding to the presence of Sb^{3+} species [365]. The O 1s spectrum showed a B.E. peak at 529.2 eV attributed to the contribution of the lattice oxygen and the higher B.E. peak at 530.8 eV due to the existence of oxygen defects [364].

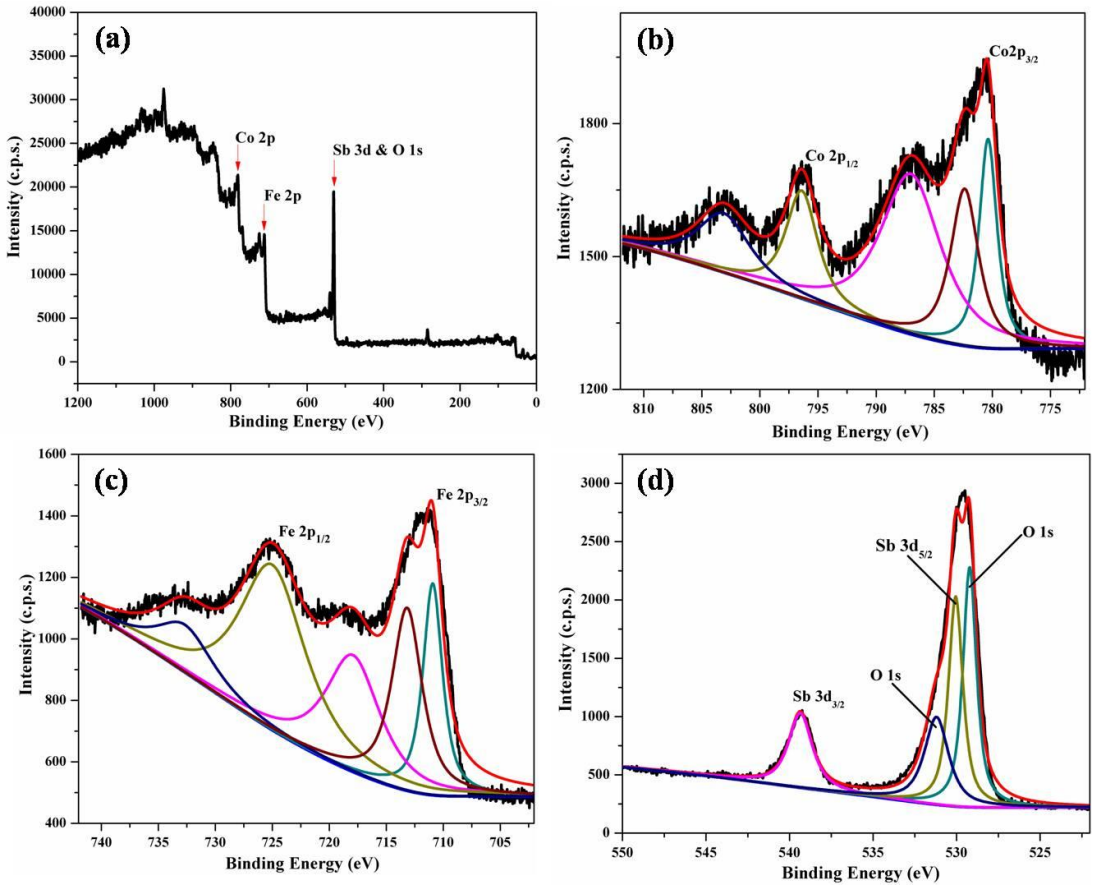

Fig. 4.62 *(a) Full scan XPS spectrum of* $CoFe_{1.94}Sb_{0.06}O_4$ *(b) HR deconvoluted XPS spectra of Co 2p (c) Fe 2p (d) Sb 3d and O 1s.*

4.8.3.1 $Co_{0.9}Cu_{0.1}Fe_{1.95}Gd_{0.05}O_4$

The full scan spectra (Fig. 4.63(a)) along with the HR XPS spectra of Co 2p, Cu2p, Fe 2p, O1s, and Gd 4d ions are plotted and deconvoluted using peak fitting software (Fig. 4.63(b-f)).

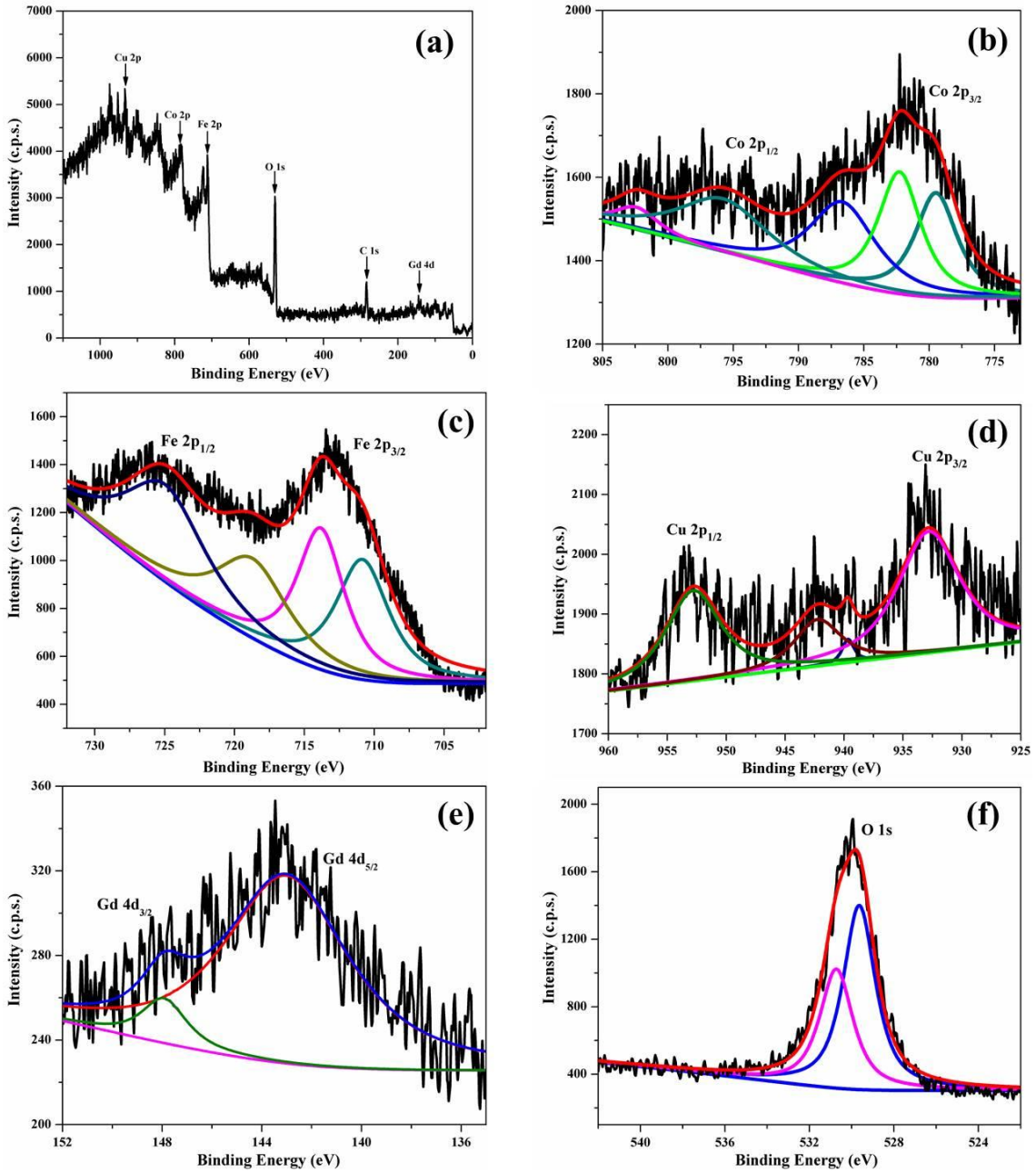

Fig. 4.63 *(a) Full scan XPS survey spectrum of $Co_{0.9}Cu_{0.1}Fe_{1.95}Gd_{0.05}O_4$ and HR deconvoluted spectra of (b) Co 2p (c) Cu 2p (d) Fe 2p (e) Gd 4d (f) O 1s.*

In the HR XPS spectrum for Co 2p, the signals for Co $2p_{1/2}$ and Co $2p_{3/2}$ were seen at 795.8 eV and 779.4 eV respectively which are characteristic binding energies for the Co^{2+} state [190]. The satellite peaks at 786.7 and 802.6 eV designates that Co is in +2 oxidation state. The two BE peaks at 779.4 eV and 782.3 eV exhibits due to the octahedral and tetrahedral bonding of Co^{2+} with oxygen respectively [366]. In the XPS spectrum of Cu 2p, the signals for Cu $2p_{3/2}$ and Cu $2p_{1/2}$ are detected at 932.8 and 952.8 eV respectively, with a typical satellite peak of Cu^{2+} at 942.2 eV signifying the presence of Cu^{2+}[361]. In the XPS spectrum of Fe 2p the Fe $2p_{1/2}$ and Fe $2p_{3/2,}$the signals are positioned at 725.2 and 710.9 eV respectively with a satellite peak at 719.1 eV. The two signals positioned at 710.9 and 713.7 eV can be allotted to Fe^{3+} ions at octahedral and tetrahedral sites respectively of Co-Cu ferrite [362]. Thus HR mode reveals the distribution of Fe^{3+} ions over tetrahedral (A) and octahedral (B) lattice sites. The difference of 6.1 eV from the satellite peak to Fe $2p_{1/2}$ peak (725.2 eV) was identified as Fe^{3+} state [363]. The BE of the oxygen species corresponding to the O 1s at 529.6 eV is credited to the contribution of the lattice oxygen and the higher BE peak at 530.8 is due to the presence of oxygen defects [364]. The Gd 4d spectrum displayed signals corresponding to Gd $4d_{5/2}$ and Gd $4d_{3/2}$ at a BE of about 143.0 and 148.0 eV which confirms the presence of Gd^{3+} ions [367].

4.8.3.2 $Co_{0.9}Cu_{0.1}Fe_{1.95}Sm_{0.05}O_4$

The full region scan XPS spectrum of $Co_{0.9}Cu_{0.1}Fe_{1.95}Sm_{0.05}O_4$ has been shown in Fig. 4.64(a) and deconvolutedHR XPS spectra of Co 2p, Cu 2p, Fe 2p, Sm 3d, and O 1s have been presented in Fig. 4.64(b-f). The full region scan reveals the existence of all the anticipated elements in the spectrum.

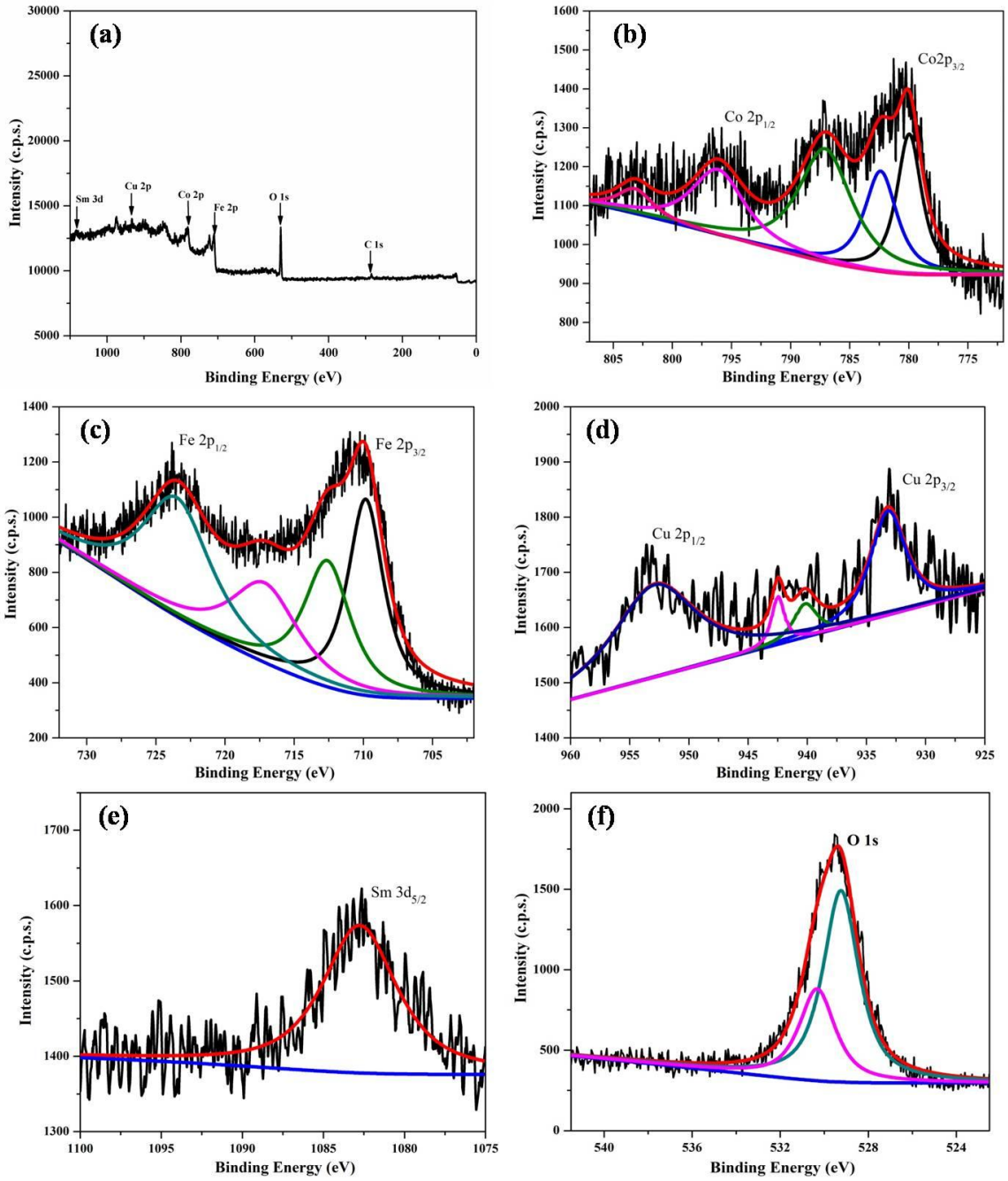

Fig. 4.64 *(a) Full region scan XPS spectrum of* $Co_{0.9}Cu_{0.1}Fe_{1.95}Sm_{0.05}O_4$ *and HR deconvoluted spectra of (b) Co 2p (c) Cu 2p (d) Fe 2p (e) Sm 3d (f) O 1s.*

The HR spectrum of Co 2p shows the Co $2p_{3/2}$, $2p_{1/2}$ signals at 779.9 eV and 796.3 eV respectively. The presence of satellite features at a BE of 787.1 eV and 803.4 eV confirms the presence of Cobalt in 2+ oxidation state [190]. The HR spectrum of Cu $2p_{3/2}$, $2p_{1/2}$ shows peaks positioned at 933.2 eV and 952.8 eV respectively. The presence

of satellite peak at 942.5 eV confirms the existence of copper in 2+ oxidation state [361]. The peaks observed for Fe $2p_{3/2}$, $2p_{1/2}$ at 709.8 eV and 723.7 eV respectively with a satellite peak at 717.9 eV confirms the presence of Fe in 3+ oxidation state [363]. In the XPS spectrum of Sm 3d, the Sm $3d_{5/2}$ peak is obtained at around 1082.7 eV which corresponds to Sm^{3+} ions [368]. The XPS spectrum of O 1s the peak obtained at 529.2 eV corresponds to lattice oxygen while the other peak at 530.4 eV corresponds to defect oxygen [364].

4.8.3.3 $Co_{0.9}Cu_{0.1}Fe_{1.95}Dy_{0.05}O_4$

The wide scan XPS survey spectrum (Fig. 4.65(a)) besides HR spectra of Co 2p, Cu2p, Fe 2p, O1s, and Dy 4d ions are plotted and de-convoluted employing peak fitting software (Fig. 4.65(b-f)). In the XPS spectrum for Co 2p, the B.E peaks for Co $2p_{3/2}$ and Co $2p_{1/2}$ were obtained at 779.7 and 796.0 eV respectively, typical of the Co^{2+} state [190]. Strong satellite features at 786.5 and 803.2 indicate the existence of Co^{2+} species. The signals at 779.7 eV and 782.2 eV belong to Co^{2+} ions in the octahedral and tetrahedral sites respectively [369]. The XPS spectrum of Cu 2p, shows peaks for Cu $2p_{3/2}$ and Cu $2p_{1/2}$ at BE of 933.0 and 952.9 eV respectively, along with satellite features at 942.2 eV suggesting the existence of Cu^{2+}[361]. In the XPS spectrum of Fe 2p, the Fe $2p_{3/2}$ and Fe $2p_{1/2}$ BE signals are located at 710.9 and 724.6 eV respectively accompanied by a satellite signal at 718.6 eV. The peaks located at 710.9 and 713.8 eV point towards the presence of Fe^{3+} ions at octahedral and tetrahedral sites respectively [362]. The difference of 6.1 eV of the satellite peak from Fe $2p_{1/2}$ peak (724.6 eV) confirms the existence of Fe in 3+ oxidation state [363]. The signals centered at 529.6 eV and 530.7 eV is due to the existence of lattice oxygen and oxygen defects respectively as shown in the HR spectrum

of O1s [364]. The Dy 4d spectrum exhibited Dy $4d_{3/2}$ peak at a BE of about 155.4 eV which verifies the existence of Dy^{3+} ions [370].

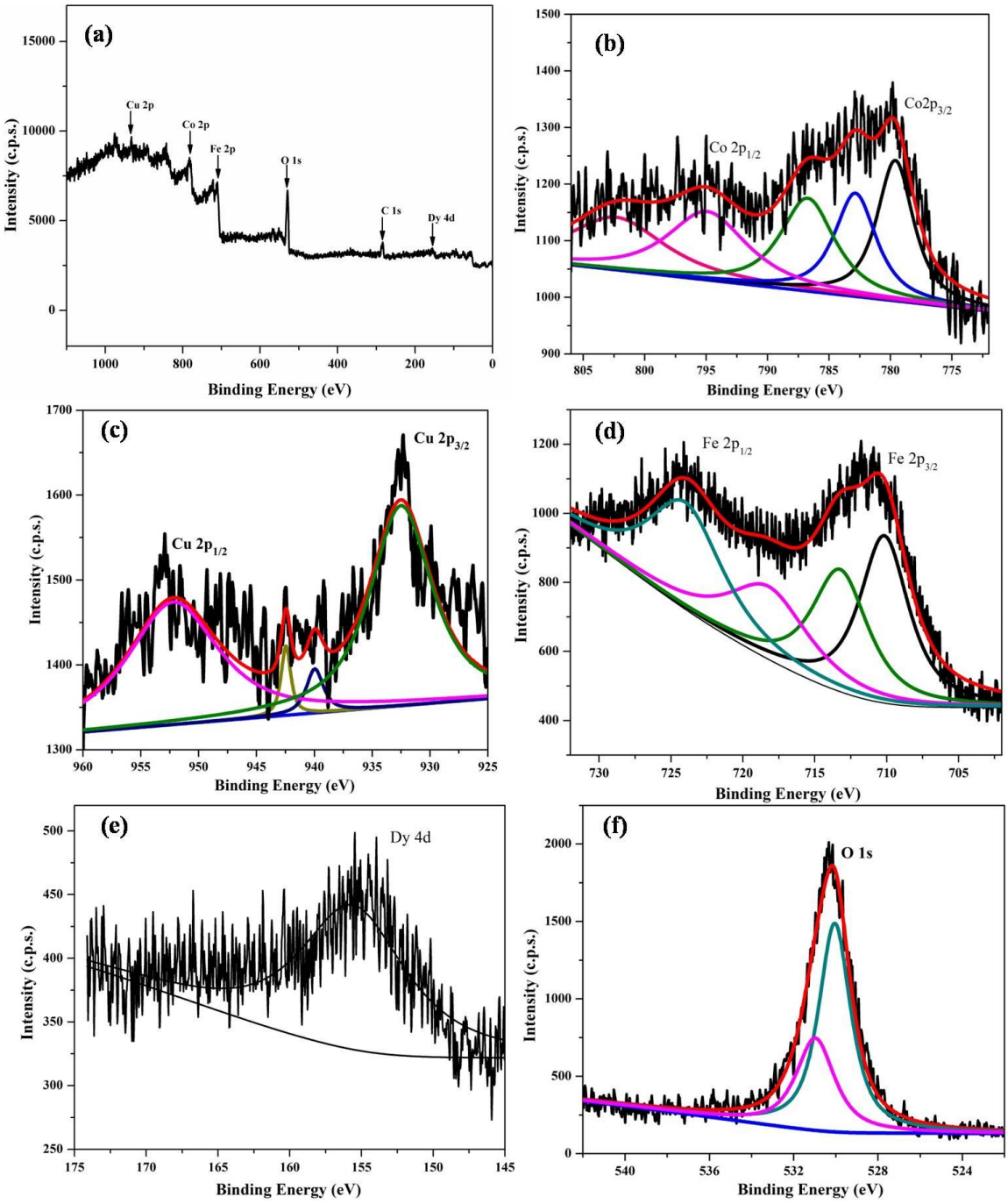

Fig. 4.65 *(a) Full region scan XPS spectrum of* $Co_{0.9}Cu_{0.1}Fe_{1.95}Dy_{0.05}O_4$ *and HR deconvoluted spectra of (b) Co 2p (c) Cu 2p (d) Fe 2p (e) Dy 4d (f) O 1s.*

4.8.3.4 $Co_{0.9}Cu_{0.1}Fe_{1.95}Yb_{0.05}O_4$

The full scan XPS spectrum for $Co_{0.9}Cu_{0.1}Fe_{1.95}Yb_{0.05}O_4$ has been presented in Fig. 4.66(a). The HR XPS spectra for Co 2p, Cu 2p, Fe 2p, Yb 4d, and O 1s have been shown in Fig. 4.66(b-f).

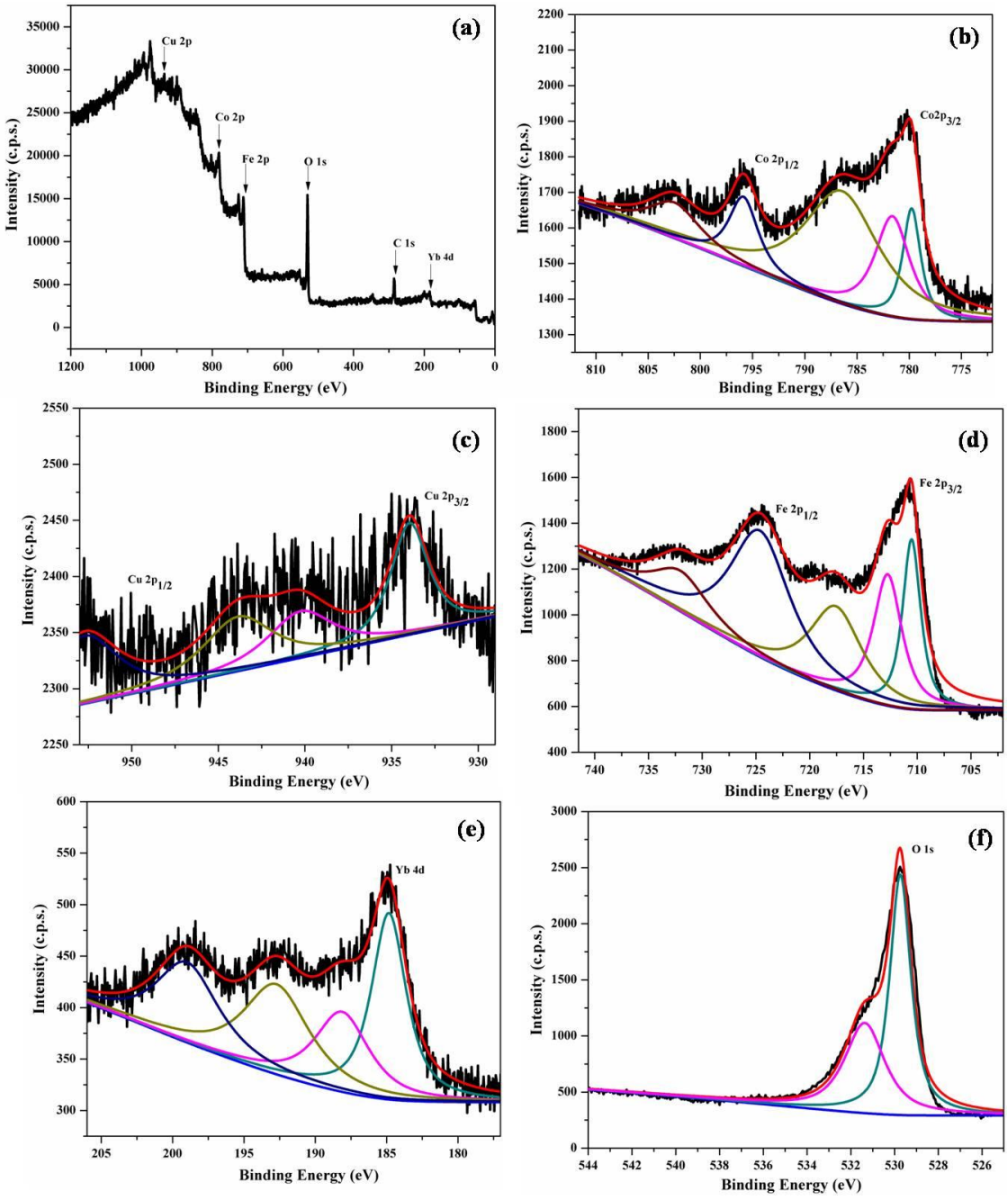

Fig. 4.66 *(a) Full region scan XPS spectrum of $Co_{0.9}Cu_{0.1}Fe_{1.95}Yb_{0.05}O_4$ and HR deconvoluted XPS spectra of (b) Co 2p (c) Cu 2p (d) Fe 2p (e) Yb 4d (f) O 1s.*

The HR XPS spectrum for Co 2p shows Co $2p_{3/2}$, $2p_{1/2}$ peaks centered at 779.8 and 795.9 eV respectively. The satellite features present at 786.7 and 802.7 eV confirms the presence of Co in 2+ oxidation state [190]. The additional peak present at 781.6 eV hints the presence of Co^{2+} at A site while the peak at 779.8 eV is due to the presence of Co^{2+} at B site. The XPS spectrum for Cu 2p shows the Cu $2p_{3/2}$, $2p_{1/2}$ signals positioned at 933.9 and 952.5 eV respectively. The satellite peaks present at 940.3 and 943.7 eV indicates the presence of Cu in 2+ oxidation state [361]. The XPS spectrum of Fe 2p shows Fe $2p_{3/2,}$ $2p_{1/2}$ peaks centered at 710.6 and 724.8 eV respectively. The presence of the additional peak at 712.7 eV indicates the presence of Fe^{3+} in the tetrahedral site while the peak at 710.6 eV signifies the existence of Fe^{3+} at the octahedral site [362]. The satellite features occurring at 717.7 and 732.2 eV reveals the presence of Fe in 3+ oxidation state. The peaks present at 529.7 and 531.4 eV in the O 1s XPS spectrum are due to the lattice oxygen and oxygen defects respectively [364]. The presence of Yb 4d peak positioned at 184.8 eV indicates the presence of Yb in 3+ oxidation state [310,321].

4.8.3.5 $Co_{0.9}Cu_{0.1}Fe_{1.95}Eu_{0.05}O_4$

Fig. 4.67(a) shows the full region XPS survey scan for $Co_{0.9}Cu_{0.1}Fe_{1.95}Eu_{0.05}O_4$. the HR XPS spectra for Co 2p, Cu 2p, Fe 2p, Eu 4d, and O 1s is shown in Fig. 4.67(b-f). The HR spectrum of Co 2p shows the Co $2p_{3/2}$, $2p_{1/2}$ signals positioned at 780.3 and 796.1 eV respectively. The peaks at 780.3 and 782.6 eV are due to the presence of Co in octahedral and tetrahedral sites respectively. The presence of satellite peaks at 787.1 and 803.4 eV indicates the existence of Co in 2+ oxidation state [190].

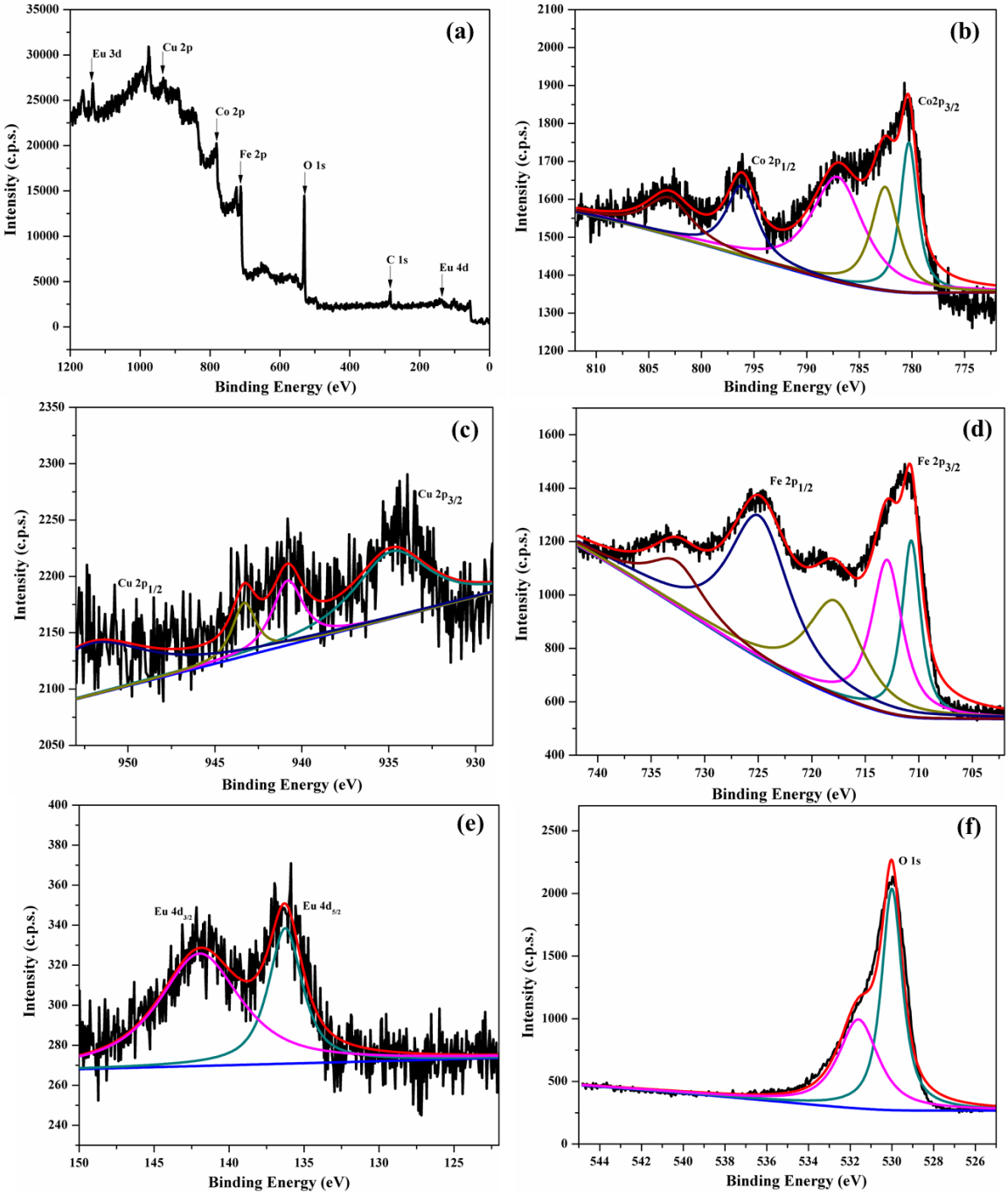

Fig. 4.67 *(a) Full region scan XPS spectrum of* $Co_{0.9}Cu_{0.1}Fe_{1.95}Eu_{0.05}O_4$ *and HR deconvoluted spectra of (b) Co 2p (c) Cu 2p (d) Fe 2p (e) Eu 4d (f) O 1s.*

The HR spectrum for Cu 2p shows peaks at 934.5 and 951.8 eV corresponding to Cu $2p_{3/2}$ and Cu $2p_{1/2}$ respectively. The satellite features at 940.8 and 943.3 eV indicates the presence of Cu in 2+ oxidation state [361]. The HR spectrum for Fe 2p shows Fe

$2p_{3/2}$and Fe $2p_{1/2}$ peaks centered at 710.7 and 725.1 eV respectively. The presence of peaks at 710.7 and 712.9 eV is credited to the existence of Fe at octahedral and tetrahedral sites respectively. The satellite features observed at 718.0 and 732.9 eV indicates the presence of Fe in 3+ oxidation state respectively [362]. The HR spectrum of O 1s shows the presence of peaks at 530.0 and 531.6 eV corresponding to lattice oxygen and oxygen defects [364]. In an HR spectrum for Eu 4d, the Eu $4d_{5/2}$ and Eu $4d_{3/2}$ peaks were obtained at 136.3 and 141.9 eV respectively which reflects the 3+ oxidation state of Europium [371].

4.8.4 $Co_{0.9}Cu_{0.1}Fe_{1.85}Cr_{0.15}O_4$

The full scan XPS survey spectrum for $Co_{0.9}Cu_{0.1}Fe_{1.85}Cr_{0.15}O_4$ has been depicted in Fig. 4.68(a). Fig. 4.68(b-f) shows the HR XPS spectra for the elements present. The HR XPS spectrum of Co 2p displays Co $2p_{3/2}$, $2p_{1/2}$ B.E peaks centered at 779.6 and 795.1 eV respectively. The existence of satellite features at a B.E of 785.5 and 801.9 eV validates the presence of Co in 2+ oxidation state [372]. The spectrum of Cu 2p shows Cu $2p_{3/2,}$ $2p_{1/2}$ peaks positioned at 933.1 and 953.3 eV respectively with a satellite peak at 940.3 eV which is a typical B.E peak for Cu in 2+ oxidation state [361]. The HR XPS spectrum of Fe 2p depicts Fe $2p_{3/2}$, $2p_{1/2}$ peaks located at B.E of 709.6 eV and 723.9 eV respectively [373]. The presence of an additional Fe $2p_{3/2}$peak at 711.9 eV, accounts for Fe^{3+} at tetrahedral sites [362]. The satellite feature at a distance of 6.0 eV from Fe $2p_{1/2}$ position at B.E of 717.1 eV affirms the chemical state of Fe to be 3+. The spectrum for Cr 2p shows Cr $2p_{3/2}$ peaks registered at 575.6 eV confirming the presence of Cr in 3+ oxidation state [374]. The HR spectrum for O 1s shows peaks at B.E of 529.0 and 530.6

eV corresponding to lattice oxygen and oxygen defects respectively [86]. Hence the XPS study verifies the presence of elements in their respective oxidation state.

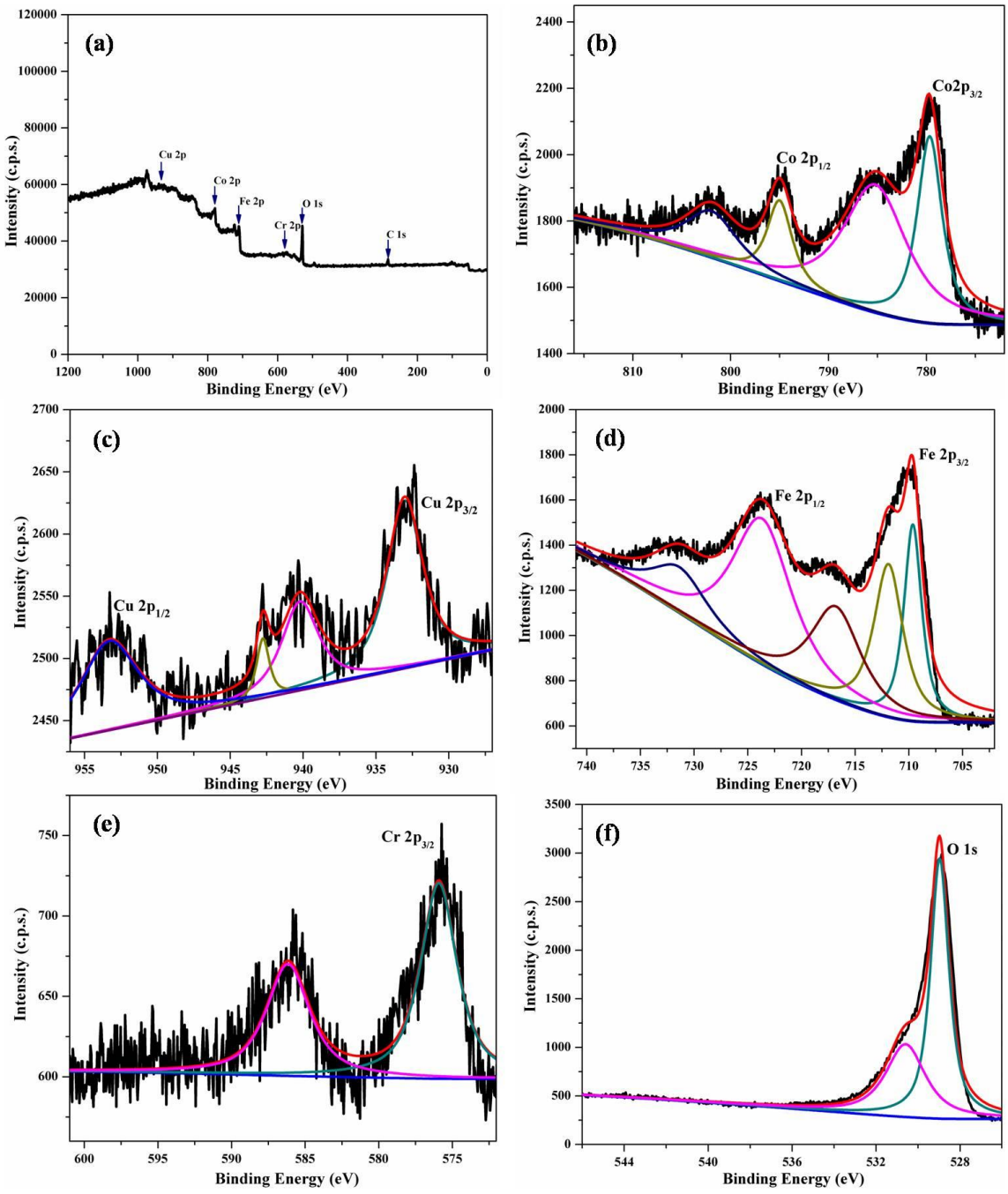

Fig. 4.68 *(a) Full region scan XPS spectrum of* $Co_{0.9}Cu_{0.1}Fe_{1.85}Cr_{0.15}O_4$ *and HR deconvoluted XPS spectra of (b) Co 2p (c) Cu 2p (d) Fe 2p (e) Cr 2p and (f) O 1s.*

4.8.5 $Co_{0.9}Cu_{0.1}Fe_{1.85}Mn_{0.15}O_4$

The wide region scan XPS survey spectrum for $Co_{0.9}Cu_{0.1}Fe_{1.85}Mn_{0.15}O_4$ has been presented in Fig. 4.69(a). Fig. 4.69(b-f) shows the HR deconvoluted XPS spectra for Co 2p, Cu 2p, Fe 2p, Mn 2p, and O 1s.

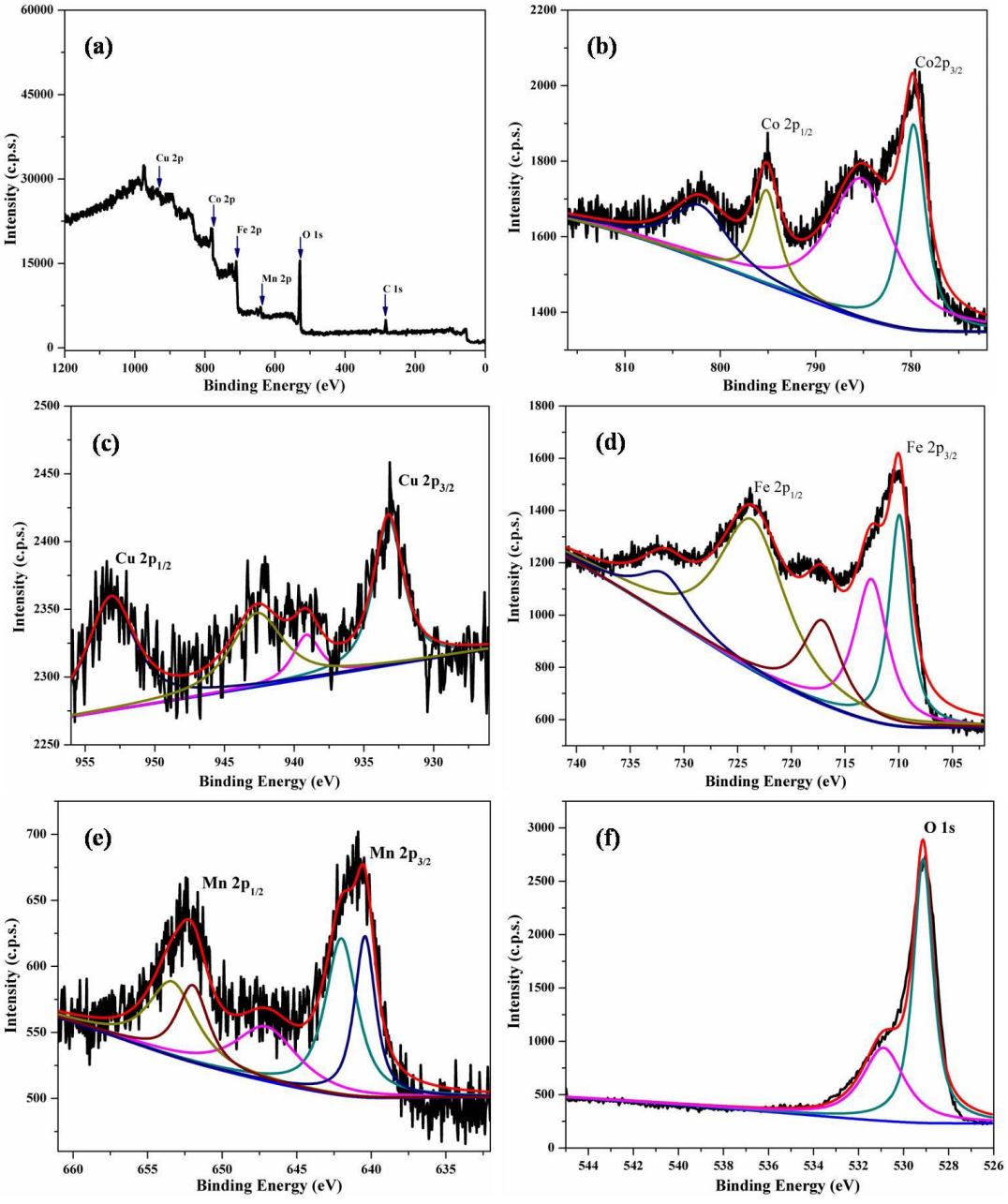

Fig. 4.69 *(a) Full region scan XPS spectrum of$Co_{0.9}Cu_{0.1}Fe_{1.85}Mn_{0.15}O_4$ and HR deconvoluted spectra of (b) Co 2p (c) Cu 2p (d) Fe 2p (e) Mn 2p and (f) O 1s.*

The HR XPS spectrum of Co 2p shows Co $2p_{3/2}$ and Co $2p_{1/2}$ B.E peaks positioned at 779.9 and 795.3 eV respectively. The presence of satellite peaks at a B.E of 785.3 and 802.3 eV confirms the presence of Co in 2+ oxidation state [372]. The HR XPS spectrum of Cu 2p shows Cu $2p_{3/2}$ and Cu $2p_{1/2}$ peaks centered at 933.3 and 953.1 eV respectively with the existence of satellite feature at 939.1 and 940.3 eV which are characteristic peaks for Cu in 2+ oxidation state [361]. The HR spectrum of Fe 2p exhibits Fe $2p_{3/2}$ and Fe $2p_{1/2}$ signals positioned at 709.9 eV and 724.0 eV respectively. The additional peak seen at 711.9 eV is due to the presence of Fe^{3+} at tetrahedral sites. The satellite peak at a distance of 6.0 eV from Fe $2p_{1/2}$ positioned at B.E of 717.1 eV confirms the presence of Fe in 3+ oxidation state [362]. The spectrum of Mn 2p displays Mn $2p_{3/2}$ and Mn $2p_{1/2}$ peaks positioned at 640.4 and 652.0 eV. The two distinct peaks present at 640.4 eV and 642.0 eV indicates the presence of Mn in 2+ and 3+ oxidation state respectively [375]. The satellite feature present at 647.2 eV also indicates the existence of Mn in the 2+ oxidation state [376]. The HR spectrum for O 1s shows peaks at B.E of 529.0 and 530.6 eV corresponding to lattice oxygen and oxygen defects respectively [86].

4.8.6 $Co_{0.9}Cu_{0.1}Fe_{1.85}In_{0.15}O_4$

The full region scan XPS spectra for $Co_{0.9}Cu_{0.1}Fe_{1.85}In_{0.15}O_4$ has been shown in Fig. 4.70(a), and HR XPS measurements have been shown in Fig. 4.70(b-f). The spectrum of Co 2p exhibited Co $2p_{3/2}$, $2p_{1/2}$ peaks centered at 780.6 and 796.2 eV respectively along with characteristic shake-up satellite peaks identified at around 786.3 and 803.1 eV confirming the existence of Co^{2+} species [377]. The HR spectrum of Cu 2p shows Cu $2p_{3/2,}$ $2p_{1/2}$spin-orbit doublets centered at binding energies around 933.7 and

954.1 eV respectively with a characteristic satellite peak at 941.5 and 943.5 eV which are assigned to the presence of Cu^{2+} on the surface [378].

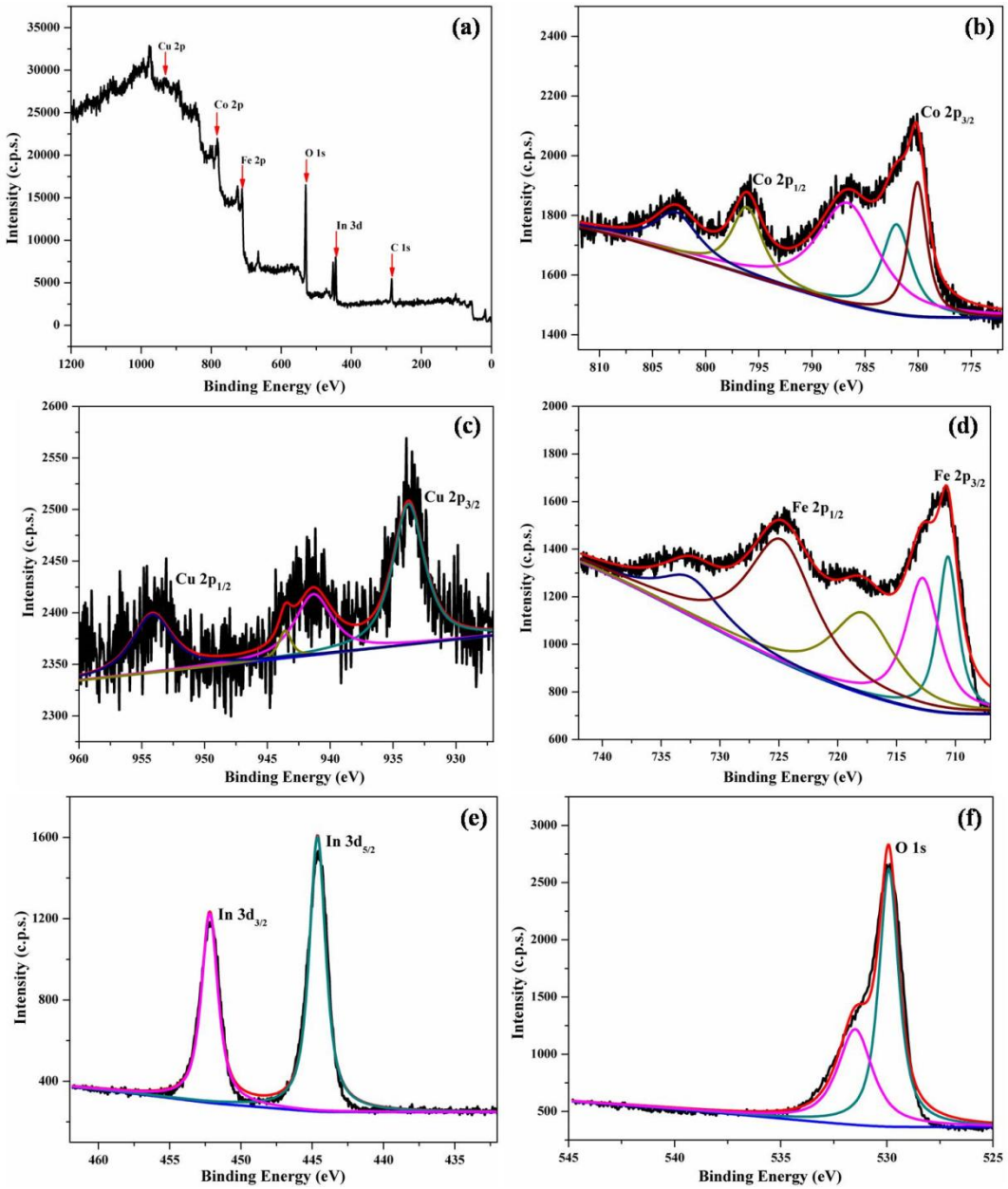

Fig 4.70. *(a) The full region scan XPS spectrum of $Co_{0.9}Cu_{0.1}Fe_{1.85}In_{0.15}O_4$, and HR deconvoluted XPS spectra of (b) Co 2p (c) Cu 2p (d) Fe 2p (e) In 3d and (f) O 1s.*

The XPS spectrum of Fe 2p exhibited two peaks of Fe $2p_{3/2}$, $2p_{1/2}$ spin-orbital components centered at binding energies of 710.7 and 724.8 eV respectively with the common satellite peak around 718.2 and 732.9 eV which could be assigned to Fe in 3+

oxidation state. The additional peak of Fe $2p_{3/2}$ present at around 712.8 eV can be assigned to the Fe^{3+} ions present at the tetrahedral sites [362]. The spectrum of In 3d shows two distinct peaks of In $3d_{5/2}$, $_{3/2}$ positioned at 444.6 and 452.1 eV respectively, confirming the existence of indium in 3+ oxidation state [86]. The O 1s signal centered at 529.9 eV is assigned to the contribution from lattice oxygen and a higher B.E. peak at around 531.5 eV is due to the existence of oxygen defects [364].

4.8.7 $Y_{1.93}Ce_{0.01}Eu_{0.06}O_3$

The full region scan XPS spectrum for $Y_{1.93}Ce_{0.01}Eu_{0.06}O_3$ has been presented in Fig. 4.71(a). The HR XPS spectra for Y 3d, Eu 3d, and O 1s has been presented in Fig. 4.71(b-d).

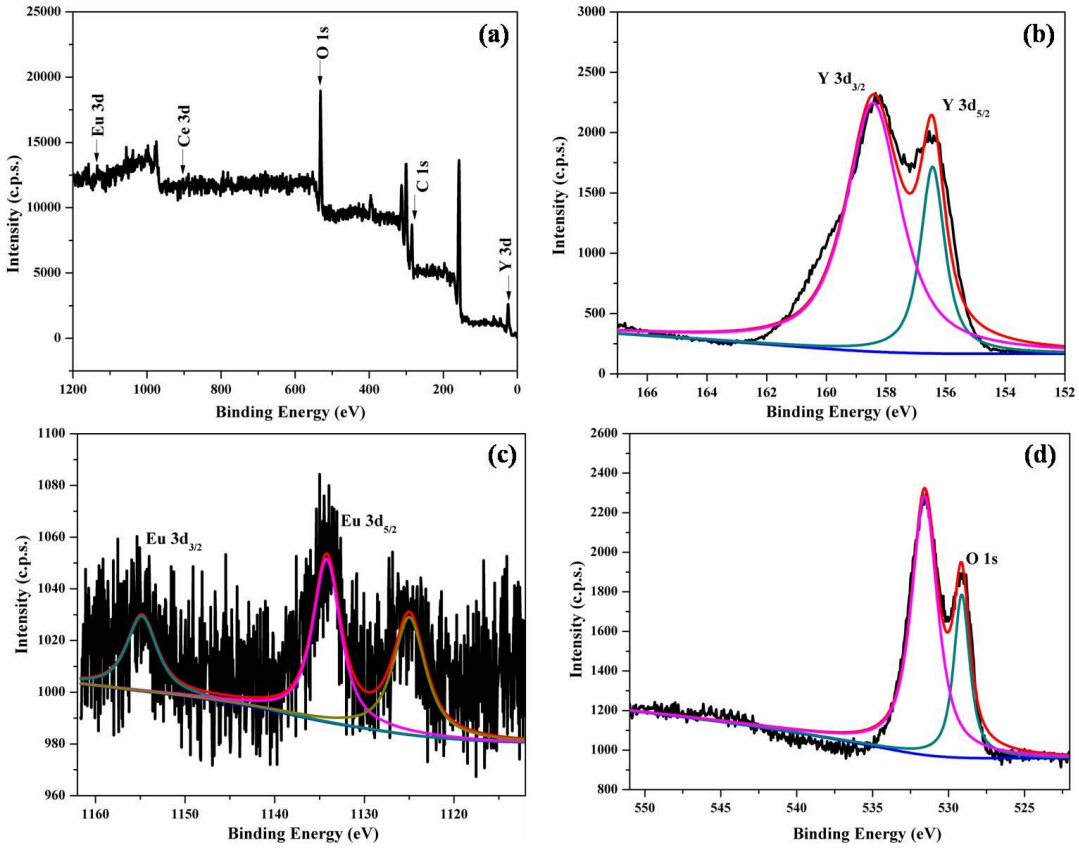

Fig. 4.71 *(a) Full scan XPS spectrum of* $Y_{1.93}Ce_{0.01}Eu_{0.06}O_3$*,high-resolution XPS spectra of (b) Y 3d (c) Eu 3d and (d) O 1s.*

The spectrum for Y 3d shows signals corresponding to Y $3d_{5/2}$ and Y $3d_{3/2}$ centered at 156.4 and 158.4 eV respectively showing the existence of Y in 3+ oxidation state [379]. The spectrum for Eu 3d shows the peaks corresponding to Eu $3d_{5/2}$ and Eu $3d_{3/2}$ positioned at 1134.2 and 1154.9 eV respectively thus indicating the presence of Eu in 3+ oxidation state [380]. The peak centered at 529.1 and 531.5 eV for O 1s corresponds to lattice oxygen and oxygen defects respectively [364].

4.8.8 $Y_{1.93}Ce_{0.01}Er_{0.06}O_3$

Fig. 4.72(a) presents the full scan XPS spectrum for $Y_{1.93}Ce_{0.01}Er_{0.06}O_3$. The HR XPS spectra for Y 3d, Er 4d, and O 1s have been shown in Fig. 4.72(b-d).

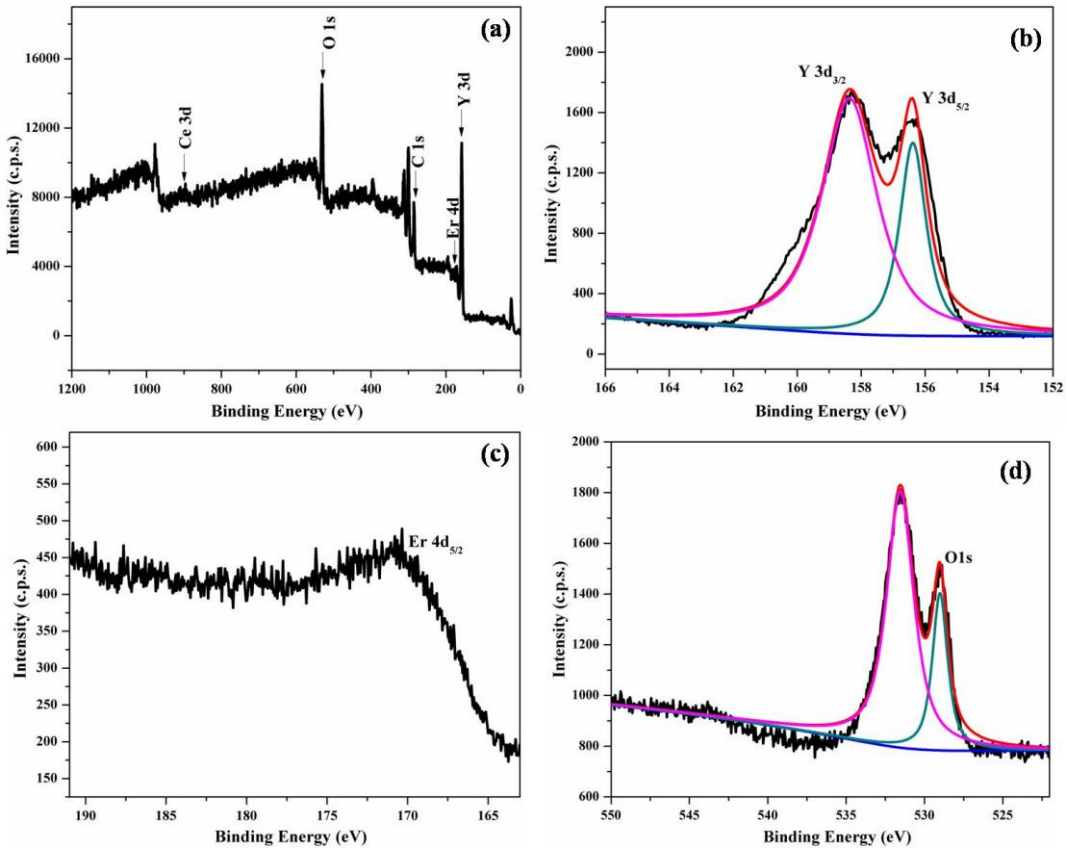

Fig. 4.72 *(a) Full scan XPS spectrum of $Y_{1.93}Ce_{0.01}Er_{0.06}O_3$,high-resolution XPS spectra of (b) Y 3d (c) Er 4d and (d) O 1s.*

The spectrum for Y 3d shows BE peaks at 156.4 and 158.4 eV which could be assigned to Y $3d_{5/2}$ and Y $3d_{3/2}$ respectively [379]. The HR XPS spectrum for Er 4d shows BE peaks positioned at 170.7 eV indicating the existence of Er in 3+ oxidation state [310]. The XPS spectrum of O 1s shows BE peaks at 529.0 and 531.6 eV corresponding to lattice oxygen and oxygen defects respectively [364]. The XPS studies confirm the oxidation states of the species present. Since the concentration of cerium is low the XPS spectrum could not be obtained.

4.8.9 $Gd_{1.84}Er_{0.04}Yb_{0.12}O_3$

The full scan XPS spectrum of $Gd_{1.84}Er_{0.04}Yb_{0.12}O_3$ have been shown in Fig. 4.73(a). The HR XPS spectra of Gd 4d, Er 4d, Yb 4d, and O 1s have been presented in Fig. 4.73(b-d).

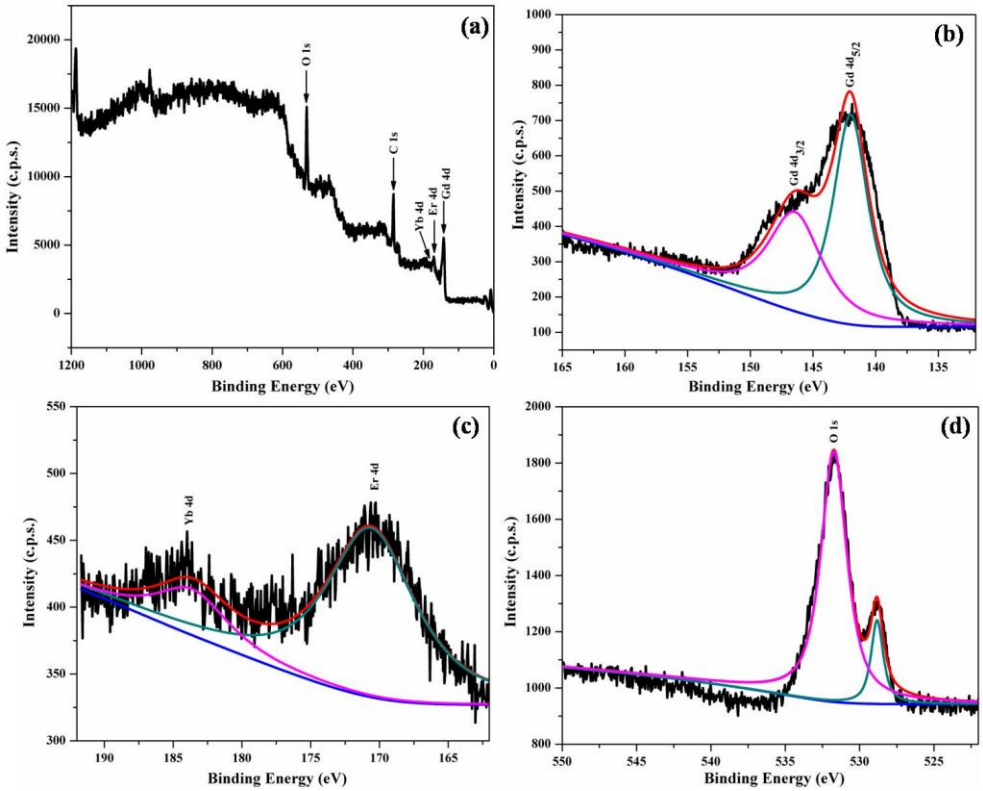

Fig. 4.73 *(a) Full scan XPS spectrum of $Gd_{1.84}Er_{0.04}Yb_{0.12}O_3$,high-resolution XPS spectra of (b) Gd 4d (c) Er 4d, Yb 4d and (d) O 1s.*

The BE peaks in the XPS spectrum of Gd 4d shows Gd $4d_{5/2}$ and Gd $4d_{3/2}$ peaks centered at 142.0 and 146.6 eV respectively corresponding to Gd in 3+ oxidation state [367]. The XPS spectrum of Er 4d shows BE peak at 170.6 eV confirming the existence of Er in 3+ oxidation state [321]. The XPS spectrum of Yb 4d shows a peak centered at 184.0 eV attributed to the existence of Yb in 3+ oxidation state [321]. The XPS spectrum of O 1s shows BE peaks at 528.9 and 531.6 eV showing the existence of lattice oxygen and oxygen defects [364].

4.8.10 $Gd_{1.84}Ho_{0.04}Yb_{0.12}O_3$

The deconvoluted HR spectra of $Gd_{1.84}Ho_{0.04}Yb_{0.12}O_3$has been shown in Fig.4.74(a-d).

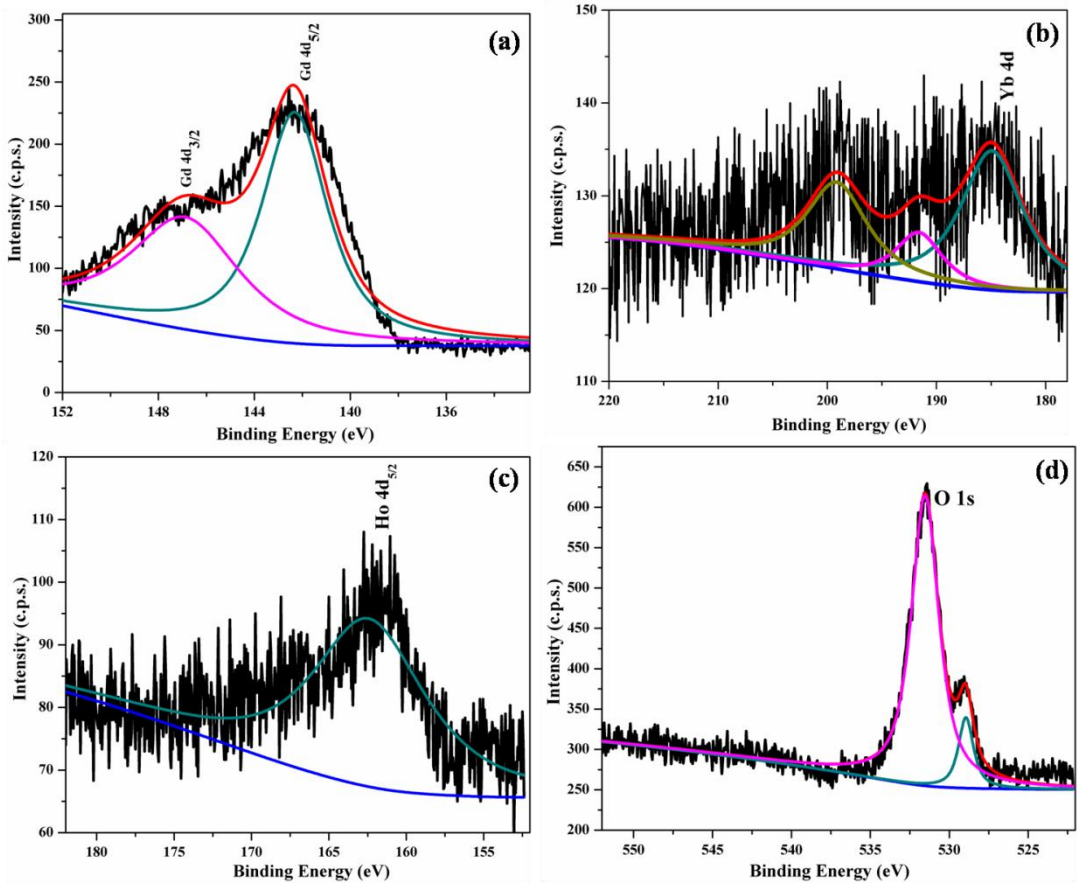

Fig. 4.74 *High-resolution XPS spectra of (a) Gd 4d (b) Yb 4d (c) Ho 4d, and (d) O 1s.*

The HR XPS spectrum of Gd 4d shows the characteristic $4d_{5/2}$ and $4d_{3/2}$ peaks positioned at 142.3 eV and 146.9 eV respectively [367]. The spectrum of Yb 4d shows the BE signal centered at 185.1 eV indicating the existence of Yb in the 3+ oxidation state [321]. The HR XPS spectrum of Ho shows XPS peak centered at 162.6 eV confirming the presence of Ho in 3+ state [381]. The deconvoluted O 1s spectrum shows two signals centered at 528.7eV and 531.5 eV highlighting the presence of lattice oxygen and defect oxygen respectively [364].

SOLID STATE AND OPTICAL STUDIES

5.1 Mössbauer Spectroscopy

In the case of spinel ferrites, Mössbauer spectroscopy is an important technique to identify ferrimagnetic and superparamagnetic materials and also to ascertain the oxidation state of iron. The Mössbauer spectra obtained was fitted using NORMOS-SITE software.

5.1.1 $CoFe_2O_4$ and $Co_{0.9}Cu_{0.1}Fe_2O_4$

The room temperature Mössbauer absorption spectra of the parent compounds ($CoFe_2O_4$ and $Co_{0.9}Cu_{0.1}Fe_2O_4$) is presented in Fig. 5.1 and Fig. 5.2 and the corresponding parameters such as isomer shift (*IS*), quadrupole splitting (*QS*), and magnetic field (*Hf*) are mentioned in Table 5.1. The spectra exhibit two well developed magnetic sextets that are corresponding to Fe^{3+} at tetrahedral A site represented by sextet A and octahedral B site represented by sextet B.

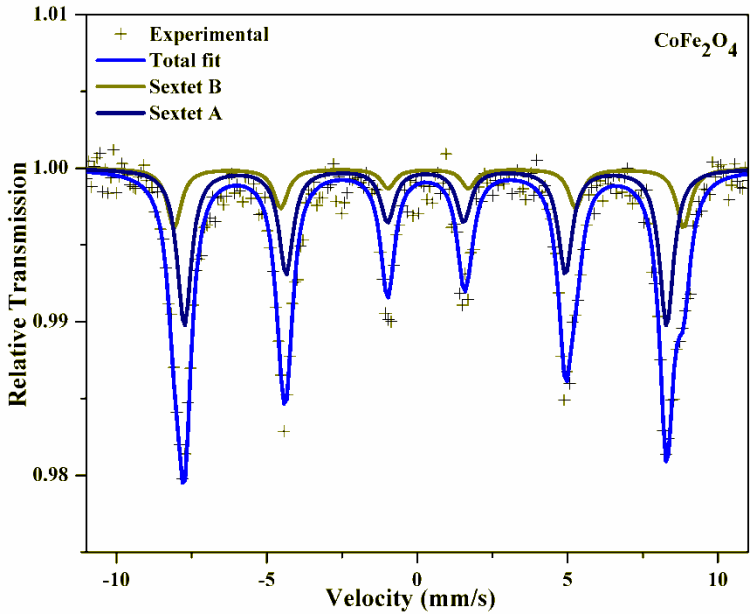

Fig. 5.1 *Room temperature Mössbauer spectrum for $CoFe_2O_4$.*

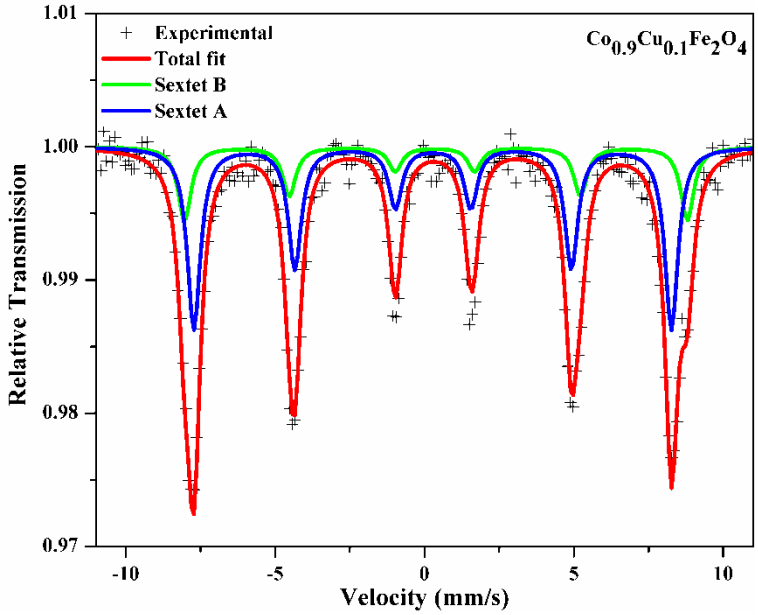

Fig 5.2 *Room temperature Mössbauer spectrum for* $Co_{0.9}Cu_{0.1}Fe_2O_4$.

The spectra show no traces of superparamagnetic behavior which confirm that the synthesized materials have ferrimagnetic nature with mixed spinel structure. The sextets were assigned as A and B site based on *IS* and *Hf* values obtained from fitting data. The A site *Hf* and *IS* values were expected to be on the lower side compared to the B site values.The greater value of *Hf* for the Fe^{3+} in the B site compared to the A site is owing to the more covalent character of the Fe_{tetra}^{3+}-O^{2-} bond than the Fe_{octa}^{3+}-O^{2-} bond [382]. The *IS* values obtained were less than 0.5 mm/s, which is consistent with high spin Fe in the 3+ oxidation state, and rules out the existence of Fe^{2+} ions in the material [383,384]. *IS* values for B site is greater than that of the A site on account of the larger bond length between Fe^{3+}-O^{2-} in B site. Consequently, the overlapping of orbital's of Fe^{3+} ions and O^{2-} anions is smaller at B site and therefore a larger *IS* is developed signifying a higher s-electron density at B site [385]. The values of *QS* were close to 0.0 mm/s, which revealed that the overall cubic symmetry is retained between Fe^{3+} ions and its vicinity [246].

Table 5.1 Mössbauer parameters for $CoFe_2O_4$ and $Co_{0.9}Cu_{0.1}Fe_2O_4$.

		FWHM (mm/s)	*IS* (δ) (mm/s)	*QS* (Δ) (mm/s)	Hyperfine field (*Hf*) (T)	χ^2
$CoFe_2O_4$	Sextet A	0.56 ± 0.02	0.28 ± 0.01	0.01 ± 0.02	49.7 ± 0.1	1.24
	Sextet B	0.56 ± 0.02	0.37 ± 0.01	-0.02 ± 0.02	52.5 ± 0.1	
$Co_{0.9}Cu_{0.1}Fe_2O_4$	Sextet A	0.53 ± 0.02	0.28 ± 0.01	-0.02 ± 0.02	49.6 ± 0.1	1.44
	Sextet B	0.53 ± 0.02	0.36 ± 0.01	-0.04 ± 0.02	52.2 ± 0.1	

5.1.2 $Co_{0.9}Cu_{0.1}Fe_{1.95}Gd_{0.05}O_4$

Room temperature Mössbauer spectrum of $Co_{0.9}Cu_{0.1}Fe_{1.95}Gd_{0.05}O_4$and parameters of hyperfine interactions such as *IS*, *QS*, and *Hf* are presented in Fig. 5.3 and Table 5.2 respectively. The spectrum exhibit two well-resolved Zeeman sextets arising due to the Fe^{3+} ions present at both A and B sites. The *IS* for the B site is higher than that of the A site. The *IS* values varied from 0.28 mm/s and 0.36 mm/s (Table 5.2), which are characteristics of the high spin Fe^{3+} charge state in spinel ferrites. The QS values at A and B sites are very small in both the samples signifying that the local symmetry of the material obtained is cubic [246]. The *Hf* value at B site is always greater than at A site. This can be illustrated based on the covalent nature of Fe^{3+}–O^{2-} bond and the difference in the bond length at A and B sites. The Fe^{3+}–O^{2-} bond is more covalent at A site than Fe^{3+}–O^{2-} bond at B site, while the s-electron charge density at A site is higher. This results in a higher value of *Hf* at B site than at A site. The value of *Hf* decreased at both A and B sites with Gd^{3+} ion substitution. The *Hf* value decreased due to the replacement of Fe^{3+} ions by Gd^{3+} ion at the B site [127]. The substitution will give rise to additional Gd^{3+}–O–Gd^{3+}, and Gd^{3+}–O–Fe^{3+} interactions which are not as strong as the Fe^{3+}–O–Fe^{3+}interactions.

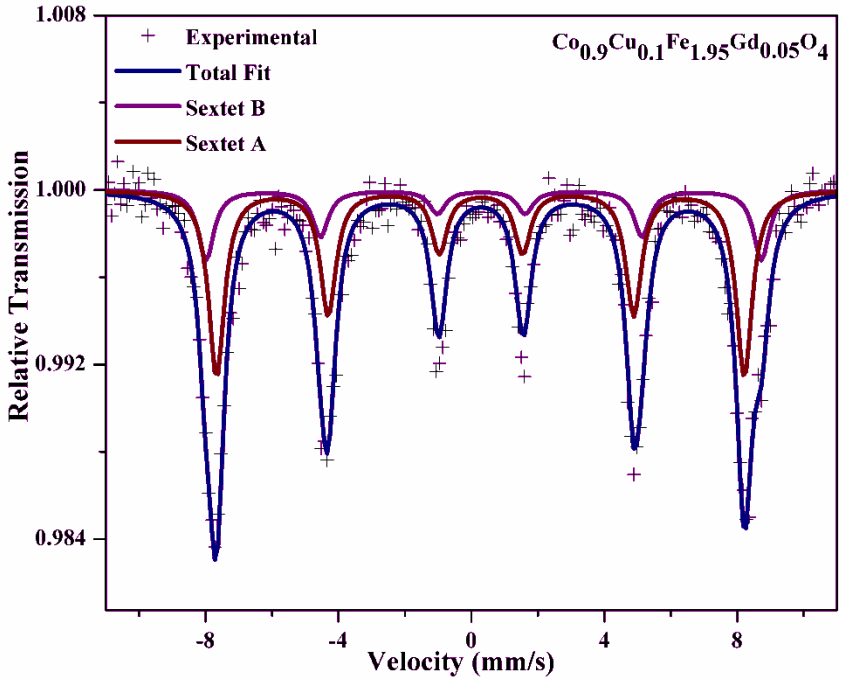

Fig. 5.3 *Room temperature Mössbauer spectrum for* $Co_{0.9}Cu_{0.1}Fe_{1.95}Gd_{0.05}O_4$.

Table 5.2 Mössbauer parameters of $Co_{0.9}Cu_{0.1}Fe_2O_4$ and $Co_{0.9}Cu_{0.1}Fe_{1.95}Gd_{0.05}O_4$.

		FWHM **(mm/s)**	***IS*** **(δ) (mm/s)**	***QS*** **(Δ) (mm/s)**	***Hf*** **(T)**	χ^2
$Co_{0.9}Cu_{0.1}Fe_2O_4$	Sextet A	0.53 ± 0.02	0.28 ± 0.01	-0.02 ± 0.02	49.6 ± 0.1	1.44
	Sextet B	0.53 ± 0.02	0.36 ± 0.01	-0.04 ± 0.02	52.2 ± 0.1	
$Co_{0.9}Cu_{0.1}Fe_{1.95}Gd_{0.05}O_4$	Sextet A	0.56 ± 0.02	0.28 ± 0.01	0.02 ± 0.02	49.2 ± 0.1	1.20
	Sextet B	0.58 ± 0.02	0.33 ± 0.01	-0.07 ± 0.02	51.8 ± 0.1	

5.1.3 $Co_{0.9}Cu_{0.1}Fe_{1.85}Cr_{0.15}O_4$

Fig. 5.4 shows the room temperature Mössbauer spectrum for $Co_{0.9}Cu_{0.1}Fe_{1.85}Cr_{0.15}O_4$ and the fitted hyperfine magnetic parameters such as *IS*, *QS*, and *Hf* are listed in Table 5.3. The spectrum exhibit two normal Zeeman sextets attributed to the existence of ferrimagnetic Fe atoms at both A and B sites. The *IS* values were in the range of 0.28 – 0.36 mm/s, expected for Fe^{3+} high spin species and rules out the presence

of Fe^{2+} in the system [383]. In most of the spinel ferrites, the value of *IS* and *Hf* is greater for the B site than A site thus the results indicate the identification of both the sites [215].

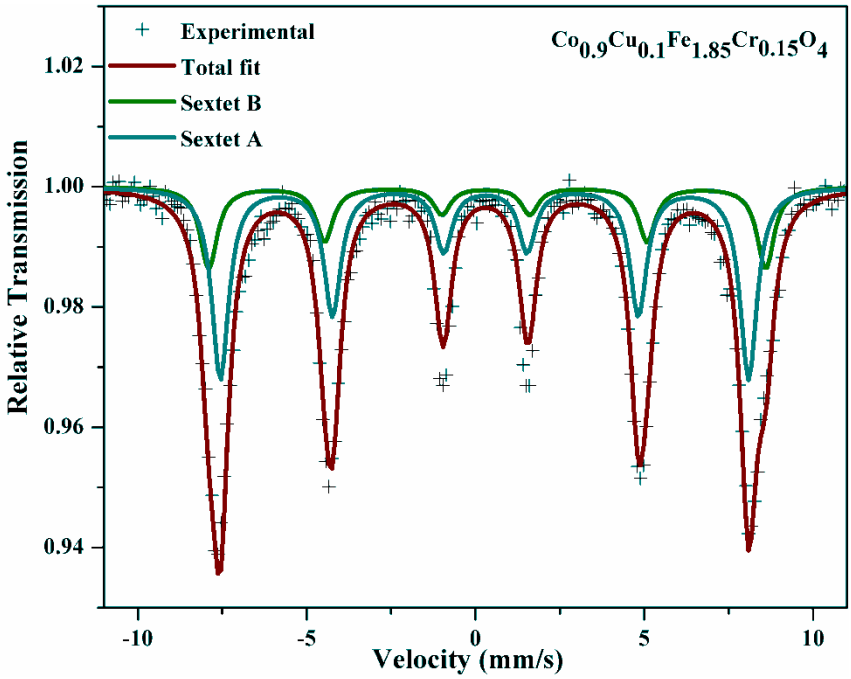

Fig. 5.4 *Room temperature Mössbauer spectrum for* $Co_{0.9}Cu_{0.1}Fe_{1.85}Cr_{0.15}O_4$.

For both A and B sites, *Hf* was observed to decrease with Cr^{3+}substitution. The decrease can be explained assuming the additional Cr^{3+}–O–Fe^{3+} and Co^{2+}–O–Cr^{3+} exchange interactions developed in the system, not being as strong as Fe^{3+}–O–Fe^{3+} interactions [202]. The *QS* values were near to zero signifying no significant deviation from cubic symmetry of Fe^{3+} surrounding.

Table 5.3 Mössbauer parameters of $Co_{0.9}Cu_{0.1}Fe_2O_4$ and $Co_{0.9}Cu_{0.1}Fe_{1.85}Cr_{0.15}O_4$.

		FWHM (mm/s)	*IS* (δ) (mm/s)	*QS* (Δ) (mm/s)	*Hf* (T)	χ^2
$Co_{0.9}Cu_{0.1}Fe_2O_4$	Sextet A	0.53 ± 0.02	0.28 ± 0.01	-0.02 ± 0.02	49.6 ± 0.1	1.44
	Sextet B	0.53 ± 0.02	0.36 ± 0.01	-0.04 ± 0.02	52.2 ± 0.1	
$Co_{0.9}Cu_{0.1}Fe_{1.85}Cr_{0.15}O_4$	Sextet A	0.60 ± 0.02	0.28 ± 0.01	0.03 ± 0.02	48.5 ± 0.1	2.90
	Sextet B	0.60 ± 0.02	0.33 ± 0.01	-0.04 ± 0.02	51.1 ± 0.1	

5.1.4 $Co_{0.9}Cu_{0.1}Fe_{1.85}Mn_{0.15}O_4$

A Mössbauer spectrum of $Co_{0.9}Cu_{0.1}Fe_{1.85}Mn_{0.15}O_4$ recorded at room temperature has been shown in Fig. 5.5 and *IS*, *QS*, and *Hf*have been tabulated in Table 5.4.The spectrum exhibits two distinct sextets which reveal that there are two different environments of Fe ions.These can be identified as Fe in A and B site within the spinel structure. The observed values of *IS* signify that the high spin Fe^{3+} ions possess different s-electron density in the two different environments.The *IS* values obtained are below 0.5 mm/s, which clearly suggests the absence of Fe^{2+} ions in the sample [383]. The *QS* values were almost close to zero which indicates the overall cubic symmetry around Fe^{3+} ions. It is observed that with Mn ion substitution the *Hf* value slightly decreases as a result of the reduction in strength of super-exchange interactions. Substituting Mn for Fe will generate weaker Mn–O–Fe, Mn-O-Mn superexchange interactions which are not as strong as the Fe–O–Fe superexchange interactions [386].

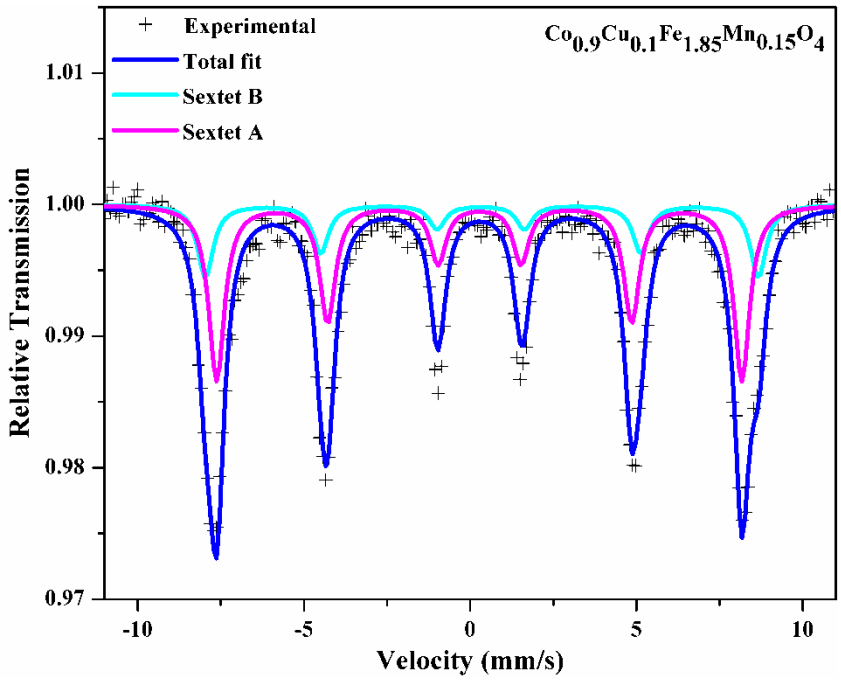

Fig. 5.5 *Room temperature Mössbauer spectrum for* $Co_{0.9}Cu_{0.1}Fe_{1.85}Mn_{0.15}O_4$.

Table 5.4 Mössbauer parameters of $Co_{0.9}Cu_{0.1}Fe_2O_4$ and $Co_{0.9}Cu_{0.1}Fe_{1.85}Mn_{0.15}O_4$.

		FWHM (mm/s)	*IS* (δ) (mm/s)	*QS* (Δ) (mm/s)	*Hf* (T)	χ^2
$Co_{0.9}Cu_{0.1}Fe_2O_4$	Sextet A	0.53 ± 0.02	0.28 ± 0.01	-0.02 ± 0.02	49.6 ± 0.1	1.44
	Sextet B	0.53 ± 0.02	0.36 ± 0.01	-0.04 ± 0.02	52.2 ± 0.1	
$Co_{0.9}Cu_{0.1}Fe_{1.85}Mn_{0.15}O_4$	Sextet A	0.53 ± 0.02	0.28 ± 0.01	-0.01 ± 0.02	48.9 ± 0.1	1.46
	Sextet B	0.58 ± 0.02	0.34 ± 0.01	-0.03 ± 0.02	51.5 ± 0.1	

5.1.5 $Co_{0.9}Cu_{0.1}Fe_{1.85}In_{0.15}O_4$

The Mössbauer spectrum recorded for $Co_{0.9}Cu_{0.1}Fe_{1.85}In_{0.15}O_4$ at room temperature has been presented in Fig. 5.6 and the Mössbauer hyperfine parameters including *Hf*, *IS*, and *QS*are listed in Table 5.5. The spectrum fitted with two six-line hyperfine patterns suggested the ferrimagnetic nature of the material. Sextet A denotes the existence of Fe^{3+} ions at the A site and sextet B denotes the presence of Fe^{3+} ions at the B site. The sextets were labeled A and B based on the *IS* and *Hf* values which are generally higher for the B site. The *IS* at B site is more than at A site due to larger Fe-O bond length at B site [385]. The values of *IS* which are less than 0.5 mm/s indicate the presence of high spin Fe in 3+ oxidation state with the absence of Fe^{2+} species [383,384]. The *QS* values were close to zero which signifies the retained cubic symmetry between Fe^{3+} ions and its surrounding [246]. The value of *Hf* decreased at both A and B sites with In^{3+} ion substitution. The *Hf* value decreased due to the replacement of Fe^{3+} ions having a higher magnetic moment (5 μB) by a non-magnetic In^{3+} ion (0 μB) at the B site [127]. Substitution causes the accumulation of a large amount of non-magnetic ions at the B site which will give rise to additional In^{3+}–O–In^{3+}, and In^{3+}–O–Fe^{3+} interactions which are not as strong as the Fe^{3+}–O–Fe^{3+}interactions.

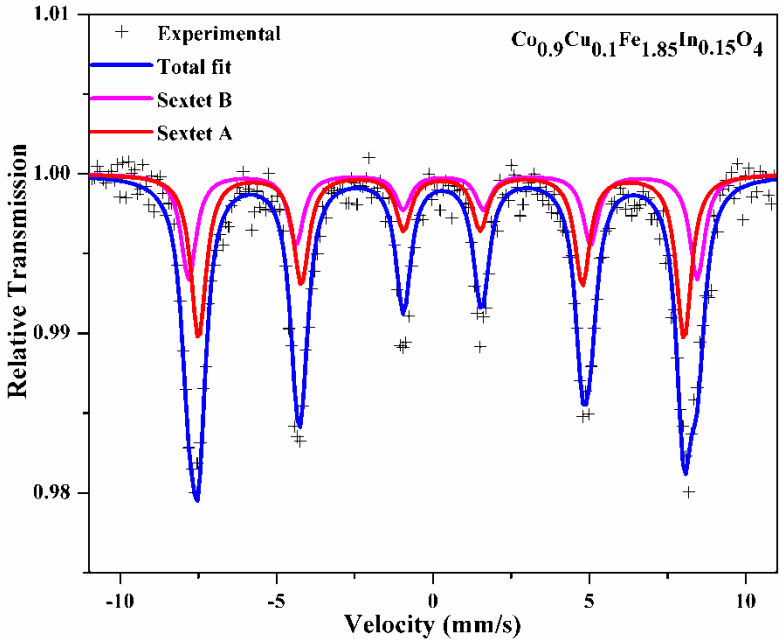

Fig. 5.6 *Room temperature Mössbauer spectrum for* $Co_{0.9}Cu_{0.1}Fe_{1.85}In_{0.15}O_4$.

Table 5.5 Mössbauer parameters of $Co_{0.9}Cu_{0.1}Fe_2O_4$ and $Co_{0.9}Cu_{0.1}Fe_{1.85}In_{0.15}O_4$.

		FWHM (mm/s)	*IS* (δ) (mm/s)	*QS* (Δ) (mm/s)	*Hf* (T)	χ^2
$Co_{0.9}Cu_{0.1}Fe_2O_4$	Sextet A	0.53 ± 0.02	0.28 ± 0.01	-0.02 ± 0.02	49.6 ± 0.1	1.44
	Sextet B	0.53 ± 0.02	0.36 ± 0.01	-0.04 ± 0.02	52.2 ± 0.1	
$Co_{0.9}Cu_{0.1}Fe_{1.85}In_{0.15}O_4$	Sextet A	0.58 ± 0.02	0.27 ± 0.01	0.02 ± 0.02	48.1 ± 0.1	1.52
	Sextet B	0.58 ± 0.02	0.33 ± 0.01	0.01 ± 0.02	50.4 ± 0.1	

5.2 Magnetic Studies

Magnetic studies were carried out on the prepared samples at 300 K, 50 K, and 5 K to determine the magnetic parameters like saturation magnetization (M_s), coercivity (H_c), remanant magnetization (M_r), etc.

5.2.1 $Co_{1-x}Cu_xFe_2O_4$ (where x = 0.00, 0.05, 0.1, 0.15, 0.20 and 0.25)

The field-dependent magnetization measurements for Cu^{2+} substituted $CoFe_2O_4$ at 300 K, and 50 K were performed to quantify the M_s and are displayed in Fig. 5.7 and 5.8

respectively. The other magnetic parameters like H_c andM_r were extracted from the hysteresis loop obtained from the M–H plots and are tabulated in Tables 5.6 and 5.7.

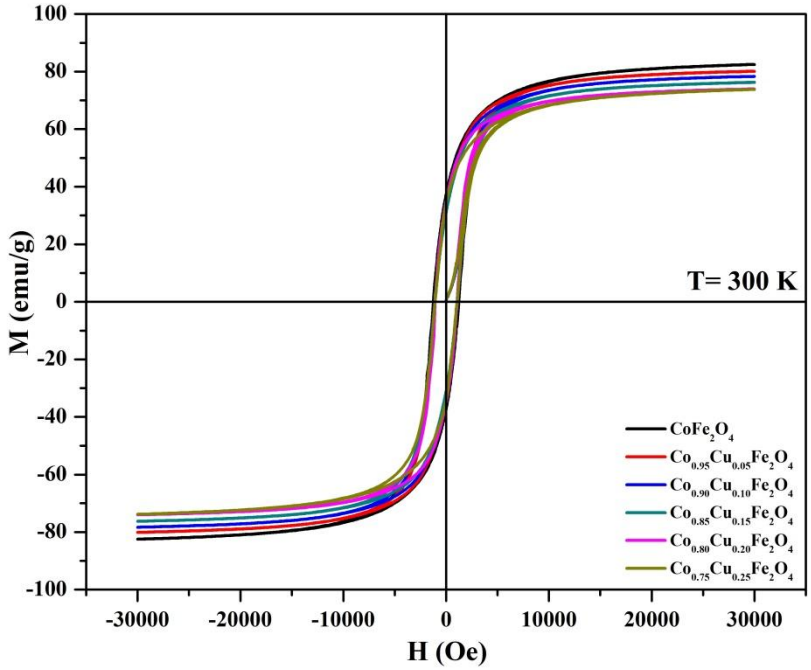

Fig. 5.7 *Magnetic hysteresis loops of $Co_{1-x}Cu_xFe_2O_4$ where x = 0.00, 0.05, 0.10, 0.15, 0.20 and 0.25 measured at 300 K.*

The magnetization measurements showed that the $M_s$values reduced marginally with increasing Cu^{2+} substitution in $CoFe_2O_4$ compared to the pristine $CoFe_2O_4$. In a cubic spinel system, the magnetic moment depends upon the net contribution of ions present at the tetrahedral (A) and octahedral (B) sub-lattices and their super-exchange interaction and the net magnetic moment is given by $M = M_B - M_A$, i.e., the difference in moments of B and A sub-lattices. Here, it can be inferred that as the Cu^{2+} concentration increases, the magnetization at the B site decreases and hence the net magnetization decreases. According to Neel's sub-lattice model, there are 3 types of interaction between these sites, such as A–A, B–B and A–B. The A–B interaction is very stronger when compared to the other 2 interactions. The replacement of Co^{2+} (3 μ_B) ions by Cu^{2+} ions (1

μ_B) having preferential octahedral site occupancy, results in the decline in the super-exchange interaction among octahedral and tetrahedral sites. The relocation of a small amount of Co^{2+} ions from B site to A site is anticipated which drives some of the Fe ions from the A site to occupy B site. Consequently, the overall magnetization decreases with the addition of Cu^{2+} ion. This behavior can be credited to the weaksuper-exchange interaction between octahedral and tetrahedral sites. The decrease in M_s with Cu^{2+} substitution has also been reported earlier in the literature [123,128,132,387].

Table 5.6 Magnetic properties of $Co_{1-x}Cu_xFe_2O_4$ (where x = 0.00, 0.05, 0.10, 0.15, 0.20, and 0.25) nanoparticles at 300 K.

Sample Composition	M_s (emu/g)	H_c (Oe)	M_r	M_r/M_s	n_B (μ_B)
$CoFe_2O_4$	82.58	1281.46	36.82	0.45	3.47
$Co_{0.95}Cu_{0.05}Fe_2O_4$	80.46	1193.3	32.35	0.40	3.38
$Co_{0.90}Cu_{0.10}Fe_2O_4$	78.75	1209.38	31.55	0.40	3.31
$Co_{0.85}Cu_{0.15}Fe_2O_4$	76.97	1177.34	32.13	0.42	3.24
$Co_{0.80}Cu_{0.20}Fe_2O_4$	74.40	1138.08	33.57	0.45	3.13
$Co_{0.75}Cu_{0.25}Fe_2O_4$	73.91	1121.28	33.86	0.46	3.12

The magnetization measurements at 300 K and 50 K indicated that with Cu^{2+} ion substitution, the H_c also declined when compared to the corresponding pure $CoFe_2O_4$. The decline in H_c can be assigned to the decrease in net magneto-crystalline anisotropysince the magnetic anisotropy of Cu^{2+} ions is smaller than that of the Co^{2+} ions [123,132,388]. This dilution of magnetic anisotropy reduces the H_c of the synthesized compositions.

The significant rise in M_s and H_c values observed at 50 K is a consequence of the proper alignment of the magnetic moments along the direction of the magnetic field due to the reduction in thermal vibrations. This, in turn, is disturbed at higher temperatures (at 300 K) due to the randomization of the magnetic moment by thermal vibrations [190].

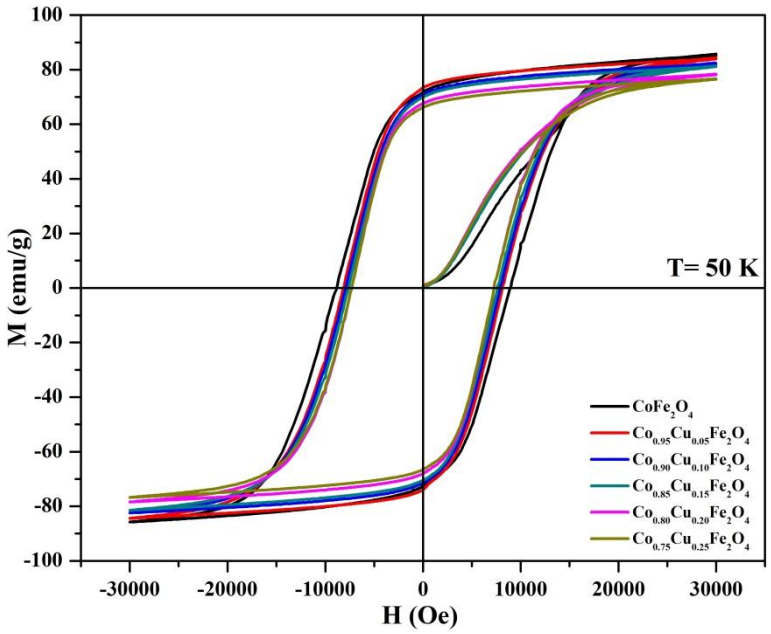

Fig. 5.8 *Magnetic hysteresis loops of $Co_{1-x}Cu_xFe_2O_4$ where x = 0.00, 0.05, 0.10, 0.15, 0.20 and 0.25 measured at 50 K.*

Table 5.7 Magnetic properties of $Co_{1-x}Cu_xFe_2O_4$ (where x = 0.00, 0.05, 0.10, 0.15, 0.20 and 0.25) nanoparticles at 50 K.

Sample Composition	M_s (emu/g)	H_c (Oe)	M_r	M_r/M_s	n_B (μ_B)
$CoFe_2O_4$	85.74	8882.14	71.87	0.84	3.60
$Co_{0.95}Cu_{0.05}Fe_2O_4$	84.36	8161.32	73.48	0.87	3.55
$Co_{0.90}Cu_{0.10}Fe_2O_4$	82.53	7913.04	70.90	0.86	3.47
$Co_{0.85}Cu_{0.15}Fe_2O_4$	81.32	7686.14	69.87	0.86	3.42
$Co_{0.80}Cu_{0.20}Fe_2O_4$	78.40	7632.72	67.69	0.86	3.31
$Co_{0.75}Cu_{0.25}Fe_2O_4$	76.52	7256.29	66.20	0.87	3.23

5.2.2 $CoFe_{2-x}Sb_xO_4$ (where x = 0.00, 0.03, 0.06, and 0.09)

Fig. 5.9 and 5.10 illustrate the detailed hysteresis loop for pristine and Sb^{3+} ion substituted $CoFe_2O_4$ at 300 K and 50 K respectively with a varying magnetic field up to 3 T. The magnetic parameters obtained from the hysteresis loop are listed in Table 5.8 and 5.9.

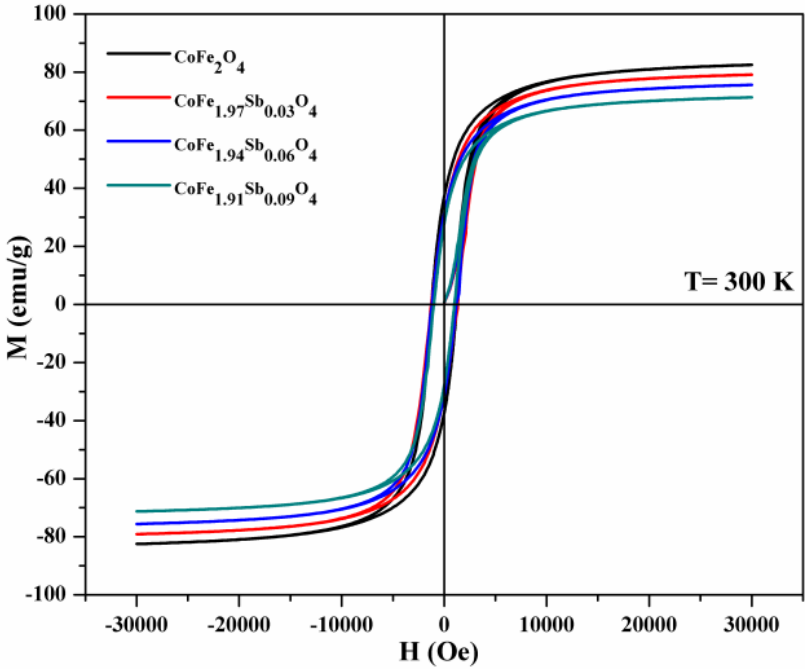

Fig. 5.9 *Magnetic hysteresis loops of $CoFe_{2-x}Sb_xO_4$ where x = 0.00, 0.03, 0.06 and 0.09 measured at 300 K.*

Table 5.8 Magnetic properties of $CoFe_{2-x}Sb_xO_4$ where x = 0.00, 0.03, 0.06 and 0.09 at 300 K.

Sample Composition	M_s (emu/g)	H_c (Oe)	M_r	M_r/M_s	n_B (μ_B)
$CoFe_2O_4$	82.58	1281.46	36.82	0.45	3.47
$CoFe_{1.97}Sb_{0.03}O_4$	79.08	1300.25	30.95	0.39	3.35
$CoFe_{1.94}Sb_{0.06}O_4$	75.59	1187.58	31.18	0.41	3.23
$CoFe_{1.91}Sb_{0.09}O_4$	71.24	1000.50	28.07	0.39	3.07

As the Sb^{3+} content increased, an overall trend of decreasing M_s was observed. The $M_s$values reduced from 82.58 to 71.24 emu/g at 300 K while a reduction from 85.74 to 75.37 emu/g was observed at 50 K. The obtained values of M_s and H_c in Sb^{3+} substituted $CoFe_2O_4$ was found to be greater than reported by Anjum et al. [20,21]. The decrease in the M_s is explained on the basis of the rearrangement of cations in the A and B sites with substitution. As the non-magnetic Sb^{3+} ions have strong tendency to occupy the B site, it will drive some of the Fe^{3+} ions from the B site towards the A site, hence reducing the number of magnetic ions in the B sub-lattice [157]. Consequently, the contribution for magnetization from the B site (*MB*) gets reduced and A site (*MA*) gets enhanced, hence the net magnetization (*M*) obtained by deducting the magnetic moments of sub-lattice A from sub-lattice B gets diminished ($M = |MB - MA|$). A decline in $M_s$with antimony ion substitution in spinel ferrite was also reported by Sridhar et al. [153], Lakshmi et al. [154], and Praveena et al. [152].

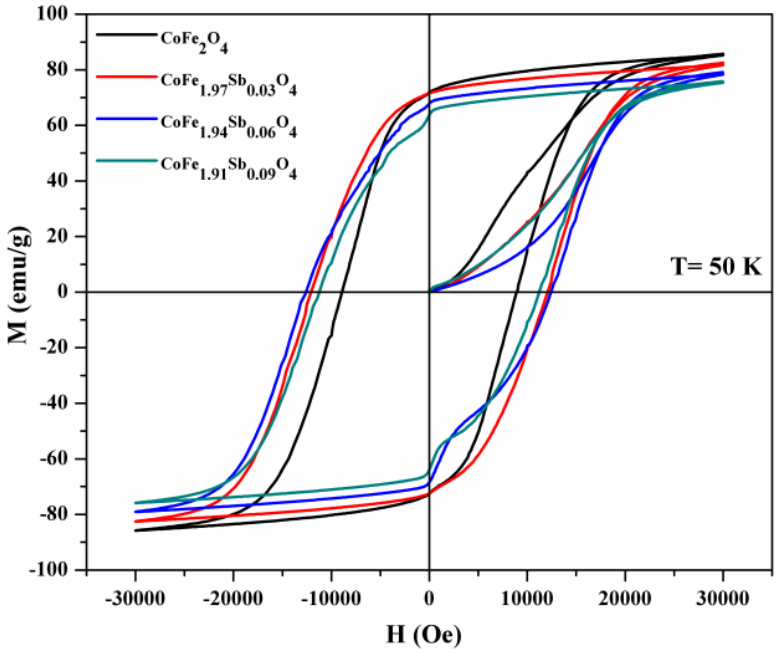

Fig. 5.10.*Magnetic hysteresis loops of $CoFe_{2-x}Sb_xO_4$ where x = 0.00, 0.03, 0.06 and 0.09measured at 50 K.*

It was noticed that the overall H_c decreased with the introduction of Sb^{3+} ions at 300 K while an increasing trend in H_c with Sb^{3+} substitution was observed at 50 K. The H_c depends on various factors like magneto-crystalline anisotropy, grain size, strain, defect, and porosity of the material [389,390]. Considerable enhancement in magnetic properties observed at 50 K can be due to proper alignment of magnetic moments along the direction of the magnetic field due to reduced thermal fluctuations.

Table 5.9 Magnetic properties of $CoFe_{2-x}Sb_xO_4$ where x = 0.00, 0.03, 0.06 and 0.09 at 50 K.

Sample Composition	M_s (emu/g)	H_c (Oe)	M_r	M_r/M_s	n_B (μ_B)
$CoFe_2O_4$	85.74	8882.14	71.87	0.84	3.60
$CoFe_{1.97}Sb_{0.03}O_4$	81.74	12074.35	71.67	0.88	3.46
$CoFe_{1.94}Sb_{0.06}O_4$	78.33	12553.69	68.22	0.87	3.35
$CoFe_{1.91}Sb_{0.09}O_4$	75.37	11232.50	63.81	0.85	3.25

5.2.3 $Co_{0.9}Cu_{0.1}Fe_{2-x}RE_xO4$ (where RE = Gd, Sm, Dy, Yb, Eu and x = 0.00, 0.03, 0.05)

The magnetic behavior with respect to the applied field (3 T) for RE^{3+} substituted Co-Cu ferrite at 300 K and 50 K is displayed in Fig. 5.11 and Fig. 5.12 respectively. The variation in M_s, H_c, and M_r at 300 K and 50 K with RE^{3+} substitution are extracted from the hysteresis loops (M-H plots) and is provided in Table 5.10 and 5.11. As can be seen in Fig. 5.11 and 5.12 the magnetization of all the compositions increases with increasing applied magnetic field and approaches saturation value. The increment of RE^{3+} substitution in Fe^{3+} site lowered the $M_s$whileH_c of the samples increased. The $M_s$values were in the range of 69.63 – 78.35 emu/g at 300 K and 74.53 – 84.65 emu/g, at 50 K while the H_c values varied from 1145.30 – 1433.63 Oe at 300 K and 7961.09 - 10876.42 Oe at 50 K. The decrease in $M_s$with improved H_c by addition of RE^{3+} ions has also been reported by Kakade et al., Avazpour et al., and Dascalu et al. [167,175,196].

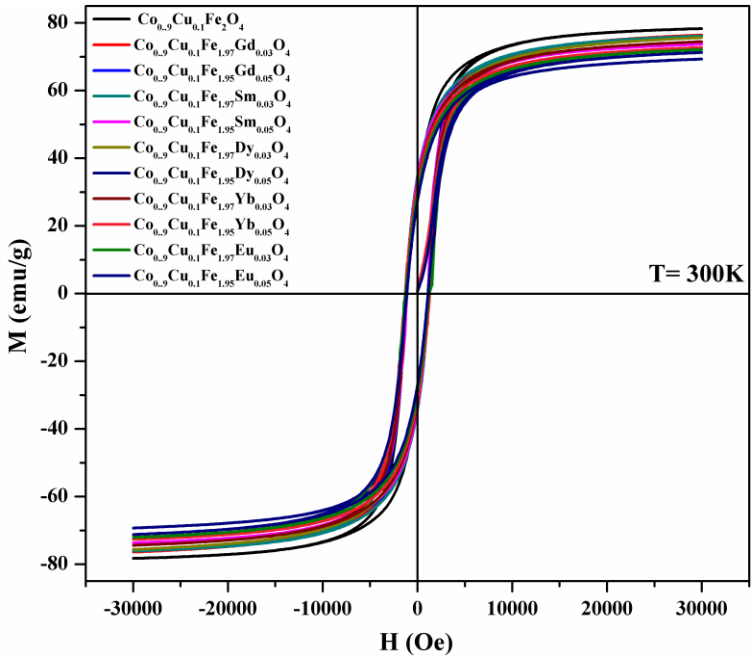

Fig. 5.11 *Magnetic hysteresis loops of $Co_{0.9}Cu_{0.1}Fe_{2-x}RE_xO_4$ (where RE = Gd, Sm, Dy, Yb, Eu and x = 0.00, 0.03 and 0.05) at 300 K.*

Table 5.10Magnetic properties of $Co_{0.9}Cu_{0.1}Fe_{2-x}RE_xO_4$ (where RE = Gd, Sm, Dy, Yb, Eu and x = 0.00, 0.03 and 0.05) at 300 K.

Sample Composition	300 K				
	M_s (emu/g)	M_r (emu/g)	H_c (Oe)	M_r/M_s	n_B (μ_B)
$Co_{0.9}Cu_{0.1}Fe_2O_4$	78.35	31.90	1145.30	0.40	3.29
$Co_{0.9}Cu_{0.1}Fe_{1.97}Gd_{0.03}O_4$	76.49	32.78	1329.51	0.43	3.26
$Co_{0.9}Cu_{0.1}Fe_{1.95}Gd_{0.05}O_4$	74.02	34.02	1249.42	0.46	3.18
$Co_{0.9}Cu_{0.1}Fe_{1.97}Sm_{0.03}O_4$	76.13	34.02	1265.44	0.45	3.24
$Co_{0.9}Cu_{0.1}Fe_{1.95}Sm_{0.05}O_4$	74.02	33.29	1177.34	0.45	3.18
$Co_{0.9}Cu_{0.1}Fe_{1.97}Dy_{0.03}O_4$	75.77	30.87	1225.40	0.41	3.23
$Co_{0.9}Cu_{0.1}Fe_{1.95}Dy_{0.05}O_4$	69.63	29.89	1233.50	0.43	3.00
$Co_{0.9}Cu_{0.1}Fe_{1.97}Yb_{0.03}O_4$	74.72	29.32	1169.34	0.39	3.19
$Co_{0.9}Cu_{0.1}Fe_{1.95}Yb_{0.05}O_4$	73.08	27.34	1433.63	0.37	3.15
$Co_{0.9}Cu_{0.1}Fe_{1.97}Eu_{0.03}O_4$	72.40	29.32	1241.19	0.40	3.09
$Co_{0.9}Cu_{0.1}Fe_{1.95}Eu_{0.05}O_4$	71.10	27.34	1150.73	0.38	3.05

The slight reduction in $M_s$is because of probable shifting of magnetically crucial Co^{2+} ions ($3d^7$) from the B to the A site in the ferrite lattice [190]. Also, a decrease in

$M_s$with increasing RE^{3+}content could be due to weak A-B super-exchange interactions developed due to the presence of RE^{3+}–O–Fe^{3+} and RE^{3+}–O–RE^{3+} interactions as they are very weak compared to Fe^{3+}–O–Fe^{3+} interaction. Hence introducing RE^{3+} can be considered as a non-magnetic ion substitution in spinel site which dilutes the exchange interaction between A and B sites that results in a decrease of the net magnetic moment.

In addition, the decrease in grain size also adds on to the reduction in magnetization. Smaller magnetic particles exhibit a greater surface effect, which causes a non-co-linearity of magnetic moments on their surfaces and breaks the exchange bonds at the external layer of the particles [391]. Theoretically, with the substitution of magnetic RE ions for Fe^{3+} is expected to enhance the magnetization. Though, in the present instance, it is noted that the M_s decreases with increase in RE^{3+} substitution.

The magnetic studies also show an enhancement in H_c value with RE substitution. The improved H_c with RE substitution compared to pristine Co-Cu ferrite is ascribed to the large single-ion anisotropy of RE ions. A larger magnetic anisotropy gives rise to larger H_c when RE ions partially replace Fe^{3+} ions. The magnetic anisotropy in materials which depends on the strength of spin-orbital coupling (L-S coupling) is usually much stronger in RE metal ions than in first-row transition metal ions. Similar results wherein they claimed an increase of H_c by RE ion substitution were reported by several authors [175,183,392]. The enhanced H_c with Gd^{3+} substitution at the octahedral site of the spinel ferrite is difficult to explain since Gd^{3+} ion has the orbital angular momentum of zero. But it has been observed by Calhoun that Gd^{3+} ions do contribute to the anisotropy of GdIG garnet [393]. Similar results were obtained by Cheng et al., Joshi et al., Amiri et al., and Zhao et al. wherein they reported a rise in H_c with Gd^{3+} substitution in the spinel

ferrites [159,183,394–396]. Thus it can be suggested that the Gd^{3+} ions contribute to the anisotropy of the spinel ferrite. Also, the proper incorporation of Gd^{3+} ions in the parent spinel ferrite results in lattice distortion and induces strain in the material which can lead to large magnetocrystalline anisotropy [159].

The values obtained by us for RE substituted $CoFe_2O_4$ were much higher than reported by Kumar et al. (28.00 emu/g, 1080.00 Oe) [397] , Virlan et al. (51.80 emu/g, 584.00 Oe) [161], Avazpour et al. (54.90 emu/g, 869.00 Oe) [167], Montemayor et al. (65.80 emu/g, 892.00 Oe) [160], Nikumbh et al. (61.60 emu/g, 509.00 Oe) [398], Bulai et al. (70.60 emu/g, 404.00 Oe) and (66.30 emu/g, 391.00 Oe) [172], Karimi et al. (56.79 emu/g, 785.13 Oe) and (54.67 emu/g, 793.99 Oe) [188]and Kambale et al. (57.19 emu/g, 1046.78 Oe) [351] for RE substituted $CoFe_2O_4$. The higher $H_c$values indicate that the prepared material can be employed for applications in recording media.

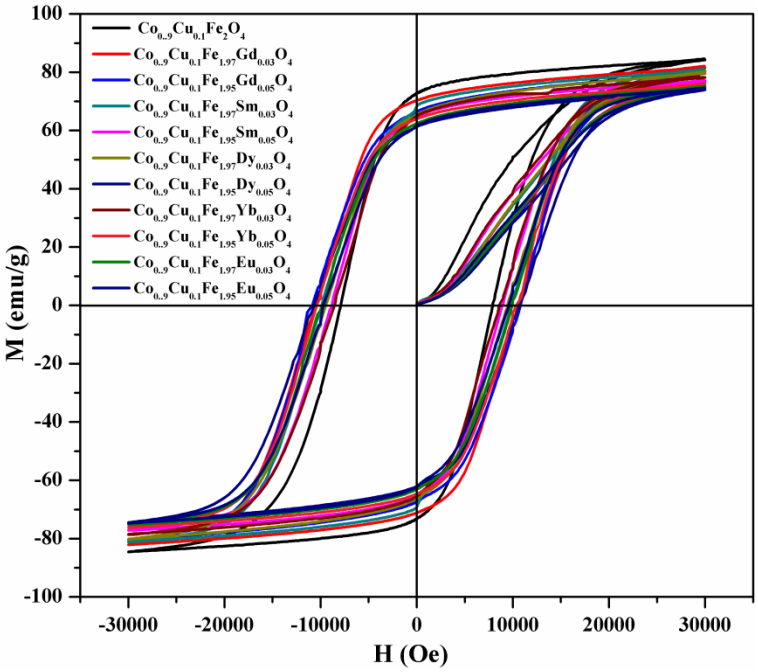

Fig. 5.12 *Magnetic hysteresis loops of $Co_{0.9}Cu_{0.1}Fe_{2-x}RE_xO_4$ (where RE = Gd, Sm, Dy, Yb, and Eu and x = 0.00, 0.03 and 0.05) at 50 K.*

The magnetization studies carried out at 50 K showed a substantial rise in the magnetic properties. The enhancement of these values is due to the systematic allignment of the magnetic moments along the direction of the magnetic field caused by the decrease of thermal vibrations.

Table 5.11 Magnetic properties of $Co_{0.9}Cu_{0.1}Fe_{2-x}RE_xO_4$ (where RE = Gd, Sm, Dy, Yb, and Eu and x = 0.00, 0.03 and 0.05) at 50 K.

Sample Composition	50 K				
	M_s (emu/g)	M_r (emu/g)	H_c (Oe)	M_r/M_s	n_B (μ_B)
$Co_{0.9}Cu_{0.1}Fe_2O_4$	84.65	72.68	7961.09	0.86	3.56
$Co_{0.9}Cu_{0.1}Fe_{1.97}Gd_{0.03}O_4$	82.13	70.27	10580.68	0.86	3.50
$Co_{0.9}Cu_{0.1}Fe_{1.95}Gd_{0.05}O_4$	80.35	66.60	10876.42	0.83	3.45
$Co_{0.9}Cu_{0.1}Fe_{1.97}Sm_{0.03}O_4$	81.09	66.49	9835.23	0.82	3.45
$Co_{0.9}Cu_{0.1}Fe_{1.95}Sm_{0.05}O_4$	77.21	64.69	8914.18	0.84	3.31
$Co_{0.9}Cu_{0.1}Fe_{1.97}Dy_{0.03}O_4$	79.89	65.40	9474.82	0.82	3.41
$Co_{0.9}Cu_{0.1}Fe_{1.95}Dy_{0.05}O_4$	74.53	61.13	10708.23	0.82	3.21
$Co_{0.9}Cu_{0.1}Fe_{1.97}Yb_{0.03}O_4$	78.63	65.05	8752.50	0.83	3.35
$Co_{0.9}Cu_{0.1}Fe_{1.95}Yb_{0.05}O_4$	76.42	63.87	10596.12	0.84	3.30
$Co_{0.9}Cu_{0.1}Fe_{1.97}Eu_{0.03}O_4$	75.46	62.56	9891.07	0.83	3.21
$Co_{0.9}Cu_{0.1}Fe_{1.95}Eu_{0.05}O_4$	74.55	61.54	9667.04	0.82	3.20

5.2.4 $Co_{0.9}Cu_{0.1}Fe_{2-x}Cr_xO_4$ (where x = 0.00, 0.03, 0.06, 0.09, 0.12, and 0.15)

The field dependent magnetization plots for the entire series of Cr^{3+} substituted Co-Cu ferrites were recorded at 300 K and 50 K and is represented in Fig. 5.13 and 5.14 respectively. The values of M_s, H_c, M_r, M_r/M_s,andn_B are summarized in Table 5.12 and 5.13.

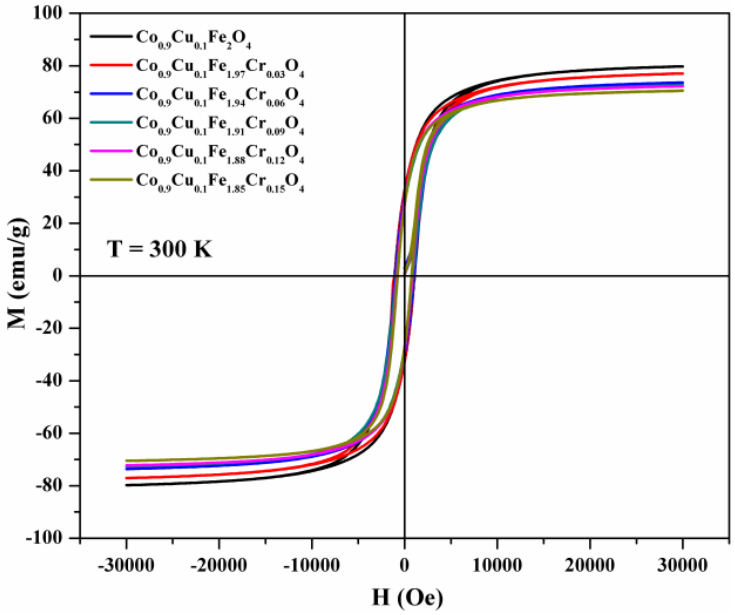

Fig. 5.13 *M-H plots for$Co_{0.9}Cu_{0.1}Fe_{2-x}Cr_xO_4$ (where x = 0.00, 0.03, 0.06, 0.09, 0.12, and 0.15) at 300 K.*

Table 5.12 Magnetic properties of $Co_{0.9}Cu_{0.1}Fe_{2-x}Cr_xO_4$ (where x = 0.00, 0.03, 0.06, 0.09, 0.12, and 0.15) at 300 K.

Sample Composition	300 K				
	M_s (emu/g)	M_r (emu/g)	H_c (Oe)	M_r/M_s	n_B (μ_B)
$Co_{0.9}Cu_{0.1}Fe_2O_4$	79.86	32.08	1209.38	0.40	3.36
$Co_{0.9}Cu_{0.1}Fe_{1.97}Cr_{0.03}O_4$	77.10	32.20	1201.37	0.42	3.24
$Co_{0.9}Cu_{0.1}Fe_{1.94}Cr_{0.06}O_4$	73.65	29.77	1121.28	0.48	3.10
$Co_{0.9}Cu_{0.1}Fe_{1.91}Cr_{0.09}O_4$	72.75	27.85	1033.18	0.40	3.06
$Co_{0.9}Cu_{0.1}Fe_{1.88}Cr_{0.12}O_4$	72.18	28.47	945.08	0.39	3.03
$Co_{0.9}Cu_{0.1}Fe_{1.85}Cr_{0.15}O_4$	70.48	27.11	889.01	0.39	3.00

It was noticed that the $M_s$values decreased from 79.86 to 70.48 emu/g at 300 K and from 82.24 to 77.83 emu/g at 50 K with the increasing Cr^{3+} ion substitution in the host lattice. The decrease in M_s with Cr^{3+} ion concentration can be due to the preferential B site occupancyof these ions since the overall magnetization in spinel ferrite is dependent on the magnetic strength of the metal ions residing in the B site [209]. Thus,

the lowering of M_s is credited to the fractional replacement of Fe^{3+} ions having a higher magnetic moment (5 μB) by magnetically weak Cr^{3+} (3 μB) ions at the B sub-lattice in the ferrite structure. In addition to this, with the introduction of Cr^{3+}ions, there occurs weakening of A-B exchange interactions due to which the ferrimagnetic ordering get shattered and generates magnetic frustration which decreases the M_s[204,399]. However, the values of M_s obtained by us were much higher than reported by Kumar et al. [203] and Vadivel et al. [199] for Cr^{3+} substituted $CoFe_2O_4$.

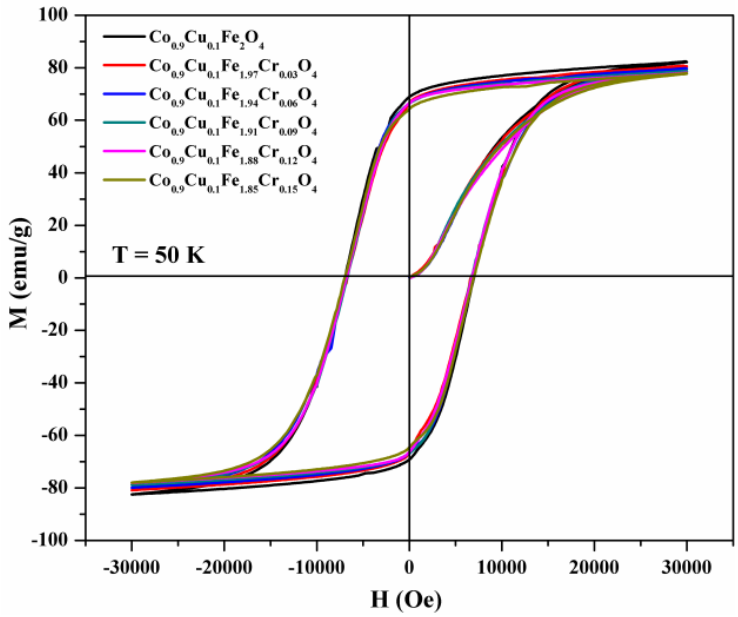

Fig. 5.14 *M-H plots for$Co_{0.9}Cu_{0.1}Fe_{2-x}Cr_xO_4$ (where x = 0.00, 0.03, 0.06, 0.09, 0.12, and 0.15) at 50 K.*

From Table 5.12 and 5.13, it is evident that H_c values decreased from 1209.38 to 889.01 Oe at 300 K and from 7104.11 Oe to 6831.80 Oe at 50 K with Cr^{3+} substitution. The decrease in H_c with increasing chromium content could be credited to the reduction in magnetocrystalline anisotropy; since chromium, ferrites comprise of negative magnetocrystalline anisotropy [400,401]. The M-H curves at 50 K showed a similar trend

in both M_s and H_c values, however, an appreciable enhancement was observed in comparison to 300 K (Table 5.12). The decrease in thermal vibrations can be accounted for the considerable enhancement in the magnetic properties at 50 K [190].

Table 5.13 Magnetic properties of $Co_{0.9}Cu_{0.1}Fe_{2-x}Cr_xO_4$ (where x = 0.00, 0.03, 0.06, 0.09, 0.12, and 0.15) at 50 K.

Sample Composition	50 K				
	M_s (emu/g)	M_r (emu/g)	H_c (Oe)	M_r/M_s	n_B (μ_B)
$Co_{0.9}Cu_{0.1}Fe_2O_4$	82.24	68.84	7104.11	0.83	3.46
$Co_{0.9}Cu_{0.1}Fe_{1.97}Cr_{0.03}O_4$	80.60	66.69	6839.81	0.83	3.39
$Co_{0.9}Cu_{0.1}Fe_{1.94}Cr_{0.06}O_4$	79.64	66.63	7024.05	0.84	3.35
$Co_{0.9}Cu_{0.1}Fe_{1.91}Cr_{0.09}O_4$	78.80	66.47	6831.80	0.84	3.31
$Co_{0.9}Cu_{0.1}Fe_{1.88}Cr_{0.12}O_4$	78.29	66.35	6911.89	0.85	3.29
$Co_{0.9}Cu_{0.1}Fe_{1.85}Cr_{0.15}O_4$	77.83	64.26	7096.10	0.83	3.27

5.2.5 $Co_{0.9}Cu_{0.1}Fe_{2-x}Mn_xO_4$ (where x = 0.00, 0.03, 0.06, 0.09, 0.12, and 0.15)

The Magnetic hysteresis loops at 300 K and 50 K of the Co-Cu ferrite and Mn ion substituted Co-Cu ferrite have been shown in Fig. 5.15 and Fig. 5.16 respectively.

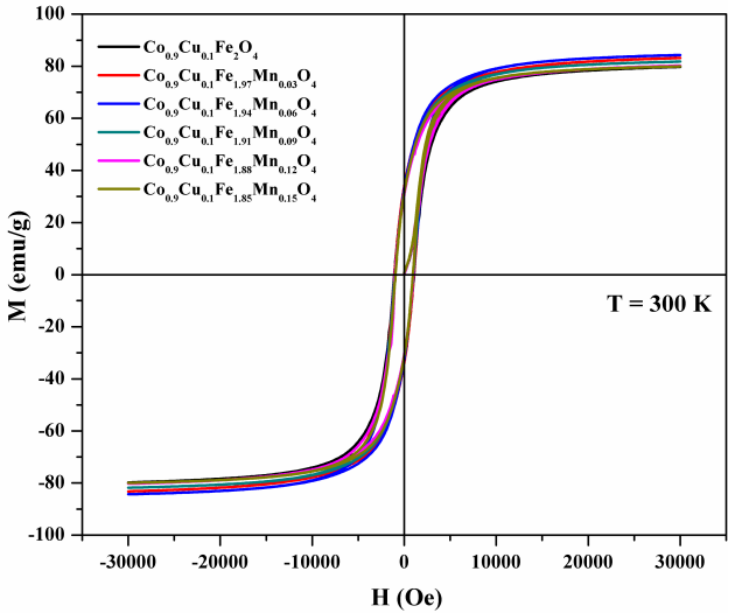

***Fig. 5.15** M-H plots for $Co_{0.9}Cu_{0.1}Fe_{2-x}Mn_xO_4$ (where x = 0.00, 0.03, 0.06, 0.09, 0.12, and 0.15) at 300 K.*

The magnetic parameters such as M_s, M_r, H_c, and M_r/M_s are listed in Table 5.14 and 5.15. It is obvious from the Tables that the $M_s$values increased initially with Mn substitution up to x = 0.06 and then decreased with further increase in Mn content up to x = 0.15. At 300 K the $M_s$values increased from 79.86 emu/g to 84.28 emu/g and further decreased to 79.92 emu/g. At 50 K M_s showed a similar trend where it increased from 82.24 emu/g to 87.98 emu/g and further decreased to 84.62 emu/g.

Table 5.14 Magnetic properties of $Co_{0.9}Cu_{0.1}Fe_{2-x}Mn_xO_4$ (where x = 0.00, 0.03, 0.06, 0.09, 0.12, and 0.15) at 300 K.

Sample Composition	300 K				
	M_s (emu/g)	M_r (emu/g)	H_c (Oe)	M_r/M_s	n_B (μ_B)
$Co_{0.9}Cu_{0.1}Fe_2O_4$	79.86	32.08	1209.38	0.40	3.36
$Co_{0.9}Cu_{0.1}Fe_{1.97}Mn_{0.03}O_4$	83.14	33.56	1185.35	0.40	3.36
$Co_{0.9}Cu_{0.1}Fe_{1.94}Mn_{.06}O_4$	84.28	32.65	1153.31	0.39	3.55
$Co_{0.9}Cu_{0.1}Fe_{1.91}Mn_{0.09}O_4$	81.85	31.30	1129.29	0.38	3.44
$Co_{0.9}Cu_{0.1}Fe_{1.88}Mn_{0.12}O_4$	80.26	30.45	1153.31	0.38	3.38
$Co_{0.9}Cu_{0.1}Fe_{1.85}Mn_{0.15}O_4$	79.92	31.35	1089.24	0.39	3.36

At lower concentration, the substituent Mn ions have a high tendency to occupy the B site. In the present case initially, the highly magnetic Mn^{2+} (5 μB) ions could have occupied the B site displacing some of the Fe^{3+} (5 μB) ions to the A site. This results in an increase in magnetization at B site which increases the overall magnetization (M = $|M_B-M_A|$). At higher concentration (i.e. x = 0.09 – 0.15) there could be the presence of less magnetic Mn^{3+} (4 μ_B) ions at the B site in addition to Mn^{2+} ion (5 μ_B) as indicated by XPS analysis so the net magnetization gets reduced. Previous reports by Tsay et al. [227], Ramana et al. [232], and Bhame et al. [231] also showed similar trends with Mn ion substitution in $CoFe_2O_4$.

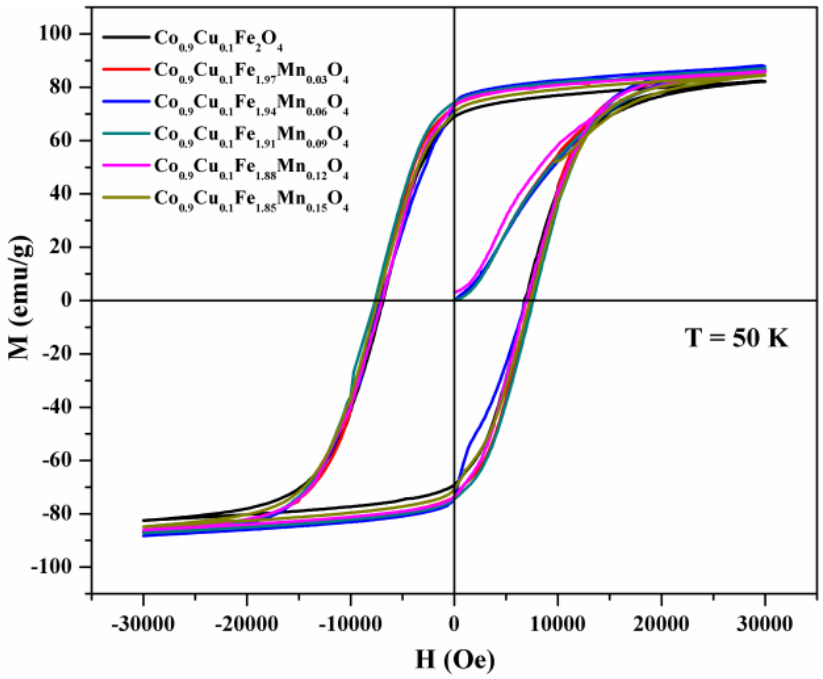

Fig. 5.16 *M-H plots for* $Co_{0.9}Cu_{0.1}Fe_{2-x}Mn_xO_4$ *(where x = 0.00, 0.03, 0.06, 0.09, 0.12, and 0.15) at 50 K.*

Table 5.15 Magnetic properties of $Co_{0.9}Cu_{0.1}Fe_{2-x}Mn_xO_4$ (where x = 0.00, 0.03, 0.06, 0.09, 0.12, and 0.15) at 50 K.

Sample Composition	50 K				
	M_s (emu/g)	M_r (emu/g)	H_c (Oe)	M_r/M_s	n_B (μ_B)
$Co_{0.9}Cu_{0.1}Fe_2O_4$	82.24	68.84	7104.11	0.83	3.46
$Co_{0.9}Cu_{0.1}Fe_{1.97}Mn_{0.03}O_4$	86.61	72.80	7408.46	0.84	3.64
$Co_{0.9}Cu_{0.1}Fe_{1.94}Mn_{.06}O_4$	87.98	73.18	7104.11	0.83	3.70
$Co_{0.9}Cu_{0.1}Fe_{1.91}Mn_{0.09}O_4$	86.92	74.30	7744.85	0.85	3.66
$Co_{0.9}Cu_{0.1}Fe_{1.88}Mn_{0.12}O_4$	85.87	73.18	7128.14	0.85	3.61
$Co_{0.9}Cu_{0.1}Fe_{1.85}Mn_{0.15}O_4$	84.62	70.50	7464.52	0.83	3.56

As can be seen from the Table 5.15 the H_c of the samples decreased with Mn ion substitution at 300 K. Whereas an increase in *Hc* values compared to Co-Cu ferrite with Mn ion substitution were observed at 50 K. The magnetic H_c is influenced by several

aspects like magnetocrystalline anisotropy, microstrain, size distribution and magnetic domain size [224,227,229,231,232].

5.2.6 $Co_{0.9}Cu_{0.1}Fe_{2-x}In_xO_4$ (where x = 0.00, 0.03, 0.06, 0.09, 0.12, and 0.15)

Magnetization curves of the sintered In^{3+} substituted and unsubstituted Co-Cu ferrite samples measured at 300 K and 5 K by applying a field of 5 T is shown in Fig. 5.17. The magnetic parameters like M_s, H_c, and M_r are listed in Table 5.16 and 5.17. With the addition of In^{3+} ions in $Co_{0.9}Cu_{0.1}Fe_2O_4$, the net $M_s$value decreased from 78.12 emu/g to 70.19 emu/g at 300 K and 87.38 emu/g to 81.26 emu/g at 50 K which indicates that the non-magnetic In^{3+} ions could have occupied the B sub-lattice which forces cation rearrangement and brings about magnetic dilution.

When In^{3+} ions (0 μ_B) replace Fe^{3+} ions (5 μ_B) at the B site, there arise additional, In^{3+}-O-In^{3+}, In^{3+}-O-Fe^{3+} interactions which are much weaker than Fe^{3+}-O-Fe^{3+} interactions, hence the magnetization of B sub-lattice drops maintaining the magnetization of the tetrahedral site constant. Therefore, the net magnetization which is the differencein magnetization between the two sites ($M = |M_B-M_A|$) is expected to decrease. Similar results where a decrease in M_s with In^{3+} substitution in spinel ferrites was reported by Hashim et al. [236], Vlazan et al. [240], Nongjai et al. [250] and Shirsath et al. [243]. However,the values of M_s obtained by us were much higher than reported by Pandit et al. (63.44 emu/g), Vlazen et al. (49.00 emu/g), and Nongjai et al. (63.00 emu/g) [240,242,250]. Literature reports show that at lower concentrations, In^{3+} ions prefer to occupy the A sub-lattice by the replacement of Fe^{3+} ions and thereby enhance the net magnetization[241,248].

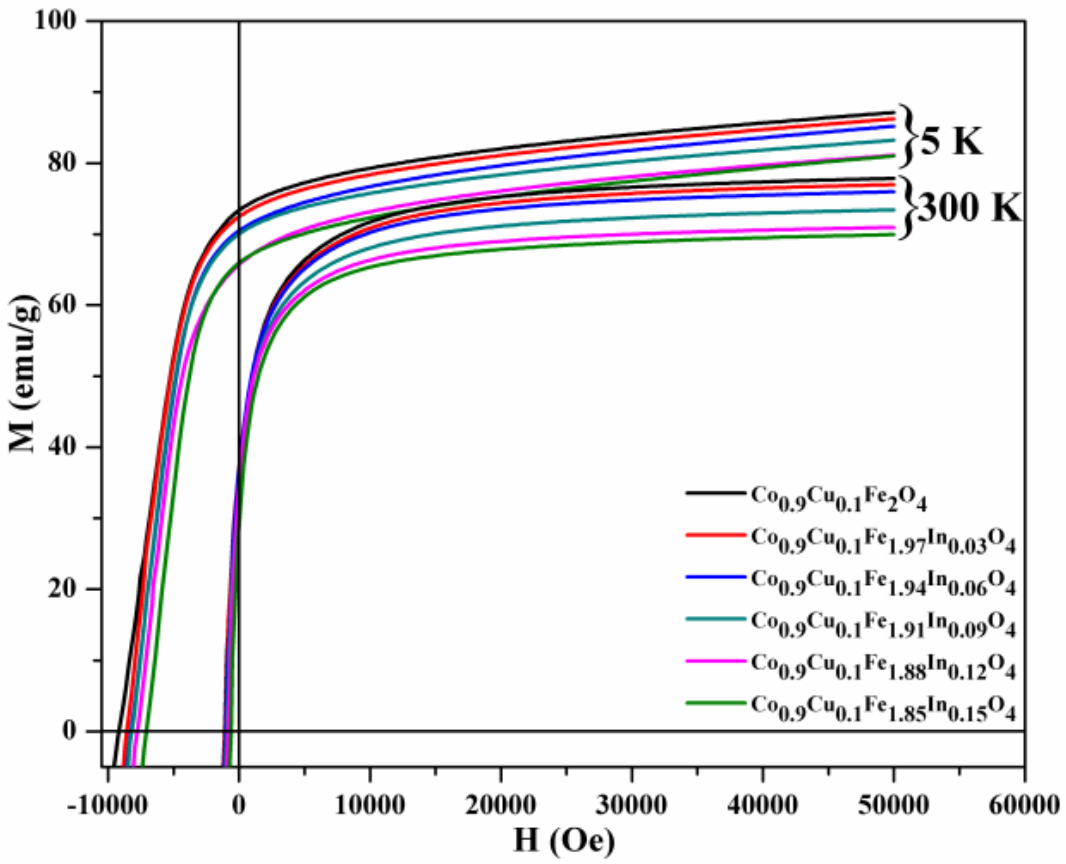

Fig. 5.17 *M-H plots for* $Co_{0.9}Cu_{0.1}Fe_{2-x}In_xO_4$ *(where x = 0.00, 0.03, 0.06, 0.09, 0.12, and 0.15) at 300 K and 5 K.*

It is clearly observed from Table 5.16 and 5.17 that the H_c of the material decreases gradually with substitution which could be due to dilution of magnetization upon the inclusion of non-magnetic Indium ions. The factors such as magneto-crystalline anisotropy, micro-strains, shape anisotropy, and magnetic domain size also influence H_c [389,390]. The decreasing nature of H_c with Indium substitution has been well narrated by Meng et al. [248]. However, the H_c values attained by us for In^{3+} substituted $Co_{0.9}Cu_{0.1}Fe_2O_4$ surpassed the literature reports [240,242].

Table 5.16 Magnetic properties of $Co_{0.9}Cu_{0.1}Fe_{2-x}In_xO_4$ (where x = 0.00, 0.03, 0.06, 0.09, 0.12, and 0.15) at 300 K.

Sample Composition	300 K				
	M_s (emu/g)	M_r (emu/g)	H_c (Oe)	M_r/M_s	n_B (μ_B)
$Co_{0.9}Cu_{0.1}Fe_2O_4$	78.12	36.94	1239.44	0.47	3.29
$Co_{0.9}Cu_{0.1}Fe_{1.97}In_{0.03}O_4$	77.23	37.03	1207.84	0.48	3.27
$Co_{0.9}Cu_{0.1}Fe_{1.94}In_{0.06}O_4$	76.19	36.79	1143.58	0.48	3.25
$Co_{0.9}Cu_{0.1}Fe_{1.91}In_{0.09}O_4$	73.69	34.27	1062.59	0.46	3.17
$Co_{0.9}Cu_{0.1}Fe_{1.88}In_{0.12}O_4$	71.20	34.42	965.25	0.48	3.09
$Co_{0.9}Cu_{0.1}Fe_{1.85}In_{0.15}O_4$	70.19	29.31	755.14	0.42	3.07

The M vs H studies carried out at 5 K exhibited a similar trend as that of 300 K but with considerably enhanced values. The enhancement in the values is due to decreased thermal vibrations at 5 K.

Table 5.17 Magnetic properties of $Co_{0.9}Cu_{0.1}Fe_{2-x}In_xO_4$ (where x = 0.00, 0.03, 0.06, 0.09, 0.12, and 0.15) at 5 K.

Sample Composition	5 K				
	M_s (emu/g)	M_r (emu/g)	H_c (Oe)	M_r/M_s	n_B (μ_B)
$Co_{0.9}Cu_{0.1}Fe_2O_4$	87.38	73.66	9338.41	0.84	3.68
$Co_{0.9}Cu_{0.1}Fe_{1.97}In_{0.03}O_4$	86.52	72.77	8709.65	0.84	3.67
$Co_{0.9}Cu_{0.1}Fe_{1.94}In_{0.06}O_4$	85.48	70.81	8402.12	0.83	3.65
$Co_{0.9}Cu_{0.1}Fe_{1.91}In_{0.09}O_4$	83.49	70.43	8338.45	0.84	3.59
$Co_{0.9}Cu_{0.1}Fe_{1.88}In_{0.12}O_4$	81.38	66.27	7902.87	0.81	3.53
$Co_{0.9}Cu_{0.1}Fe_{1.85}In_{0.15}O_4$	81.26	65.80	7225.73	0.81	3.55

5.3 AC- magnetic susceptibility

5.3.1 $Co_{1-x}Cu_xFe_2O_4$ (where x = 0.00, 0.05, 0.10, 0.15, 0.20 and 0.25)

Curie temperature (T_c) is an essential parameter in case of ferrites for applications based on magnetic properties. It mainly depends on the material composition. The

magnetic susceptibility of the sample with increasing temperature as a function of the magnetic field (5 kOe) has been illustrated in Fig. 5.18. The magnetization increased with rising temperature and attained a maximum at around 750 K. The position and intensity of the maxima varied depending on the Cu^{2+} content. This indicates that the magnetic ordering increases slightly attains a maximum and drops sharply at a specific temperature reaching the T_c.

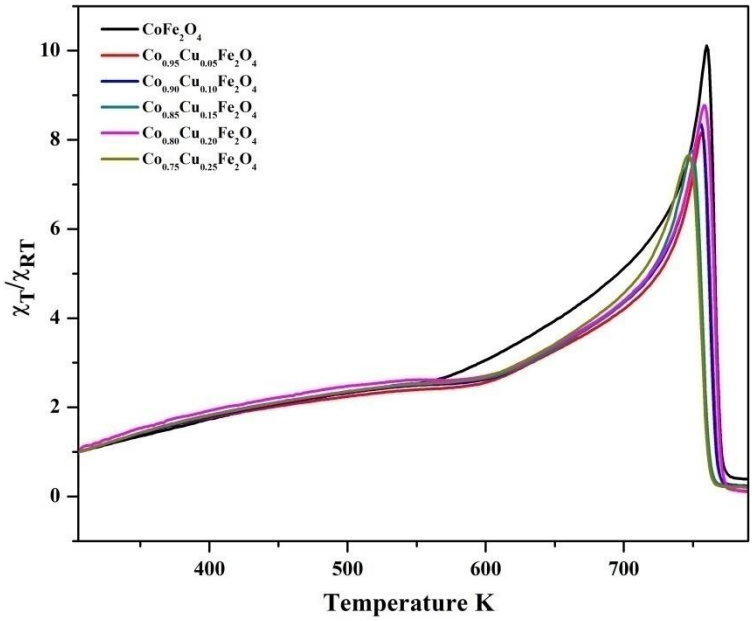

Fig. 5.18 *AC susceptibility plots for $Co_{1-x}Cu_xFe_2O_4$ (where x = 0.00, 0.05, 0.10, 0.15, 0.20 and 0.25).*

The exact values of $T_c$have been summarized in Table 5.18. After T_c, the material acts as a typical paramagnetic material. At T_c, thermal energy overshadows the exchange energy, and the crystal anisotropy becomes zero. Hence, there is no preferred crystallographic direction for the magnetization, and the material transforms to paramagnetic phase [402]. With the Cu^{2+}substitution, the T_c shifts to a lower temperature, as a result of the weakening in the strength of the ($Fe_{(A)}$–O–$Fe_{(B)}$) interaction with the migrationof small quantity of Co^{2+} ions from octahedral to the tetrahedral sites.

Table 5.18 Curie temperature obtained for the compounds from AC- Susceptibility measurements.

Sample Composition	Curie Temperature T_c (K)
$CoFe_2O_4$	780
$Co_{0.95}Cu_{0.05}Fe_2O_4$	779
$Co_{0.90}Cu_{0.10}Fe_2O_4$	779
$Co_{0.85}Cu_{0.15}Fe_2O_4$	778
$Co_{0.80}Cu_{0.20}Fe_2O_4$	772
$Co_{0.75}Cu_{0.25}Fe_2O_4$	770

5.3.2 $CoFe_{2-x}Sb_xO_4$ (where x = 0.00, 0.03, 0.06, and 0.09)

AC magnetic susceptibility plots for Sb^{3+} substituted $CoFe_2O_4$ have been given in Fig. 5.19, which shows that the susceptibility values increased gradually with increasing temperature,acquired a maximum value of ~740 K and then dropped sharply just before the T_c.

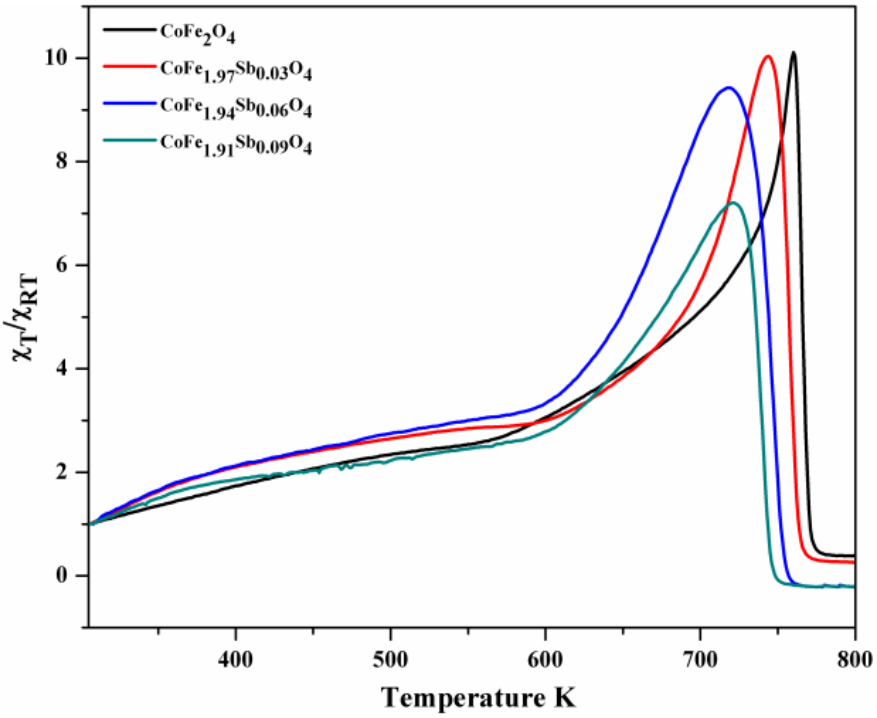

Fig. 5.19 *AC susceptibility plots for $CoFe_{2-x}Sb_xO_4$ (where x = 0.00, 0.03, 0.06, and 0.09).*

It was noticed that the T_c of the material declined with increasing Sb^{3+} ion concentration. The decrease in T_c can be due to weaker A-B interactions since the substitution of Sb^{3+} ions will establish weaker $Fe^{3+}{}_A$–O–$Sb^{3+}{}_B$ interactions in addition to the stronger $Fe^{3+}{}_A$–O–$Fe^{3+}{}_B$ interactions. The value of T_c decreased from 780 to 755 K with Sb^{3+} ion substitution (Table 5.19).

Table 5.19 Curie temperature obtained for the compounds from AC- Susceptibility measurements.

Sample Composition	Curie Temperature T_c (K)
$CoFe_2O_4$	780
$CoFe_{1.97}Sb_{0.03}O_4$	772
$CoFe_{1.94}Sb_{0.06}O_4$	764
$CoFe_{1.91}Sb_{0.09}O_4$	755

5.3.3 $Co_{0.9}Cu_{0.1}Fe_{2-x}RE_xO4$ (where RE = Gd, Sm, Dy, Yb, Eu, and x = 0.00, 0.03, 0.05)

Fig. 5.20 shows the response of magnetic susceptibility to the applied temperature for RE^{3+} substituted Co-Cu ferrite. It can be seen that initially as the temperature increased magnetization started increasing and reached a maximum value and there is a sharp fall just before the T_c. AboveT_c the material exhibits Paramagnetism. The sharp fall in magnetization after a sharp increase just before T_c is referred to as Hopkinson's effect. Hopkinson effect is shown by nano-crystalline single domain particles where the size of particles are neither very small to be super-paramagnetic nor very large to be multi-domain in nature [403].

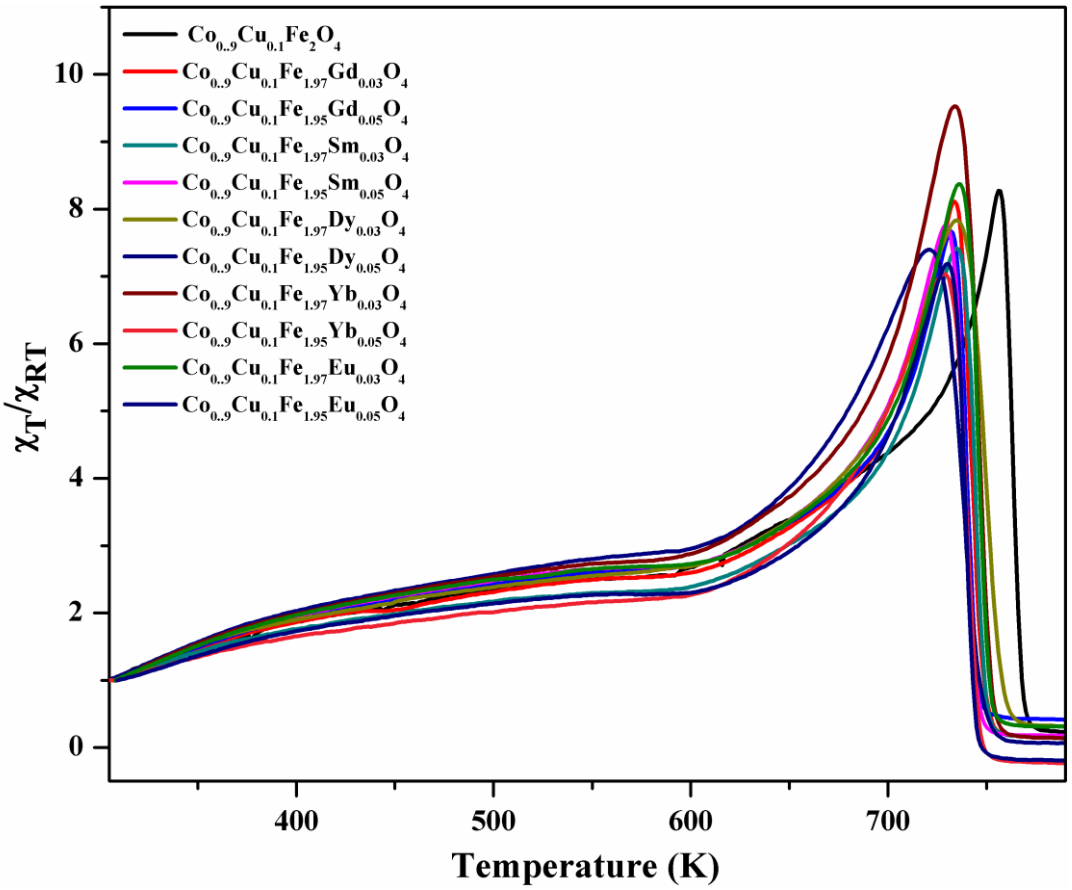

Fig. 5.20 *AC susceptibility plots for $Co_{0.9}Cu_{0.1}Fe_{2-x}RE_xO_4$ (where RE = Gd, Sm, Dy, Yb, and Eu and x = 0.00, 0.03 and 0.05).*

It was observed that with RE^{3+} substitution the $T_c$shifted to a lower temperature. The lowering of T_c with RE^{3+} substitution can be due to the dilution of exchange interactions (AB interactions). The exchange interactions are weakened due to RE-Fe interactions (3d-4f) occurred because of RE^{3+} substitution, since RE^{3+} has a larger ionic radius. The observed values of T_c range from 749 - 779 K (Table 5.20).

Table 5.20 Curie temperature (T_c) obtained for the compounds from AC- Susceptibility measurements.

Sample Composition	Curie Temperature T_c (K)
$Co_{0.9}Cu_{0.1}Fe_2O_4$	779
$Co_{0.9}Cu_{0.1}Fe_{1.97}Gd_{0.03}O_4$	758
$Co_{0.9}Cu_{0.1}Fe_{1.95}Gd_{0.05}O_4$	750
$Co_{0.9}Cu_{0.1}Fe_{1.97}Dy_{0.03}O_4$	764
$Co_{0.9}Cu_{0.1}Fe_{1.95}Dy_{0.05}O_4$	753
$Co_{0.9}Cu_{0.1}Fe_{1.97}Sm_{0.03}O_4$	754
$Co_{0.9}Cu_{0.1}Fe_{1.95}Sm_{0.05}O_4$	749
$Co_{0.9}Cu_{0.1}Fe_{1.97}Yb_{0.03}O_4$	765
$Co_{0.9}Cu_{0.1}Fe_{1.95}Yb_{0.05}O_4$	753
$Co_{0.9}Cu_{0.1}Fe_{1.97}Eu_{0.03}O_4$	760
$Co_{0.9}Cu_{0.1}Fe_{1.95}Eu_{0.05}O_4$	749

5.3.4 $Co_{0.9}Cu_{0.1}Fe_{2-x}Cr_xO_4$ (where x = 0.00, 0.03, 0.06, 0.09, 0.12, and 0.15)

The dependence of magnetic susceptibility on temperature for Cr^{3+} substituted Co-Cu ferrite has been shown in Fig. 5.21. A steady rise in magnetic susceptibility was observed with increasing temperature and a sharp maximum was recorded just before attaining the T_c(Fig. 5.21). The T_c was determined by extrapolating the linear segment of the curve touching the temperature axis. A persistent decrease in T_c from 779 K to 711 K was observed with increasing Cr^{3+} ion concentration which could be associated with weak exchange interactions evolved on the addition of Cr^{3+} ions. The substitution of magnetically weak Cr^{3+} ions in place of highly magnetic Fe^{3+} ions at B site gives rise to additional Cr^{3+}–O–Fe^{3+}, Cr^{3+}–O–Cr^{3+} exchange interactions which are weaker than already existing Fe^{3+}–O–Fe^{3+} exchange interactions [404,405]. The exact values of T_c for all the compositions have been listed in Table 5.21.

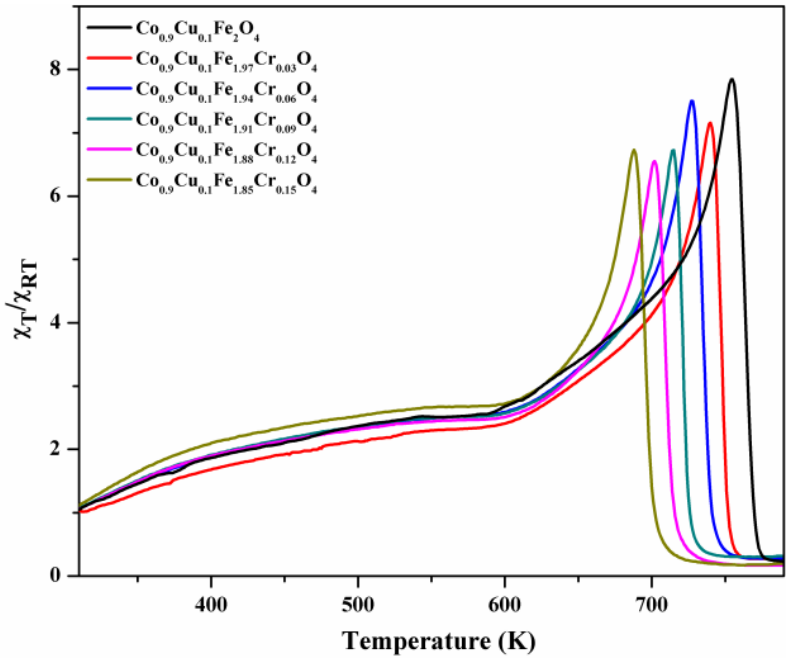

Fig. 5.21 *AC susceptibility plots for $Co_{0.9}Cu_{0.1}Fe_{2-x}Cr_xO_4$ (where x = 0.00, 0.03, 0.06, 0.09, 0.12, and 0.15).*

Table 5.21 Curie temperature (T_c) obtained for the compounds from AC- Susceptibility measurements.

Sample Composition	T_c (K)
$Co_{0.9}Cu_{0.1}Fe_2O_4$	779
$Co_{0.9}Cu_{0.1}Fe_{1.97}Cr_{0.03}O_4$	760
$Co_{0.9}Cu_{0.1}Fe_{1.94}Cr_{0.06}O_4$	749
$Co_{0.9}Cu_{0.1}Fe_{1.91}Cr_{0.09}O_4$	735
$Co_{0.9}Cu_{0.1}Fe_{1.88}Cr_{0.12}O_4$	726
$Co_{0.9}Cu_{0.1}Fe_{1.85}Cr_{0.15}O_4$	711

5.3.5 $Co_{0.9}Cu_{0.1}Fe_{2-x}Mn_xO_4$ (where x = 0.03, 0.06, 0.09, 0.12, and 0.15)

Fig. 5.22 shows the thermal variation of AC-magnetic susceptibility measured by applying a magnetic field of 5 kOe. It was noticed that initially with rising temperature magnetic susceptibility also increases steadily and after attaining a certain point it drops sharply to give a T_c. T_c was obtained by extrapolating the linear section of the falling

curve to intercept the temperature axis. After the T_c, the sample acts like a typical paramagnetic material.

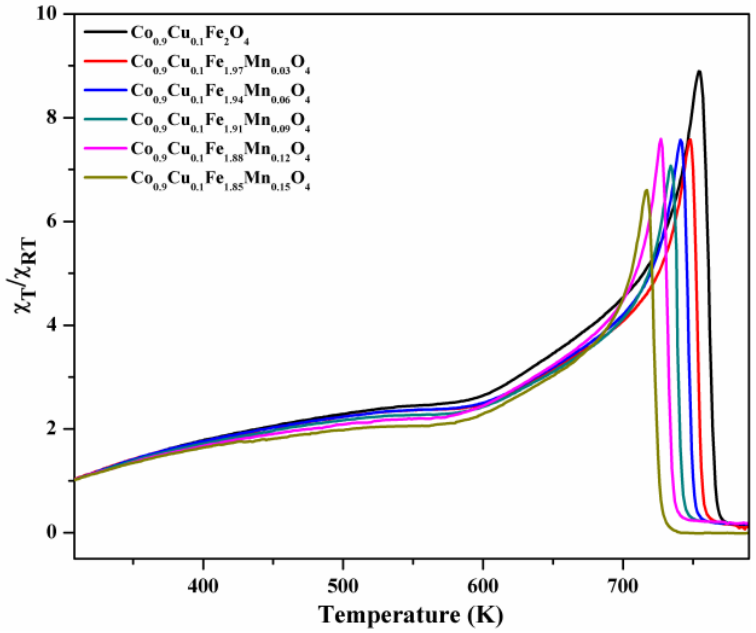

Fig. 5.22 *AC susceptibility plots for $Co_{0.9}Cu_{0.1}Fe_{2-x}Mn_xO_4$ (where x = 0.00, 0.03, 0.06, 0.09, 0.12, and 0.15).*

The T_c value declined from 779 K to 732 K (Table 5.22) with Mn ion substitution in Co-Cu ferrite. With the introduction of Mn ions, there will be additional weaker Mn-O-Mn, Mn-O-Fe interactions developed in addition to existing stronger Fe-O-Fe interactions. Since the T_c value depends on the strength of AB exchange interactions it decreases with Mn ion substitution in Co-Cu ferrite.

Table 5.22 Curie temperature (T_c) obtained for the compounds from AC- Susceptibility measurements.

Sample Composition	T_c (K)
$Co_{0.9}Cu_{0.1}Fe_2O_4$	779
$Co_{0.9}Cu_{0.1}Fe_{1.97}Mn_{0.03}O_4$	763
$Co_{0.9}Cu_{0.1}Fe_{1.94}Mn_{.06}O_4$	757
$Co_{0.9}Cu_{0.1}Fe_{1.91}Mn_{0.09}O_4$	749
$Co_{0.9}Cu_{0.1}Fe_{1.88}Mn_{0.12}O_4$	741
$Co_{0.9}Cu_{0.1}Fe_{1.85}Mn_{0.15}O_4$	732

5.3.6 $Co_{0.9}Cu_{0.1}Fe_{2-x}In_xO_4$ (where x = 0.00, 0.03, 0.06, 0.09, 0.12, and 0.15)

The AC-magnetic susceptibility studies at a constant field of 5 kOe showed that the magnetic susceptibility increased linearly with rising temperature and on reaching a certain point it drops sharply to attain a constant value. As can be seen from Fig. 5.23, the T_c decreased considerably with increased concentration of In^{3+} ions in the host material. The T_c value depends on the strength of exchange interactions in the two sub-lattices. The substantial decrease in T_c from 779 K to 707 K (Table 5.23) with Indium substitution can be explained on the basis of weaker exchange interactions developed in the material.

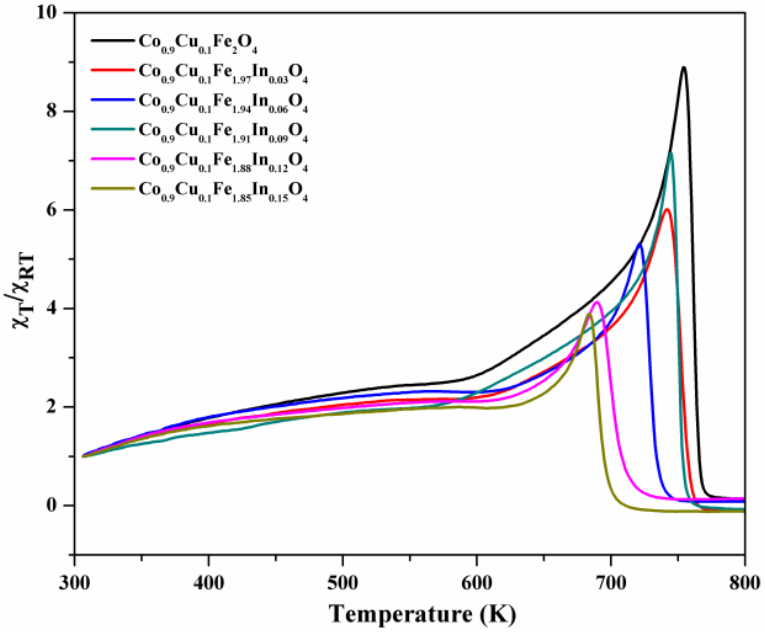

Fig. 5.23 *AC susceptibility plots for $Co_{0.9}Cu_{0.1}Fe_{2-x}In_xO_4$ (where x = 0.00, 0.03, 0.06, 0.09, 0.12, and 0.15).*

Table 5.23Curie temperature obtained for the compounds from AC- susceptibility measurements.

Sample Composition	T_c (K)
$Co_{0.9}Cu_{0.1}Fe_2O_4$	779
$Co_{0.9}Cu_{0.1}Fe_{1.97}In_{0.03}O_4$	769
$Co_{0.9}Cu_{0.1}Fe_{1.94}In_{0.06}O_4$	761
$Co_{0.9}Cu_{0.1}Fe_{1.91}In_{0.09}O_4$	746
$Co_{0.9}Cu_{0.1}Fe_{1.88}In_{0.12}O_4$	726
$Co_{0.9}Cu_{0.1}Fe_{1.85}In_{0.15}O_4$	707

5.4 DC- Electrical resistivity

5.4.1 $Co_{1-x}Cu_xFe_2O_4$ (where x = 0.00, 0.05, 0.1, 0.15, 0.20 and 0.25)

The electrical properties provide significant information about the conduction mechanism in spinel ferrites. Fig. 5.24 presents the DC electrical resistivity plots for $Co_{1-x}Cu_xFe_2O_4$ (where x = 0.00, 0.05, 0.10, 0.15, 0.20 and 0.25). It was observed that the resistivity of the compounds decreased with increasing temperature thus depicting their semiconducting nature. The mechanism of conduction can be explained on the basis of hopping of electrons between Fe^{2+} and Fe^{3+} ions at the octahedral site. This is due to the enhanced thermally activated drift mobility of charge carriers according to the hopping conduction mechanism.

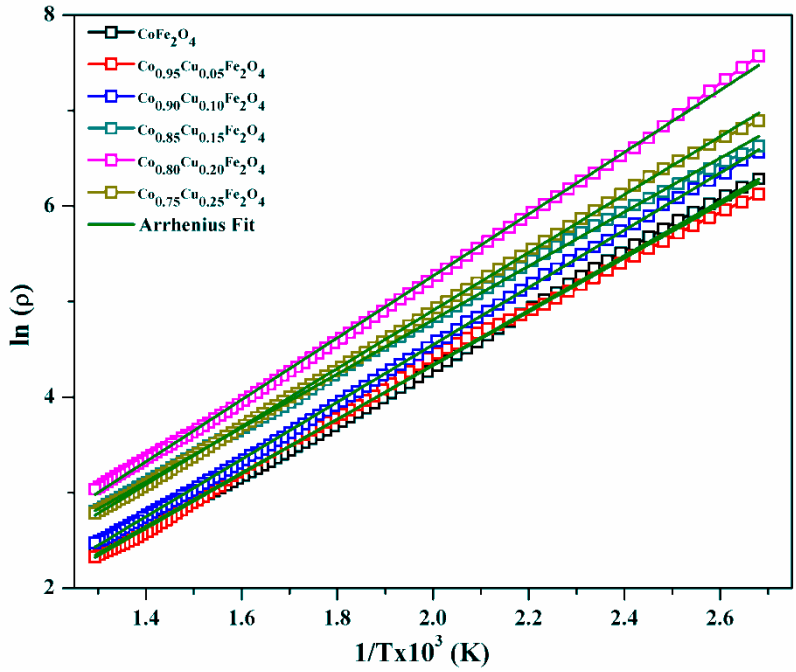

Fig. 5.24 *DC – electrical resistivity plots for $Co_{1-x}Cu_xFe_2O_4$ (where x = 0.00, 0.05, 0.1, 0.15, 0.20 and 0.25).*

A gradual rise in resistivity with Cu^{2+} substitution in $CoFe_2O_4$ was observed. This rise can be attributed to the formation of stable electric bonds between the Cu^{2+} and

Fe^{2+}ions at the octahedral site, which localizes Fe^{2+} charge carriers [406,407]. This consecutively hinders the Verwey mechanism and hence increases the DC electrical resistivity. The values of activation energy calculated from the Arrhenius equation has been shown in Table 5.24.

Table 5.24 Activation energy calculated from DC- electrical resistivity plot.

Sample Composition	Activation energy E_a (eV)
$CoFe_2O_4$	0.24
$Co_{0.95}Cu_{0.05}Fe_2O_4$	0.24
$Co_{0.90}Cu_{0.10}Fe_2O_4$	0.25
$Co_{0.85}Cu_{0.15}Fe_2O_4$	0.24
$Co_{0.80}Cu_{0.20}Fe_2O_4$	0.27
$Co_{0.75}Cu_{0.25}Fe_2O_4$	0.26

5.4.2 $CoFe_{2-x}Sb_xO_4$ (where x = 0.00, 0.03, 0.06, and 0.09)

It was observed that resistivity decreases with rising temperature for all the samples like most of the ferrites materials reported in the literature, showing a semiconducting nature of the prepared ferrites (Fig. 5.25).

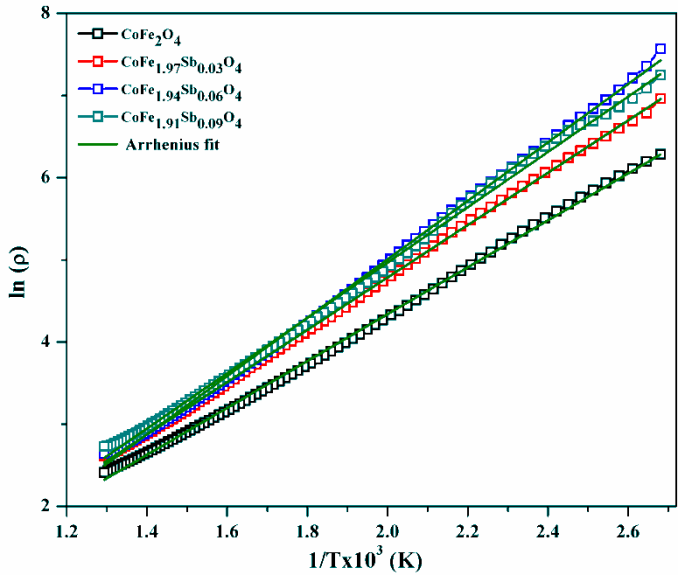

Fig. 5.25 *DC – electrical resistivity plots for $CoFe_{2-x}Sb_xO_4$ (where x = 0.00, 0.03, 0.06, and 0.09).*

Conduction mechanism in ferrites is owing to the hopping of charge carriers between Fe^{2+} and Fe^{3+} ions at the octahedral site, and at a raised temperature, there is an enhancement in the hopping of charges. It was observed that with the introduction of Sb^{3+} ions, the resistivity of the material increased due to the replacement of Fe^{3+} ions with Sb^{3+} ions at the octahedral site. Substitution forces some of the Fe^{3+} ions to migrate from octahedral to the tetrahedral site as discussed in section 5.2.2**,** which decreases the number of electron pair (Fe^{3+}/Fe^{2+}) hopping at octahedral site accountable for conduction in ferrites [408]. The values of activation energy have been summarised in Table 5.25.

Table 5.25 Activation energy calculated from DC-electrical resistivity plot.

Sample Composition	Activation energy E_a (eV)
$CoFe_2O_4$	0.24
$CoFe_{1.97}Sb_{0.03}O_4$	0.27
$CoFe_{1.94}Sb_{0.06}O_4$	0.30
$CoFe_{1.91}Sb_{0.09}O_4$	0.28

5.4.3 $Co_{0.9}Cu_{0.1}Fe_{2-x}RE_xO4$ (where RE = Gd, Sm, Dy, Yb, Eu and x = 0.00, 0.03, 0.05)

The plots of variation in DC electrical resistivity with respect to temperature for the RE substituted Co-Cu ferrite are presented in Fig. 5.26. It was observed that resistivity of the ferrites decreases with increasing temperature which is a characteristic feature of ferrites specifying their semiconducting nature. This could be explained as at lower temperature hopping of electrons and holes is least due to which resistivity is maximum. At raised temperature, there is a decrease in resistivity due to the increase in hopping of charges.

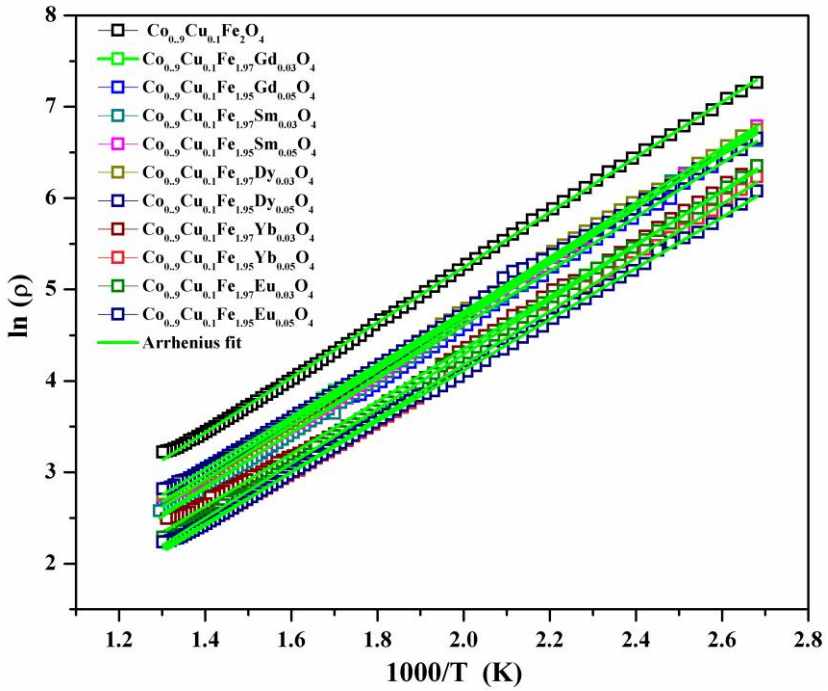

Fig. 5.26 *DC electrical resistivity plots for $Co_{0.9}Cu_{0.1}Fe_{2-x}RE_xO_4$ (where RE = Gd, Sm, Dy, Yb, and Eu and x = 0.00, 0.03 and 0.05).*

With the substitution of RE^{3+}ions, the resistivity of the material is decreased compared to corresponding to pure Co-Cu ferrite. The observed trend can be attributed to the redistribution of cations when the iron is replaced by RE^{3+} ions at the octahedral site. This increases Fe^{3+} ions in the octahedral site and hence increases the number of Fe^{2+} and Fe^{3+} pairs in the octahedral site [196,409]. Since the conduction in ferrites is considered as the electron hopping between Fe^{2+} and Fe^{3+} at the octahedral site according to verwey mechanism, the conductivity increases while resistivity decreases with RE^{3+} ion substitution in Co-Cu ferrite [408]. The values of activation energy estimated from the Arrhenius equation have been shown in Table 5.26.

Table 5.26 Activation energy calculated from DC-electrical resistivity plot.

Sample Composition	Activation energy E_a *(eV)*
$Co_{0.9}Cu_{0.1}Fe_2O_4$	0.25
$Co_{0.9}Cu_{0.1}Fe_{1.97}Gd_{0.03}O_4$	0.25
$Co_{0.9}Cu_{0.1}Fe_{1.95}Gd_{0.05}O_4$	0.25
$Co_{0.9}Cu_{0.1}Fe_{1.97}Dy_{0.03}O_4$	0.26
$Co_{0.9}Cu_{0.1}Fe_{1.95}Dy_{0.05}O_4$	0.25
$Co_{0.9}Cu_{0.1}Fe_{1.97}Sm_{0.03}O_4$	0.25
$Co_{0.9}Cu_{0.1}Fe_{1.95}Sm_{0.05}O_4$	0.24
$Co_{0.9}Cu_{0.1}Fe_{1.97}Yb_{0.03}O_4$	0.24
$Co_{0.9}Cu_{0.1}Fe_{1.95}Yb_{0.05}O_4$	0.25
$Co_{0.9}Cu_{0.1}Fe_{1.97}Eu_{0.03}O_4$	0.25
$Co_{0.9}Cu_{0.1}Fe_{1.95}Eu_{0.05}O_4$	0.24

5.4.4 $Co_{0.9}Cu_{0.1}Fe_{2-x}Cr_xO_4$ (where x = 0.00, 0.03, 0.06, 0.09, 0.12, and 0.15)

Fig. 5.27 depicts the DC electrical resistivity plots for the Cr^{3+} substituted Co-Cu ferrite sintered at 800 °C. The results clearly showed a decrease in resistivity with increasing temperature indicating the semiconducting nature of the material under investigation.

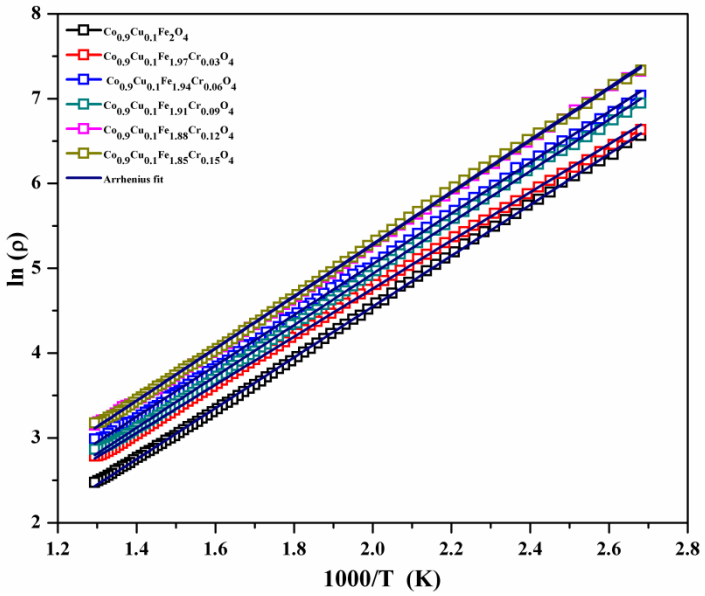

Fig. 5.27 *DC – electrical resistivity plots for* $Co_{0.9}Cu_{0.1}Fe_{2-x}Cr_xO_4$.

With Cr^{3+} ion substitution in Co-Cu ferrite, a slight increase in resistivity values can be noticed. The substitution leads to the development of stable electric bonds among the Cr^{3+} and Fe^{2+} ions at the B sub-lattice, which localizes Fe^{2+} charge carriers and obstructs the Verwey hopping mechanism responsible for conduction in ferrites thus increasing the resistivity [215,408]. The activation energy (E_a) calculated employing the Arrhenius equation ranged from 0.245 eV to 0.265 eV (Table 5.27). The similar values of E_a for Cr^{3+} ion substituted spinel ferrite were reported by Kumari et al. [410].

Table 5.27 Activation energy calculated from DC- electrical resistivity plot.

Sample Composition	Activation energy E_a (eV)
$Co_{0.9}Cu_{0.1}Fe_2O_4$	0.25
$Co_{0.9}Cu_{0.1}Fe_{1.97}Cr_{0.03}O_4$	0.24
$Co_{0.9}Cu_{0.1}Fe_{1.94}Cr_{0.06}O_4$	0.25
$Co_{0.9}Cu_{0.1}Fe_{1.91}Cr_{0.09}O_4$	0.26
$Co_{0.9}Cu_{0.1}Fe_{1.88}Cr_{0.12}O_4$	0.26
$Co_{0.9}Cu_{0.1}Fe_{1.85}Cr_{0.15}O_4$	0.26

5.4.5 $Co_{0.9}Cu_{0.1}Fe_{2-x}Mn_xO_4$ (where x = 0.00, 0.03, 0.06, 0.09, 0.12, and 0.15)

The variations in DC electrical resistivity with temperature for Mn ion substituted and unsubstituted Co-Cu ferrite is presented in Fig. 5.28. It is seen that the resistivity declines with an increase in the temperature highlighting the semiconducting nature of the material.

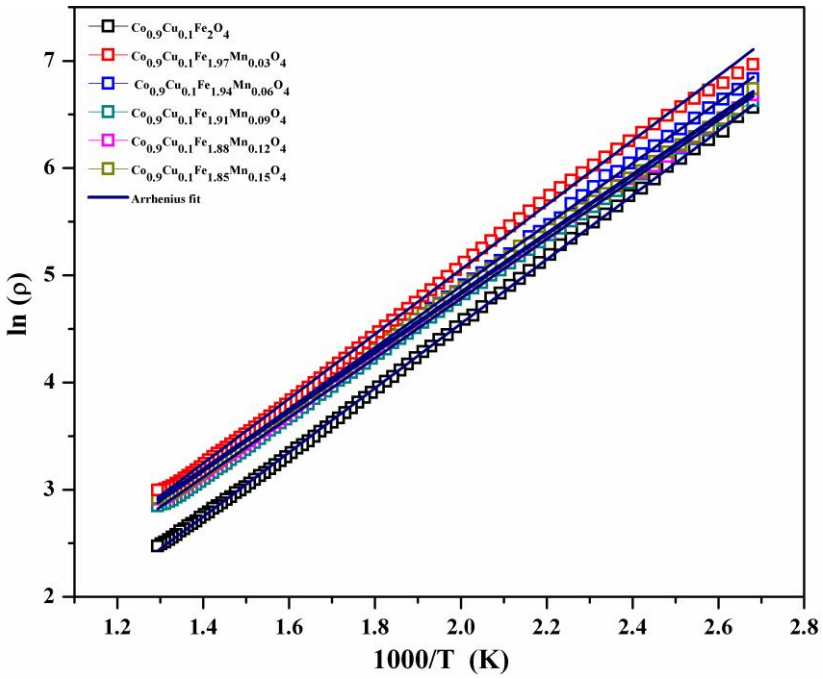

Fig. 5.28 *DC – electrical resistivity plots for $Co_{0.9}Cu_{0.1}Fe_{2-x}Mn_xO_4$ (where x = 0.00, 0.03, 0.06, 0.09, 0.12, and 0.15).*

The variation of DC electrical resistivity with increasing Mn ion concentration showed that with the Mn ion concentration, the DC resistivity increased at lower Mn concentration and then decreased marginally at higher concentrations. The increase in DC resistivity can be credited to a large number of Mn^{2+} ions occupying B site, forcing some of the Fe^{3+} ions at B site to migrate to A site, which reduces the hopping rate between Fe^{3+} and Fe^{2+} ions at B site. As a result, DC resistivity increased at lower Mn ion concentration. Whereas at higher concentration the hopping probabilities among Mn^{3+} and Mn^{2+} ions could be contributing towards the observed decrease in resistivity. This behavior is in accordance with Verwey's hopping conduction mechanism. The values of activation energy were determined by using the Arrhenius relation from the resistivity plots and the values are given in Table 5.28.

Table 5.28 Activation energy calculated from DC-electrical resistivity plot.

Sample Composition	Activation energy E_a (eV)
$Co_{0.9}Cu_{0.1}Fe_2O_4$	0.25
$Co_{0.9}Cu_{0.1}Fe_{1.97}Mn_{0.03}O_4$	0.25
$Co_{0.9}Cu_{0.1}Fe_{1.94}Mn_{.06}O_4$	0.24
$Co_{0.9}Cu_{0.1}Fe_{1.91}Mn_{0.09}O_4$	0.23
$Co_{0.9}Cu_{0.1}Fe_{1.88}\ Mn_{0.12}O_4$	0.23
$Co_{0.9}Cu_{0.1}Fe_{1.85}\ Mn_{0.15}O_4$	0.23

5.4.6 $Co_{0.9}Cu_{0.1}Fe_{2-x}In_xO_4$ (where x = 0.00, 0.03, 0.06, 0.09, 0.12, and 0.15)

It is observed from Fig. 5.29 that, the DC electrical resistivity of the samples under investigation decreased with increasing temperature reflecting the typical semiconducting behavior of spinel ferrites. The decrease in DC resistivity with rising temperature is due to the increased drift mobility of the charge carriers which gets thermally activated with temperature [242].

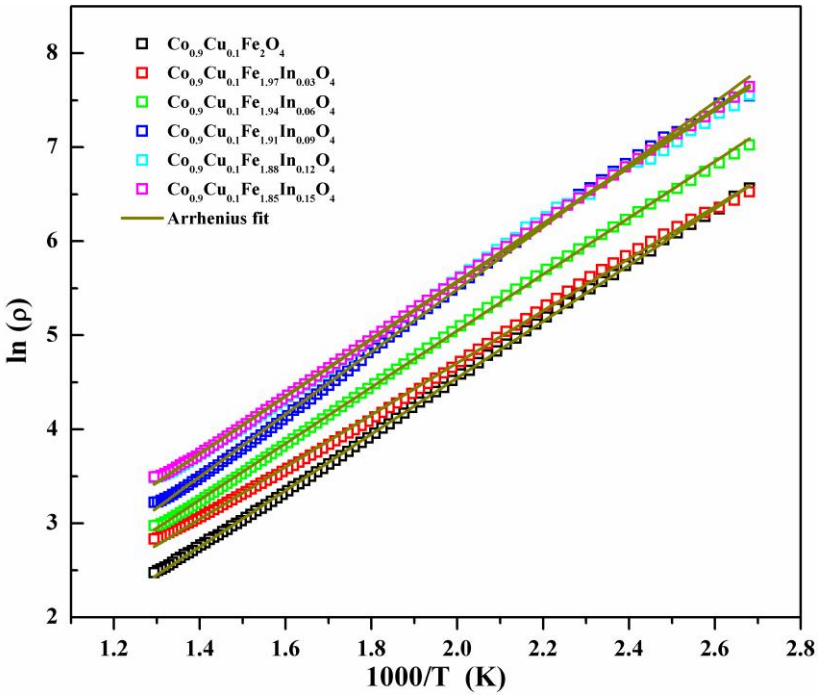

Fig. 5.29 *DC – electrical resistivity plots for $Co_{0.9}Cu_{0.1}Fe_{2-x}In_xO_4$ (where x = 0.00, 0.03, 0.06, 0.09, 0.12, and 0.15).*

D.C. resistivity increased gradually with increasing substituent concentration. As discussed in section 3.6, the In^{3+} ions are likely to occupy the B site, thus displacing an equal number of Fe^{3+} ions to the A site, which will decrease the concentration of Fe^{3+}/Fe^{2+} ion pairs at the B site which are accountable for conduction in ferrites as explained by Verwey's hopping mechanism [408]. According to Verwey, the conduction in ferrites is because of electron hopping between ions of the same elements existing in more than one valence state. The addition of In^{3+} ions in place of Fe^{3+} ions hinders the Verwey's hopping mechanism, which consequently increases the DC electrical resistivity.The activation energy for all the compositions was calculated from the DC electrical resistivity plots and is presented in Table 5.29. The activation energy determined ranged from 0.235 to 0.286 eV, which indicated no significant difference with In^{3+} substitution. Comparable values of the activation energy were obtained by Nongjai et al. [19] and Pandit et al. [18] in In^{3+}-substituted $CoFe_2O_4$.

Table 5.29 Activation energy calculated from DC-electrical resistivity plot.

Sample Composition	Activation energy E_a (eV)
$Co_{0.9}Cu_{0.1}Fe_2O_4$	0.25
$Co_{0.9}Cu_{0.1}Fe_{1.97}In_{0.03}O_4$	0.23
$Co_{0.9}Cu_{0.1}Fe_{1.94}In_{0.06}O_4$	0.25
$Co_{0.9}Cu_{0.1}Fe_{1.91}In_{0.09}O_4$	0.28
$Co_{0.9}Cu_{0.1}Fe_{1.88}In_{0.12}O_4$	0.26
$Co_{0.9}Cu_{0.1}Fe_{1.85}In_{0.15}O_4$	0.26

5.5 Dielectric Properties

5.5.1 $Co_{1-x}Cu_xFe_2O_4$ (where x = 0.00, 0.05, 0.1, 0.15, 0.20 and 0.25)

There is an exponential decrease in ε' with increasing frequency signifying the dielectric dispersion in the lower frequency range as presented in Fig. 5.30. There is a sharp fall in ε' in the lower frequency region, and as the frequency is increased, it remained almost constant for all the compositions under investigation. The polarization in ferrites depends on the hopping between Fe^{2+} and Fe^{3+} ions present at the B site. The Maxwell–Wagner type interfacial polarization may be held responsible for the variation of ε' with a frequency which is in good accordance with Koop's phenomenological theory [411,412]. In general, the ε' in solid materials is mainly due to four types of polarization: (i) interfacial polarization (ii) dipolar polarization (iii) atomic polarization and (iv) electronic polarization [242]. It was observed in Fig. 5.30(a) that the insertion of Cu^{2+} ions in $CoFe_2O_4$ enhanced the ε' in the lower frequency region. Majority of the Cu^{2+} ions replace Co^{2+} ions and take up the preferential B site along with the occupation of A site. Consequently, it drives Co^{2+} ions to migrate from the B site and fractions of Fe^{3+} ions from A site to B site due to the charge compensation mechanism [413]. The Fe^{3+} and Fe^{2+} ion concentration are increased at B site whereas the concentration of Co^{2+} ions is decreased at this site. The increased electron hopping of Fe^{2+}/Fe^{3+} ion pairs at the B site leads to an increase in the ε' at lower frequencies.

As can be seen from Fig. 5.30(b), the *tan* δ also exhibits very similar dispersion as that of a ε' in the lower frequency region at room temperature and for all the values of x. The *tan* δdetermines the energy loss within the materialand arises due to lag of

polarization behind the applied alternating electric field which must be generated by grain boundaries, defects, and impurities in the crystal [414].

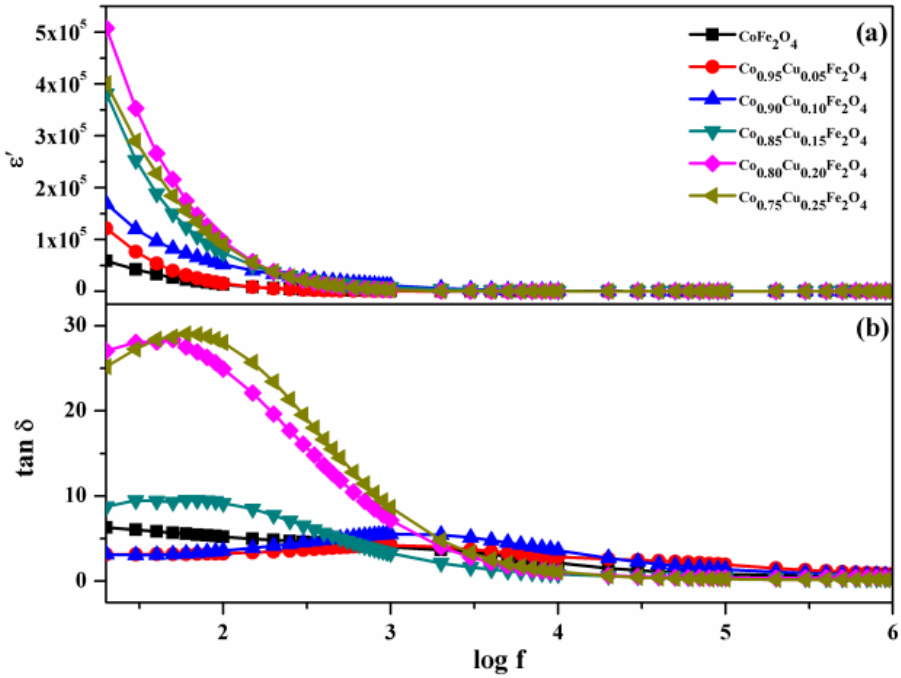

Fig. 5.30 *Room temperature, frequency dependence of dielectric constant and dielectric loss for* $Co_{1-x}Cu_xFe_2O_4$ *where x = 0.00, 0.05, 0.10, 0.15, 0.20 and 0.25.*

Fig. 5.31 depicts the trend in ε' and *tan* δ with temperature and also with Cu^{2+} substitution at 1MHz. Fig. 5.31(a) suggests that there is a noticeable increase in ε' with temperature. The enhancement ofε' with temperature can be explained on the basis of thermal energy. At lower temperature, the thermal energy is inadequate to increase the carrier mobility, and in most instances, the carriers are unable to orient themselves concerning the field direction. But at a highertemperature, the thermal energy is more than enough to increase the rate of hopping and hence the charge carrier mobility so that they can easily align themselves with the field direction [184]. This increases their contribution to polarization and increases the ε′ of the material.

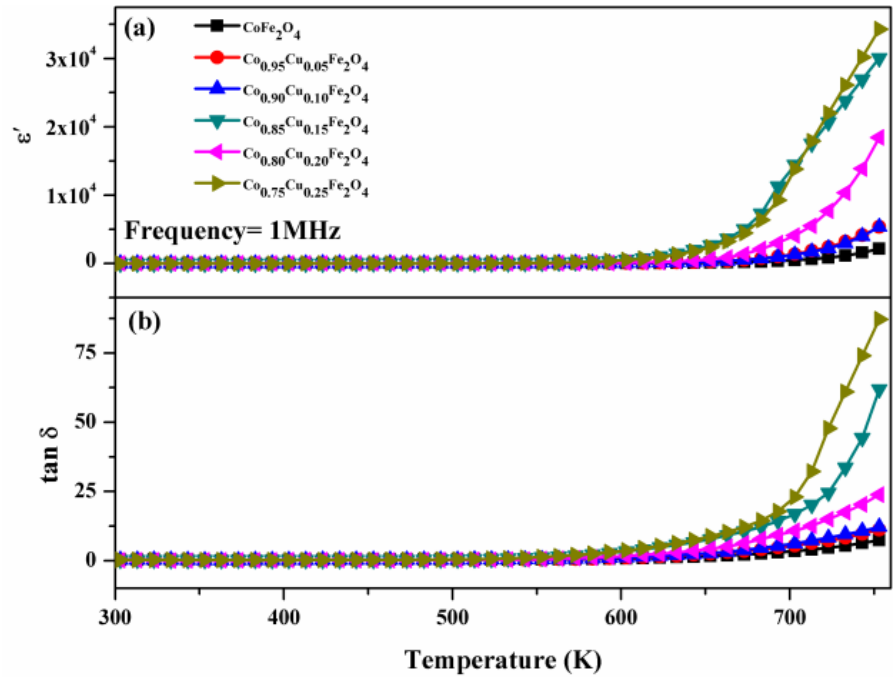

Fig. 5.31 *Temperature dependence of dielectric constant and dielectric loss for* $Co_{1-x}Cu_xFe_2O_4$ *where x = 0.00, 0.05, 0.10, 0.15, 0.20 and 0.25 at 1 MHz.*

5.5.2 $CoFe_{2-x}Sb_xO_4$ (where x = 0.00, 0.03, 0.06, and 0.09)

As seen in Fig. 5.32(a), the room temperature frequency-dependent ε′ has a higher value in the lower frequency region but decreases as the frequency increases and becomes almost constant in the higher frequency region, exhibiting the usual dielectric dispersion. The dispersion behavior of ε′ with frequency is credited to Maxwell-Wagner type interfacial polarization in accordance with Koop's theory of dielectrics [411,412].

The Maxwell–Wagner model is based on the existence of two layers in the dielectric structure of spinel ferrites, leading to interfacial polarization. The initial being a conducting layer made up of larger grains and the other consists of highly resistive grain boundaries. At lower frequencies, the highly resistive grain boundaries are more active than the conductive grains[415]. The higher values of ε' obtained in the lower frequency

region are due to the buildup of charges at the boundaries under the influence of the electric field. This generates a considerable amount of interfacial polarization [415]. Beyond a certain frequency limit, the electrons are no longer capable of chasing the rapidly-varying applied field due to which polarization drops with increasing frequency.

It is noticed that ε' increased with an increasing amount of Sb^{3+} ions in the lower frequency region. While it does not show a prominent effect on ε' in the higher-frequency region. The increase in ε' with Sb^{3+} content could be due to increased Fe-O and Sb-O bond length at the octahedral (B) site which increases the atomic polarizability and subsequently ε'. The enhancement in ε' with Sb^{3+} ion substitution in spinel ferrites has been observed by several researchers [149,152,155].

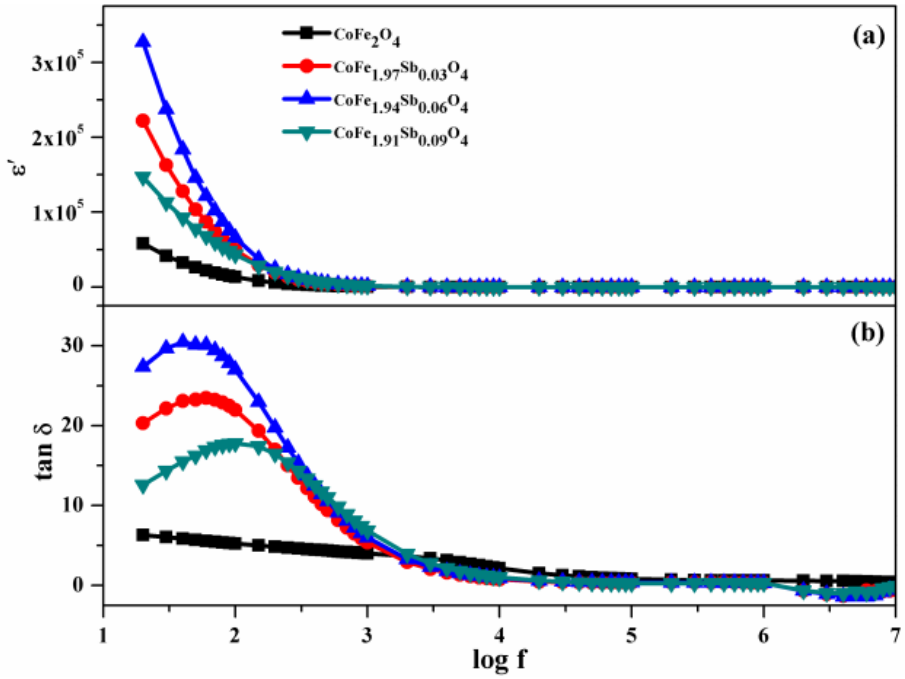

Fig. 5.32 *Room temperature, frequency dependence of dielectric constant and dielectric loss for $CoFe_{2-x}Sb_xO_4$ where x = 0.00, 0.03, 0.06 and 0.09.*

The *tan* δ as shown in Fig. 5.32(b) shows similar behavior to that of ε'. This dispersion behavior of *tan* δ in the lower frequency regime again obeys the Maxwell–

Wagner type of interfacial polarization. In spinel ferrites, the contribution to *tan δ* is generally from grain boundaries, impurities, sintering conditions, imperfections and defects in the crystal lattice [415].

The variation in *ε′* and *tan δ* as a function of temperature at a constant frequency of 1 MHz has been shown in Fig. 5.33. It was observed that *ε′* and *tan δ* increases gradually with increasing temperature for all the compositions under investigation. On increasing the temperature, the drift mobility of thermally activated electric charge carrier's increases, and the rate of hopping increases. Which in turn enhances the dielectric polarization causing a notable increase in *ε′* [404]. On the other hand, at lower temperatures, the thermal energy provided to the samples is inadequate to increase the charge carrier mobility.

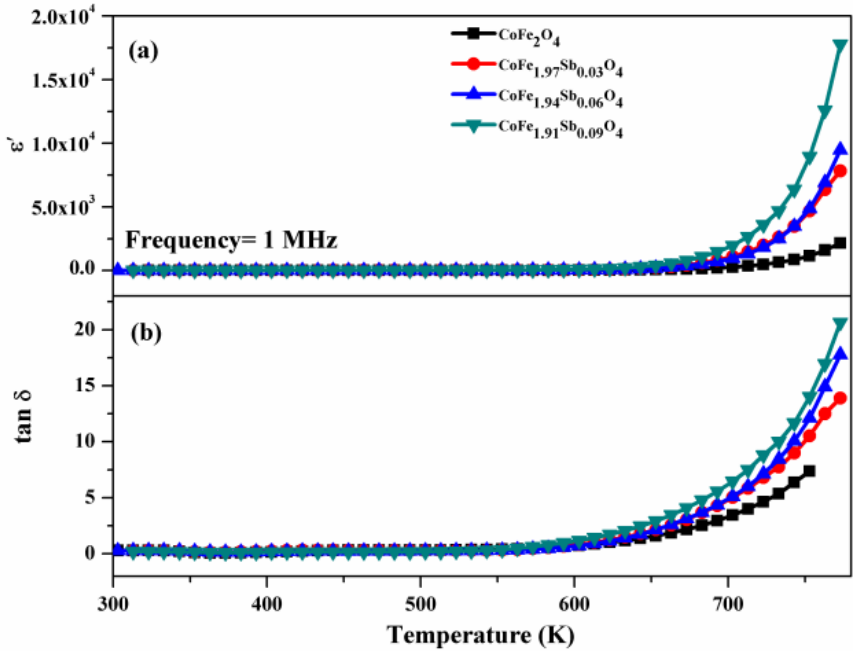

Fig. 5.33 *Temperature dependence of dielectric constant and dielectric loss for $CoFe_{2-x}Sb_xO_4$ where x = 0.00, 0.03, 0.06 and 0.09.*

5.5.3 $Co_{0.9}Cu_{0.1}Fe_{2-x}RE_xO4$ (where RE = Gd, Sm, Dy, Yb, Eu and x = 0.00, 0.03, 0.05)

Room temperature frequency-dependent ε' and *tan* δ of all samples in the frequency range 20 Hz to 1 MHz is shown in Fig. 5.34.

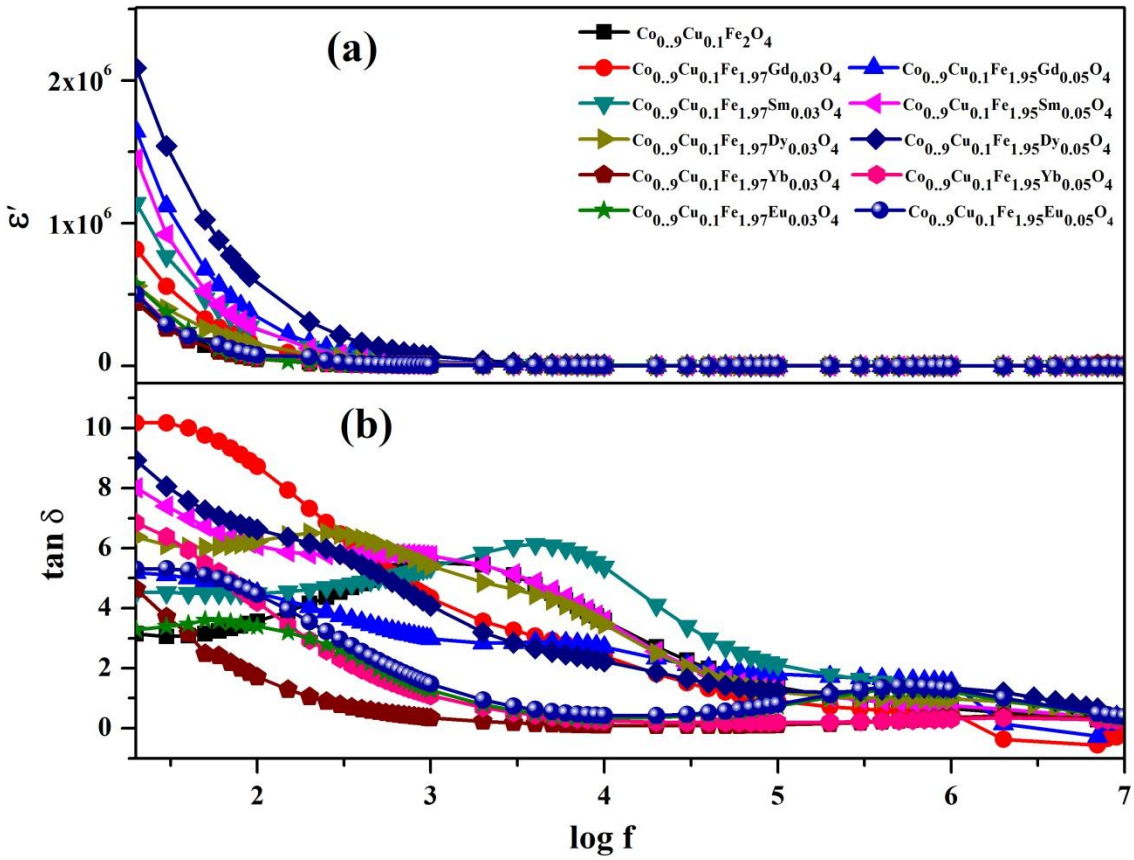

Fig. 5.34 *Room temperature, the frequency dependence of dielectric constant and dielectric loss for* $Co_{0.9}Cu_{0.1}Fe_{2-x}RE_xO_4$ *(where RE = Gd, Sm, Dy, Yb, and Eu and x = 0.00, 0.03 and 0.05).*

It was observed that both ε' and *tan* δ for RE^{3+} substituted and corresponding pure Co-Cu ferrite strongly depends on frequency. It can be noted that ε' and *tan* δ shows higher values atlower frequencies while remains almost unchanged at higher frequencies. The interfacial and dipolar polarization, which have a strong dependence on temperature as well as the frequencyis mainly responsible for the rapid increase in ε' at low frequencies. On the other hand at higher frequencies the very slow variation in ε' is due to

both ionic and electronic polarization which remain almost independent of temperature and frequency [242]. The dielectric behavior of spinel ferrites is due to the electric dipole moments developed due to the charge transfer between the di and trivalent metal cations within the spinel structure. The substantial decline in dielectric parameters with frequency is due to the inability of electric dipoles to follow the variation in an applied field and is associated with the Maxwell Wagner type interfacial polarization which is well in accordance with the Koop's phenomenological theory [411,412].

Fig. 5.35 depicts the variation in ε' and *tan* δ with temperature and with RE^{3+} substitution at 1MHz. The curves suggest that the ε' increases dramatically with temperature. The variation of ε' with temperature can be illustrated on the basis of thermal energy. At lower temperature, the thermal energy is not sufficient to enhance the carrier mobility and in most cases the carriers unable to orient themselves with respect to the field direction. But at elevated temperature the thermal energy is large and it increases the rate of hopping and hence the mobility of the charge carrier so that they are able to align themselves along the field direction effortlessly [184]. This boosts their contribution to temperature-dependent interfacial and dipolar polarization and leads to an increase in the ε' of the material. The *tan* δ also showsa similar dispersion as that of a ε' which can be seen from Fig. 5.35(b). The *tan* δ arises when the polarization lags behind the applied field and this must be caused by grain boundary effect, impurities and the defects in the crystal.

It is evident from Fig. 5.34 and 5.35 that the RE^{3+} content strongly influences the ε' of the prepared material. The ε' increases with increasing RE^{3+} content in Co - Cu ferrite. The rise in the ε' with the inclusion of RE^{3+} ions could be due to the fact that, with

the inclusion of RE^{3+}, the lattice is distorted and increases Fe−O and RE−O bond lengths at B site giving rise to an increase in the atomic polarizability and subsequently the ε'. Similar results were obtained by Sebastian et al. and Murugesan et al. where an enhancement in ε' was observed with RE^{3+} substitution in spinel ferrite [183,416]. The other aspect that contributes to the ε' enhancement is the reduction in crystallite size and grain size with RE^{3+} content as evidenced by XRD and TEM results. The enhancement in ε' due to a decrease in particle size has been reported in literature several times [196,417]. The dielectric properties of ferrites also depend on few factors such as the structure, technique of preparation, grain size, porosity, density, chemical composition, site occupancy of metal cations, sintering time and temperature.

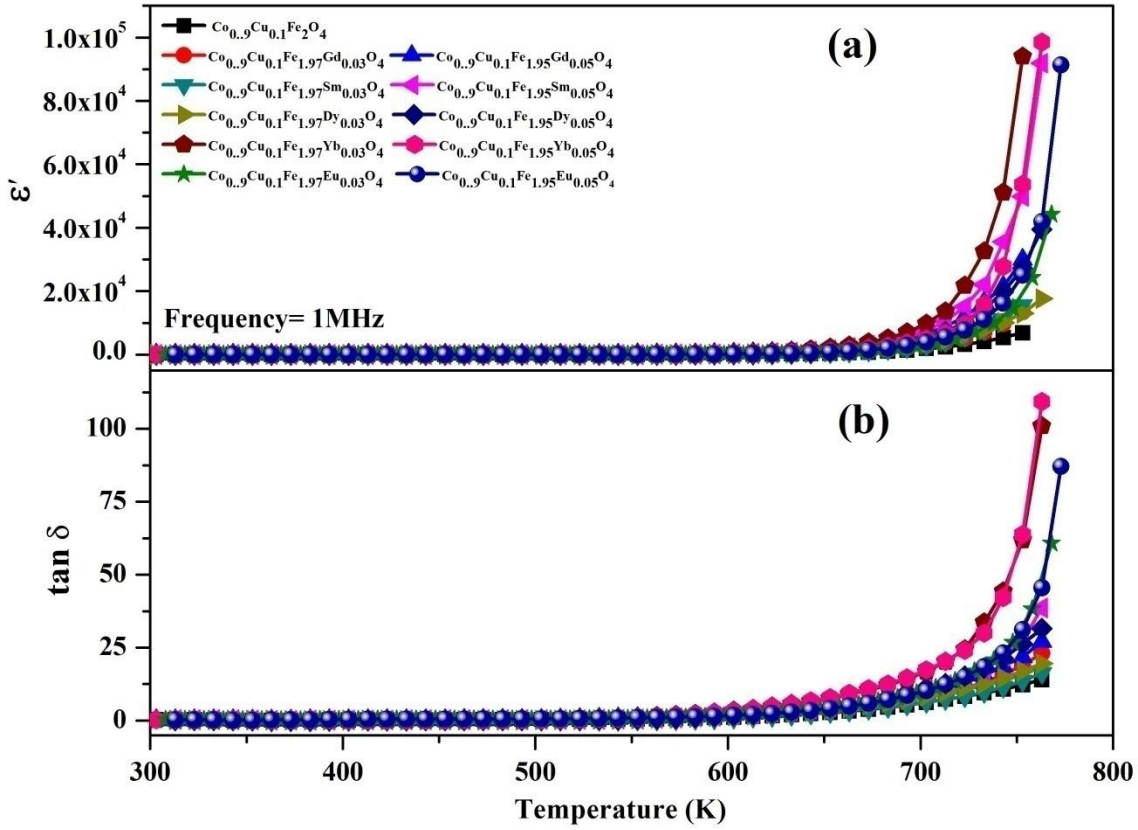

Fig. 5.35 *Temperature dependence of dielectric constant and dielectric loss for $Co_{0.9}Cu_{0.1}Fe_{2-x}RE_xO_4$ (where RE = Gd, Sm, Dy, Yb, and Eu and x = 0.00, 0.03 and 0.05).*

5.5.4 $Co_{0.9}Cu_{0.1}Fe_{2-x}Cr_xO_4$ (where x = 0.00, 0.03, 0.06, 0.09, 0.12, and 0.15)

The dielectric properties such as ε' and *tan δ* for the materials under study were measured as a function of frequency (20 Hz to 1MHz) and temperature (300 K to 773 K). Fig. 5.36 shows the room temperature variation in ε' as a function of frequency recorded for the various concentrations of Cr^{3+} ions. The ε' was found to soar at lower frequencies and a decreasing trend in ε' was seen on approaching towards a relatively higher frequency region, which revealed the typical dielectric behavior of spinel ferrites.

Generally, at lower frequencies, spinel ferrites exhibit all four types of polarization namely interfacial, dipolar, ionic, and electronic [418]. However, interfacial and dipolar polarization are highly active at lower frequencies since electronic and ionic polarizations remain almost unchanged at these frequencies [418].

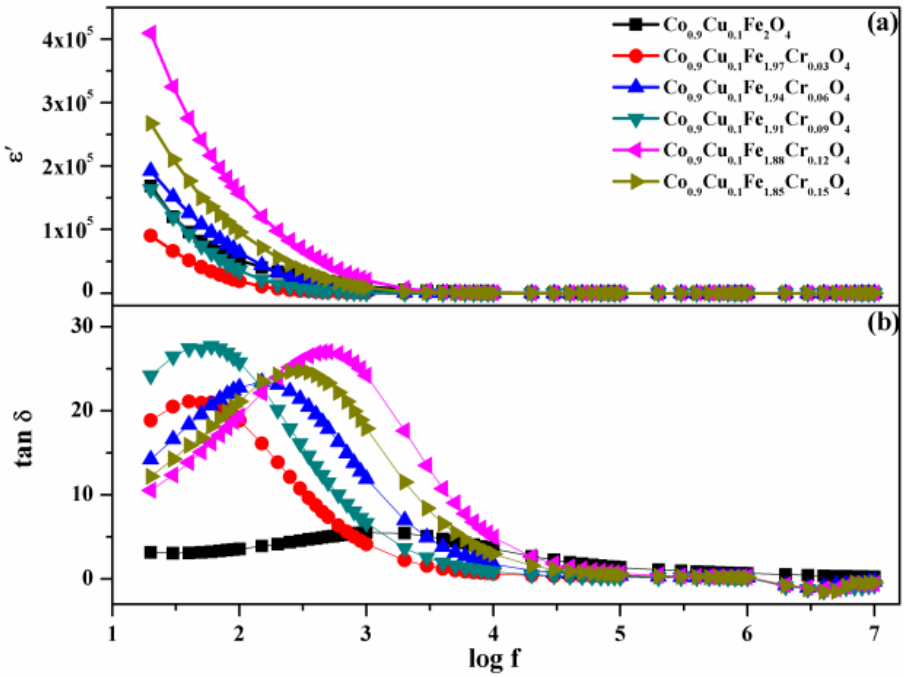

Fig. 5.36 *Room temperature, frequency-dependent dielectric constant and dielectric loss for $Co_{0.9}Cu_{0.1}Fe_{2-x}Cr_xO_4$ (where x = 0.00, 0.03, 0.06, 0.09, 0.12, and 0.15).*

In most cases, interfacial polarization appears owing to the inhomogeneous structure of the dielectric material, and as explained by Maxwell–Wagner kind of interfacial polarization which complies with the Koop's theory [411,412]. According to this theory, the decline in ε' with rising frequency could be interpreted considering dielectric materials to be made up of well-conducting grains which are separated by weakly conducting grain boundaries [419]. The grains are strongly effective at higher frequencies while the grain boundaries are dominant at lower frequencies. Highly conducting grains separated by grain boundaries brings about the localized buildup of charge carriers under the applied electric field increasing interfacial polarization and ε' at lower frequencies. Beyond a particular frequency, electron exchange between bivalent and trivalent ions is not able to keep pace with a rapidly changing field. Consequently, the possibility of electrons attaining the grain boundaries gets reduced which decreases the contribution from interfacial polarization and hence the ε' drops at higher frequencies [199,405,420,421]. The variation in *tan* δ as a function of frequency is depicted in Fig. 5.36(b) which also exhibits a comparable trend as that of ε'. Furthermore, the present investigation revealed that the ε' and *tan* δ of Cr^{3+} substituted Co-Cu ferrite was higher than that of corresponding Co-Cu ferrite in the lower frequency region.

The frequency-dependent (1 MHz) ε' and *tan* δ at various temperatures (300 to 773 K) are depicted in Fig. 5.37. It was noticed that both the parameters gradually increases with rising temperature. As the material is thermally activated, the mobility of the charge carrier gets enhanced owing to the increased thermal energy which facilitates them to align in the course of the applied electric field. This adds their contribution to the temperature-dependent interfacial and dipolar polarization resulting in increased ε' [422].

At a relatively lower temperature, the charge carriers are unable to align themselves in the applied field direction; thus, the contribution to the polarization is not significant [184,199]. The trend in *tan δ* could be elucidated in a similar manner as thatof in the case of *ε'*.

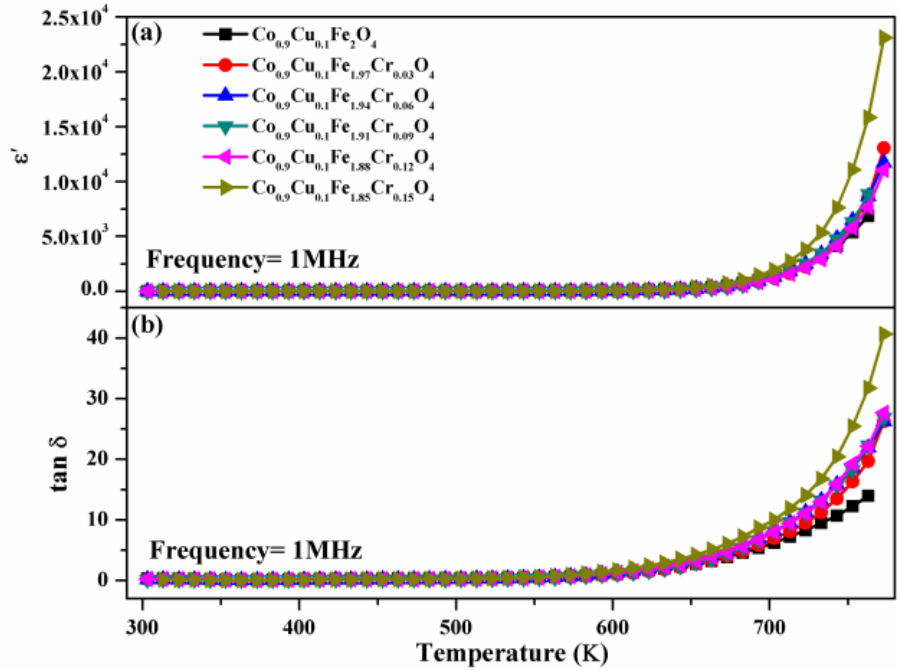

Fig. 5.37 *Temperature dependent dielectric constant and dielectric loss for* $Co_{0.9}Cu_{0.1}Fe_{2-x}Cr_xO_4$ *(where x = 0.00, 0.03, 0.06, 0.09, 0.12, and 0.15).*

5.5.5 $Co_{0.9}Cu_{0.1}Fe_{2-x}Mn_xO_4$ (where x = 0.03, 0.06, 0.09, 0.12, and 0.15)

The variation of the *ε′* and*tan δ* with frequency at room temperature for $Co_{0.9}Cu_{0.1}Fe_{2-x}Mn_xO_4$ (where x = 0.03, 0.06, 0.09, 0.12, and 0.15) were studied in the frequency range from 20 Hz to 1 MHz and is shown in Fig. 5.38.A maximum*ε′* and *tan δ* were observed in the lower frequency region and both the parameters decreased as moved towards a higher frequency region indicating the normal behavior of ferrite samples. The observed dispersion behavior can be attributed to the Maxwell–Wagner interfacial polarization theory for the inhomogeneous two-layer dielectric structure, which is in accordance with Koop's phenomenological theory [411,412].

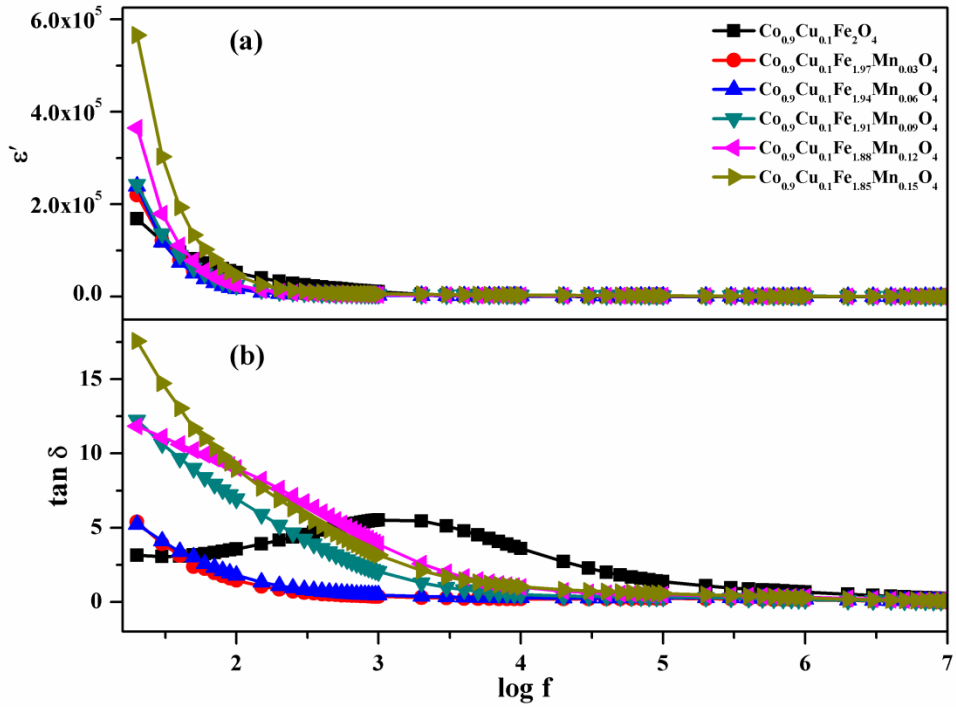

Fig. 5.38 *Room temperature, frequency dependent dielectric constant and dielectric loss for* $Co_{0.9}Cu_{0.1}Fe_{2-x}Mn_xO_4$ *(where x = 0.00, 0.03, 0.06, 0.09, 0.12, and 0.15).*

It is observed from Fig. 5.38 that the ε' showed higher values for higher Mn ion concentration as compared to the unsubstituted sample. In spinel ferrites, rotation of Fe^{2+} and Fe^{3+} dipoles may be visualized as the exchange of electrons between the ions so that the dipoles align themselves in response to the applied alternating field. In the present case at higher Mn ion concentration, the Mn^{2+} and Mn^{3+} ions possibly present at the octahedral site will also contribute towards polarization hence a higher value of ε' was observed. So the polarization at lower frequencies may have resulted from electron hopping between Fe^{2+} and Fe^{3+} and Mn^{2+} and Mn^{3+} ions in the ferrite lattice.

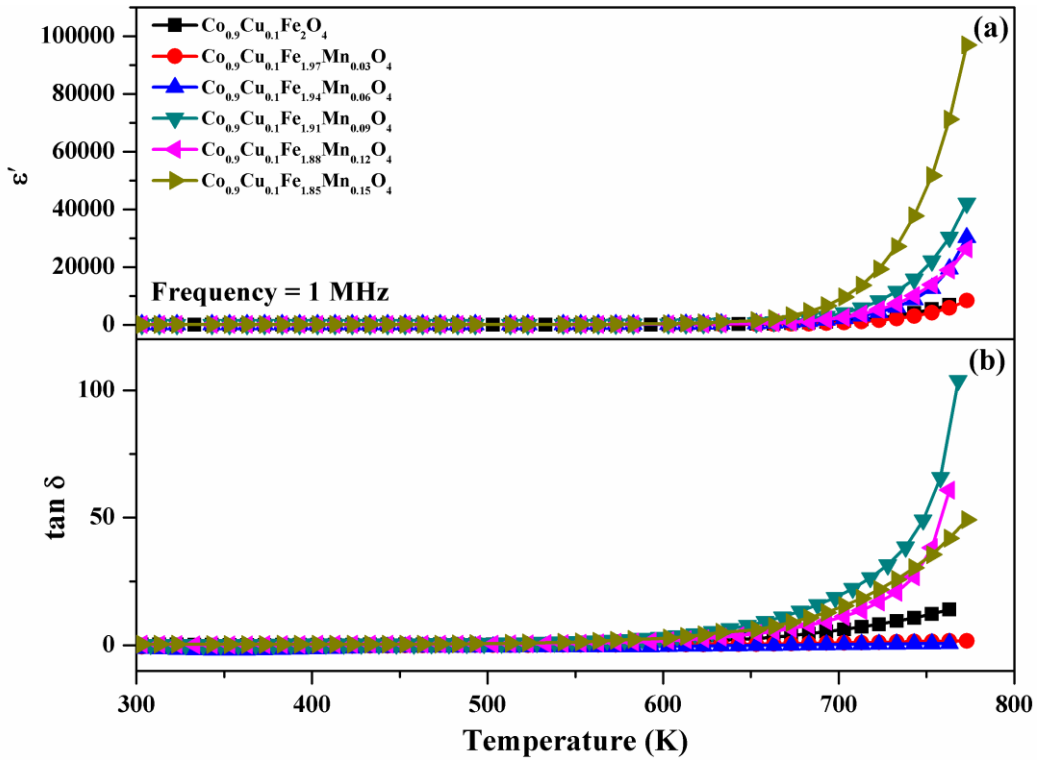

Fig. 5.39 *Temperature dependent dielectric constant and dielectric loss for* $Co_{0.9}Cu_{0.1}Fe_{2-x}Mn_xO_4$ *(where x = 0.00, 0.03, 0.06, 0.09, 0.12, and 0.15).*

The temperature dependence of ε' and *tan* δ at a constant frequency of 1 MHz has been shown in Fig. 5.39. It was observed that the ε' increased with the increasing temperature. The enhancement in ε' at elevated temperature is due to the increased mobility of thermally activated charge carriers. As a result, the rate of hopping increases, which enhances the contribution of charge carriers to the temperature-dependent interfacial and dipolar polarization. The *tan* δ also showed a similar trend as that of ε'.

5.5.6 $Co_{0.9}Cu_{0.1}Fe_{2-x}In_xO_4$ (where x = 0.03, 0.06, 0.09, 0.12, and 0.15)

The room temperature dielectric properties of In^{3+} substituted and un-substituted Co-Cu ferrite was examined over a wide range of frequencies (20 Hz to 1 MHz). Relatively high values of ε' were observed for all the compositions in the lower frequencyregion and it declined sharply as moved to the higher frequency region as

shown in Fig. 5.40, which is typical behavior of spinel ferrite materials. This kind of dispersion in ε' could be credited to Maxwell-Wagner theory of interfacial polarization and Koops' theory [411,412].

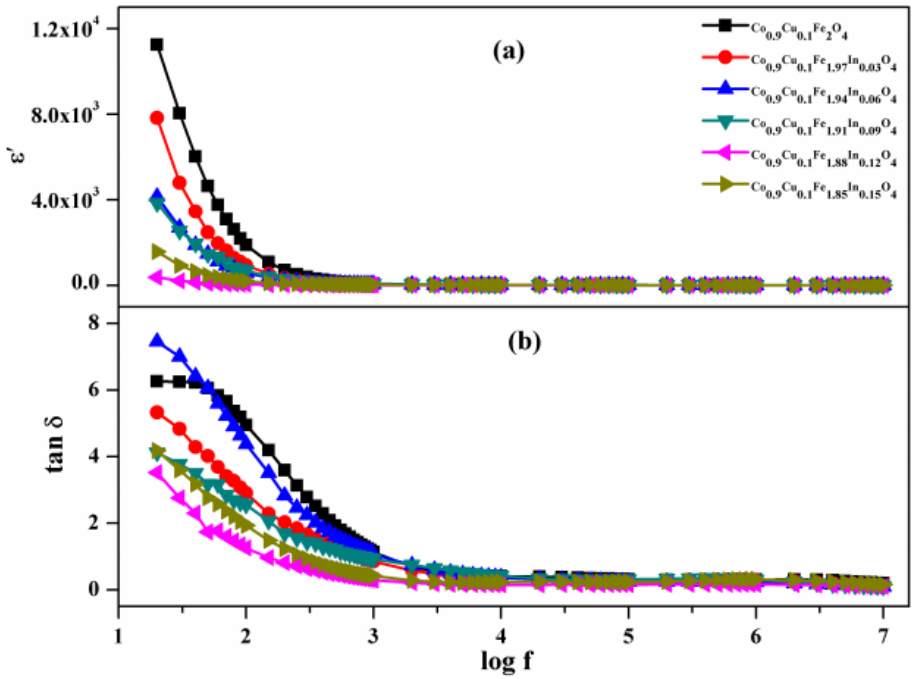

Fig. 5.40*Frequency-dependent (a) dielectric constant and (b) dielectric loss for* $Co_{0.9}Cu_{0.1}Fe_{2-x}In_xO_4$ *(where x = 0.00, 0.03, 0.06, 0.09, 0.12, and 0.15).*

The interfacial and dipolar polarization, which are strongly dependent on temperature and frequency is mainly accountable for the higher value of ε' at lower applied frequencies. At higher applied frequencies, the slow variation in ε' is due to the contribution from ionic and electronic polarizations which are temperature and frequency independent [242]. The *tan δ* values obtained also showed a similar trend as that ofε'. It showed higher values in the lower frequencies and remained almost unchanged athigher frequencies.

The compositional dependence of ε' at applied frequencies showed a decrease in ε' with successive addition of In^{3+} ions. As discussed in section 5.2.6, In^{3+} ions could have occupied the B site in $Co_{0.9}Cu_{0.1}Fe_2O_4$ replacing Fe^{3+} ions. This reduces the electron hopping interaction between Fe^{2+} and Fe^{3+} charge carriers at the B site, accountable for polarization in spinel ferrites which consequently decreases the polarization and hence the ε'[242]. Similar conclusions were drawn by Hashim et al.[236] and Lakshman et al. [251] for In^{3+} substituted spinel ferrites.

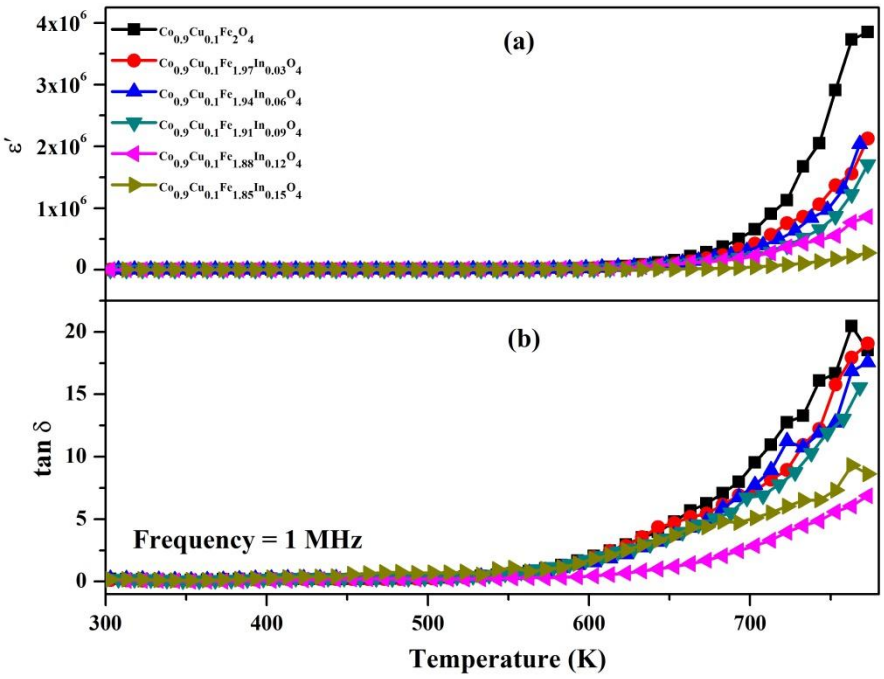

Fig. 5.41*Temperature-dependent (a) dielectric constant and (b) dielectric loss for* $Co_{0.9}Cu_{0.1}Fe_{2-x}In_xO_4$ *(where x = 0.00, 0.03, 0.06, 0.09, 0.12, and 0.15) at 1 MHz.*

The variation in ε' and *tan* δ with the temperature at a constant frequency of 1 MHz is shown in Fig. 5.41. At higher temperature a strong temperature dependence of ε' was observed while at a lower temperature it is almost temperature independent. The enhancement in ε' at elevated temperature is due to the increased mobility of thermally activated charge carriers, thereby increasing the rate of hopping and hence the ε'[423].

However, at lower temperatures, the thermal energy provided to the samples is insufficient to enhance the mobility of the charge carriers, as a result, it reduces the hopping process [228].

5.6 UV-Vis diffuse reflectance spectroscopy (UV-DRS)

5.6.1 $Y_{2-x}Ce_yEu_xO_3$ (where y = 0.00, 0.01 and x = 0.00, 0.02, 0.04, and 0.06)

The diffuse reflectance spectra of the substituted and co-substituted Y_2O_3 phosphors were measured against the reference barium sulphate. Figure 5.42 shows diffuse reflectance spectra of the $Y_{2-x}Ce_yEu_xO_3$ (where y = 0.00, 0.01 and x = 0.00, 0.02, 0.04, and 0.06) phosphor. A sharp band was observed ~215 nm for all the compositions suggesting that light having this particular wavelength was absorbed.

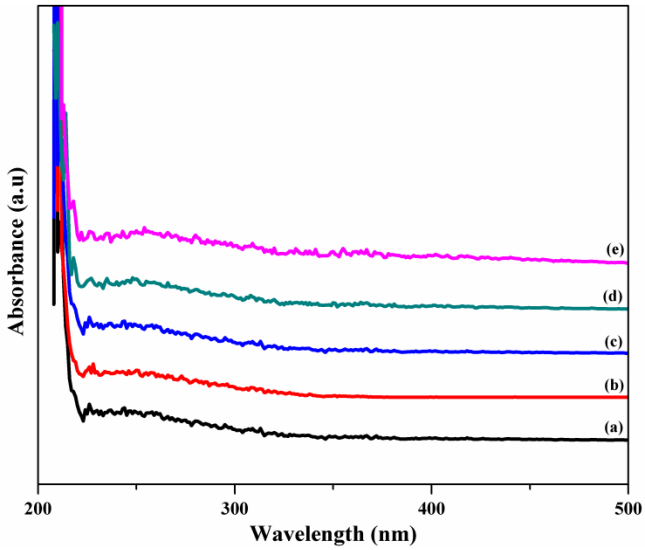

Fig. 5.42 *UV-DRS plots of (a) Y_2O_3 (b) $Y_{1.99}Ce_{0.01}O_3$ (c) $Y_{1.97}Ce_{0.01}Eu_{0.02}O_3$ (d) $Y_{1.95}Ce_{0.01}Eu_{0.04}O_3$ (e) $Y_{1.93}Ce_{0.01}Eu_{0.06}O_3$.*

The band-gap of the prepared samples were estimated with the help of Kubelka-Munk function using diffuse reflectance spectra (Fig. 5.43) and the values obtained are tabulated in Table 5.30. Similar band gap values for substituted Y_2O_3 were obtained by Som et al. [273].

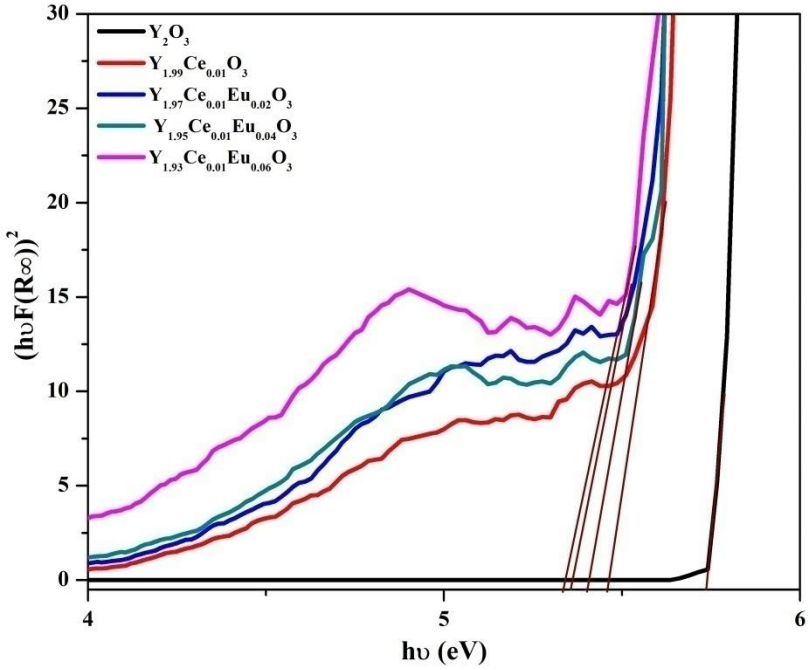

Fig. 5.43*Tauc plots of $Y_{2-x}Ce_yEu_xO_3$ (where y = 0.00, 0.01 and x = 0.00, 0.02, 0.04, and 0.06).*

Table 5.30 Estimated band gap values for $Y_{2-x}Ce_yEu_xO_3$ (where y = 0.00, 0.01 and x = 0.00, 0.02, 0.04, and 0.06).

Sample Composition	Band gap (eV)
Y_2O_3	5.73
$Y_{1.99}Ce_{0.01}O_3$	5.48
$Y_{1.97}Ce_{0.01}Eu_{0.02}O_3$	5.31
$Y_{1.95}Ce_{0.01}Eu_{0.04}O_3$	5.36
$Y_{1.93}Ce_{0.01}Eu_{0.06}O_3$	5.35

5.6.2 $Y_{2-x}Ce_yEr_xO_3$ (where y = 0.00, 0.01 and x = 0.00, 0.02, 0.04, and 0.06)

Fig. 5.44 shows the UV-DRS spectra of the Ce and Er co-substituted Y_2O_3. A sharp absorption band was observed at ~215 nm which confirms that the light having this particular wavelength was absorbed by the phosphor.

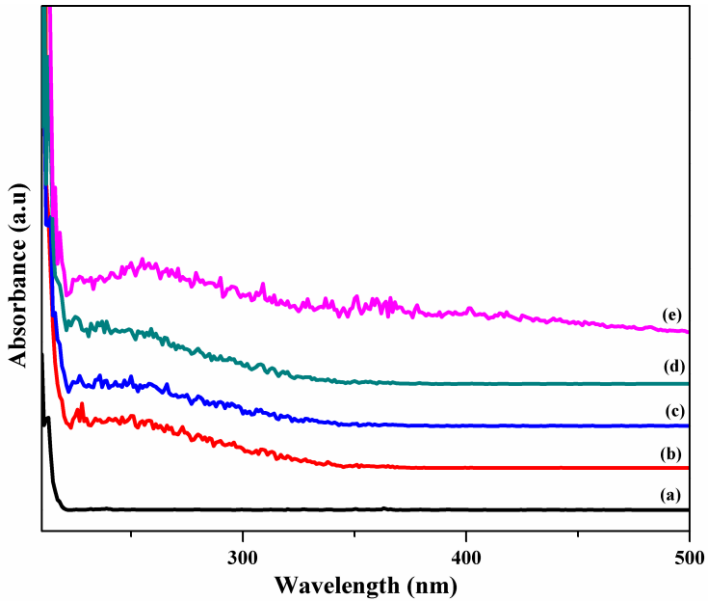

Fig. 5.44 *UV-DRS plots of (a) Y_2O_3 (b) $Y_{1.99}Ce_{0.01}O_3$ (c) $Y_{1.97}Ce_{0.01}Er_{0.02}O_3$ (d) $Y_{1.95}Ce_{0.01}Er_{0.04}O_3$ (e) $Y_{1.93}Ce_{0.01}Er_{0.06}O_3$.*

The plots of $(\alpha hv)^2$ versus hv from the optical absorption spectral data is presented in Fig. 5.45. Extrapolating the linear section of the curves to touch the x-axis yields the band gap values (Table 5.31). The values obtained were in close agreement with the literature reports.

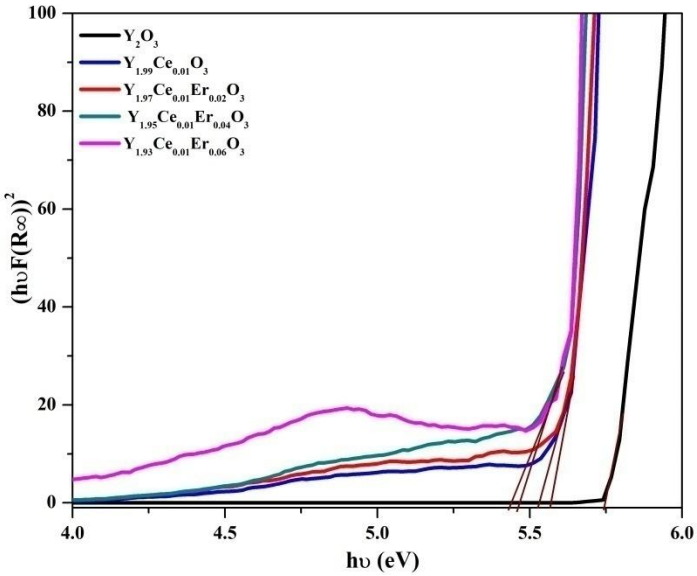

Fig. 5.45 *Tauc plots for $Y_{2-x}Ce_yEr_xO_3$ (where y = 0.00, 0.01 and x = 0.00, 0.02, 0.04, and 0.06).*

Table 5.31 Estimated band gap values for $Y_{2-x}Ce_yEr_xO_3$ (where y = 0.00, 0.01 and x = 0.00, 0.02, 0.04, and 0.06).

Sample Composition	Band gap (eV)
Y_2O_3	5.73
$Y_{1.99}Ce_{0.01}O_3$	5.48
$Y_{1.97}Ce_{0.01}Er_{0.02}O_3$	5.47
$Y_{1.95}Ce_{0.01}Er_{0.04}O_3$	5.41
$Y_{1.93}Ce_{0.01}Er_{0.06}O_3$	5.43

5.6.3 $Gd_{1.96-x}Er_{0.04}Yb_xO_3$ (where x = 0.04, 0.08, 0.12, 0.16 and 0.20)

The diffuse reflectance spectra of $Gd_{1.96-x}Er_{0.04}Yb_xO_3$ (where x = 0.04, 0.08, 0.12, 0.16 and 0.20)have been presented in Fig. 5.46.

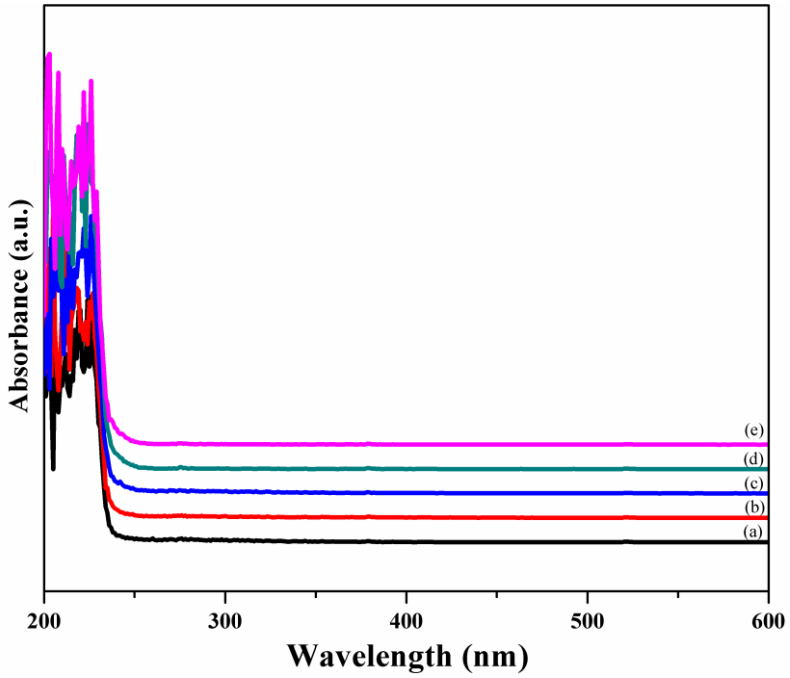

Fig. 5.46 *UV-DRS spectra of (a) $Gd_{1.92}Er_{0.04}Yb_{0.04}O_3$ (b) $Gd_{1.88}Er_{0.04}Yb_{0.08}O_3$ (c) $Gd_{1.84}Er_{0.04}Yb_{0.12}O_3$ (d) $Gd_{1.80}Er_{0.04}Yb_{0.16}O_3$ (e) $Gd_{1.76}Er_{0.04}Yb_{0.20}O_3$.*

Taucs plot was used to estimate the band gap and is represented in Fig. 5.47. and the band gap values obtained are tabulated in Table 5.32. Kumar et al. [332] reported similar band gap values for substituted Gd_2O_3.

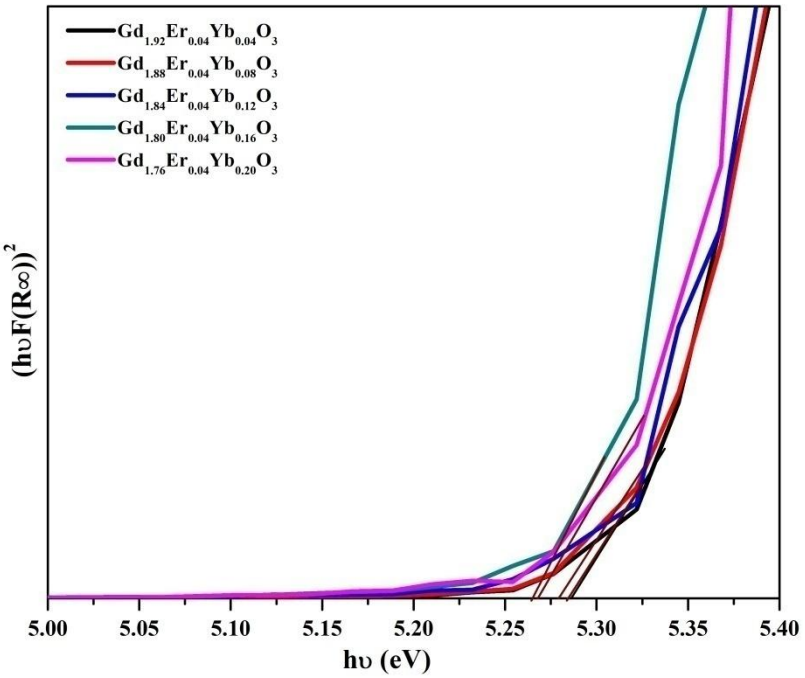

Fig. 5.47 *Tauc plots of $Gd_{1.96-x}Er_{0.04}Yb_xO_3$ (where x = 0.04, 0.08, 0.12, 0.16 and 0.20).*

Table 5.32 Estimated band gap values for *$Gd_{1.96-x}Er_{0.04}Yb_xO_3$ (where x = 0.04, 0.08, 0.12, 0.16 and 0.20)*

Sample Composition	Band gap (eV)
$Gd_{1.92}Er_{0.04}Yb_{0.04}O_3$	5.28
$Gd_{1.88}Er_{0.04}Yb_{0.08}O_3$	5.28
$Gd_{1.84}Er_{0.04}Yb_{0.12}O_3$	5.27
$Gd_{1.80}Er_{0.04}Yb_{0.16}O_3$	5.27
$Gd_{1.76}Er_{0.04}Yb_{0.20}O_3$	5.27

5.6.4 $Gd_{1.96-x}Ho_{0.04}Yb_xO_3$ (where x = 0.04, 0.08, 0.12, 0.16 and 0.20)

Fig. 5.48 shows the UV-DRS spectra of $Gd_{1.96-x}Ho_{0.04}Yb_xO_3$ (where x = 0.04, 0.08, 0.12, 0.16 and 0.20) phosphor.

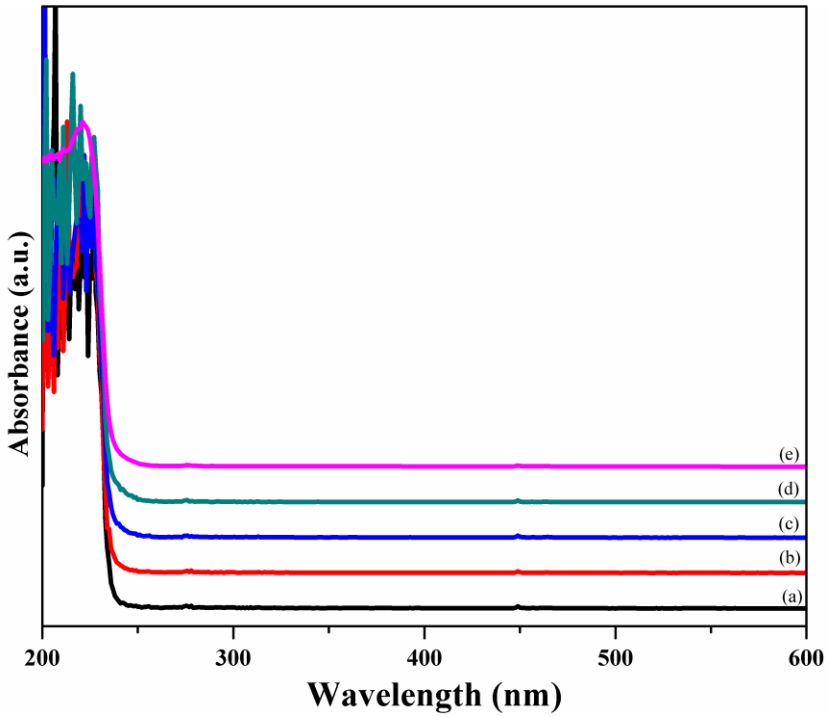

Fig. 5.48 *UV-DRS spectra of (a) $Gd_{1.92}Ho_{0.04}Yb_{0.04}O_3$ (b) $Gd_{1.88}Ho_{0.04}Yb_{0.08}O_3$ (c) $Gd_{1.84}Ho_{0.04}Yb_{0.12}O_3$ (d) $Gd_{1.80}Ho_{0.04}Yb_{0.16}O_3$ (e) $Gd_{1.76}Ho_{0.04}Yb_{0.20}O_3$.*

The band gap values obtained from the Tauc plot (Fig. 5.49)are tabulated in Table 5.33. Similar band gap values for Gd_2O_3 were obtained by Dhananjaya et al. [424]. The existence of surface defects, oxygen vacancies, and distortion inside the material could be accountable for the variation in the band gap of the phosphors.

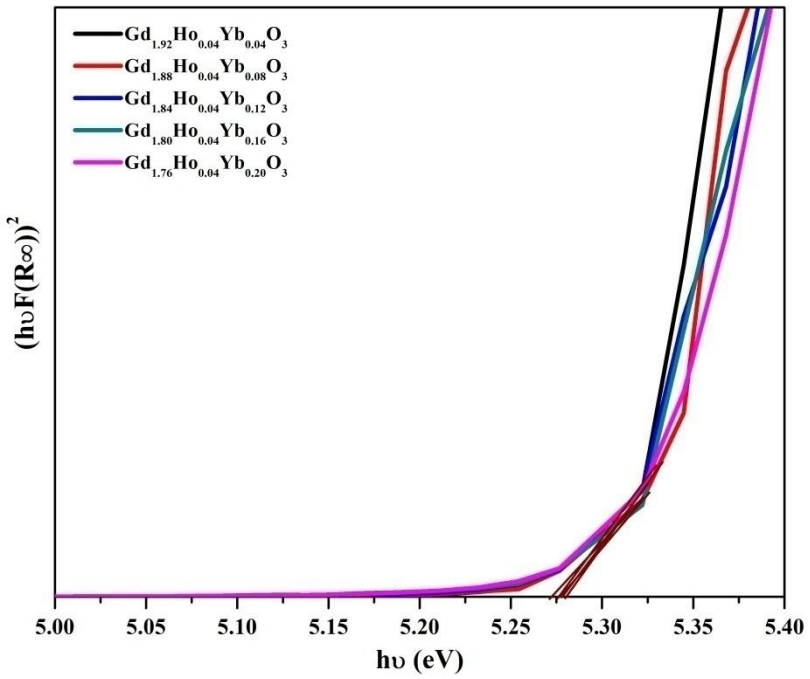

Fig. 5.49 *Tauc plots of $Gd_{1.96-x}Ho_{0.04}Yb_xO_3$ (where x = 0.04, 0.08, 0.12, 0.16 and 0.20).*

Table 5.33 Estimated band gap values for $Gd_{1.96-x}Ho_{0.04}Yb_xO_3$ (where x = 0.04, 0.08, 0.12, 0.16 and 0.20).

Sample Composition	Band gap (eV)
$Gd_{1.92}Ho_{0.04}Yb_{0.04}O_3$	5.27
$Gd_{1.88}Ho_{0.04}Yb_{0.08}O_3$	5.29
$Gd_{1.84}Ho_{0.04}Yb_{0.12}O_3$	5.28
$Gd_{1.80}Ho_{0.04}Yb_{0.16}O_3$	5.28
$Gd_{1.76}Ho_{0.04}Yb_{0.20}O_3$	5.26

5.7 Photoluminescence studies

5.7.1 $Y_{2-x}Ce_yEu_xO_3$ (where y = 0.00, 0.01 and x = 0.00, 0.02, 0.04, and 0.06)

The excitation spectrum of Ce^{3+} substituted Y_2O_3 was monitored at 430 nm emission wavelength (Fig. 5.50). The spectrum showed a peak at ~383 nm.

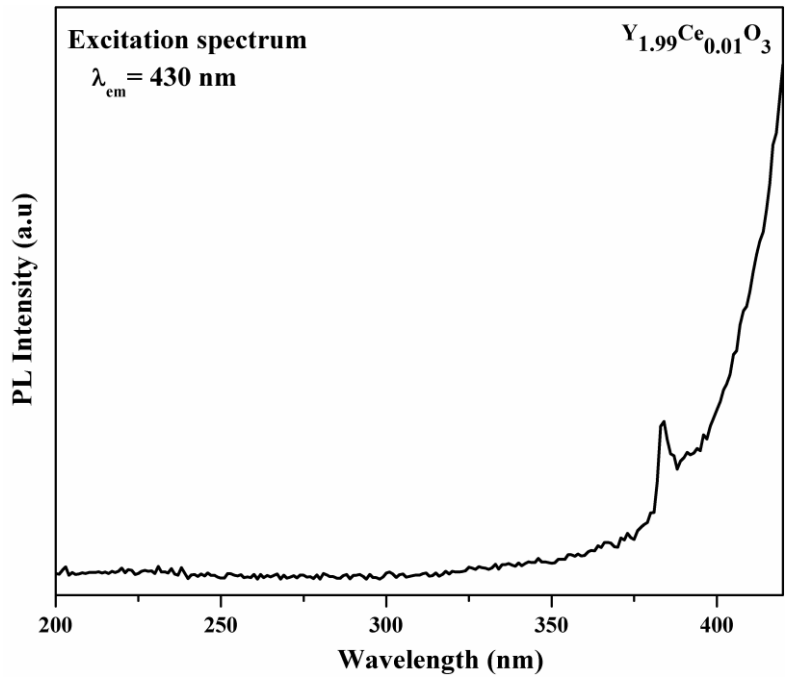

Fig. 5.50 *Excitation spectrum of* $Y_{1.99}Ce_{0.01}O_3$ *monitored at 430 nm.*

.

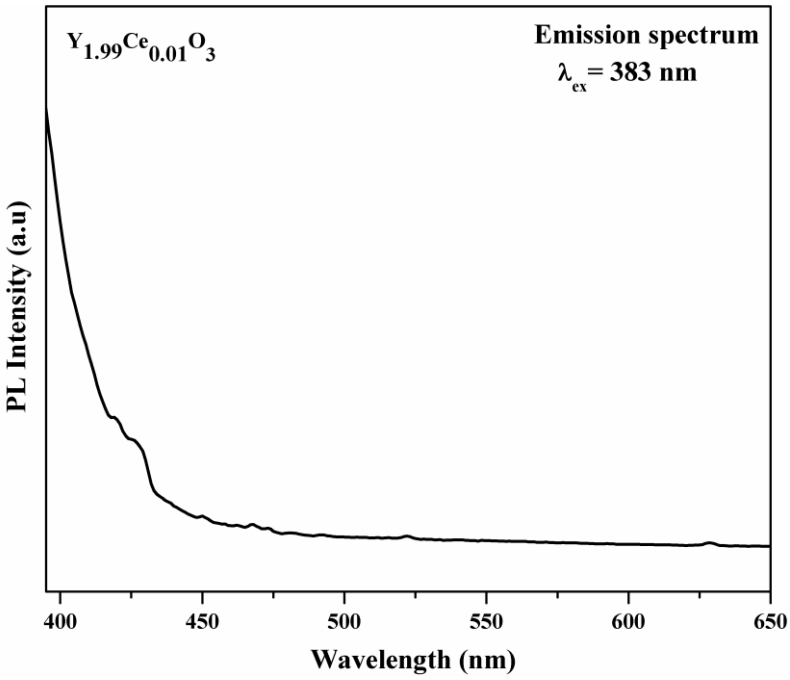

Fig. 5.51 *Emission spectrum of* $Y_{1.99}Ce_{0.01}O_3$ *under excitation of 383 nm.*

The excitation spectrum for Eu^{3+} and Ce^{3+}co-substituted Y_2O_3 phosphor spectra were monitored at the 611 nm emission wavelength, corresponding to the $^5D_0 \rightarrow {}^7F_2$ transition of Eu^{3+} (Fig. 5.52).There are several bands, located at 361 nm, 381 nm, 393

nm, 415 nm, 465 nm, and 532 nm which correspond to the transitions $^7F_0 \rightarrow {}^5D_4$, $^7F_0 \rightarrow {}^5G_2$, $^7F_0 \rightarrow {}^5L_6$, $^7F_0 \rightarrow {}^5D_3$, $^7F_0 \rightarrow {}^5D_2$, and $^7F_0 \rightarrow {}^5D_1$ respectively. The strongest excitation bands for Eu^{3+} is found at 393 and 465 nm hence the samples were excited at these wavelengths.

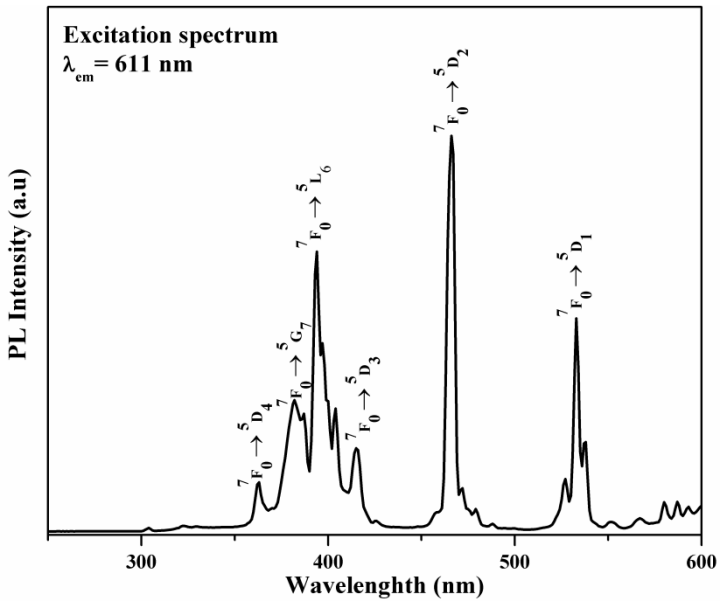

Fig. 5.52 *Excitation spectrum of $Y_{1.93}Ce_{0.01}Eu_{0.06}O_3$ monitored at 611 nm.*

In the room temperature emission spectra (Fig. 5.53, 5.54, 5.55) of Eu^{3+} and Ce^{3+}co-substituted Y_2O_3, Eu^{3+} showed its characteristic emission pattern. The emission spectra showed strong red emission. The sharp emission peaks were observed at 580, 587, 593, 599, 611, 630, and 650 nm associated with the $^5D_0 \rightarrow {}^7F_0$, $^5D_0 \rightarrow {}^7F_1$, $^5D_0 \rightarrow {}^7F_1$, $^5D_0 \rightarrow {}^7F_1$, $^5D_0 \rightarrow {}^7F_2$, $^5D_0 \rightarrow {}^7F_3$ and $^5D_0 \rightarrow {}^7F_3$ transition of Eu^{3+} ions respectively the strongest emission peak located at 611 nm corresponding to $^5D_0 \rightarrow {}^7F_2$ transition of Eu^{3+} ions (Fig. 5.53, Fig. 5.54, Fig. 5.55).These observations are in line with the previously reported results. It was also observed that the emission intensity increases with the increase of Eu^{3+} concentration. The Ce^{3+} emission has also shown its existence in the emission spectra, which indicates that there is no effective energy transfer between

$Ce^{3+}$and Eu^{3+} which is expected taking into consideration the sensitizing nature of Ce^{3+} ions. The only observation that could be made from the spectra is that the intensity of Ce^{3+} emission decreased when the Eu^{3+} substitution increased from 2 to 6 mol%, highlighting the concentration-dependent energy transfer or in other words it can be said that the increase in Eu^{3+} concentration in Y_2O_3 lattice has increased the interaction between Eu^{3+} and Ce^{3+} ions.

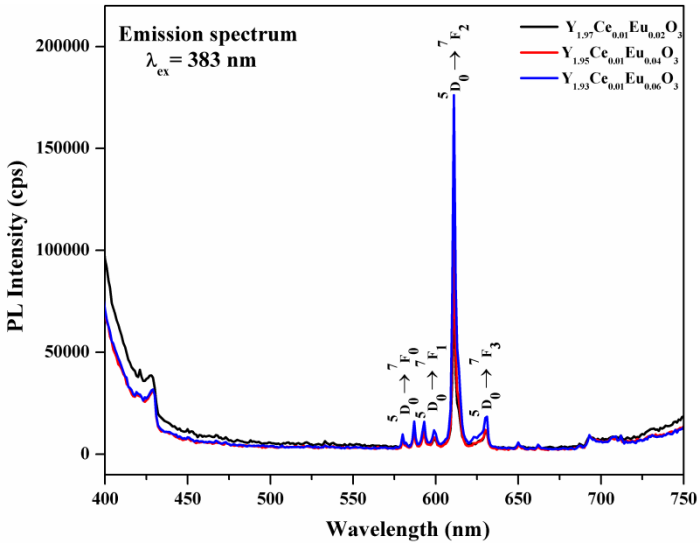

Fig. 5.53 *Emission spectra of $Y_{1.99-x}Ce_{0.01}Eu_xO_3$ (where x = 0.02, 0.04, and 0.06) under an excitation of 383 nm.*

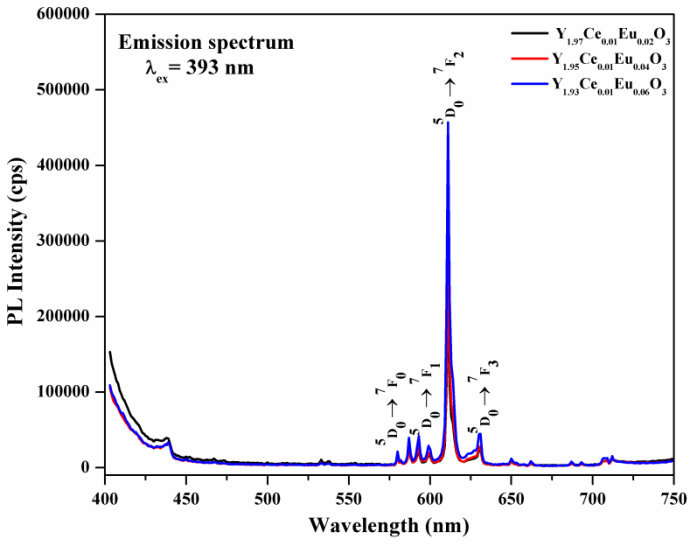

Fig. 5.54 *Emission spectra of $Y_{1.99-x}Ce_{0.01}Eu_xO_3$ (where x = 0.02, 0.04, and 0.06) under an excitation of 393 nm.*

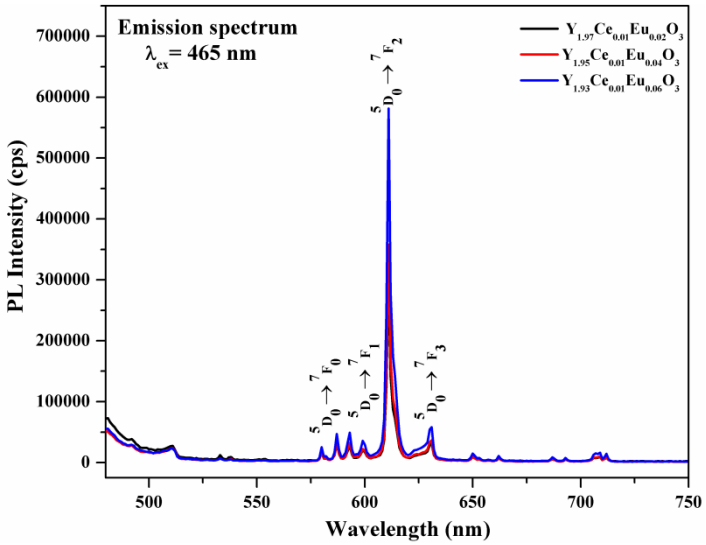

Fig. 5.55 *Emission spectra of $Y_{1.99-x}Ce_{0.01}Eu_xO_3$ (where x = 0.02, 0.04, and 0.06) under an excitation of 465 nm.*

Fig. 5.56 depicts the CIE chromaticity diagram estimated from GoCIE software in order to understand the overall emission color of Ce^{3+} and Eu^{3+} co-substituted Y_2O_3 phosphors. The position of CIE coordinates was marked considering a 393 nm excitation, and the emission spectra recorded from 400-750 nm were displayed in Fig. 5.53. The coordinates shifted towards the red region from the pink region with rising Eu^{3+} content. The CIE colour coordinates obtained were (0.37, 0.24), (0.43, 0.26), and (0.48, 027) for $Y_{1.97}Ce_{0.01}Eu_{0.02}O_3$,$Y_{1.95}Ce_{0.01}Eu_{0.04}O_3$, and $Y_{1.93}Ce_{0.01}Eu_{0.06}O_3$ respectively.

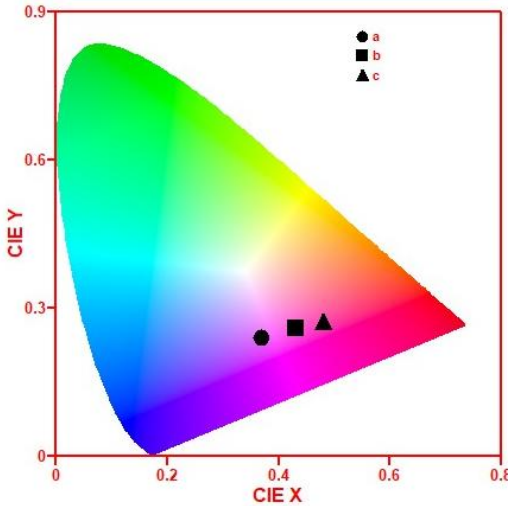

Fig. 5.56 *CIE diagram for (a) $Y_{1.97}Ce_{0.01}Eu_{0.02}O_3$ (b) $Y_{1.95}Ce_{0.01}Eu_{0.04}O_3$ and(c) $Y_{1.93}Ce_{0.01}Eu_{0.06}O_3$.*

5.7.2 $Y_{2-x}Ce_yEr_xO_3$ (where y = 0.00, 0.01 and x = 0.00, 0.02, 0.04, and 0.06)

Fig. 5.57 shows the PL excitation spectrum of the Ce^{3+} and Er^{3+} co-substituted Y_2O_3 phosphor recorded in the wavelength range of 200 - 550 nm (λ_{em}= 565 nm). A strong peak at 377 nm is assigned to the $^4I_{15/2}\rightarrow{}^4G_{11/2}$ transition and other bands with a maximum at 407, 453 and 490 nm are assigned to $^4I_{15/2}\rightarrow{}^2H_{9/2}$, $^4I_{15/2}\rightarrow{}^4F_{5/2}$, and $^4I_{15/2}\rightarrow{}^4F_{7/2}$ excited states of Er^{3+} ion transitions respectively.

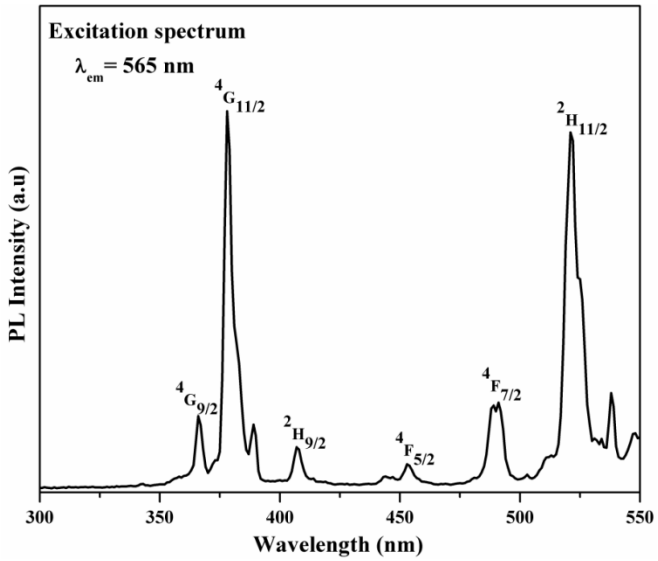

Fig. 5.57 *Excitation spectrum of $Y_{1.93}Ce_{0.01}Er_{0.06}O_3$ monitored at 565 nm.*

Figure5.58 and 5.59 shows the emission spectra of Ce^{3+} and Er^{3+} co-substituted Y_2O_3phosphor under 377 and 383 nm excitation. The emission spectra display the characteristic emission peaks of Er^{3+} ions in cubic Y_2O_3. The intense emission peaks observed in the green region (520–565 nm) were assigned to the ($^2H_{11/2}$, $^4S_{3/2}$) $\rightarrow{}^4I_{15/2}$ transitions of Er^{3+} ions. The PL intensity at 524, 538, 553 and 563 nm was found to increase with substituent concentration up to 4 mol% of Er^{3+} and then decreased with a further increase in the substituent concentration. At lower concentrations of the Er^{3+}, the optical activation of the Er^{3+} ions becomes more, which results in an increase in the PL

emission intensity. As the concentration of Er^{3+} exceeds the critical concentration, the emission intensity of the ($^2H_{11/2}$, $^4S_{3/2}$) $\rightarrow$ $^4I_{15/2}$ transitions gets reduced. The decrease was attributed to the concentration quenching, as the distance between the Er^{3+} ions in the host lattice gets reduced, it causes the bunching of the Er^{3+} ions which results in an increase of the crosslinking which leads to the PL quenching. The concentration quenching effects have been well documented in the literature.

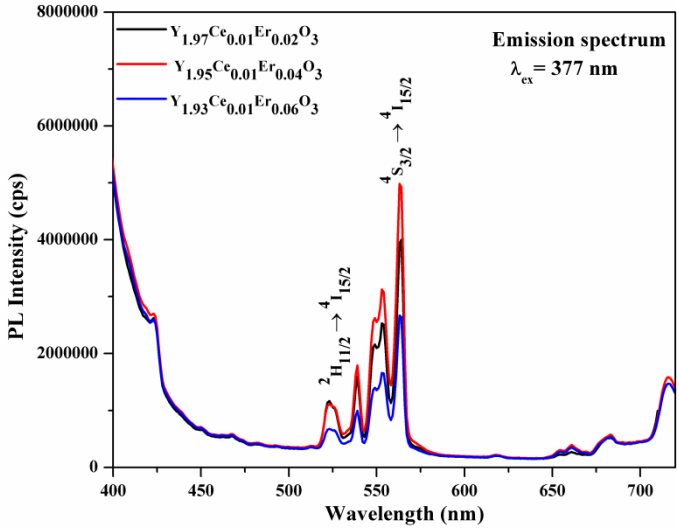

Fig. 5.58 *Emission spectra of $Y_{1.99-x}Ce_{0.01}Er_xO_3$ (where x = 0.02, 0.04, and 0.06) under an excitation of 377 nm.*

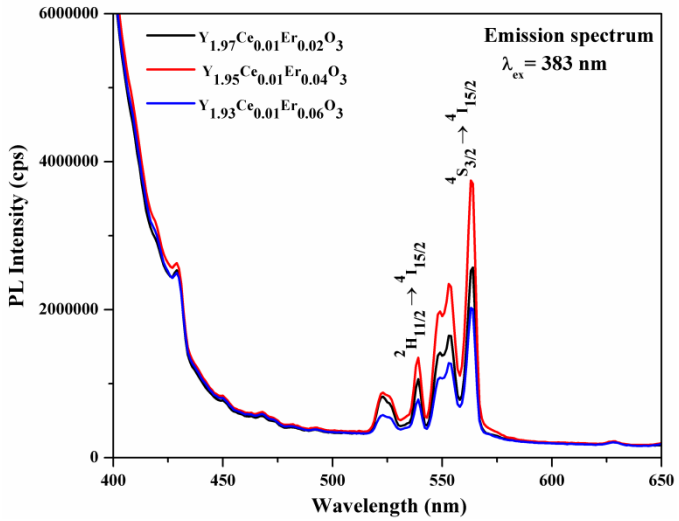

Fig. 5.59 *Emission spectra of $Y_{1.99-x}Ce_{0.01}Er_xO_3$ (where x = 0.02, 0.04, and 0.06) under an excitation of 383 nm.*

The CIE diagram (Fig. 5.60) presents the overall emission color of Ce^{3+} and Er^{3+} co-substituted Y_2O_3 phosphor samples and indicates that the blue-green emission color approaches green color with an increase in the Er^{3+} concentration. The position of CIE coordinates was marked considering a 377 nm excitation, and the emission spectra recorded in the range of 420-750 nm were shown in Fig. 5.58. The CIE coordinates were found to be (0.26, 0.28), (0.27, 0.28) and (0.26, 0.31) for $Y_{1.97}Ce_{0.01}Er_{0.02}O_3$, $Y_{1.95}Ce_{0.01}Er_{0.04}O_3$ and $Y_{1.93}Ce_{0.01}Er_{0.06}O_3$ respectively.

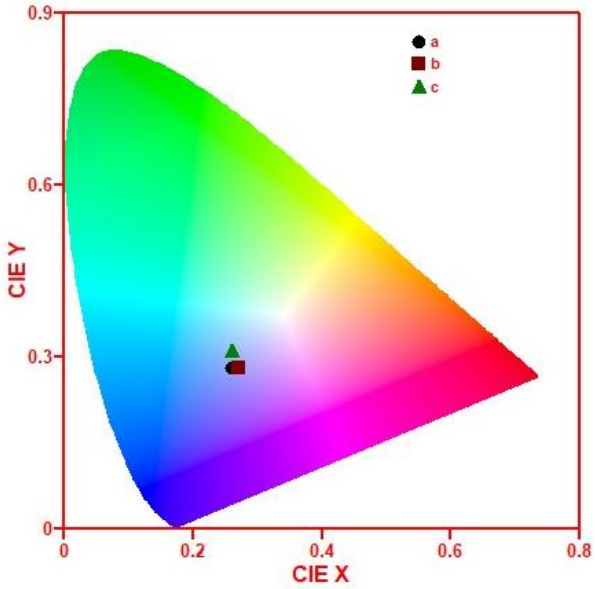

Fig. 5.60 *CIE diagram for (a) $Y_{1.97}Ce_{0.01}Er_{0.02}O_3$ (b) $Y_{1.95}Ce_{0.01}Er_{0.04}O_3$ and(c) $Y_{1.93}Ce_{0.01}Er_{0.06}O_3$.*

5.7.3 $Gd_{1.96-x}Er_{0.04}Yb_xO_3$ (where x = 0.04, 0.08, 0.12, 0.16 and 0.20)

Up-conversion (UC) is a phenomenon in which the absorption of two or more low-energy photons results in the emission of a higher-energy photon. Therefore, the wavelength of the emitted light is shorter than that of the excitation light. The UC emission spectra of $Gd_{1.96-x}Er_{0.04}Yb_xO_3$ (where x = 0.04, 0.08, 0.12, 0.16 and 0.20) under the laser excitation of 980 nm are presented in Figure 5.61. The major emission peaks of

Er^{3+} ions shift from 562 ($^2H_{11/2}/^4S_{3/2} \rightarrow {}^4I_{15/2}$) to 660 nm ($^4F_{9/2} \rightarrow {}^4I_{15/2}$), resulting in the increased integrated intensity ratios of red-to-green emission which results in the UC emission color shifting from green to red. The red emission could be enhanced further by varying the Yb^{3+} ion concentration in Er^{3+}/Yb^{3+} co-substituted Gd_2O_3. The emission intensity at 562 nm was maximum at 16 mol%. For 20 mol%, the emission intensity of 660 nm peak was found to decrease which is attributed to the concentration quenching between the Yb^{3+} ions.

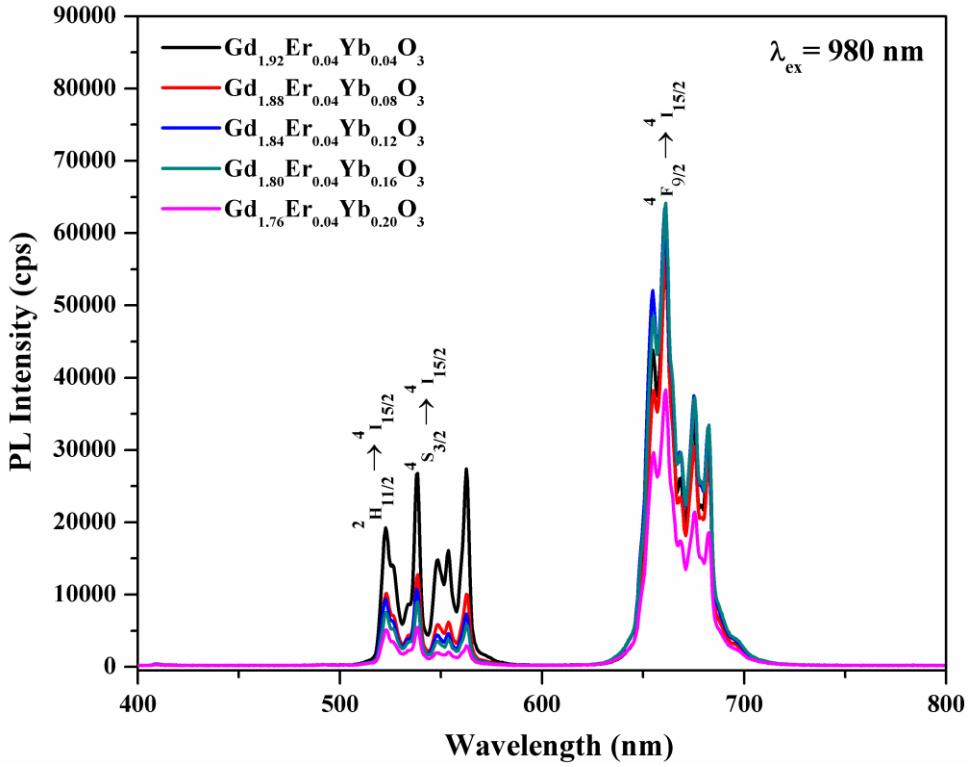

Fig. 5.61 *UC emission spectra of $Gd_{1.96-x}Er_{0.04}Yb_xO_3$ (where x = 0.04, 0.08, 0.12, 0.16 and 0.20).*

The CIE diagram for Up-conversion emission of various concentrations of Yb^{3+} and 4.0 mol% Er^{3+} co-substituted Gd_2O_3 phosphors under 980 nm laser excitation with 1.5 W pump power is shown in Fig. 5.62. From the figure, it was observed that the overall emission color of sample shifts from green to yellow and then orange as the

Yb^{3+}content is increased. The colour co-ordinates estimated from CIE diagram are tabulated in Table 5.34.

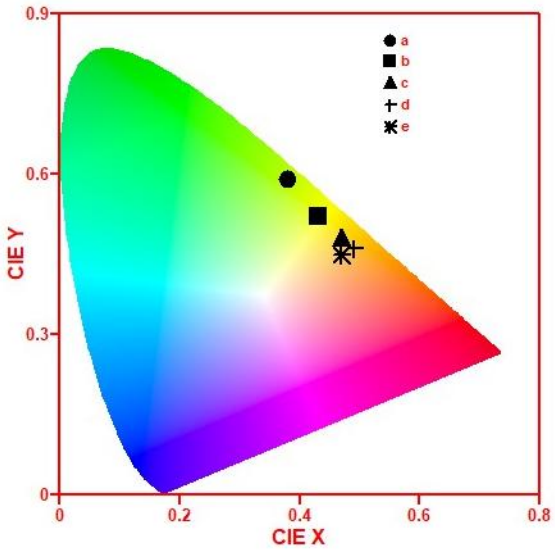

Fig. 5.62 *CIE diagram for (a) $Gd_{1.92}Er_{0.04}Yb_{0.04}O_3$ (b) $Gd_{1.88}Er_{0.04}Yb_{0.08}O_3$ (c) $Gd_{1.84}Er_{0.04}Yb_{0.12}O_3$ (d) $Gd_{1.80}Er_{0.04}Yb_{0.16}O_3$ (e) $Gd_{1.76}Er_{0.04}Yb_{0.20}O_3$.*

Table 5.34 X, Y coordinates for CIE diagram for $Gd_{1.96-x}Er_{0.04}Yb_xO_3$ (where x = 0.04, 0.08, 0.12, 0.16 and 0.20).

Sample Composition	X	Y
$Gd_{1.92}Er_{0.04}Yb_{0.04}O_3$	0.38	0.59
$Gd_{1.88}Er_{0.04}Yb_{0.08}O_3$	0.43	0.52
$Gd_{1.84}Er_{0.04}Yb_{0.12}O_3$	0.47	0.48
$Gd_{1.80}Er_{0.04}Yb_{0.16}O_3$	0.49	0.46
$Gd_{1.76}Er_{0.04}Yb_{0.20}O_3$	0.47	0.45

5.7.4 $Gd_{1.96-x}Ho_{0.04}Yb_xO_3$ (where x = 0.04, 0.08, 0.12, 0.16 and 0.20)

The UC luminescence spectra of $Gd_{1.96-x}Ho_{0.04}Yb_xO_3$ (where x = 0.04, 0.08, 0.12, 0.16 and 0.20)phosphors under laser excitation of 980 nm has been shown in Fig. 5.63. The effect of various concentration of Yb^{3+} (4, 8, 12, 16 and 20 mol %) was tried on 4 mol% Ho^{3+} substituted Gd_2O_3. The dominant green emission peaks ~550 nm, ($^5S_2/^5F_4 \rightarrow$

$^5I_8$) accompanied by relatively weak red emission peaks ~667 nm, ($^5F_5 \rightarrow {}^5I_8$) were detected. For UC materials the individually substituted Ho^{3+} ions are too weak to absorb the 980 nm photons, hence Yb^{3+} ions are taken as the NIR sensitizer. The Yb^{3+} ion acts as a sensitizer and Ho^{3+} ion as a luminescent ion. The emission intensity of red emission was found to decrease while that of green emission increased with Yb^{3+} substitution up to 8 mol%. Further, a continuous decrease in emission intensity was observed with Yb^{3+} substitution. The decreased intensity could be considered as the consequence of the quenching effect, which transfers energy from the Ho^{3+} ions back toYb^{3+} ions.

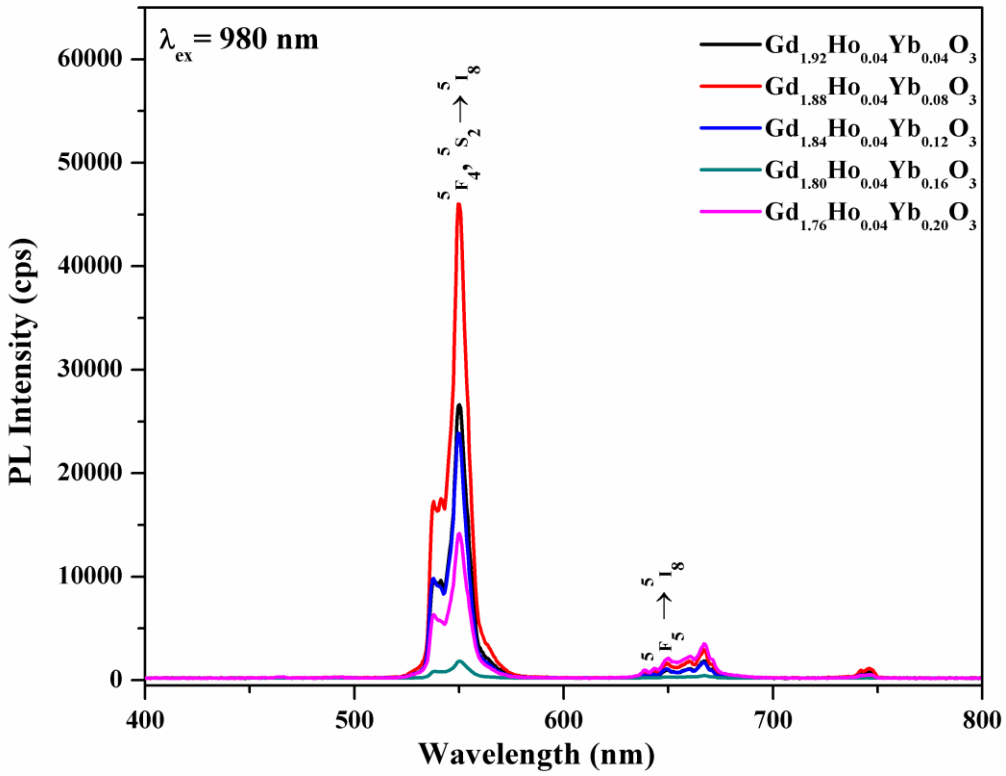

Fig. 5.63 *UC emission spectra of $Gd_{1.96-x}Ho_{0.04}Yb_xO_3$ (where x = 0.04, 0.08, 0.12, 0.16 and 0.20).*

For understanding the overall emission color of the emitted light for Ho^{3+} and Yb^{3+} co-substituted Gd_2O_3 under the laser excitation of 980 nm, the color coordinates

were determined (Table 5.35) and are presented in the CIE chromaticity diagram (Fig. 5.64). The calculated color coordinates showed that the overall emission color shifts from green to yellow region with increasing Yb^{3+} substitution. For $Gd_{1.80}Ho_{0.04}Yb_{0.16}O_3$ an unexpected greenish-blue emission was observed.

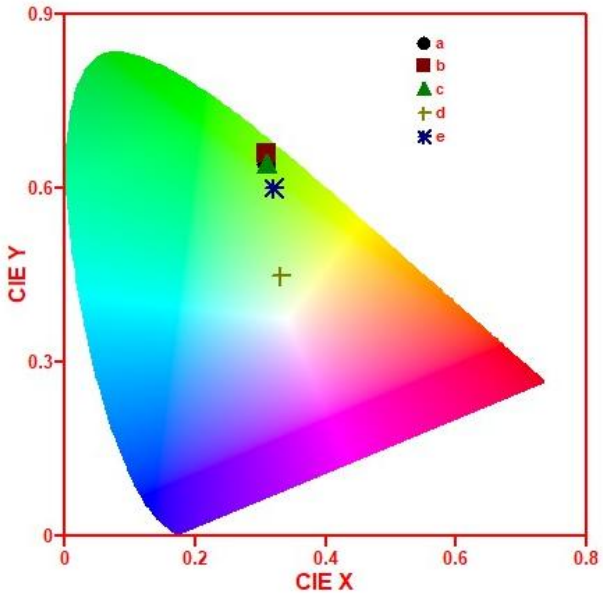

Fig. 5.64 *CIE diagram for (a) $Gd_{1.92}Ho_{0.04}Yb_{0.04}O_3$ (b) $Gd_{1.88}Ho_{0.04}Yb_{0.08}O_3$ (c) $Gd_{1.84}Ho_{0.04}Yb_{0.12}O_3$ (d) $Gd_{1.80}Ho_{0.04}Yb_{0.16}O_3$ (e) $Gd_{1.76}Ho_{0.04}Yb_{0.20}O_3$.*

Table 5.35 X, Y coordinates for CIE diagram for $Gd_{1.96-x}Ho_{0.04}Yb_xO_3$ (where x = 0.04, 0.08, 0.12, 0.16 and 0.20).

Sample Composition	X	Y
$Gd_{1.92}Ho_{0.04}Yb_{0.04}O_3$	0.31	0.64
$Gd_{1.88}Ho_{0.04}Yb_{0.08}O_3$	0.31	0.66
$Gd_{1.84}Ho_{0.04}Yb_{0.12}O_3$	0.31	0.64
$Gd_{1.80}Ho_{0.04}Yb_{0.16}O_3$	0.33	0.45
$Gd_{1.76}Ho_{0.04}Yb_{0.20}O_3$	0.32	0.60

5.8 Antimicrobial Studies

5.8.1 Antimicrobiocity of Cu^{2+} substituted $CoFe_2O_4$ nanoparticles against six microbial pathogens by disc diffusion method

A series of Cu^{2+} ion substituted $CoFe_2O_4$ nanoparticles ($Co_{1-x}Cu_xFe_2O_4$wherein x = 0.00, 0.05, 0.10, 0.15, 0.20 and 0.25) were tested against six different microbial pathogens viz. *Escherichia coli*, *Proteus vulgaris, Salmonella typhi, Staphylococcus aureus, Streptococcus pyogenes,*and*Candida albicans*using: i) Nutrient-rich solid media and Kirby-Bauer agar disc diffusion method [425] ii) Liquid nutrient-rich growth media. Individual pathogens maintained on nutrient agar were plated on the same agar. Filter paper discs of uniform size, incorporated with 3 mg/ml of different concentrations of Cu^{2+} in $CoFe_2O_4$ nanoparticles were placed on the agar and incubated at 37 ℃ for 24 h. Areas around the sample discs showing no growth of corresponding pathogens were recorded as a zone of inhibition.

The response of Gram-negative *E. coli* and Gram-positive *S. aureus* were studied against each concentration of Cu^{2+} in $CoFe_2O_4$ nanoparticles in nutrient broth. The aliquots were removed every 4 h to check growth at 600 nm for 32 h. Antimicrobial effect of nanocomposites was monitored in terms of the number of colonies obtained at 12 h of growth and expressed as survival percentage using the following equation.

$$\text{Survival } \% = \frac{\text{Number of Colony Forming Units in the presence of nanocomposites}}{\text{Number of Colony Forming Units in the absence of nanocomposites}} \times 100$$

5.8.2 Antimicrobial properties of substituted spinel ferrites on *E. Coli* by well diffusion method.

Minimum inhibitory concentrations (MIC) of the substituted $CoFe_2O_4$ and cobalt copper ferrite were carried out using 100 mg/ml stock solutions of each sample suspended in methanol as solvent. *E. coli* maintained on nutrient agar was grown to log phase and added to the wells of microtitre plate containing nutrient broth with different concentrations (1 to 10 mg/ml) of the prepared materials under static condition. The plate was incubated at 37 °C and checked for growth in terms of turbidity at 600 nm for 24 h. The experiments were carried out in triplicates and appropriate methanol as control was maintained. The MIC is the lowest concentration of the material at which the absorbance was less than 0.05 and no visible growth of the *E. coli* was seen. A further effect was seen in terms of a number of colonies obtained at 12 h of growth and expressed as survival percentage using the equation mentioned in section 5.7.1.

5.8.3 Antimicrobiocity of Cu^{2+} substituted $CoFe_2O_4$ nanoparticles

Replacement of Co^{2+} ions by Cu^{2+}ions significantly inhibited the growth of all six pathogens in the order of *E. coli* > *S. aureus* > *P. vulgaris*> *S. typhi*> *S. pyogenes*> *C. albicans* (Fig. 5.65). Zone of inhibition of growth in *E. coli, P. vulgaris,* and *S. typhi* was very sharp and clear while that of the Gram-positive cultures, the zones were fuzzy. Additionally *C. albicans* showed minimum sensitivity to the increasing concentration of Cu^{2+}ions. It can be seen in Fig. 5.66, that the zone of inhibition of growth for all pathogens increases with increase in Cu^{2+} ion concentration in $CoFe_2O_4$ nanoparticles with the highest zone of inhibition of 20.66 mm attained for $Co_{0.75}Cu_{0.25}Fe_2O_4$ against Gram-negative*E. coli*whileGram-positive yeast *C. albicans* showed the least (5.00 mm).

This clearly demonstrates the ability of Cu^{2+} substituted $CoFe_2O_4$ to inhibit microbial pathogens. Such an effect of$Co_{0.5}Cu_{0.5}Fe_2O_4$ at 1 mg/ml concentration against *E. coli* and *S. aureus* has been reported earlier [145]. Also using 2 mg/ml of different concentrations of Cu^{2+} substituted $CoFe_2O_4$ has been checked for antibacterial activity against *E. coli* [426].

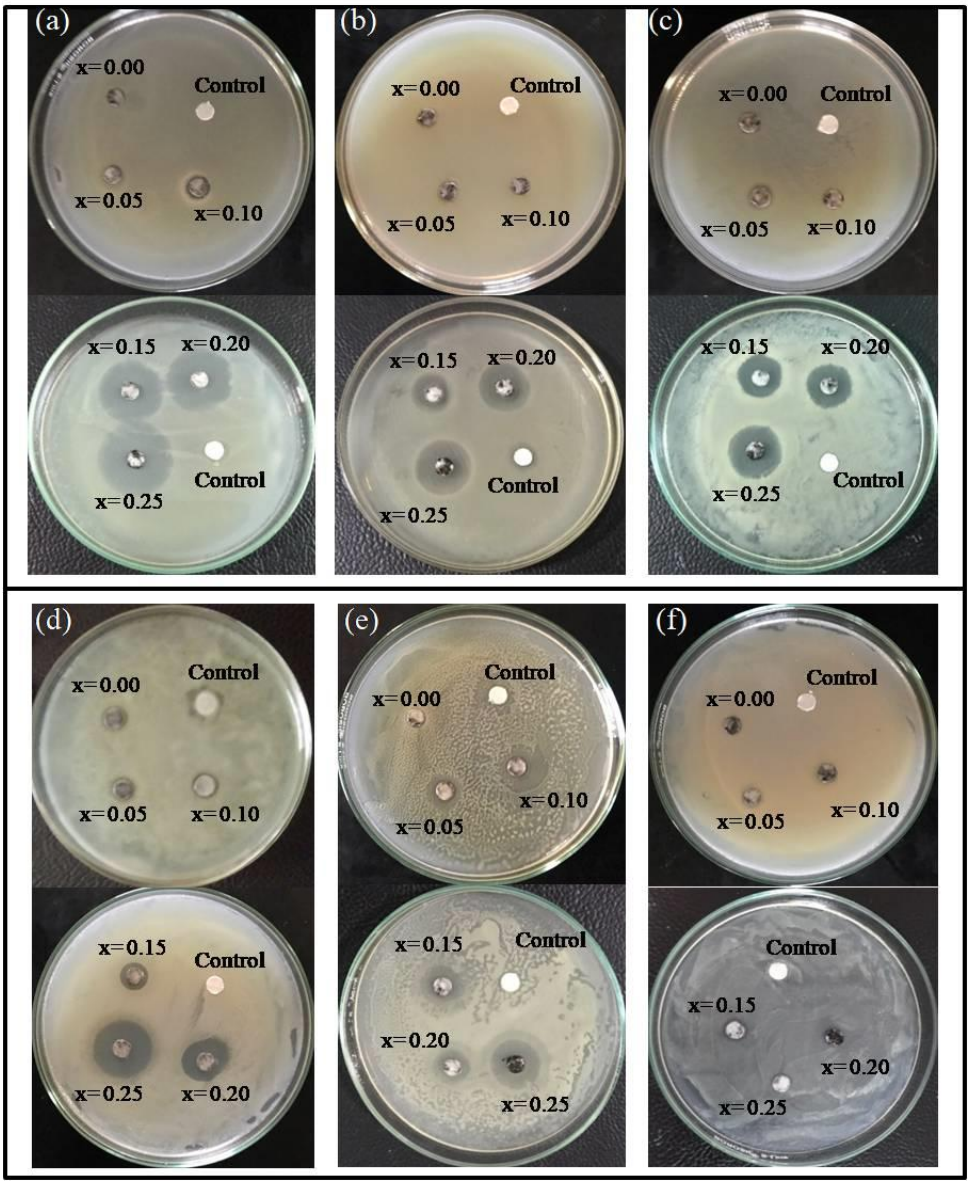

Fig. 5.65 *Effect of* $Co_{1-x}Cu_xFe_2O_4$ *where x = 0.00, 0.10, 0.15, 0.20, and 0.25 on growth of six clinical pathogens : (a) E. coli, (b) P. vulgaris, (c) S. typhi, (d) S. aureus, (e) S. pyogenes and (f) C. albicans evaluated by Kirby-Bauer agar disc diffusion assay.*

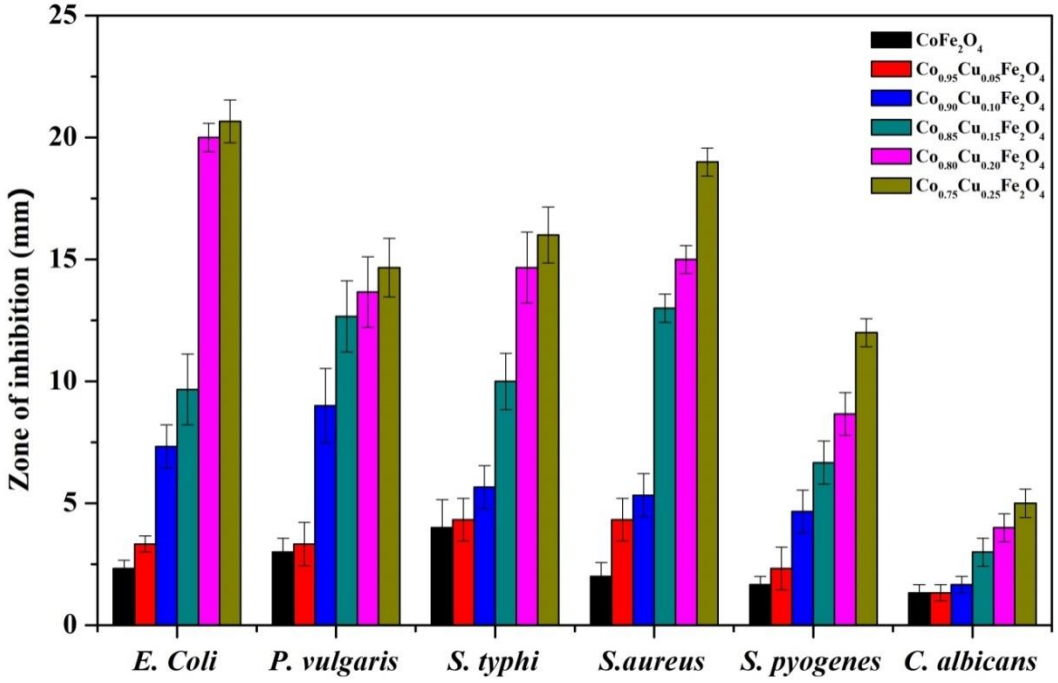

Fig. 5.66*Zone of Inhibition of growth of: E. coli, P. vulgaris, S. typhi, S. aureus, S. pyogenes, and C. albicans by* $Co_{1-x}Cu_xFe_2O_4$ *(where x = 0.00, 0.10, 0.15, 0.20, and 0.25)*

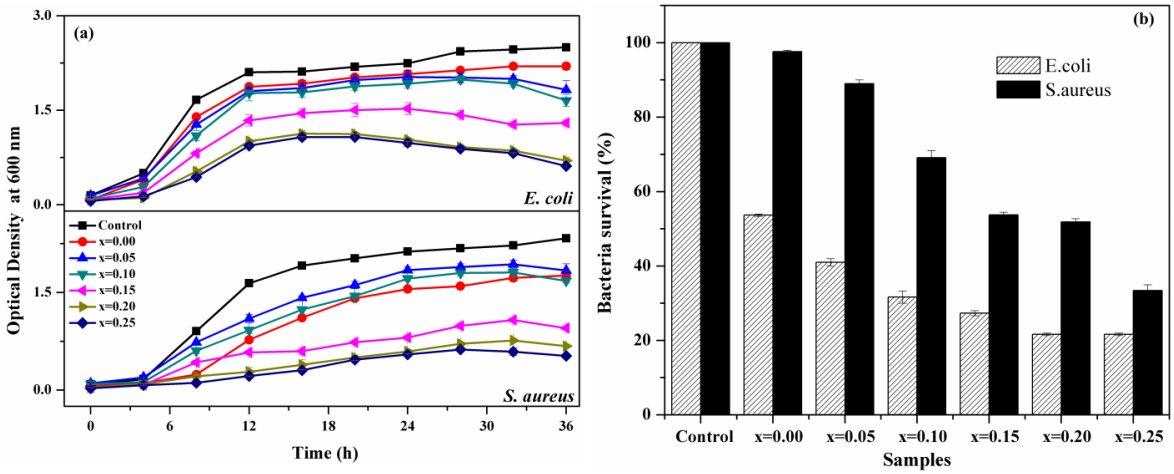

Fig. 5.67*Growth (a) and Survival (b) of: E. coli and S. aureus in presence of* $Co_{1-x}Cu_xFe_2O_4$ *where x = 0.00, 0.10, 0.15, 0.20, and 0.25.*

As seen in Fig. 5.67(a), the growth of *E. coli* and *S. aureus* decreased with increase in Cu^{2+} ion concentration in $CoFe_2O_4$. The results indicate that the augmentation of the Cu^{2+}substituent in $CoFe_2O_4$ enriches the nanoparticles in its

antimicrobial potency. The $Co_{0.80}Cu_{0.20}Fe_2O_4$ and $Co_{0.75}Cu_{0.25}Fe_2O_4$ showed 50% of cell death for both *E. coli* and *S. aureus*. Further as depicted in Fig. 5.67(b), the overall percent survival in the presence of Cu^{2+} substituted $CoFe_2O_4$ nanoparticles is lower for Gram-negative*E. coli* than Gram-positive*S. aureus*. It is seen that *E. coli* are 79% more susceptible to $Co_{0.75}Cu_{0.25}Fe_2O_4$ at 3 mg/ml concentration as compared to *S. aureus.*

The microbicidal activity of copper species against a wide variety of bacterial strains, both as metal and complexed species, have been well documented. The studies allow us to emphasize that the antimicrobial effect of Cu is directly linked to its higher oxidation states [427]. However, the exact mechanism behind this phenomenon still remains debatable, and it emerges that several co-acting mechanisms may be involved.

The Cu^{2+} substituted $CoFe_2O_4$ may have two probable modes of action against pathogens. The first involves the adhesion of nanoparticles to the bacterial cell wall followed by penetration inducing damage to the cellular membrane [428,429]. Secondly, Cu^{2+} ions generate reactive oxygen species which bind to biologically active micro and macromolecules causing lipid peroxidation, protein oxidationand DNA degradation which results in the loss of metabolic functions and ultimately killing the cells [430,431].

Conclusively thestudy depicts the broad spectral antimicrobial property of Cu^{2+} substituted $CoFe_2O_4$ nanoparticles against emerging Gram-negative and Gram-positive pathogens from the state hospital and which have been obtained from Urinary Tract Infection (UTI), inflammation of mucosa lining, diarrhoea and Hospital-acquired nosocomial infections [432–434].

5.8.4 Evaluation of antibacterial properties of substituted cobalt ferrites

As seen in Fig. 5.68 and Table 5.36, except In^{3+}, other metal (Sb^{3+}, Dy^{3+}, Sm^{3+}, Gd^{3+}, Yb^{3+}, and Eu^{3+}) substituted cobalt copper ferrite showed MIC of 8 mg/ml against Gram-negative *E. coli*. On the other hand, MIC of the Cr^{3+} and Mnion substituted Co-Cu ferrite reduced to 6 and 6.5 mg/ml respectively.

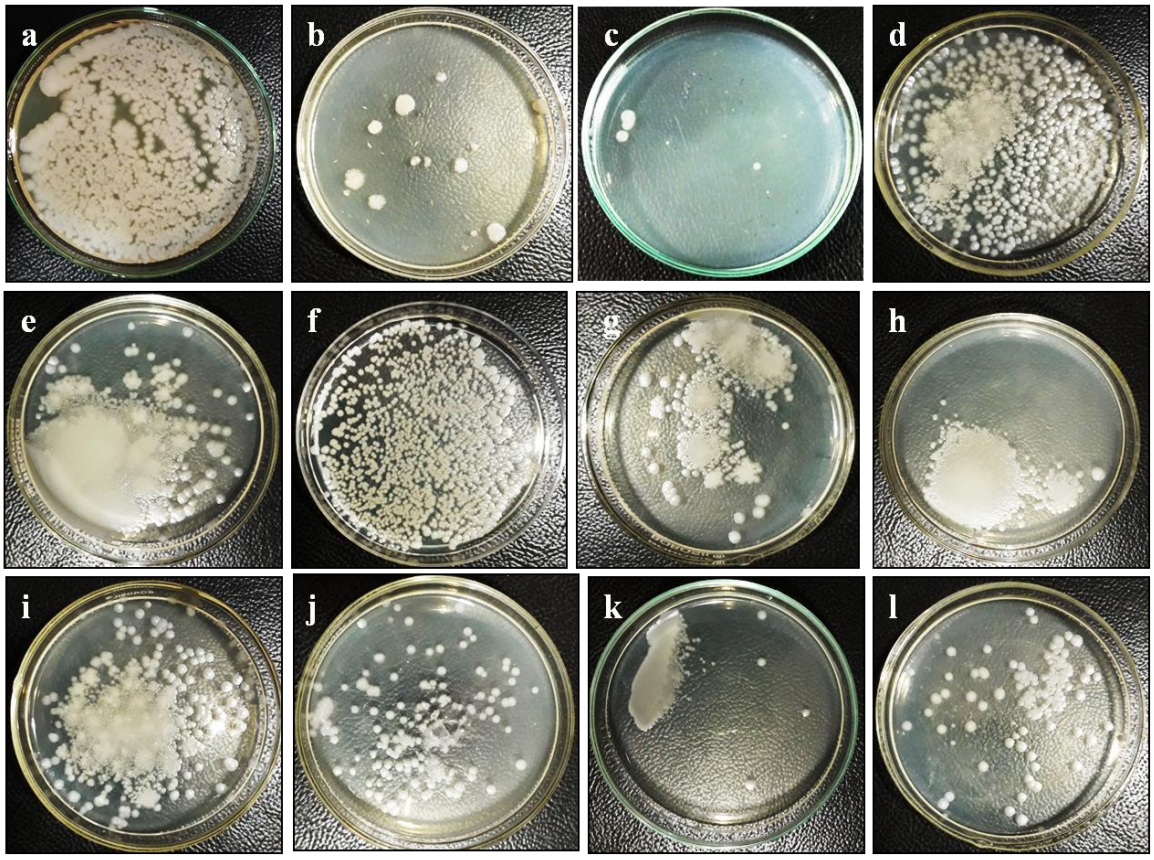

Fig.5.68 *Representative plates showing the % survival of E coli (a) Control (b)* $Co_{0.90}Cu_{0.10}Fe_2O_4$ *(c)* $Co_{0.75}Cu_{0.25}Fe_2O_4$ *(d)* $CoFe_{1.91}Sb_{0.09}O_4$ *(e)* $Co_{0.90}Cu_{0.10}Fe_{1.95}Dy_{0.05}O_4$ *(f)* $Co_{0.90}Cu_{0.10}Fe_{1.95}Sm_{0.05}O_4$ *(g)* $Co_{0.90}Cu_{0.10}Fe_{1.95}Gd_{0.05}O_4$ *(h)* $Co_{0.90}Cu_{0.10}Fe_{1.95}Yb_{0.05}O_4$ *(i)* $Co_{0.90}Cu_{0.10}Fe_{1.95}Eu_{0.05}O_4$ *(j)* $Co_{0.9}Cu_{0.1}Fe_{1.85}In_{0.15}O_4$ *(k)* $Co_{0.90}Cu_{0.10}Fe_{1.85}Cr_{0.15}O_4$ *(l)* $Co_{0.90}Cu_{0.10}Fe_{1.85}Mn_{0.15}O_4$.

It was observed that, when compared to Cu^{2+} ion substituted spinel ferrite which showed MIC of 3 mg/ml and 4 mg/ml, other substituted metals would result in a decrease in the antimicrobial property against *E. coli*. A report by Sanpo et al. [145]on

antibacterial activity of transition metal-substituted $CoFe_2O_4$ nanoparticles revealed that Cu-Co ferrite nanoparticles have the most effective contact biocidal property among Zn, Mn, and Ni ion substituted $CoFe_2O_4$ nanoparticles. In another study by Ashour et al. [223] showed Cu, Mn, and Zn ion substituted $CoFe_2O_4$ nanoparticles inhibit the growth of *E. coli* at a concentration of 5 mg/ml with Zn-Co ferrite being a most potent antimicrobial agent. In a recent study light active Gd^{3+} substituted $ZnFe_2O_4$ has been evaluated for antibacterial activities against Gram-negative strains (*Pseudomonas aeruginosa and E. coli*) [435]. Recently, Nanocrystalline spinel ferrite nanoparticles such as $CoFe_2O_4$, Zn-Co ferrite, Co-Cu ferrite, and Mn-Co ferrite have been tested against multidrug-resistant bacteria and fungal strains by agar disc diffusion method [436].

Table 5.36 MICs (mg/ml) and survival percentage (%) values of substituted Cobalt ferrite.

Sample composition	MIC (mg/ml)	% Survival
$Co_{0.9}Cu_{0.10}Fe_2O_4$	4	19.04
$Co_{0.75}Cu_{0.25}Fe_2O_4$	3	15.00
$CoFe_{1.91}Sb_{0.09}O_4$	8	61.90
$Co_{0.90}Cu_{0.10}Fe_{1.95}Dy_{0.05}O_4$	8	64.28
$Co_{0.9}Cu_{0.1}Fe_{1.95}Sm_{0.05}O_4$	8	60.00
$Co_{0.9}Cu_{0.1}Fe_{1.95}Gd_{0.05}O_4$	8	69.00
$Co_{0.9}Cu_{0.1}Fe_{1.95}Yb_{0.05}O_4$	8	66.00
$Co_{0.9}Cu_{0.1}Fe_{1.95}Eu_{0.05}O_4$	8	71.42
$Co_{0.9}Cu_{0.1}Fe_{1.85}In_{0.15}O_4$	7	66.00
$Co_{0.9}Cu_{0.1}Fe_{1.85}Cr_{0.15}O_4$	6	42.85
$Co_{0.9}Cu_{0.1}Fe_{1.85}Mn_{0.15}O_4$	6.5	45.23

SUMMARY AND CONCLUSION

6.1 Summary

This thesis deals with the preparation, detailed characterization, microstructural, magnetic, electrical and dielectric studies of fractionally substituted cobalt ferrite and cobalt–copper ferrite with magnetic and non-magnetic ions. In addition, the thesis also describes the preparation, characterization,down and Up-conversion luminescence studies of rare-earth substituted Y_2O_3 and Gd_2O_3 respectively. The effect of substitution and the trends observed were evaluated systematically with the most appropriate scientific reason supported by analytical data.

Chapter 1 described the importance of metal oxides and mixed metal oxides in various fields. The significance of spinel ferrites and mixed rare earth oxides were presented. The properties of the materials can be tuned to specific applications by substitution with various metal ions was also elaborated. The work carried out was highlighted and the organization of the thesis has been described in this chapter.

Chapter 2presented a detailed literature review on the spinel ferrites, substituted spinel ferrites, and substituted Y_2O_3 and Gd_2O_3. A brief summary of the preparation methods, potential applications reported was described. A general idea on the effect of substituent ions on the magnetic, electric, dielectric and luminescence properties of the host material was obtained from this chapter.

Chapter 3 described the sample preparation procedures used in the present work. Spinel ferrites were prepared using sol-gel auto combustion process at a sintering temperature of 800 ℃. In this process, malic acid was used as a complexing agent while

ethylene glycol was used as a gelling agent. The mixed rare earth oxides were prepared employing the combustion method utilizing glycine as a fuel at a sintering temperature of 1000 ℃.It also gave brief procedures and principles regardingthe instrumental techniques employed in the characterization process. The samples were characterized by TG-DTA, XRD, ICP-AES, IR, Raman, and XPS. The surface morphology and particle size were estimated from SEM-EDX and TEM-SAED techniques. Material studies such as magnetic, DC-electrical resistivity, dielectric properties, and photoluminescence studies were performed and analyzed on the samples.

Chapter 4 presented detailedcharacterization and spectroscopic studies of the prepared spinel ferrites and mixed rare earth oxides. Thermal analysis (TG-DTA) performed on the samples determined the combustion temperature, calcination temperature, and stability of the compounds. X-ray diffraction technique was employed to determine the phase purity and crystallinity. ICP-AES analysis was performed to estimate the precise chemical composition. IR analysis of spinel ferrites showed two prominent absorption peaks ~ 400 cm^{-1} and ~ 600 cm^{-1} which are typical peaks for spinel ferrites. The IR spectra of substituted Y_2O_3 and Gd_2O_3 showed absorption peaks in the range ~ 400 – 560 cm^{-1} attributed to metal-oxygen stretching. Raman spectra of spinel ferrites showed characteristic Raman modes. Analysis of SEM images showed the presence of spherical agglomerates on the surface of the samples. EDX pattern of the representative samples from each series showed the presence of expected elements. The analysis of TEM images revealed the particle size of the materials. The XPS studies confirmed and validated the chemical states of the elements.

Chapter 5 showed the solid-state studies and optical studies carried out on the prepared compositions. The room temperature Mössbauer studies showed the magnetic nature of the material and also indicated the oxidation state of the Fe species. The magnetization measurements carried out by varying magnetic field up to 3 T and 5 T showed the effect of Cu^{2+} and Sb^{3+} ion substitution in cobalt ferrite. Also, the effect of substitution of RE^{3+} ions (RE= Gd, Dy, Sm, Yb, and Eu), Cr^{3+}, In^{3+}, and Mn ions was investigated. The magnetization measurement carried out at 50 K and 5 K by varying the field up to 3 T and 5 T showed a similar trend as that of 300 K but showed considerably higher values. AC magnetic susceptibility studies carried out at a constant field of 5 kOe by varying the temperature and the Curie temperature was determined. DC electrical resistivity studies showed a decrease in resistivity with increasing temperature in spinel ferrites highlighting the semiconducting nature of spinel ferrites. Dielectric studies showed higher values of dielectric constant and dielectric loss in the lower frequency region. Also with increasing temperature at a fixed frequency dielectric constant increased which was attributed to an increase in temperature-dependent interfacial and dipolar polarization.The band gap values for mixed rare earth oxides were evaluated from UV-DRS technique. The Pl emission spectra of Ce^{3+}/Eu^{3+} and Ce^{3+}/Er^{3+} co-substituted Y_2O_3 showed its typical emission peaks. The UC luminescence spectra of Er^{3+}/Yb^{3+} co substituted Gd_2O_3 under the laser excitation of 980 nm showed a strong red luminescence along with weak green emission. The UC luminescence spectra of Ho^{3+}/Yb^{3+} co-substituted Gd_2O_3 under laser excitation of 980 nm showed a dominant green emission with feeble red emission.

The Cu^{2+} substituted cobalt ferrite was tested for inhibitory activity against 6 different pathogens. The Cu^{2+} substitution enhanced the activity of cobalt ferrite against both Gram-positive and Gram-negative pathogens.

6.2 Conclusions

In conclusion, a feasible preparative procedurewas developed to prepare substituted spinel ferrites and mixed rare earth oxides at a relatively lower temperature compared to previous reports. The monophasic Cu^{2+} and Sb^{3+} ion substituted cobalt ferrite and RE^{3+} (where RE= Gd, Dy, Sm, Yb, and Eu), Cr^{3+}, $In^{3+,}$ and Mn ion substituted Co-Cu ferrite were successfully prepared employing sol-gel auto combustion process at a sintering temperature of 800 ℃. The mixed rare earth oxides were successfully prepared by combustion process using glycine as a fuel at a sintering temperature of 1000 ℃. The thermal analysis suggested the combustion temperature, calcination temperature and stability of the compounds. XRD analysis revealed that all the compositions are monophasic having a cubic structure and no traces of impurity phases were noticed in the pattern. The XRD analysis also indicated the highly crystalline nature of the samples. The lattice parameters calculated from the XRD data were in close agreement with the reported values. Crystallite size was also estimated from the XRD data using the Scherrer's equation. ICP-AES results verified the formation of formulated compounds since the results obtained were close to the expected values. Infrared spectroscopic analyses supported the presence of metal-oxygen stretching in the compounds with no readable impurity. The results attained using Raman studies confirmed the spinel cubic structure formation. Also, the absence of impurity peaks confirmed the formation of monophasic compounds.

The SEM images showed the uniform distribution of sphericle agglomerates which is due to the high-temperature heat treatment given to the sample and magnetic forces present in the sample in case of spinel ferrites. The TEM measurements indicated that the particle size decreased with substitution. The particle size estimated from TEM studies showed that the particle size varied from 25 nm to 120 nm for spinel ferritesand 40 nm to 120 nm for mixed rare earth oxides. The corresponding SAED pattern showed bright rings and dark spots which indicated the highly crystalline nature of the materials. The detailed XPS studies of individual Co 2p, Cu 2p, Fe 2p, O1s, Sb 3d, Gd 4d, Dy 4d, Sm 3d, Yb 4d, Eu 4d, Cr 2p, Mn 2p, In 3d, Y 3d, Er 4d, and Ho 4d spectra revealed and substantiated the expected chemical states. The Mössbauer spectra showed two six-line hyperfine patterns suggesting the ferrimagnetic nature of the spinel ferrites. The isomer shift values below 0.5 mm/s also indicated the presence of high spin Fe in 3+ oxidation state with the absence of Fe^{2+} species.

Cu^{2+} ion substitution in $CoFe_2O_4$was quite effective in lowering the coercivity which was credited to the small magnetic anisotropy of copper. Also, a slight decrease in the saturation magnetization and Curie temperature was obtained with the insertion of Cu^{2+}(1 μ_B) ions by replacing Co^{2+}(3 μ_B) ions. The copper substitution improved the value of the dielectric constant in the lower frequency region with an insignificant quantity of dielectric loss. The Cu^{2+} ion substitution resulted in a decrease in the Curie temperature indicating the generation of weak exchange interactions in the materials with the prominent Hopkinson peaks observed for all samples. AC susceptibility studies also suggested the multidomain – single domain nature of the particles. The replacement of cobalt with Cu^{2+} ions in $CoFe_2O_4$ considerably improved the antimicrobial activity

against *E. coli*.Consequently, the results indicated that the inclusion of Cu^{2+} ions strongly affects the microstructure, crystal structure, particle diameter and antimicrobial activity of the $CoFe_2O_4$ nanoparticles.

For Sb^{3+} ions substituted $CoFe_2O_4$ the magnetic studies showed that the saturation magnetization decreased with the incorporation of non-magnetic Sb^{3+} ions in the $CoFe_2O_4$,which also suggested the probable site occupied by Sb^{3+} ions. It was also observed that the enhancement of DC electrical resistivity and dielectric constantcould be achieved by introducing Sb^{3+} ions.The increased DC electrical resistivity with Sb^{3+} ion substitution is due to decreased electron pair hopping at the octahedral sites accountable for conduction in ferrites.The increase in dielectric constant with Sb^{3+} content wasattributed to increased Fe-O and Sb-O bond length at the octahedral sites which increased the atomic polarizability and subsequentlydielectric constant.

The substitution of RE^{3+} ions in Co-Cu ferrite enhanced the coercive field due to anisotropy and size effect, whereas the saturation magnetization decreased.RE^{3+} ions played a considerable role in lowering the Curie temperature due to the weakening of exchange interactions. The introduction of RE^{3+} ions in place of Fe^{3+} ions in Co-Cu ferrite improved the dielectric constantwith a negligible amount of dielectric loss. Accordingly, the results suggested that by the addition of the desired amount of selected RE ions, one can tune the magnetic as well as electric properties of Co-Cu ferrite for desired applications.

In theCr^{3+} ion substituted Co-Cu ferrite the saturation magnetization, as well as coercivity decreased, as the Cr^{3+} ion contentincreased, which is credited to the replacement of Fe^{3+} ions by weak magnetic ions on the octahedral site of the spinel

lattice. The obtained coercivity valuesare relatively higher than those reported which suggests, the utilization of the entire Co-Cu ferrite in permanent magnets applications.The Curie temperature of the ferrites under investigation decreased with increase in Cr^{3+} concentration due to reduced magnetic superexchange interactions with the prominent Hopkinson peaks observed for all samples. The Cr^{3+} ion substitution had a noticeable impact on the DC electrical resistivity and dielectric features of Co-Cu ferrite.

The Mn ion substituted Co-Cu ferrite showed an initial increase in saturation magnetization followed by a decrease. The initial increase in saturation magnetization can be attributed to the occupancy of highly magnetic Mn^{2+}(5 μ_B) ions at the B site, whereas at higher concentration the presence of less magnetic Mn^{3+}(4 μ_B) ions at the B site decreases the saturation magnetization. The DC resistivity increased at lower Mn concentration and then decreased marginally at higher concentrations. The increase in DC resistivity can be credited to a large number of Mn^{2+} ions occupying B sites, forcing some of the Fe^{3+} ions at B sites to migrate to A sites, which reduces the hopping rate between Fe^{3+} and Fe^{2+} ions at B site. The dielectric constant showed higher values for higher Mn ion concentration as compared to the unsubstituted sample. This can be due to the presence of Mn^{2+} and Mn^{3+} ions at the octahedral sites at a higher concentration which also contributed towards polarization.

The magnetic studies performed on In^{3+} ion substituted Co-Cu ferrite, indicated a decrease in saturation magnetization and coercivity with increasing In^{3+} ion content,whichsuggested the B site occupancy of the substituent. A considerable decrease in Curie temperature was observed with Indium ion substitution due to the weakening of the exchange interactions. DC resistivity showed a gradual increase with increasing

substituent concentration. The In^{3+} ions are likely to occupy the B sites, displacing an equal number of Fe^{3+} ions to the A sites, which will decrease the concentration of Fe^{3+}/Fe^{2+} ion pairs at B site accountable for conduction in ferrites. The considerably higher value of dielectric constant with an insignificant amount of dielectric loss suggested that the materials under investigation have an immense potential for applications in microwave devices. The overall results of this study indicated that the magnetic and dielectric properties of $Co_{0.9}Cu_{0.1}Fe_2O_4$ can be tuned to a specific application with fractional Indium ion substitution.

For Ce^{3+}/Eu^{3+}co-substituted $Y_2O_3$the dominant emission was observed in the red region with the strongest emission peak located at 611 nm corresponding to the $^5D_0 \rightarrow {}^7F_2$ transition of Eu^{3+} ions.The emission intensity increased with the increase of Eu^{3+} concentration. The Ce^{3+} emission showed its existence in the emission spectra, which indicated that there is no effective energy transfer between Ce^{3+} and Eu^{3+}but the intensity of Ce^{3+} emission decreased when the Eu^{3+} substitution increased from 2 to 6 mol%. Highlighting at the concentration-dependent energy transfer.The CIE diagram showed that the coordinates shifted towards the red region from the pink region with rising Eu^{3+} content. The band gap values obtained were ranged from 5.31 - 5.73 eV indicating the insulator type nature of the prepared materials.

The emission spectraCe^{3+}/Er^{3+}co-substituted Y_2O_3displayed the characteristic emission peaks of Er^{3+} ions in cubic Y_2O_3. A strong emission was noticed in the green region(520–565 nm) which were assigned to the $(^2H_{11/2}, {}^4S_{3/2}) \rightarrow {}^4I_{15/2}$ transitions of Er^{3+} ions. The PL intensity increased with substituent concentration up to 4 mol% of Er^{3+} and then decreased. At lower concentrations of the Er^{3+}, the optical activation of the Er^{3+} ions

becomes more, which results in an increase in the PL emission intensity. The decrease was attributed to the concentration quenching, as the distance between the Er^{3+} ions in the host lattice gets reduced. The CIE diagram showed that the overall emission color of Ce^{3+} and Er^{3+} co-substituted Y_2O_3 phosphor samples and indicated that the blue-green emission color approaches green color with an increase in the Er^{3+} concentration.

The UC emission spectra of Er^{3+}/Yb^{3+}co-substituted Gd_2O_3under the laser excitation of 980 nm showed major emission peaks of Er^{3+} ions shift from 562 ($^2H_{11/2}/^4S_{3/2} \rightarrow {}^4I_{15/2}$) to 660 nm ($^4F_{9/2} \rightarrow {}^4I_{15/2}$), resulting in the UC emission color shifting from green to red. For 20 mol%, the emission intensity of 660 nm peak was found to decrease which was attributed to the concentration quenching between the Yb^{3+} ions. The red emission could be enhanced further by varying the Yb^{3+} ion concentration in Er^{3+}/Yb^{3+} co-substituted Gd_2O_3.The CIE diagram suggested that the overall emission color of sample shifted from green to yellow and then orange as the Yb^{3+} content is increased.

The Up-conversion luminescence spectra of Ho^{3+}/Yb^{3+} co-substituted Gd_2O_3 showed the dominant green emission peaks ~550 nm, ($^5S_2/^5F_4 \rightarrow {}^5I_8$) accompanied by relatively weak red emission peaks ~667 nm, ($^5F_5 \rightarrow {}^5I_8$). The emission intensity of red emission decreased while that of green emission increased with Yb^{3+} substitution up to 8 mol%. Further, a continuous decrease in emission intensity could be due to the quenching effect, which transfers energy from the Ho^{3+} ions back to Yb^{3+} ions.The calculated color coordinates showed that the overall emission color shifts from green to yellow region with increasing Yb^{3+} substitution.

References

[1] J.B. Prasannakumar, Y.S. Vidya, K.S. Anantharaju, G. Ramgopal, H. Nagabhushana, S.C. Sharma, B. Daruka Prasad, S.C. Prashantha, R.B. Basavaraj, H. Rajanaik, K. Lingaraju, K.R. Prabhakara, H.P. Nagaswarupa, Spectrochim. Acta - Part A Mol. Biomol. Spectrosc. 151 (2015) 131–140.

[2] A. Manikandan, J.J. Vijaya, L.J. Kennedy, M. Bououdina, J. Mol. Struct. 1035 (2013) 332–340.

[3] S.H. Mousavi, H. Haratizadeh, H. Minaee, Opt. Commun. 284 (2011) 3558–3561.

[4] R. Fareghi-Alamdari, N. Zekri, F. Mansouri, Res. Chem. Intermed. 43 (2017) 6537–6551.

[5] R. Moalla, S. Cueff, J. Penuelas, B. Vilquin, G. Saint-Girons, N. Baboux, R. Bachelet, Sci. Rep. 8 (2018) 4332.

[6] M. Srivastava, S.K. Alla, S.S. Meena, N. Gupta, R.K. Mandal, N.K. Prasad, Ceram. Int. 45 (2019) 12028–12034.

[7] B. Zhao, J. Wang, H. Li, X. Jia, L. Dong, D. den Engelsen, ChemistrySelect. 1 (2016) 1136–1139.

[8] Z. Yan, L. Jiang, Nanomaterials. 7 (2017) 1–18.

[9] M. Polking, A. Alivisatos, R. Ramesh, MRS Commun. 5 (2015) 27–44.

[10] W. Arachchige, D. Madushanka, K. Qi, Y. Qin, A. Chinnappan, W. Serrano-garcía, C. Baskar, H. Wang, J. He, S. Cui, S.W. Thomas, S. Ramakrishna, Adv.

Mater. 1805921 (2018) 1–21.

[11] X. Guo, C. Yang, G. Huang, Q. Mou, H. Zhang, B. He, J. Alloys Compd. 764 (2018) 128–135.

[12] M. Gholinejad, B. Karimi, F. Mansouri, J. Mol. Catal. A. 386 (2014) 20–27.

[13] B. Bhujun, M.T.T. Tan, A.S. Shanmugam, Ceram. Int. 42 (2016) 6457–6466.

[14] M.P. Das, B.J. Wilson, Adv. Nat. Sci. Nanosci. Nanotechnol. 6 (2015) 013001.

[15] F.O. Odio, E. Reguera, Magnetic Spinels- Synthesis, Properties and Applications the, Intechopen, 2017.

[16] M.M. Dutta, P. Phukan, Catal. Commun. 109 (2018) 38–42.

[17] M. Raghasudha, D. Ravinder, P. Veerasomaiah, J. Magn. Magn. Mater. 420 (2016) 45–50.

[18] N. Sanpo, Solution Precursor Plasma Spray System, Springer, 2014.

[19] T.S. Chin, J. Magn. Magn. Mater. 209 (2000) 75–79.

[20] S. Anjum, S. Hameed, F. Bashir, Mater. Today Proc. 2 (2015) 5329–5336.

[21] S. Anjum, A. Shabab, S. Rafique, R. Zia, S. Riaz, S. Hameed, M. Riaz, Opt. - Int. J. Light Electron Opt. 127 (2016) 8487–8498.

[22] Z. Xia, Q. Liu, Prog. Mater. Sci. 84 (2016) 59–117.

[23] K. Binnemans, Chem. Rev. 109 (2009) 4283–4374.

[24] H. Miao, R. Ji, X. Hu, L. Han, Y. Hao, Q. Sun, D. Zhang, J. Alloys Compd. 629 (2015) 74–79.

[25] J.G. Bu, Chem. Rev. 110 (2010) 2729–2755.

[26] L. Ozawa, K. Oki, Mater. Chem. Phys. 60 (1999) 274–281.

[27] A. Polman, J. Appl. Phys. 82 (1997) 1–39.

[28] E. Antolini, J. Perez, Int. J. Hydrogen Energy. 36 (2011) 15752–15765.

[29] C. Sun, H. Li, L. Chen, Energy Environ. Sci. 5 (2012) 8475–8505.

[30] Z. Xu, P. Ma, C. Li, Z. Hou, X. Zhai, S. Huang, J. Lin, Biomaterials. 32 (2011) 4161–4173.

[31] P. Kumar, Kanika, S. Singh, R. Lahon, A. Gundimeda, G. Gupta, B.K. Gupta, J. Lumin. 196 (2018) 207–213.

[32] Z. Ci, Q. Sun, S. Qin, M. Sun, X. Jiang, X. Zhang, Y. Wang, Phys.Chem.Chem.Phys. 16 (2014) 11597–11602.

[33] G. Chen, S. Tao, C. Yang, X. Zhao, J. Mater. Sci. Mater. Electron. 26 (2015) 5970–5974.

[34] D. Matsuura, T. Ikeuchi, K. Soga, J. Lumin. 128 (2008) 1267–1270.

[35] G. De, W. Qin, J. Zhang, J. Zhang, Y. Wang, C. Cao, Y. Cui, J. Lumin. 119–120 (2006) 258–263.

[36] L. Yang, H. Song, L. Yu, Z. Liu, S. Lu, J. Lumin. 116 (2006) 101–106.

[37] F. Vetrone, J.C. Boyer, J.A. Capobianco, A. Speghini, M. Bettinelli, J. Appl. Phys. 96 (2004) 661–667.

[38] J. Wang, H. Song, B. Sun, X. Ren, B. Chen, W. Xu, Chem. Phys. Lett. 379 (2003) 507–511.

[39] N. Dhananjaya, H. Nagabhushana, B.M. Nagabhushana, R.P.S. Chakradhar, C. Shivakumara, B. Rudraswamy, Phys. B Condens. Matter. 405 (2010) 3795–3799.

[40] N. Dhananjaya, H. Nagabhushana, S.C. Sharma, B. Rudraswamy, C. Shivakumara, B.M. Nagabhushana, J. Alloys Compd. 587 (2014) 755–762.

[41] S.S. Yi, J.S. Bae, H.K. Yang, B.K. Moon, B.C. Choi, J.H. Jeong, Y.S. Kim, J.H. Kim, Mater. Sci. Eng. B Solid-State Mater. Adv. Technol. 127 (2006) 159–163.

[42] M. Ajmal, T.S. Atabaev, Opt. Mater. (Amst). 35 (2013) 1288–1292.

[43] H. Zhang, M. L??, Z. Xiu, S. Wang, G. Zhou, Y. Zhou, S. Wang, Z. Qiu, A. Zhang, Mater. Res. Bull. 42 (2007) 1145–1152.

[44] S. Gai, P. Yang, D. Wang, C. Li, N. Niu, F. He, X. Li, CrystEngComm. 13 (2011) 5480.

[45] Q. Dai, M.E. Foley, C.J. Breshike, A. Lita, F. Strouse, J. Am. Chem. Soc. 133 (2011) 15475–15486.

[46] S. Hoon, J. Hyuk, D. Young, D. Sik, J. Lumin. 114 (2005) 275–280.

[47] C.Y. Yang, S. Som, S. Das, C.H. Lu, J. Mater. Sci. Mater. Electron. 28 (2017) 9174–9181.

[48] C. CAO, A. XIE, J. Rare Earths. 35 (2017) 58–62.

[49] L.A. Rocha, R.L. Siqueira, J. Esbenshade, M.A. Schiavon, J.L. Ferrari, J. Alloys Compd. 731 (2018) 889–897.

[50] C. Zuo, A. Xiao, S. Liu, Y. Chen, Y. Shen, X. Zhang, Z. Zhou, L. Zhu, J. Non. Cryst. Solids. 472 (2017) 65–69.

[51] Q. Zhang, H. Ni, L. Wang, F. Xiao, Ceram. Int. 42 (2016) 6115–6120.

[52] N.J. Shivaramu, B.N. Lakshminarasappa, F. Singh, E. Coetsee, H.C. Swart, Mater. Res. Bull. 102 (2018) 62–69.

[53] R.S. Yadav, S.B. Rai, J. Phys. Chem. Solids. 114 (2018) 179–186.

[54] K. Upadhyay, R.K. Tamrakar, D.P. Bisen, I.P. Sahu, M. Sahu, Optik (Stuttg). 127 (2016) 3693–3697.

[55] E. Ranjith Kumar, P. Siva Prasada Reddy, G. Sarala Devi, S. Sathiyaraj, J. Magn. Magn. Mater. 398 (2016) 281–288.

[56] R.C. Kambale, K.M. Song, C.J. Won, K.D. Lee, N. Hur, J. Cryst. Growth. 340 (2012) 171–174.

[57] N.J. Shivaramu, K.R. Nagabhushana, B.N. Lakshminarasappa, F. Singh, J. Lumin. 169 (2016) 627–634.

[58] Y. Guo, D. Wang, X. Wu, Q. Wang, Y. He, J. Alloys Compd. 688 (2016) 816–819.

[59] W. Kong, J. Shan, Y. Ju, Mater. Lett. 64 (2010) 688–691.

[60] J. Zhang, C. Jiang, Funct. Mater. Lett. 07 (2014) 1450047.

[61] T. Pang, W. hui Lu, Ceram. Int. 43 (2017) 1061–1065.

[62] H. Liu, B. Zhang, H. Shi, Y. Tang, K. Jiao, X. Fu, J. Mater. Chem. 18 (2008) 2573–2580.

[63] Y. Zhydachevskyy, V. Tsiumra, M. Baran, L. Lipińska, P. Sybilski, A. Suchocki, J. Lumin. 196 (2018) 169–173.

[64] Q. Xu, B. Lin, Y. Mao, J. Lumin. 128 (2008) 1965–1968.

[65] A. Kumar, S.P. Tiwari, A.K. Singh, K. Kumar, Appl. Phys. B Lasers Opt. 122 (2016) 1–10.

[66] N.J. Shivaramu, B.N. Lakshminarasappa, K.R. Nagabhushana, H.C. Swart, S. Fouran, Spectrochim. Acta - Part A Mol. Biomol. Spectrosc. 189 (2018) 349–356.

[67] T.S. Atabaev, Z. Piao, Y.H. Hwang, H.K. Kim, N.H. Hong, J. Alloys Compd. 572 (2013) 113–117.

[68] L. Yang, S. Quan, Y. Yang, Z. Li, W. Wang, L. Guo, Solid State Commun. 149 (2009) 1814–1817.

[69] S.K. Singh, K. Kumar, S.B. Rai, Sensors Actuators, A Phys. 149 (2009) 16–20.

[70] Y. Li, G. Hong, Y. Zhang, Y. Yu, J. Alloys Compd. 456 (2008) 247–250.

[71] H. Guo, N. Dong, M. Yin, W. Zhang, L. Lou, S. Xia, J. Phys. Chem. B. 108 (2004)

19205–19209.

[72] T. Shen, Y. Zhang, A.M. Kirillov, H. Cai, K. Huang, W. Liu, Y. Tang, Chem. Commun. 52 (2016) 1447–1450.

[73] D.S. Mathew, R.S. Juang, Chem. Eng. J. 129 (2007) 51–65.

[74] R.K. Tamrakar, D.P. Bisen, N. Bramhe, Luminescence. 30 (2015) 668–676.

[75] B. Van Hao, P.T. Huy, T.N. Khiem, N.T. Thanh Ngan, P.H. Duong, J. Phys. Conf. Ser. 187 (2009) 012074.

[76] H.F. Nabavi, M. Aliofkhazraei, M. Hasanpoor, Int. J. Appl. Ceram. Technol. 7 (2016) 1–7.

[77] A.P. Jadhav, C.W. Kim, H.G. Cha, A.U. Pawar, N.A. Jadhav, U. Pal, Y.S. Kang, Mater. Trans. 56 (2009) 1412–1415.

[78] J. Kaszewski, M.M. Godlewski, B.S. Witkowski, A. Słońska, E. Wolska-Kornio, Ł. Wachnicki, H. Przybylińska, B. Kozankiewicz, A. Szal, M.A. Domino, E. Mijowska, M. Godlewski, Opt. Mater. (Amst). 59 (2016) 157–164.

[79] Y. Iwako, Y. Akimoto, M. Omiya, T. Ueda, T. Yokomori, J. Lumin. 130 (2010) 1470–1474.

[80] K.Y. Jung, C.H. Lee, Y.C. Kang, Mater. Lett. 59 (2005) 2451–2456.

[81] G. Xia, S. Wang, S. Zhou, J. Xu, Nanotechnology. 21 (2010) 345601.

[82] K. Kombaiah, J.J. Vijaya, L.J. Kennedy, M. Bououdina, B. Al-Najar, J. Phys.

Chem. Solids. 115 (2018) 162–171.

[83] K.C. Patil, M. Hegde, T. Rattan, S. Aruna, Nanocrystalline Oxide Materials, World Scientific Publishing, 2008.

[84] M. Kaur, N. Kaur, Vibha, ACS Symp. Ser. 1238 (2016) 113–136.

[85] M. Pardavi-Horvath, J. Magn. Magn. Mater. 215 (2000) 171–183.

[86] M.Z. Naik, A. V. Salker, Mater. Sci. Eng. B Solid-State Mater. Adv. Technol. 211 (2016) 37–44.

[87] O. Mounkachi, R. Lamouri, B. Abraime, H. Ez-Zahraouy, A. El Kenz, M. Hamedoun, A. Benyoussef, Ceram. Int. 43 (2017) 14401–14404.

[88] B. Abraime, A. Mahmoud, F. Boschini, M. Ait Tamerd, A. Benyoussef, M. Hamedoun, Y. Xiao, A. El Kenz, O. Mounkachi, J. Magn. Magn. Mater. 467 (2018) 129–134.

[89] A. López-Ortega, E. Lottini, C.D.J. Fernández, C. Sangregorio, Chem. Mater. 27 (2015) 4048–4056.

[90] W. Hu, N. Qin, G. Wu, Y. Lin, S. Li, D. Bao, J. Am. Chem. Soc. 134 (2012) 14658–14661.

[91] Y. Yang, X. Liu, Y. Yang, W. Xiao, Z. Li, D. Xue, F. Li, J. Ding, J. Mater. Chem. C. 1 (2013) 2875–2885.

[92] S. Nasrin, F.U.Z. Chowdhury, S.M. Hoque, J. Magn. Magn. Mater. 479 (2019) 126–134.

[93] S. Munjal, N. Khare, B. Sivakumar, D. Nair Sakthikumar, J. Magn. Magn. Mater. 477 (2019) 388–395.

[94] D. Lachowicz, W. Górka, A. Kmita, A. Bernasik, J. Żukrowski, W. Szczerba, M. Sikora, C. Kapusta, S. Zapotoczny, J. Mater. Chem. B. 7 (2019) 2962–2973.

[95] L.A. Dubraja, C. Reitz, L. Velasco, R. Witte, R. Kruk, H. Hahn, T. Brezesinski, ACS Appl. Nano Mater. 1 (2017) 65–72.

[96] G. Wang, F. Zhou, X. Li, J. Li, Y. Ma, J. Mu, Z. Zhang, H. Che, X. Zhang, Ceram. Int. 44 (2018) 13588–13594.

[97] C. Dey, A. Ghosh, M. Ahir, A. Ghosh, M.M. Goswami, ChemPhysChem. 19 (2018) 2872–2878.

[98] G. Wang, D. Zhao, Y. Ma, Z. Zhang, H. Che, J. Mu, X. Zhang, Z. Zhang, Appl. Surf. Sci. 428 (2018) 258–263.

[99] N. Sattarahmady, M. Heidari, T. Zare, M. Lotfi, H. Heli, Appl. Magn. Reson. 47 (2016) 925–935.

[100] A. Alazmi, V. Singaravelu, N.M. Batra, J. Smajic, M. Alyami, N.M. Khashab, P.M.F.J. Costa, RSC Adv. 9 (2019) 6299–6309.

[101] J. Leng, J. Li, J. Ren, L. Deng, C. Lin, Mater. Lett. 152 (2015) 185–188.

[102] X. Wu, W. Wang, F. Li, S. Khaimanov, N. Tsidaeva, Appl. Surf. Sci. 389 (2016) 1003–1011.

[103] P. Xiong, L. Wang, X. Sun, X. Wang, Ind. Eng. Chem. Res. 52 (2013) 10105–

10113.

[104] I. Khosravi, M. Eftekhar, Powder Technol. 250 (2013) 147–153.

[105] U. Narkiewicz, W. Konicki, D. Sibera, E. Mijowska, Z. Lendzion-bielun, J. Colloid Interface Sci. 398 (2013) 152–160.

[106] Y. Tu, C. You, C. Chang, S. Wang, T. Chan, Chem. Eng. J. 198–199 (2012) 440–448.

[107] Y. Tu, C. You, C. Chang, J. Hazard. Mater. 235–236 (2012) 116–122.

[108] J. Zhu, S. Wei, H. Gu, S.B. Rapole, Q. Wang, Z. Luo, N. Haldolaarachchige, D.P. Young, Z. Guo, Environ. Sci. Technol. 46 (2012) 977−985.

[109] B. Qiu, Y. Wang, D. Sun, Q. Wang, X. Zhang, B.L. Weeks, R. O'Connor, X. Huang, S. Wei, Z. Guo, J. Mater. Chem. A. 3 (2015) 9817–9825.

[110] V. Srivastava, T. Kohout, M. Sillanpää, J. Environ. Chem. Eng. 4 (2016) 2922–2932.

[111] B. Lakshminarayana, J. Chakraborty, G. Satyanarayana, C. Subrahmanyam, RSC Adv. 8 (2018) 21030–21039.

[112] T. Kiyokawa, N. Ikenaga, ChemistrySelect. 3 (2018) 6426–6433.

[113] K.B. Rasal, G.D. Yadav, Catal. Today. 309 (2018) 51–60.

[114] A. Goyal, S. Bansal, P. Samuel, V. Kumar, S. Singhal, J. Mater. Chem. A. 2 (2014) 18848–18860.

[115] P.B. Bhat, F. Inam, B.R. Bhat, ACS Comb. Sci. 16 (2014) 397–402.

[116] J. Deng, Y. Shao, N. Gao, C. Tan, S. Zhou, X. Hu, J. Hazard. Mater. 262 (2013) 836–844.

[117] P. V Kumar, M.P. Short, S. Yip, B. Yildiz, J. Phys. Chem. C. 4 (2013) 5678−5683.

[118] P. Gaikwad, S. Zimur, S. Sabale, P. Kamble, J. Supercond. Nov. Magn. 4 (2019) 2551–2558.

[119] M. Sun, X. Han, S. Chen, Mater. Sci. Semicond. Process. 91 (2019) 367–376.

[120] Y. Huang, C. Han, Y. Liu, M.N. Nadagouda, L. Machala, K.E. O'Shea, V.K. Sharma, D.D. Dionysiou, Appl. Catal. B Environ. 221 (2018) 380–392.

[121] E. Skliri, J. Miao, J. Xie, G. Liu, T. Salim, B. Liu, Q. Zhang, G.S. Armatas, Appl. Catal. B Environ. 227 (2018) 330–339.

[122] S. Gautam, S. Muthurani, M. Balaji, P. Thakur, D.P. Padiyan, K.H. Chae, S.S. Kim, K. Asokan, J. Nanosci. Nanotechnol. 11 (2011) 386–90.

[123] J. Balavijayalakshmi, N. Suriyanarayanan, R. Jayapraksah, Mater. Lett. 81 (2012) 52–54.

[124] S.Y. An, I.S. Kim, S.H. Son, S.Y. Song, J.W. Hahn, S.W. Hyun, C.M. Kim, C.S. Kim, Thin Solid Films. 519 (2011) 8296–8298.

[125] M. Hashim, S. Kumar, B.H. Koo, S.E. Shirsath, E.M. Mohammed, J. Shah, R.K. Kotnala, H.K. Choi, H. Chung, R. Kumar, J. Alloys Compd. 518 (2012) 11–18.

[126] C. Cao, S. Ren, L. Zhang, A. Xia, J. Mater. Sci. Mater. Electron. 25 (2014) 4851–4855.

[127] K.M. Batoo, D. Salah, G. Kumar, A. Kumar, M. Singh, M. Abd El-Sadek, F.A. Mir, A. Imran, D.A. Jameel, J. Magn. Magn. Mater. 411 (2016) 91–97.

[128] B. Chandra Sekhar, G.S.N. Rao, O.F. Caltun, B. Dhana Lakshmi, B. Parvatheeswara Rao, P.S. V Subba Rao, J. Magn. Magn. Mater. 398 (2016) 59–63.

[129] M. a Ahmed, S.F. Mansour, M. a Abdo, Phys. Scr. 84 (2011) 055602.

[130] M.A. Ahmed, S.F. Mansour, M.A. Abdo, Phys. Scr. 86 (2012) 025705.

[131] A. Faraz, A. Maqsood, N.M. Ahmad, Adv. Appl. Ceram. 111 (2012) 228–237.

[132] D.M. Jnaneshwara, D.N. Avadhani, B. Daruka Prasad, H. Nagabhushana, B.M. Nagabhushana, S.C. Sharma, S.C. Prashantha, C. Shivakumara, Spectrochim. Acta - Part A Mol. Biomol. Spectrosc. 132 (2014) 256–262.

[133] R. Ghadari, H. Namazi, M. Aghazadeh, Appl. Organomet. Chem. 32 (2018) 1–10.

[134] V.S. Kirankumar, S. Sumathi, J. Mater. Sci. Mater. Electron. 29 (2018) 8738–8746.

[135] N. Velinov, D. Dimitrov, K. Koleva, K. Ivanov, I. Mitov, Acta Metall. Sin. 28 (2015) 367–372.

[136] N. Velinov, K. Koleva, T. Tsoncheva, D. Paneva, E. Manova, B. Kunev, I. Mitov, Cent. Eur. J. Chem. 12 (2013) 11–12.

[137] E.E. Ateia, A.A.E. Galila, A. Fatma, J. Mater. Sci. Mater. Electron. 28 (2017) 241–249.

[138] N. Sanpo, J. Wang, C.C. Berndt, J. Nano Res. 22 (2013) 95–106.

[139] S. Briceño, H. Del Castillo, V. Sagredo, W. Bramer-Escamilla, P. Silva, Appl. Surf. Sci. 263 (2012) 100–103.

[140] C. Tian, S. Fu, L.A. Lucia, Cellulose. 22 (2015) 2571–2587.

[141] H. Bayrakdar, O. Yalcin, S. Vural, K. Esmer, J. Magn. Magn. Mater. 343 (2013) 86–91.

[142] C. Singh, S. Bansal, V. Kumar, K.B. Tikko, S. Singhal, RSC Adv. 5 (2015) 39052–39061.

[143] P.P. Hankare, P.D. Kamble, M.R. Kadam, K.S. Rane, P.N. Vasambekar, Mater. Lett. 61 (2007) 2769–2771.

[144] S. Ounnunkad, S. Phanichphant, Mater. Res. Bull. 47 (2012) 473–477.

[145] N. Sanpo, C.C. Berndt, C. Wen, J. Wang, Acta Biomater. 9 (2013) 5830–5837.

[146] N. Sanpo, J. Tharajak, Y. Li, C.C. Berndt, C. Wen, J. Wang, J. Nanoparticle Res. 16 (2014) 2510.

[147] N. Sanpo, J. Wang, C.C. Berndt, J. Nano Res. 22 (2013) 95–106.

[148] A. Samavati, M.K. Mustafa, A.F. Ismail, M.H.D. Othman, M.A. Rahman, Mater. Express. 6 (2016) 473–482.

[149] X.L. Fu, Q.K. Xing, Z.J. Peng, C.B. Wang, Z.Q. Fu, L.H. Qi, H.Z. Miao, Int. J. Mod. Phys. B. 27 (2013) 1–12.

[150] M.V.K. Meher, K. Samatha, K. V. Ramesh, A.S. Kumar, Int. J. Mod. Phys. B. 26 (2012) 1250204.

[151] V. Petrovic, J. Bobic, T. Ramosˇka, J. Banys, B. Stojanovic, Ceram. Int. 37 (2011) 2669–2677.

[152] K. Praveena, S. Srinath, J. Electroceramics. 31 (2013) 168–175.

[153] C.S.L.N. Sridhar, C.S. Lakshmi, G. Govindraj, S. Bangarraju, L. Satyanarayana, J. Phys. Chem. Solids. 92 (2016) 70–84.

[154] C.S. Lakshmi, C.S.L.N. Sridhar, G. Govindraj, S. Bangarraju, D.M. Potukuchi, Phys. B Phys. Condens. Matter. 459 (2015) 97–104.

[155] E. Pervaiz, I.H.G. Amir, J. Supercond. Nov. Magn. 27 (2014) 881–890.

[156] S. Anjum, A. Shabab, S. Rafique, R. Zia, S. Riaz, S. Hameed, M. Riaz, Optik (Stuttg). 127 (2016) 8487–8498.

[157] M. Naeem, M. Fahad, M. Javed, I. Hussain, J. Alloys Compd. 509 (2011) 5119–5126.

[158] E. Demirci, P.K. Manna, Y. Wroczynskyj, S. Aktürk, J. van Lierop, J. Magn. Magn. Mater. 458 (2018) 253–260.

[159] S. Joshi, M. Kumar, S. Chhoker, A. Kumar, M. Singh, J. Magn. Magn. Mater. 426 (2017) 252–263.

[160] S.M. Montemayor, C. Mallada, N. Vázquez, J.L. Menéndez, J.A. Díaz-Guillén, O.S. Rodríguez-Fernández, R. Betancourt-Galindo, Ceram. Int. 43 (2017) 14122–14127.

[161] C. Virlan, G. Bulai, O. Florin, R. Hempelmann, A. Pui, Ceram. Int. 42 (2016) 11958–11965.

[162] S. Abbas, Fatima-Tuz-Zahra, M. Anis-Ur-Rehman, J. Alloys Compd. 677 (2016) 143–147.

[163] K.K. Patankar, D.M. Ghone, V.L. Mathe, S.D. Kaushik, J. Magn. Magn. Mater. 454 (2018) 71–77.

[164] S.I. Ahmad, S.A. Ansari, D. Ravi Kumar, Mater. Chem. Phys. 208 (2018) 248–257.

[165] R. Samad, M. ud D. Rather, K. Asokan, B. Want, J. Alloys Compd. 744 (2018) 453–462.

[166] G. Xi, L. Wang, T. Zhao, J. Magn. Magn. Mater. 424 (2017) 130–136.

[167] L. Avazpour, H. Shokrollahi, M.R. Toroghinejad, M.A. Zandi Khajeh, J. Alloys Compd. 662 (2016) 441–447.

[168] W. Chen, D. Liu, W. Wu, H. Zhang, J. Wu, J. Magn. Magn. Mater. 422 (2017) 49–56.

[169] X. Wu, Z. Ding, N. Song, L. Li, W. Wang, Ceram. Int. 42 (2015) 4246–4255.

[170] X. Wu, W. Wang, N. Song, X. Yang, S. Khaimanov, N. Tsidaeva, Chem. Eng. J.

306 (2016) 382–392.

[171] J. Peng, M. Hojamberdiev, Y. Xu, B. Cao, J. Wang, H. Wu, J. Magn. Magn. Mater. 323 (2011) 133–138.

[172] G. Bulai, L. Diamandescu, I. Dumitru, S. Gurlui, M. Feder, O.F. Caltun, J. Magn. Magn. Mater. 390 (2015) 123–131.

[173] V.S. Puli, S. Adireddy, C.V. Ramana, J. Alloys Compd. 644 (2015) 470–475.

[174] M.A. Rahman, M.A. Rahman, A.K.M.A. Hossain, J. Magn. Magn. Mater. 369 (2014) 168–175.

[175] G. Dascalu, T. Popescu, M. Feder, O.F. Caltun, J. Magn. Magn. Mater. 333 (2013) 69–74.

[176] K.K. Bharathi, C.V. Ramana, J. Mater. Res. 26 (2011) 584–591.

[177] T. Sodaee, A. Ghasemi, E. Paimozd, A. Paesano, A. Morisako, J. Electron. Mater. 42 (2013) 2771–2783.

[178] A. Ghasemi, A. Paesano, C.F.C. MacHado, IEEE Trans. Magn. 48 (2012) 1528–1531.

[179] R.C. Kambale, K.M. Song, Y.S. Koo, N. Hur, J. Appl. Phys. 110 (2011) 053910.

[180] L. Ben Tahar, M. Artus, S. Ammar, L.S. Smiri, F. Herbst, M.J. Vaulay, V. Richard, J.M. Grenèche, F. Villain, F. Fiévet, J. Magn. Magn. Mater. 320 (2008) 3242–3250.

[181] I. Ali, M.U. Islam, M. Ishaque, H.M. Khan, M. Naeem Ashiq, M.U. Rana, J. Magn. Magn. Mater. 324 (2012) 3773–3777.

[182] Y. Mohammadifar, H. Shokrollahi, Z. Karimi, L. Karimi, J. Magn. Magn. Mater. 366 (2014) 44–49.

[183] C. Murugesan, G. Chandrasekaran, RSC Adv. 5 (2015) 73714.

[184] M.T. Rahman, M. Vargas, C. V. Ramana, J. Alloys Compd. 617 (2014) 547–562.

[185] M. Ishaque, M. Azhar Khan, I. Ali, H.M. Khan, M. Asif Iqbal, M.U. Islam, M.F. Warsi, J. Magn. Magn. Mater. 372 (2014) 68–73.

[186] L. Guo, X. Shen, F. Song, L. Lin, Y. Zhu, Mater. Chem. Phys. 129 (2011) 943–947.

[187] S.G. Kakade, R.C. Kambale, Y.D. Kolekar, C. V Ramana, J. Phys. Chem. Solids. 98 (2016) 20–27.

[188] Z. Karimi, Y. Mohammadifar, H. Shokrollahi, S.K. Asl, G. Yousefi, L. Karimi, J. Magn. Magn. Mater. 361 (2014) 150–156.

[189] M.M. Rashad, R.M. Mohamed, H. El-Shall, J. Mater. Process. Technol. 198 (2008) 139–146.

[190] S.R. Naik, A. V. Salker, J. Mater. Chem. 22 (2012) 2740–2750.

[191] W.J. Nellis, S. Legvold, Phys. Rev. 180 (1969) 581–590.

[192] K.S. Lohar, A.M. Pachpinde, M.M. Langade, R.H. Kadam, S.E. Shirsath, J. Alloys

Compd. 604 (2014) 204–210.

[193] S. Prathapani, T. V Jayaraman, E.K. Varaprasadarao, J. Appl. Phys. 116 (2014) 023908.

[194] X. Meng, H. Li, J. Chen, L. Mei, K. Wang, X. Li, J. Magn. Magn. Mater. 321 (2009) 1155–1158.

[195] R.A. Pawar, S.M. Patange, Q.Y. Tamboli, V. Ramanathan, S.E. Shirsath, Ceram. Int. 42 (2016) 16096–16102.

[196] S.G. Kakade, R.C. Kambale, C. V Ramanna, Y.D. Kolekar, RSC Adv. 6 (2016) 33308–33317.

[197] B.D. Kevadiya, A.N. Bade, C. Woldstad, B.J. Edagwa, J.E.M. McMillan, B.R. Sajja, M.D. Boska, H.E. Gendelman, Acta Biomater. 49 (2017) 507–520.

[198] S.P. Kharat, R. Swadipta, R.C. Kambale, Y.D. Kolekar, C.V. Ramana, J. Appl. Phys. 122 (2017) 0–9.

[199] M. Vadivel, R.R. Babu, K. Sethuraman, K. Ramamurthi, M. Arivanandhan, J. Magn. Magn. Mater. 362 (2014) 122–129.

[200] E. Pervaiz, I.H. Gul, J. Magn. Magn. Mater. 324 (2012) 3695–3703.

[201] N. Kumari, V. Kumar, S. Khasa, S.K. Singh, Ceram. Int. 41 (2015) 1907–1911.

[202] R.K. Panda, R. Muduli, G. Jayarao, D. Sanyal, D. Behera, J. Alloys Compd. 669 (2016) 19–28.

[203] L. Kumar, P. Kumar, V. Kuncser, S. Greculeasa, B. Sahoo, M. Kar, Mater. Chem. Phys. 211 (2018) 54–64.

[204] P. Jadoun, J. Sharma, S. Kumar, S.N. Dolia, D. Bhatnagar, V.K. Saxena, Ceram. Int. 44 (2018) 6747–6753.

[205] B.G. Toksha, S.E. Shirsath, M.L. Mane, S.M. Patange, S.S. Jadhav, K.M. Jadhav, J. Phys. Chem. C. 4 (2011) 20905–20912.

[206] S. Singhal, S. Bhukal, Solid State Phenom. 202 (2013) 173–192.

[207] P. Muthukumarasamy, T. Nagarajan, A. Narayanasamy, J. Phys. C Solid State Phys. 13 (1980) 3961–3968.

[208] A. Lakshman, P.S. V. Subba Rao, K.H. Rao, Mod. Phys. Lett. B. 24 (2010) 1657–1667.

[209] K. Krieble, C.C.H. Lo, Y. Melikhov, J.E. Snyder, J. Appl. Phys. 99 (2006) 97–100.

[210] N. Jahan, F.U.Z. Chowdhury, A.K.M. Zakaria, M.N.I. Khan, M.S. Aktar, M.A. Hakim, J. Supercond. Nov. Magn. 30 (2017) 261–268.

[211] W. Zhang, X. Zuo, D. Zhang, C. Wu, S.R.P. Silva, Nanotechnology. 27 (2016) 245707.

[212] A.M. Abu-dief, M.S.M. Abdelbaky, D. Martínez-blanco, Z. Amghouz, S. García-granda, Mater. Chem. Phys. 174 (2016) 164–171.

[213] A. Xia, S. Liu, C. Jin, S. Su, J. Mater. Sci. Mater. Electron. 24 (2013) 4166–4169.

[214] S.J. Lee, C.C.H. Lo, P.N. Matlage, S.H. Song, Y. Melikhov, J.E. Snyder, D.C. Jiles, J. Appl. Phys. 102 (2007) 073910.

[215] M. Raghasudha, D. Ravinder, P. Veerasomaiah, K.M. Jadhav, M. Hashim, P. Bhatt, S.S. Meena, J. Alloys Compd. 694 (2017) 366–374.

[216] R.N. Singh, N.K. Singh, J.P. Singh, Electrochim. Acta. 47 (2002) 3873–3879.

[217] J.C. Maurya, S. V. Bhoraskar, V.L. Mathe, Phys. B Condens. Matter. 436 (2014) 220–226.

[218] A. Cojocariu, M. Soroceanu, L. Hrib, V. Nica, O. Florin, Mater. Chem. Phys. 135 (2012) 728–732.

[219] R.C. Kambale, P.A. Shaikh, C.H. Bhosale, K.Y. Rajpure, Y.D. Kolekar, Smart Mater. Struct. 18 (2009) 115028.

[220] E.R. Kumar, A.S. Kamzin, K. Janani, J. Magn. Magn. Mater. 417 (2016) 122–129.

[221] A. Manikandan, M. Durka, S. Antony, J. Supercond. Nov. Magn. 27 (2014) 2841–2857.

[222] S.P. Yadav, S.S. Shinde, A.A. Kadam, K.Y. Rajpure, J. Semicond. 34 (2013) 093002.

[223] A.H. Ashour, A.I. El-Batal, M.I.A.A. Maksoud, G.S. El-Sayyad, S. Labib, E. Abdeltwab, M.M. El-Okr, Particuology. 40 (2018) 141–151.

[224] S. Jauhar, S. Singhal, M. Dhiman, Appl. Catal. A, Gen. 486 (2014) 210–218.

[225] A. Goyal, S. Bansal, V. Kumar, J. Singh, S. Singhal, Appl. Surf. Sci. 324 (2015) 877–889.

[226] M. Atif, M. Idrees, M. Nadeem, M. Siddique, M.W. Ashraf, RSC Adv. 6 (2016) 20876–20885.

[227] C.Y. Tsay, Y.H. Lin, S.U. Jen, Ceram. Int. 41 (2015) 5531–5536.

[228] Y.D. Kolekar, L.J. Sanchez, C. V. Ramana, J. Appl. Phys. 115 (2014) 144106.

[229] S.D. Bhame, P.A. Joy, J. Appl. Phys. 99 (2006) 073901.

[230] P. Vlazan, I. Miron, P. Sfirloaga, Ceram. Int. 41 (2015) 3760–3765.

[231] S.D. Bhame, P.A. Joy, J. Phys. D. Appl. Phys. 40 (2007) 3263–3267.

[232] C. V. Ramana, Y.D. Kolekar, K. Kamala Bharathi, B. Sinha, K. Ghosh, J. Appl. Phys. 114 (2013) 183907.

[233] J.A. Paulsen, A.P. Ring, C.C.H. Lo, J.E. Snyder, D.C. Jiles, J. Appl. Phys. 97 (2005) 044502.

[234] P.N. Anantharamaiah, P.A. Joy, J. Phys. D. Appl. Phys. 50 (2017) 435005.

[235] S. Verma, J. Chand, K.M. Batoo, M. Singh, J. Alloys Compd. 565 (2013) 148–153.

[236] M. Hashim, S.E. Shirsath, S. Kumar, R. Kumar, A.S. Roy, J. Shah, R.K. Kotnala, J. Alloys Compd. 549 (2013) 348–357.

[237] S. Kumar, T.J. Shinde, P.N. Vasambekar, J. Magn. Magn. Mater. 379 (2015) 179–

185.

[238] S. Kumar, T.J. Shinde, P.N. Vasambekar, K. Bhatt, IEEE Trans. Magn. 51 (2015).

[239] P. Mathur, A. Thakur, M. Singh, J. Phys. Chem. Solids. 69 (2008) 187–192.

[240] P. Vlazan, S.F. Rus, I. Grozescu, E. Vasile, Phys. Scr. T157 (2013) 014047.

[241] C.Y. Tsay, S.C. Liang, C.M. Lei, C.C. Chang, Ceram. Int. 42 (2016) 4748–4753.

[242] R. Pandit, K.K. Sharma, P. Kaur, R. Kumar, Mater. Chem. Phys. 148 (2014) 988–999.

[243] S.E. Shirsath, B.G. Toksha, K.M. Jadhav, Mater. Chem. Phys. 117 (2009) 163–168.

[244] A. Lakshman, K.H. Rao, R.G. Mendiratta, J. Magn. Magn. Mater. 250 (2002) 92–97.

[245] B.P. Rao, K.H. Rao, J. Magn. Magn. Mater. 292 (2005) 44–48.

[246] S. Thakur, S.C. Katyal, A. Gupta, V.R. Reddy, M. Singh, J. Appl. Phys. 105 (2009) 10–13.

[247] S. Verma, J. Chand, M. Singh, J. Magn. Magn. Mater. 324 (2012) 3252–3260.

[248] F. Meng, X. Shang, W. Zhang, Y. Zhang, Phys. B Condens. Matter. 504 (2017) 69–73.

[249] M. Singh, S.P. Sud, Mater. Sci. Eng. B Solid-State Mater. Adv. Technol. 83 (2001) 180–184.

[250] R. Nongjai, S. Khan, K. Asokan, H. Ahmed, I. Khan, J. Appl. Phys. 112 (2012) 084321.

[251] A. Lakshman, P.S.V.S. Rao, B.P. Rao, K.H. Rao, J. Phys. D. Appl. Phys. 38 (2005) 673–678.

[252] G. Chen, W. Qi, Y. Li, C. Yang, X. Zhao, J. Mater. Sci. Mater. Electron. 27 (2016) 5628–5634.

[253] L. Zhao, D. Wang, D. Meng, W. Chen, Optik (Stuttg). 156 (2018) 8–12.

[254] J. Zhou, Y. Zhu, H. Liu, L. Wang, J. Mater. Sci. Mater. Electron. 28 (2017) 14758–14762.

[255] M.D. Rabasović, B.D. Murić, V. Čelebonović, M. Mitrić, B.M. Jelenković, M.G. Nikolić, J. Phys. D. Appl. Phys. 49 (2016) 485104.

[256] J.B. Prasanna Kumar, G. Ramgopal, Y.S. Vidya, K.S. Anantharaju, B. Daruka Prasad, S.C. Sharma, S.C. Prashantha, H.B. Premkumar, H. Nagabhushana, Spectrochim. Acta - Part A Mol. Biomol. Spectrosc. 141 (2015) 149–160.

[257] A. Gupta, N. Brahme, D.P. Bisen, Phys. Procedia. 76 (2015) 16–24.

[258] Y.N. Zhu, G.H. Zheng, X. Xin, R. Zhuang, L.Y. Zhang, J. Mater. Sci. Mater. Electron. 28 (2017) 1485–1488.

[259] K. Lingadurai, B. Sundarakannan, E.R. Nagarajan, H. Kominami, Y. Nakanishi, M. Kottaisamy, J. Lumin. 177 (2016) 249–253.

[260] G.A. Sobral, M.A. Gomes, J.F.M. Avila, J.J. Rodrigues, Z.S. Macedo, J.M.

Hickmann, M.A.R.C. Alencar, J. Phys. Chem. Solids. 98 (2016) 81–90.

[261] A.P. Jadhav, S. Khan, S.Y. Lee, J.K. Park, S.W. Park, J.H. Oh, B.K. Moon, K. Jang, S.S. Yi, J.H. Kim, S.H. Cho, J.H. Jeong, Mater. Res. Bull. 83 (2016) 186–192.

[262] S. Nigam, C.S. Kamal, K.R. Rao, V. Sudarsan, R.K. Vatsa, J. Lumin. 178 (2016) 219–225.

[263] M. Kabir, M. Ghahari, M. Shafiee Afarani, Ceram. Int. 40 (2014) 10877–10885.

[264] Y. Jin, H.-P. Zhou, M.-S. Jiang, J. Nanosci. Nanotechnol. 16 (2016) 704–708.

[265] W. Chen, M. Zhuo, Y. Liu, S. Fu, Y. Liu, Y. Wang, Z. Li, Y. Li, Y. Li, L. Yu, J. Alloys Compd. 656 (2016) 764–770.

[266] W. Xie, Y. Wang, C. Zou, J. Quan, L. Shao, J. Alloys Compd. 619 (2015) 244–247.

[267] G. Chen, Y. Li, W. Qi, C. Yang, X. Zhao, J. Mater. Sci. Mater. Electron. 29 (2018) 2841–2847.

[268] Y. Wu, G. Jin, Z. Liu, T. He, J. Mater. Sci. Mater. Electron. 27 (2016) 6188–6192.

[269] A. García-Murillo, F. de J. Carrillo-Romo, J. Oliva-Uc, T.A. Esquivel-Castro, S.D. de la Torre, Ceram. Int. 43 (2017) 12196–12204.

[270] H.J. Devi, W.R. Singh, R.S. Loitongbam, J. Fluoresc. 26 (2016) 875–889.

[271] A.M. Khachatourian, F. Golestani-Fard, H. Sarpoolaky, C. Vogt, E. Vasileva, M.

Mensi, S. Popov, M.S. Toprak, J. Lumin. 169 (2016) 1–8.

[272] L. Lamiri, L. Guerbous, M. Samah, A. Boukerika, S. Ouhenia, Luminescence. 30 (2015) 1336–1343.

[273] S. Som, S.K. Sharma, T. Shripathi, J. Fluoresc. 23 (2013) 439–450.

[274] S. Som, S.K. Sharma, J. Phys. D. Appl. Phys. 45 (2012) 415102.

[275] M.K. Devaraju, S. Yin, T. Sato, IOP Conf. Ser. Mater. Sci. Eng. 1 (2009) 012011.

[276] K. Higashi, Y. Watanabe, Y. Iso, T. Isobe, RSC Adv. 7 (2017) 6671–6678.

[277] D. Kumar, M. Sharma, O.P. Pandey, Opt. Mater. (Amst). 36 (2014) 1131–1138.

[278] Y. Gao, S. Zhan, Y. Liu, Opt. Commun. 285 (2012) 3150–3153.

[279] L. Gao, G. Wang, H. Zhu, W. Zhou, G. Ou, Mater. Res. Bull. 70 (2015) 876–880.

[280] J.S. Cho, K.M. Yang, Y.C. Kang, CrystEngComm. 16 (2014) 6170.

[281] Y. Xiao, D. Wu, Y. Jiang, N. Liu, J. Liu, K. Jiang, J. Alloys Compd. 509 (2011) 5755–5760.

[282] S. Zhong, J. Chen, S. Wang, Q. Liu, Y. Wang, S. Wang, J. Alloys Compd. 493 (2010) 322–325.

[283] T. Yan, D. Zhang, L. Shi, H. Yang, H. Mai, J. Fang, Mater. Chem. Phys. 117 (2009) 234–243.

[284] H.Q. Yu, H. Zheng, Y. Li, H.D. Wang, Y.B. Wu, P. Li, J. Nanosci. Nanotechnol. 14 (2014) 3648–3652.

[285] A. Boukerika, L. Guerbous, J. Lumin. 145 (2014) 148–153.

[286] R. Hari Krishna, B.M. Nagabhushana, H. Nagabhushana, N.S. Murthy, S.C. Sharma, C. Shivakumara, R.P.S. Chakradhar, J. Phys. Chem. C. 117 (2013) 1915–1924.

[287] M. Back, E. Trave, R. Marin, N. Mazzucco, D. Cristofori, P. Riello, J. Phys. Chem. C. 118 (2014) 30071−30078.

[288] J.A. Dorman, J.H. Choi, G. Kuzmanich, J.P. Chang, J. Phys. Chem. C. 116 (2012) 10333–10340.

[289] M. Kaur, D.P. Bisen, N. Brahme, P. Singh, I.P. Sahu, Luminescence. 31 (2016) 728–737.

[290] V. Singh, V.K. Rai, I. Ledoux-Rak, S. Watanabe, T.K. Gundu Rao, J.F.D. Chubaci, L. Badie, F. Pelle, S. Ivanova, J. Phys. D. Appl. Phys. 42 (2009) 065104.

[291] F. Vetrone, J.-C. Boyer, J.A. Capobianco, A. Speghini, M. Bettinelli, J. Mater. Res. 19 (2004) 3398–3407.

[292] L. Zong, P. Xu, Y. Ding, K. Zhao, Z. Wang, X. Yan, R. Yu, J. Chen, X. Xing, Small. 11 (2015) 2768–2773.

[293] P. Kumar, J. Dwivedi, B.K. Gupta, J. Mater. Chem. C. 2 (2014) 10468–10475.

[294] K. Yamamoto, M. Fujii, S. Sowa, K. Imakita, K. Aoki, J. Phys. Chem. C. 119 (2015) 1175–1179.

[295] A.N. Gruzintsev, Y. V. Ermolaeva, N.A. Matveevskaya, A.S. Bezkrovnyi, A. V.

Tolmachev, G.A. Emel'chenko, Inorg. Mater. 50 (2014) 1099–1103.

[296] T. Kodama, M. Fujii, T. Nakano, K. Imakita, S. Hayashi, Opt. Mater. (Amst). 35 (2013) 2394–2399.

[297] S. Huang, J. Xu, Z. Zhang, X. Zhang, L. Wang, S. Gai, F. He, N. Niu, M. Zhang, P. Yang, J. Mater. Chem. 22 (2012) 16136.

[298] A. Peeva, A.O. Dikovska, P.A. Atanasov, M.J. de Castro, W. Skorupa, Appl. Surf. Sci. 253 (2007) 8165–8168.

[299] A. Scarangella, R. Reitano, G. Franzò, F. Priolo, M. Miritello, J. Lumin. 191 (2017) 92–96.

[300] Y. Mao, X. Guo, T. Tran, K.L. Wang, C.K. Shih, J.P. Chang, J. Appl. Phys. 105 (2009) 094329.

[301] V. Kumar Rai, A. Pandey, R. Dey, J. Appl. Phys. 113 (2013) 083104.

[302] X. Zhao, H. Suo, Z. Zhang, C. Guo, Ceram. Int. 44 (2018) 2911–2918.

[303] J. Leng, J. Chen, D. Wang, J.X. Wang, Y. Pu, J.F. Chen, Ind. Eng. Chem. Res. 56 (2017) 7977–7983.

[304] D. Li, W. Qin, T. Aidilibike, P. Zhang, S. Liu, L. Wang, S. Li, J. Alloys Compd. 675 (2016) 31–36.

[305] Y. Tian, B. Tian, C. Cui, P. Huang, L. Wang, B. Chen, RSC Adv. 5 (2015) 14123–14128.

[306] R.K. Tamrakar, D.P. Bisen, K. Upadhyay, N. Bramhe, Superlattices Microstruct. 81 (2015) 34–48.

[307] R.K. Tamrakar, D.P. Bisen, K. Upadhyay, I.P. Sahu, J. Alloys Compd. 655 (2016) 423–432.

[308] J. Liu, L. Huang, X. Tian, X. Chen, Y. Shao, F. Xie, D. Chen, L. Li, Int. J. Nanomedicine. 12 (2017) 1–14.

[309] J. Tang, Y. Zhang, J. Gou, Z. Ma, G. Li, Y. Man, N. Cheng, J. Alloys Compd. 740 (2018) 229–236.

[310] N. Babayevska, B. Peplińska, M. Jarek, L. Yate, K. Tadyszak, J. Gapiński, I. Iatsunskyi, S. Jurga, RSC Adv. 6 (2016) 89305–89312.

[311] D.H. Chávez, O.E. Contreras, G.A. Hirata, Nanomater. Nanotechnol. 6–7 (2016) 1–10.

[312] H. Guo, Y. Li, D. Wang, W. Zhang, M. Yin, L. Lou, S. Xia, J. Alloys Compd. 376 (2004) 23–27.

[313] K.W. Chae, T.R. Park, C. Il Cheon, N. In Cho, J. Seog Kim, J. Lumin. 132 (2012) 2293–2301.

[314] D.K. Xu, C.F. Liu, J.W. Yan, H.Q. Ouyang, S.H. Yang, Y.L. Zhang, Phys. Procedia. 76 (2015) 160–164.

[315] M.L. Pang, J. Lin, J. Fu, R.B. Xing, C.X. Luo, Y.C. Han, Opt. Mater. (Amst). 23 (2003) 547–558.

[316] E. Hemmer, H. Takeshita, T. Yamano, T. Fujiki, Y. Kohl, K. Löw, N. Venkatachalam, H. Hyodo, H. Kishimoto, K. Soga, J. Mater. Sci. Mater. Med. 23 (2012) 2399–2412.

[317] G. Bilir, O. Erguzel, Mater. Res. Express. 3 (2016) 106201.

[318] S.K. Singh, K. Kumar, S.B. Rai, Appl. Phys. B Lasers Opt. 94 (2009) 165–173.

[319] H. Li, S. Song, W. Wang, K. Chen, Dalt. Trans. 44 (2015) 16081–16090.

[320] M. Hanioka, S. Arimoto, H. Samata, Optik (Stuttg). 154 (2018) 226–233.

[321] J. Liu, H. Deng, Z. Huang, Y. Zhang, D. Chen, Y. Shao, Phys. Chem. Chem. Phys. 17 (2015) 15412–15418.

[322] Y. Lei, H. Song, L. Yang, L. Yu, Z. Liu, G. Pan, X. Bai, L. Fan, J. Chem. Phys. 123 (2005) 174710.

[323] D. Li, W. Qin, P. Zhang, L. Wang, M. Lan, P. Shi, Opt. Mater. Express. 7 (2017) 329.

[324] S.K. Singh, K. Kumar, S.B. Rai, J. Appl. Phys. 106 (2009) 093520.

[325] S.K. Ranjan, R. Dey, A.K. Soni, V. Rai, IEEE Sens. J. 16 (2016) 18494–8500.

[326] S. Zhang, J. Zhou, R. Wu, L. Lei, Z. Xiao, J. Zhang, S. Xu, RSC Adv. 5 (2015) 92988–92994.

[327] Z. Liu, F. Pu, S. Huang, Q. Yuan, J. Ren, X. Qu, Biomaterials. 34 (2013) 1712–1721.

[328] P. Singh, P.K. Shahi, A. Rai, A. Bahadur, S.B. Rai, Opt. Mater. (Amst). 58 (2016) 432–438.

[329] Ž. Antić, V. Lojpur, M.G. Nikolić, V. Crossed D Signorcrossed D Signević, P.S. Ahrenkiel, M.D. Dramićanin, J. Lumin. 145 (2014) 466–472.

[330] Y. Gao, Q. Zhao, Q. Fang, Z. Xu, Dalt. Trans. 42 (2013) 11082.

[331] Y. Jia, Y. Song, Y. Bai, Y. Wang, Luminescence. 26 (2011) 259–263.

[332] A. Kumar, S.P. Tiwari, K. Kumar, V.K. Rai, Spectrochim. Acta - Part A Mol. Biomol. Spectrosc. 167 (2016) 134–141.

[333] J. Yin, C. Li, Y. Yang, W. Hu, H. Liu, Y. Shao, RSC Adv. 6 (2016) 72836–72844.

[334] E.B. Michael, Introduction to Thermal Analysis Techniques and Applications, Kluwer Academic Publisher, 2004.

[335] P. Gabbott, Principles and Applications of Thermal Analysis, Blackwell Publishing, 2008.

[336] A.R. West, Solid State Chemistry and its Applications, John Wiley & Sons, 1984.

[337] B. Culity, S. Stock, Elements of X-Ray Diffraction, Pearson Education Limited, 2014.

[338] G.L. Moore, Introduction to inductively coupled plasma atomic emission spectrometry, Elsevier science publishers, 1989.

[339] C. Boss, K. Fredeen, Concepts, Instrumentation and Techniques in Inductively

Coupled Plasma Optical Emission Spectrometry, Perkin Elmer, 2004.

[340] K. Nakamoto, Infrared and Raman Spectra of Inorganic and Coordination Compounds Part A : Theory and Applications, John Wiley & Sons, 2008.

[341] K. Nakamoto, Infrared and Raman Spectra of Inorganic and Coordination Compounds, John Wiley & Sons, 2008.

[342] J. Ferraro, K. Nakamoto, C. Brown, Introductory Raman Spectroscopy, Elsevier, 2003.

[343] J. Goldstein, D. Newbury, J. Michael, N. Ritchie, J. Scott, D. Joy, Scanning Electron Microscopy and X-Ray Microanalysis, Springer Science Business Media, 2018.

[344] D. Williams, C. Carter, Transmission Electron Microscopy, Springer Science+Business Media, 1996.

[345] P. Heide, X-ray photoelectron spectroscopy: An Introduction to Principles and Practices, A John Wiley & sons, INC., publication, 2012.

[346] R.K. Gupta, F. Yakuphanoglu, F.M. Amanullah, Phys. E Low-Dimensional Syst. Nanostructures. 43 (2011) 1666–1668.

[347] J. Dharma, A. Pisal, PerkinElmer, Inc. (2009) 4.

[348] Y. Yoshida, G. Langouche, Mössbauer Spectroscopy, Springer-Verlag Berlin Heidelberg, 2013.

[349] G.P. Michael Gaft, Renata Reisfeld, Luminescence Spectroscopy of Minerals and

Materials, Springer-Verlag Berlin Heidelberg, 2005.

[350] F. Zhang, Photon Upconversion Nanomaterials, Springer-Verlag Berlin Heidelberg, 2015.

[351] R.C. Kambale, K.M. Song, Y.S. Koo, N. Hur, J. Appl. Phys. 110 (2011) 053910.

[352] M.A. Khan, M.U. Islam, M. Ishaque, I.Z. Rahman, A. Genson, S. Hampshire, Mater. Charact. 60 (2009) 73–78.

[353] K.N. Harish, H.S. Bhojya Naik, P.N. Prashanth Kumar, R. Viswanath, ACS Sustain. Chem. Eng. 1 (2013) 1143–1153.

[354] R. Waldron, Phys. Rev. 99 (1955) 1727–1735.

[355] S. Kapoor, A. Goyal, S. Bansal, S. Singhal, New J. Chem. 42 (2018) 14965–14977.

[356] L. Hernández-Adame, A. Méndez-Blas, J. Ruiz-García, J.R. Vega-Acosta, F.J. Medellín-Rodríguez, G. Palestino, Chem. Eng. J. 258 (2014) 136–145.

[357] P. Chandramohan, M.P. Srinivasan, S. Velmurugan, S.V. Narasimhan, J. Solid State Chem. 184 (2011) 89–96.

[358] P. Anantharamaiah, P. Joy, Phys. Chem. Chem. Phys. 18 (2016) 10516–10527.

[359] F.D. Saccone, S. Ferrari, D. Errandonea, F. Grinblat, V. Bilovol, S. Agouram, J. Appl. Phys. 118 (2015) 075903.

[360] M. Vadivel, R. Ramesh, B.R. Arivanandhan, J. Supercond. Nov. Magn. 30 (2016)

441–453.

[361] W. Zhang, B. Quan, C. Lee, S.K. Park, X. Li, E. Choi, G. Diao, Y. Piao, ACS Appl. Mater. Interfaces. 7 (2015) 2404–2414.

[362] Z. Gu, X. Xiang, G. Fan, F. Li, J. Phys. Chem. C. 112 (2008) 18459–18466.

[363] R. Tholkappiyan, K. Vishista, Phys. B Condens. Matter. 448 (2014) 177–183.

[364] S.R. Naik, A. V. Salker, S.M. Yusuf, S.S. Meena, J. Alloys Compd. 566 (2013) 54–61.

[365] Y. Zhang, J. Tian, K. Jiang, J. Huang, H. Wang, Y. Song, Mater. Lett. 209 (2017) 23–26.

[366] R.S. Yadav, J. Havlica, J. Masilko, L. Kalina, J. Supercond. Nov. Magn. 29 (2015) 759–769.

[367] N. Zhang, D. Chen, F. Niu, S. Wang, L. Qin, Y. Huang, Sci. Rep. 6, 26467 (2016) 1–11.

[368] A. Mukherjee, S. Basu, P.K. Manna, S.M. Yusuf, M. Pal, J. Mater. Chem. C. 2 (2014) 5885–5891.

[369] R.S. Yadav, J. Havlica, I. Kuritka, Z. Kozakova, M. Palou, E. Bartonickova, M. Bohac, F. Frajkorova, J. Masilko, L. Kalina, M. Hajduchova, V. Enev, J. Wasserbauer, J. Supercond. Nov. Magn. 28 (2015) 2097–2107.

[370] G. Rekha, R. Tholkappiyan, K. Vishista, F. Hamed, Appl. Surf. Sci. 385 (2016) 171–181.

[371] R.J. Choudhary, S. Kumar, R. Prakash, D.M. Phase, V. Kumar, G.M. Bhalerao, Adv. Powder Technol. 26 (2015) 1263–1268.

[372] Q. He, K. Rui, C. Chen, J. Yang, Z. Wen, ACS Appl. Mater. Interfaces. 9 (2017) 36927–36935.

[373] K. Zhang, J. Li, F. Wu, M. Sun, Y. Xia, A. Xie, ACS Appl. Nano Mater. 2 (2018) 315–324.

[374] A. Bumajdad, S. Al-Ghareeb, M. Madkour, F. Al Sagheer, Sci. Rep. 7 (2017) 2–10.

[375] F. Pan, W. Liu, Y. Yu, X. Yin, Q. Wang, Z. Zheng, M. Wu, D. Zhao, Q. Zhang, X. Lei, D. Xia, Sci. Rep. 6 (2016) 1–11.

[376] P. Liu, H. He, G. Wei, X. Liang, F. Qi, F. Tan, W. Tan, J. Zhu, R. Zhu, Appl. Catal. B Environ. 182 (2016) 476–484.

[377] J. Bennet, R. Tholkappiyan, K. Vishista, N.V. Jaya, F. Hamed, Appl. Surf. Sci. 383 (2016) 113–125.

[378] O. Akhavan, R. Azimirad, S. Safa, E. Hasani, J. Mater. Chem. 21 (2011) 9634–9640.

[379] P. Rao, R.C. Chikate, S. Bhagwat, New J. Chem. 40 (2016) 1720–1728.

[380] H. Li, Y. Ding, Y. Wang, CrystEngComm. 14 (2012) 4767–4771.

[381] T.M. Pan, C.H. Chen, J.H. Liu, RSC Adv. 4 (2014) 29300–29304.

[382] S.J. Stewart, R.C. Mercader, R.E. Vandenberghe, G. Cernicchiaro, R.B. Scorzelli, J. Appl. Phys. 97 (2005) 054304.

[383] D.C. Dobson, J.W. Linnett, M.M. Rahman, J. Phys. Chem. Solids. 31 (1970) 2727–2733.

[384] M. Kaiser, Mater. Res. Bull. 73 (2016) 452–458.

[385] P.P. Naik, R.B. Tangsali, S.S. Meena, P. Bhatt, B. Sonaye, S. Sugur, Radiat. Phys. Chem. 102 (2014) 147–152.

[386] K. Krieble, T. Schaeffer, J.A. Paulsen, A.P. Ring, C.C.H. Lo, J.E. Snyder, J. Appl. Phys. 97 (2005) 10F101.

[387] C. Cao, L. Zhang, S. Ren, J. Mater. Sci. Mater. Electron. 25 (2014) 2578–2582.

[388] K. Li, K. Sun, C. Chen, X. Liu, R. Guo, H. Liu, Z. Yu, X. Jiang, Z. Lan, J. Alloys Compd. 752 (2018) 395–401.

[389] P.K. Roy, B.B. Nayak, J. Bera, J. Magn. Magn. Mater. 320 (2008) 1128–1132.

[390] D. Pal, M. Mandal, A. Chaudhuri, B. Das, D. Sarkar, K. Mandal, J. Appl. Phys. 108 (2010) 124317–5.

[391] L. Ben Tahar, M. Artus, S. Ammar, L.S. Smiri, F. Herbst, M.J. Vaulay, V. Richard, J.M. Greneche, F. Villain, F. Fievet, J. Magn. Magn. Mater. 320 (2008) 3242–3250.

[392] F.-X. Cheng, J.-T. Jia, Z.-G. Xu, B. Zhou, C.-S. Liao, C.-H. Yan, L.-Y. Chen, H.-B. Zhao, J. Appl. Phys. 86 (1999) 2727–2732.

[393] B.A. Calhoun, M.J. Freiser, J. Appl. Phys. 34 (1963) 1140–1145.

[394] F. Cheng, C. Liao, J. Kuang, Z. Xu, C. Yan, L. Chen, H. Zhao, Z. Liu, J. Appl. Phys. 85 (1999) 2782–2786.

[395] S. Amiri, H. Shokrollahi, J. Magn. Magn. Mater. 345 (2013) 18–23.

[396] L. Zhao, H. Yang, L. Yu, Y. Cui, X. Zhao, S. Feng, J. Magn. Magn. Mater. 305 (2006) 91–94.

[397] H. Kumar, R.C. Srivastava, J. Pal, P. Negi, H.M. Agrawal, D. Das, J. Magn. Magn. Mater. 401 (2016) 16–21.

[398] A.K. Nikumbh, R.A. Pawar, D. V Nighot, G.S. Gugale, M.D. Sangale, M.B. Khanvilkar, A. V Nagawade, J. Magn. Magn. Mater. 355 (2014) 201–209.

[399] A.K. Sijo, Ceram. Int. 43 (2016) 2288–2290.

[400] L.Z. Li, X.Q. Tu, R. Wang, L. Peng, J. Magn. Magn. Mater. 381 (2015) 328–331.

[401] S.T. Alone, S.E. Shirsath, R.H. Kadam, K.M. Jadhav, J. Alloys Compd. 509 (2011) 5055–5060.

[402] H. Bahiraei, M. Zargar, K. Gheisari, C.K. Ong, J. Magn. Magn. Mater. 371 (2014) 29–34.

[403] N.S. Gajbhiye, S. Prasad, G. Balaji, IEEE Trans. Magn. 35 (1999) 2155–2161.

[404] M.A. Gabal, Y.M. Al Angari, J. Magn. Magn. Mater. 322 (2010) 3159–3165.

[405] S.M. Patange, S.E. Shirsath, B.G. Toksha, S.S. Jadhav, K.M. Jadhav, J. Appl.

Phys. 106 (2009) 023914.

[406] M. Ul-Islam, T. Abbas, M. Ashraf Chaudhry, Mater. Lett. 53 (2002) 30–34.

[407] G.R. Kumar, Y.C. Venudhar, A.T. Raghavender, K.V. Kumar, J. Korean Phys. Soc. 60 (2012) 1082–1086.

[408] E.J.W. Verwey, P.W. Haayman, Physica. 8 (1941) 979–987.

[409] A.A. Kadam, S.S. Shinde, S.P. Yadav, P.S. Patil, K.Y. Rajpure, J. Magn. Magn. Mater. 329 (2013) 59–64.

[410] N. Kumari, V. Kumar, S.K. Singh, J. Alloys Compd. 622 (2015) 628–634.

[411] J. Maxwell, Electricity and Magnetism, Oxford Univ. Press, London, 1973.

[412] C.G. Koops, Phys. Rev. 83 (1951) 121–124.

[413] P.S. Das, G.P. Singh, J. Magn. Magn. Mater. 401 (2016) 918–924.

[414] R. V Mangalaraja, P. Manohar, F.D. Gnanam, J. Mater. Sci. 9 (2004) 2037–2042.

[415] S.G. Kakade, Y.R. Ma, R.S. Devan, Y.D. Kolekar, C. V. Ramana, J. Phys. Chem. C. 120 (2016) 5682–5693.

[416] R.M. Sebastian, E.M. Mohammed, Ferroelectrics. 504 (2016) 53–63.

[417] D. Rathore, R. Kurchania, R. Pandey, J. Compos. Mater. 21 (2014) 408–414.

[418] A. Verma, O.P. Thakur, C. Prakash, T.C. Goel, R.G. Mendiratta, Mater. Sci. Eng. B. 116 (2005) 1–6.

[419] R.C. Kambale, P.A. Shaikh, C.H. Bhosale, K.Y. Rajpure, Y.D. Kolekar, Smart Mater. Struct. 18 (2009) 115028.

[420] M. Maisnam, S. Phanjoubam, H.N.K. Sarma, L.R. Devi, O.P. Thakur, C. Prakash, Mod. Phys. Lett. B. 21 (2007) 497–503.

[421] M. Lakshmi, K.V. Kumar, K. Thyagarajan, Adv. Mater. Phys. Chem. 6 (2016) 141–148.

[422] M. Hashim, M. Raghasudha, J. Shah, S.E. Shirsath, D. Ravinder, S. Kumar, S.S. Meena, P. Bhatt, Alimuddin, R. Kumar, R.K. Kotnala, J. Phys. Chem. Solids. 112 (2018) 29–36.

[423] A.R. Shitre, V.B. Kawade, G.K. Bichile, K.M. Jadhav, Mater. Lett. 56 (2002) 188–193.

[424] N. Dhananjaya, H. Nagabhushana, B.M. Nagabhushana, B. Rudraswamy, C. Shivakumara, R.P.S. Chakradhar, Bull. Mater. Sci.,. 35 (2012) 519–527.

[425] A. Bauer, W. Kirby, J. Sherris, M. Turck, Am. J. Clin. Pathol. 45 (1966) 493–496.

[426] A. Samavati, A.F. Ismail, Particuology. 30 (2016) 158–163.

[427] M. Vincent, P. Hartemann, M. Engels-Deutsch, Int. J. Hyg. Environ. Health. 219 (2016) 585–591.

[428] R. Brayner, R. Ferrari-Iliou, N. Brivois, S. Djediat, M.F. Benedetti, F. Fiévet, Nano Lett. 6 (2006) 866–870.

[429] J.R. Morones, J.L. Elechiguerra, A. Camacho, K. Holt, J.B. Kouri, J.T. Ramírez,

M.J. Yacaman, Nanotechnology. 16 (2005) 2346–2353.

[430] A.K. Chatterjee, R. Chakraborty, T. Basu, Nanotechnology. 25 (2014) 135101.

[431] R. Hong, T.Y. Kang, C.A. Michels, N. Gadura, Appl. Environ. Microbiol. 78 (2012) 1776–1784.

[432] R. Trevejo, M. Barr, R. Robinson, Vet. Res. 36 (2005) 493–506.

[433] K. Gurleen, R. Savio, J. Dent. Med. Sci. 15 (2016) 47–49.

[434] U. Kamat, A. Fereirra, D. Amonkar, D. Motghare, M. Kulkarni, Indian J. Urol. 25 (2009) 76–80.

[435] S.B. Patil, H.S.B. Naik, G. Nagaraju, R. Viswanath, S.K. Rashmi, Eur. Phys. J. Plus. 132 (2017) 1–12.

[436] M.I.A. Abdel Maksoud, G.S. El-Sayyad, A.H. Ashour, A.I. El-Batal, M.S. Abd-Elmonem, H.A.M. Hendawy, E.K. Abdel-Khalek, S. Labib, E. Abdeltwab, M.M. El-Okr, Mater. Sci. Eng. C. 92 (2018) 644–656.

APPENDIX I

PUBLICATIONS

1. **Chandan C. Naik** and A. V. Salker

   Tailoring magnetic and dielectric properties of $Co_{0.9}Cu_{0.1}Fe_2O_4$ with substitution of small fractions of Gd^{3+} ions.

   J. Mater. Sci. Mater. Electron. 29 (2018) 5380–5390.

2. **Chandan C. Naik**, S. K. Gaonkar, I. Furtado and A. V. Salker

   Effect of Cu^{2+} substitution on structural, magnetic and dielectric properties of cobalt ferrite with its enhanced antimicrobial property.

   J. Mater. Sci. Mater. Electron. 29 (2018) 14746–14761.

3. **Chandan C. Naik** and A. V. Salker

   Investigation of the effect of fractional In^{3+} ion substitution on the structural, magnetic, and dielectric properties of Co-Cu ferrite.

   J. Phys. Chem. Solids. 133 (2019) 151–162.

4. **Chandan C. Naik** and A. V. Salker

   Structural, magnetic and dielectric properties of Dy^{3+} and Sm^{3+} substituted Co–Cu ferrite.

   Mater. Res. Express. 6 (2019) 1–32.

5. **Chandan C. Naik** and A. V. Salker

   Effect Cr^{3+} Ion Substitution on the Structural, Magnetic, and Dielectric Behavior of Co–Cu Ferrite.

   J. Supercond. Nov. Magn. (2019), DOI:10.1007/s10948-019-05153-1.

6. **Chandan C. Naik** and A. V. Salker

   Effect of fractional substitution of Sb^{3+} ions on structural, magnetic and electrical properties of cobalt ferrite.

   (Communicated 2018)

APPENDIX II

CONFERENCE/SYMPOSIUM PRESENTATIONS

1. **Chandan C. Naik** and A.V.Salker, **"A magnetic, dielectric and antimicrobial study on Cu^{2+} substituted Cobalt ferrite.",**Frontiers in Chemical Sciences (FICS-2018), December 6-8, 2018, IIT-Guwahati.
2. **Chandan C. Naik** and A.V.Salker, **"Thermal and electrical studies of Gd^{3+} substituted Cobalt-copper ferrite prepared by sol-gel autocombustion method."** (**Oral presentation**), THERMANS - 2018, January 18-20, 2018, Goa University.
3. **Chandan C. Naik** and A.V.Salker, **"Investigation on the photoluminescence properties of Ce^{3+} and Eu^{3+} co-doped Y_2O_3 prepared by solution combustion method."**, NCAST – 2019, February 9th 2019, Govt. college of Arts, Science and commerce, Khandola-Goa.